Ultra-High-Resolution Optical Imaging for Silicon Integrated-Circuit Inspection

Keith Andrew Serrels, MPhys (Hons)

Submitted for the degree of Doctor of Philosophy

Heriot-Watt University

Ultrafast Optics Group

School of Engineering and Physical Sciences (EPS)

David Brewster Building

Riccarton Campus

EH14 4AS

May 2009

ABSTRACT

This thesis concerns the development of novel resolution-enhancing optical techniques for the purposes of non-destructive sub-surface semiconductor integrated-circuit (IC) inspection. This was achieved by utilising solid immersion lens (SIL) technology, polarisation-dependent imaging, pupil-function engineering and optical coherence tomography (OCT).

A SIL-enhanced two-photon optical beam induced current (TOBIC) microscope was constructed for the acquisition of ultra-high-resolution two- and three-dimensional images of a silicon flip-chip using a 1.55µm modelocked Er:fibre laser. This technology provided diffraction-limited lateral and axial resolutions of 166nm and 100nm, respectively - an order of magnitude improvement over previous TOBIC imaging work.

The ultra-high numerical aperture (NA) provided by SIL-imaging in silicon (NA=3.5) was used to show, for the first time, the presence of polarisation-dependent vectorial-field effects in an image. These effects were modelled using vector diffraction theory to confirm the increasing ellipticity of the focal-plane energy density distribution as the NA of the system approaches unity. An unprecedented resolution performance ranging from 240nm to ~100nm was obtained, depending of the state of polarisation used.

The resolution-enhancing effects of pupil-function engineering were investigated and implemented into a nonlinear polarisation-dependent SIL-enhanced laser microscope to demonstrate a minimum resolution performance of 70nm in a silicon flip-chip. The performance of the annular apertures used in this work was modelled using vectorial diffraction theory to interpret the experimentally-obtained images.

The development of an ultra-high-resolution high-dynamic-range OCT system is reported which utilised a broadband supercontinuum source and a balanced-detection scheme in a time-domain Michelson interferometer to achieve an axial resolution of 2.5µm (in air). The examination of silicon ICs demonstrated both a unique substrate profiling and novel inspection technology for circuit navigation and characterisation. In addition, the application of OCT to the investigation of artwork samples and contemporary banknotes is demonstrated for the purposes of art conservation and counterfeit prevention.

To my Family…

For reminding me everyday that I can.

ACKNOWLEDGEMENTS

First of all, I would like to say a huge thank you to my academic supervisor Prof. Derryck Reid. His belief and confidence in me to demonstrate my potential within his group will not be forgotten. Thank you for your guidance, support, ideas and encouragement over the past 3 and a half years. You are an exceptional supervisor and mentor.

Enormous gratitude must be given to Dr Euan Ramsay. His knowledge, advice and patience have been immensely valuable, not only in the lab, but also during our generally random coffee-break conversations. I would like to take this opportunity to wish both him and his family every success in the future.

To all the members of the Ultrafast Group (past and present) for their support and helpful conversations – Euan Ramsay (experimental work and MATLAB simulations), Karl Tillman, Stuart Campbell, Reda El-Agmy, Łukasz Kornaszewski, Jinghua Sun, Barry Gale, Tobias Lamour and Teresa Ferrerio, as well as final year MPhys students Bernd Stark and Michael Renner (OCT and MATLAB development)…… it's been a pleasure!

To my family. Mum, Dad, Craig, Shaun, Nana Wilma, Scott, Nana Elsie, Grandad Harry, Christine, Davy, Conor and, of course, Tristin. Thank you all for your encouragement, support and love. I would not be where I am today without you.

I would also like to thank all the academic and technical staff within the physics department who I have had the opportunity to work with – especially Martin Thomson for generating ASAP simulations and Henry Bookey for providing the PM-DS-HNLF. Their valuable contributions towards this work are greatly appreciated.

Finally, to all the friends I have made within the department and beyond who have made me laugh and kept me sane. The old office and Friday lunchtime crowd - Ian Thomson, Ryan Warburton, Spyros Brown and Richard Moag. Apologies to anyone else I have forgotten to mention (you know who you are!)

A special thanks to Marcel Leutenegger for the advice on vectorial-field modelling.

ACADEMIC REGISTRY
Research Thesis Submission

Name*:*	Keith Andrew Serrels		
School/PGI:	Engineering and Physical Sciences		
Version: *(i.e. First, Resubmission, Final)*	Final	Degree Sought:	PhD / Physics

Declaration

In accordance with the appropriate regulations I hereby submit my thesis and I declare that:

1) the thesis embodies the results of my own work and has been composed by myself
2) where appropriate, I have made acknowledgement of the work of others and have made reference to work carried out in collaboration with other persons
3) the thesis is the correct version of the thesis for submission and is the same version as any electronic versions submitted*.
4) my thesis for the award referred to, deposited in the Heriot-Watt University Library, should be made available for loan or photocopying and be available via the Institutional Repository, subject to such conditions as the Librarian may require
5) I understand that as a student of the University I am required to abide by the Regulations of the University and to conform to its discipline.

** Please note that it is the responsibility of the candidate to ensure that the correct version of the thesis is submitted.*

Signature of Candidate*:*		Date:	

Submission

Submitted By *(name in capitals):*	
Signature of Individual Submitting:	
Date Submitted:	

For Completion in Academic Registry

Received in the Academic Registry by *(name in capitals):*			
Method of Submission *(Handed in to Academic Registry; posted through internal/external mail):*			
E-thesis Submitted			
Signature:		Date:	

ABBREVIATIONS

FA	Failure Analysis
IC	Integrated-Circuit
CMOS	Complimentary Metal Oxide Semiconductor
FIB	Focused Ion Beam
IRM	Infrared Microscope
SEM	Scanning Electron Microscope
AFM	Atomic Force Microscope
SNOM	Scanning Near-Field Optical Microscope
SPM	Scanning Probe Microscopy
EBIC	Electron Beam Induced Current
OBIC	Optical Beam Induced Current
TOBIC	Two-Photon Optical Beam Induced Current
OBIRCH	Optical Beam Induced Resistance Change
LIVA	Laser Induced Voltage Alteration
LADA	Laser Assisted Device Alteration
TIVA	Thermally Induced Voltage Alteration
SHG	Second Harmonic Generation
EFISHG	Electric-Field Induced Second Harmonic Generation
THG	Third Harmonic Generation
TPA	Two-Photon Absorption
TPF	Two-Photon Fluorescence
SIL	Solid Immersion Lens
h-SIL	Hemispherical Solid Immersion Lens
s-SIL	Super Solid Immersion Lens
FOSSIL	Forming the substrate into a SIL
ESA	Excited State Absorption
EDFA	Erbium-Doped Fibre Amplifier
NALM	Nonlinear Amplifying Loop Mirror
APM	Additive Pulse Mode-locking
NPR	Nonlinear Polarisation Rotation
FWHM	Full-Width Half-Maximum
PSF	Point-Spread Function
OCT	Optical Coherence Tomography

OCM	Optical Coherence Microscopy
S/N	Signal-to-Noise
A2D	Analogue-to-Digital
SC	Supercontinuum
CCD	Charge-Coupled Device
NEP	Noise Equivalent Power

TABLE OF CONTENTS

Chapter 1: Introduction

PUBLICATIONS LIST

Journal Publications

K. A. Serrels, E. Ramsay and D. T. Reid, *70nm resolution in sub-surface optical beam induced current microscopy through pupil-function engineering in the vectorial-focusing regime,* Applied Physics Letters, 94, 073113 (2009)

K. A. Serrels, E. Ramsay, P. A. Dalgarno, B. D. Gerardot, J. A. O'Conner, R. H. Hadfield, R. J. Warburton and D. T. Reid, *Solid immersion lens applications for nanophotonic devices*, Journal of Nanophotonics, 2, 021854 (2008)

K. A. Serrels, E. Ramsay, R. J. Warburton and D. T. Reid, *Nanoscale optical microscopy in the vectorial focusing regime*, Nature Photonics 2, 311-314 (2008)

Co-Authored Journal Publications

E. Ramsay, K. A. Serrels, A. J. Waddie, M. R. Taghizadeh, and D. T. Reid, *Optical super-resolution with aperture-function engineering*, American Journal of Physics, 76, 1002 (2008)

E. Ramsay, K. A. Serrels, M. J. Thomson, A. J. Waddie, M. R. Taghizadeh, R. J. Warburton and D. T. Reid, *Three-dimensional nanoscale subsurface optical imaging of silicon circuits,* Applied Physics Letters 90, 131101 (2007)

E. Ramsay, K. A. Serrels, M. J. Thomson, A. J. Waddie, R. J. Warburton, M. R. Taghizadeh and D. T. Reid, *Three-dimensional nanometric sub-surface imaging of a silicon flip-chip using the two-photon optical beam induced current method*, Microelectronics Reliability 47, 1534-1538 (2007)

Conference Publications

K. A. Serrels, E. Ramsay and D. T. Reid, *70nm Resolution in Sub-Surface Two-Photon Optical Beam Induced Current Microscopy through Pupil-Function Engineering in the Vectorial Focusing Regime,* International Quantum Electronics Conference (IQEC), Baltimore, MA, United States, 2009

K. A. Serrels, E. Ramsay, R. J. Warburton and D. T. Reid, *Nanoscale Optical Microscopy in the Vectorial Focusing Regime*, Photon 08, Heriot-Watt University, Edinburgh, Scotland, 2008

K.A. Serrels, E. Ramsay, R.J. Warburton, and D.T. Reid, *Nanoscale microscopy of silicon integrated circuits*, LPHYS08, Trondheim, Norway, 2008

K. A. Serrels, E. Ramsay, R. J. Warburton and D. T. Reid, *Nanoscale Optical Microscopy in the Vectorial Focusing Regime*, Quantum Electronics and Lasers (QELS), San Jose, CA, United States, 2008

K. A. Serrels, E. Ramsay, R. J. Warburton and D. T. Reid, *Nanoscale Optical Microscopy in the Vectorial Focusing Regime*, International Conference on Ultrafast Phenomena (UP2008), Stresa, Lago Maggiore, Italy, 2008

E. Ramsay, K. A. Serrels, M. J. Thomson, A. J. Waddie, R. J. Warburton, M. R. Taghizadeh and D. T. Reid, *Three-dimensional nanometric sub-surface imaging of a silicon flip-chip using the two-photon optical beam induced current method*, International Symposium for Testing and Failure Analysis (ISTFA), San Jose, CA, United States, 2007

E. Ramsay, K. A. Serrels, M. J. Thomson, A. J. Waddie, R. J. Warburton, M. R. Taghizadeh and D. T. Reid, *Three-dimensional nanometric sub-surface imaging of a silicon flip-chip using the two-photon optical beam induced current method*, European Symposium Reliability of Electron Devices, Failure Physics and Analysis (ESREF), Bordeau, France, 2007

E. Ramsay, K. A. Serrels, M. J. Thomson, A. J. Waddie, R. J. Warburton, M. R. Taghizadeh and D. T. Reid, *Three-dimensional nanometric sub-surface imaging of a silicon flip-chip using the two-photon optical beam induced current method*, Conference on Lasers and Electro-Optics Europe (ECLEO), Munich, Germany, 2007

E. Ramsay, K. A. Serrels, M. J. Thomson, A. J. Waddie, R. J. Warburton, M. R. Taghizadeh and D. T. Reid, *Nanometric Three-Dimensional Sub-Surface Imaging of a Silicon Flip-Chip*, Conference on Lasers and Electro-Optics (CLEO), Baltimore, Maryland, United States, 2007

E. Ramsay, K. A. Serrels, M. J. Thomson, A. J. Waddie, R. J. Warburton, M. R. Taghizadeh and D. T. Reid, *Nanometric Three-Dimensional Sub-Surface Imaging of a Silicon Flip-Chip*, European Optical Society (EOS) Annual Meeting 2006, Paris, France, 2006

E. Ramsay, K. A. Serrels, M. J. Thomson, A. J. Waddie, R. J. Warburton, M. R. Taghizadeh and D. T. Reid, *Ultra-high Resolution, Three-Dimensional, Solid-Immersion Imaging of a Silicon Flip-Chip using the Optical-Beam Induced Current Method*, Photon 06, Manchester University, England, 2006

Conference Poster Presentations

K. A. Serrels, E. Ramsay, A. J. Waddie, M. R. Taghizadeh, R. J. Warburton and D. T. Reid, *100 nm Optical Resolution in Flip-Chip Integrated Circuit Inspection*, ESSDERC/ESSCIRC, Edinburgh, Scotland, 2008.

K. A. Serrels, E. Ramsay, R. J. Warburton and D. T. Reid, *Optical Super-Resolution through Aperture-Function Engineering and Vectorial Focusing Effects*, Conference on Lasers and Electro-Optics (CLEO), San Jose, CA, United States, 2008

Chapter 1

Introduction

1.1 Background and Motivation

The microelectronics industry is driven by the endeavours of material scientists and research and development engineers to maintain a rate of product evolution that adheres to the demands of Moore's Law [1]. Gordon. E. Moore, the co-founder of Intel, stated in 1965 that the number of transistors that can be fabricated on an integrated-circuit (IC), at minimum cost, would increase exponentially, doubling every two years [2]. This prediction has held true for almost half a century and will continue over the next decade and beyond. The semiconductor IC industry is therefore in constant pursuit of the latest cutting-edge technologies in order to address this requirement. As a result, the level of complexity required to fabricate such devices is elevated to such a degree that an entirely new collection of possible mechanical / electrical errors and failure modes become difficult to avoid. The current state-of-the-art in IC design relies on a fusion of both sophisticated material parameters and dense three-dimensional (3D) multilayer architectures; therefore the characterisation capabilities of the failure analyst must be expanded in order to maintain a state of parallel progression.

The failure analysis (FA) community occupies a global collection of both highly motivated industrial and academic groups. From the development of personal computers to the advance of custom mobile telephones and entertainment systems, failure analysis plays a major role in the progression of a large number of organisations since the continuous generation of quality products demands market attention and distinction. It is common for individual companies to isolate their interests and ideas and refuse potential collaborative efforts between competitors, yet a large international connection is still available to those who wish to discuss and reveal their latest innovations. There are a number of annual local and international FA conferences and technical meetings which are of great interest to many organisations, examples of which include the European Symposium on Reliability of Electron Devices (ESREF) and the International Symposium for Testing and Failure Analysis (ISFTA). These conferences highlight cutting-edge FA techniques and provide a unique platform for discussing current technological demands.

Microelectronic FA is the study of why ICs fail and what the implications may be for systems reliability. FA is a crucial aspect of IC fabrication and evaluation since it ultimately governs a company's position and perception in the industrial marketplace given that poor quality devices result in poor device yield and quality, and therefore low

market impact and influence. Consequently, for effective and in-depth FA of semiconductor ICs, it is a major requirement that a wide range of investigative techniques and systems are applied to sufficiently interrogate a device under test. These techniques must probe a large number of potential failure modes, such as mechanical packaging or electrical transport obstacles. There are several device reliability evaluation parameters which must be addressed in order to fully understand the nature of each problem [3]. These are broken down into a definitive list of actions:

- Initially, a failure *Mode* must be identified. This describes the nature of the device breakdown which has resulted in the observed failure characteristic. This may be caused by an open-circuit or a leakage.
- Then, the failure *Defect* has to be considered. This describes what has actually caused the device to stop working properly. This may be a consequence of micro-cracking, for example.
- Afterwards, a failure *Mechanism* must be found. This describes the phenomena that produced the failure – e.g. corrosion.
- Then, a failure *Cause* has to be found. This is the exact action that has caused the failure mechanism to take place – i.e. poor design or isolated mechanical stress.

There are other types of device failure that exist also. These describe entire devices that can either work, but not to the optimum design specifications e.g. at full clock speed, or a device that is simply inoperative. These are known as *specification* failures and *hard* failures respectively.

Although the failure mechanisms introduced above can take place in a number of different devices, for the purposes of efficient and effective FA it is vital that an organised step-by-step set of procedures exist to describe the formal treatment given to a single semiconductor chip that will ensure that no important information is lost or overlooked due to a random or disorderly FA cross examination. This prescribed FA schedule involves several basic stages that strip back a post-production device until it is fully exposed and returned to its early development appearance. This involves examining the package prior to actually opening it up, then removing the chip from its enclosed storage unit, internally inspecting the chip, removing specific layers of the device, identifying the exact location of the actual fault, consideration of the reliability

evaluation parameters discussed previously, then finally initiating a series of simulations or final examination routines. All of these stages require an in-depth and thorough analysis to prove successful; however, for the purposes of this discussion, it is not necessary to reveal the intricacies of such procedures. Nonetheless, an appreciation and general understanding of these techniques is helpful.

The complete assortment of investigative procedures and apparatus that are available to the semiconductor failure analyst is vast, since it is paramount that an exhaustive interrogation of electrical, environmental, highly accelerated stress tests (HAST), etc, can take place. All of these examination practices are of enormous importance, however a central theme of IC FA that has not yet been discussed, and one which can provide an abundance of device information, is that of complementary microscopical techniques.

Microscopic imaging offers detailed technical maps, and even functionality maps, of specific device geometries and is therefore an essential FA tool to utilise. The various imaging techniques that are available to the failure analyst address a wide range of issues and rely on the management of different optomechanical arrangements. Each microscope naturally has a set of limitations and therefore each one is more suited to address particular problems or ideas that may arise during the FA investigation. Depending on the issue that has been highlighted, the manner in which the microscope is used, its energy or wavelength, and incident power are all vital parameters that need to be considered when determining the transparency of an inspected material, and therefore, obtaining access to the feature(s) of interest. Once this has been achieved, it is then a question of whether or not a particular ‘failure’ or defect can be effectively captured in an image. This will depend on whether or not the analyst can control the image contrast through the manipulation of a suitable variable, i.e. reflectivity from the sample.

The following section introduces and reviews a selective portion of popular FA imaging modalities. These microscopy techniques are generally used in particular situations to alleviate certain problematic issues such as the reduction of device feature geometries towards the nanometre scale (spatial resolution), packaging restraints (optical penetration), and device contamination and/or electrical charging (non-destructive analysis – note that non-destructive analysis, in an industrial context and of that used throughout this work, describes the interrogation of a device that will not alter any

designed operational characteristics post-test). Microscopy can be broken down into three individual sections: optical, electron and scanning probe microscopy. All of these imaging acquisition procedures will be covered in the next section.

1.2 Review of Conventional and Advanced Imaging Modalities in Semiconductor Failure Analysis

The semiconductor IC industry is characterised by the exponential rate at which its products increase in speed, integration density and functionality, all trends that can be attributed to a steady fall in the feature sizes of ICs. As feature sizes below 100nm become routine, the International Technology Roadmap for Semiconductors has identified a critical need for ‘‘non-destructive wafer/mask level microscopy for measuring the critical dimensions of 3D structures and defect detection’’ [1]. In this context, optical imaging has a significant role to play in IC FA, inspection and metrology.

Here we review a number of conventional, and some more advanced FA microscopy instruments and their applications. The diversity of FA microscopy sets a limit on the total number of instruments that can be discussed in this section due to both the relevance and the capacity restrictions of this thesis. Therefore, I have limited the review to contain only those imaging techniques that are commonly used in standard FA laboratories and will then proceed to discuss specific laser signal injection microscopes that are compatible with the central imaging concept which was adopted throughout this work.

1.2.1 The Optical Microscope

An optical microscope is a fundamental instrument that can contain only a single lens to produce a magnified image of an object, either in transmission or reflection mode, which is located in the focal plane of the lens in the optical arrangement. These devices have been the workhorse of microsystem optical inspection for several years [4] and remain a dominant analysis tool in many biological, material science and general cutting-edge research laboratories today.

The use of an optical microscope, or ‘light microscope’, to examine the front-side of a semiconductor chip is regarded as the first naturally progressive step in FA after initial inspection with the unaided eye. The first stage is to examine a package with a relatively

low numerical aperture (*NA*), or focussing power, objective lens to generate an image of high quality and full depth perception. This permits mechanical manipulation (i.e. repositioning) of the device which is ideal for the first examination process. Once the package has been opened and the front side of the semiconductor die exposed, then the microscope can be altered to accommodate a higher *NA* objective lens for closer examination. This bright-field arrangement operates by collecting and imaging the light that is transmitted through the sample and has the advantage of revealing some initially hidden internal features on the die, for example the possibility of stress-induced failure modes such as delamination – delamination is the process by which several initially contacted layers become separated from each other. Nevertheless, these bright-field images can suffer from poor contrast or excessive glare from the object surface.

However, in addition, the investigator of FA may decide to use the optical microscope in a dark-field arrangement as opposed to the conventional bright-field imaging mode. This form of optical microscopy functions by illuminating the sample with suitably filtered light that will not be collected by the objective lens and, therefore, not form part of the image. Only the scattered light from the sample will be collected. This produces the appearance of a dark background that contains bright objects on it. The major benefit of the dark-field microscope is that it can effectively image non-planar surface features. These features can include certain etched edges or surface roughness. The use of a dark-field microscope to investigate these types of failure modes is ideal since it requires less time to capture these images than any other technique.

Another complimentary microscopical technique to the dark-field microscope is the polarisation-sensitive microscope. This FA instrument can also provide stress-induced information about a device under test; however, the disadvantage of this technique is that it relies on the requirement that optically active device materials have been used during the fabrication process i.e. some materials alter their transmission or reflection properties when the polarisation state of the incident illumination is changed.

Although the optical microscope can be deployed in transmission mode, this approach requires an extra level of sample preparation since the die must be physically removed from its packaging in order for it to be illuminated from below. Furthermore, a sample may have to be optically polished or thinned to optimise the transmission or the illumination in order to improve image contrast. A simple solution to overcome this

problem is to use a stereo microscope. This arrangement collects light that has been reflected from the sample surface rather than light that has been transmitted by the sample. Due to its slightly different design (the use of two objective lenses and two eyepieces to provide different viewing angles for each eye) it offers a 3D image of the sample under study. This microscope can be configured into either a bright or dark-field arrangement.

In general, an optical microscope can generate a significant level of primary information about a device and is therefore a major imaging tool in the FA process; however, it is ultimately limited in its ability to offer an advanced evaluation of an inspected chip or die. These limitations fall into two main categories: the first is that it is restricted by the wavelengths available (visible spectrum) to purely surface analysis with a limited spatial resolution, and secondly it has a limited depth-of-focus at high-*NA* (magnification). It is the limit of spatial resolution which is the most crucial aspect of the microscope since an optical resolution of approximately 1µm is simply not good enough to meet the demands of today's device technologies. Furthermore, the lack of detailed sub-surface interrogation is a major inconvenience since almost every state-of-the-art microprocessor is currently designed around an immersed 3D architecture.

1.2.2 The Infrared Microscope (IRM)

The microelectronics industry traditionally employs silicon as the semiconductor substrate of choice when fabricating ICs due to its ideal thermal, electrical, and mechanical properties. These characteristics can be easily controlled and manipulated through careful design stages to fabricate sophisticated devices that will respond in a predetermined manner to a particular stimulus. The success of this technology has resulted in the burgeoning field of silicon photonics [5] where the emission, transmission, detection, modulation and amplification of radiation in the visible and near-IR are tailored to create various optoelectronic devices such as lasers [6, 7], photodetectors [5, 8] and waveguides [9, 10]. These can be fairly complex technologies to engineer; however a simple requirement that must be addressed in each of these applications is the ability to gain optical access to their sub-surface environments.

The transmission window for silicon traverses an impressive range which starts at approximately 1.1µm and extends out to around 20µm. Since optical radiation in the visible spectrum covers only 0.4 – 0.7µm, any incident light at these wavelengths on a

silicon chip will simply be absorbed. Therefore, a custom microscope with the use of near-IR transmitting optical components and a suitable laser source can be deployed to overcome this problem and provide advanced images of sub-surface features that would otherwise be concealed [11].

The beauty of this technique is that once a device has been suitably prepared, where the external packaging has been removed and the plastic encapsulation polished back to reveal the silicon substrate, the incident IR illumination can be focused to different depths within the die and a collection of sample planes mapped out to exposed the intricate 3D topology of the microchip.

There are two main factors to consider before optical illumination can efficiently access the buried device layer in silicon microelectronic components. The first is the thickness of the silicon substrate and the second concerns the doping concentration of the silicon. These two parameters can be effectively controlled in order to optimise transmission of the near-IR illumination. These considerations have been theoretically analysed by Phang *et al* [12]. In this study the numerical expressions derived by Aw *et al* [13] were utilised to model the transmission of light through various silicon doping concentrations and substrate thicknesses. Fig.1 (a) shows the transmission of light through 500µm of p-doped silicon for different doping concentrations and Fig.1 (b) shows the effect of reducing the substrate thickness for p-doped silicon at $10^{19}cm^{-3}$.

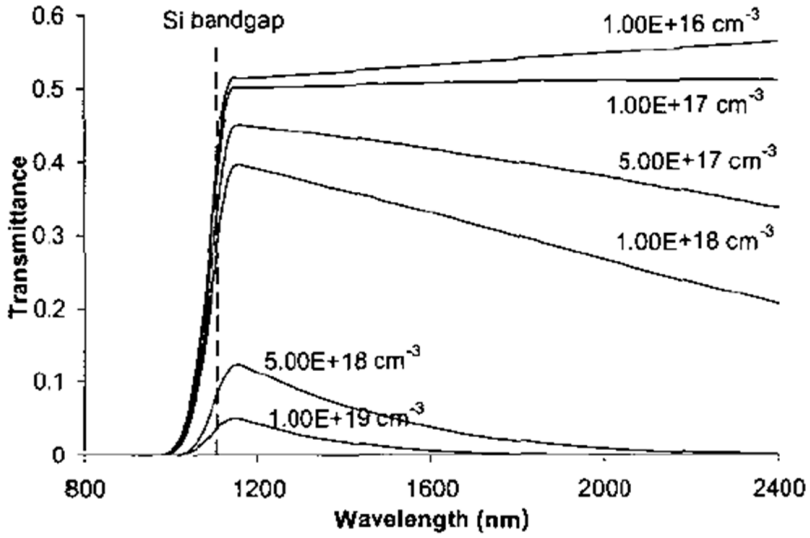

Figure 1 (a) – Light transmittance through 500µm of p-doped silicon with different doping concentrations [12, 13]

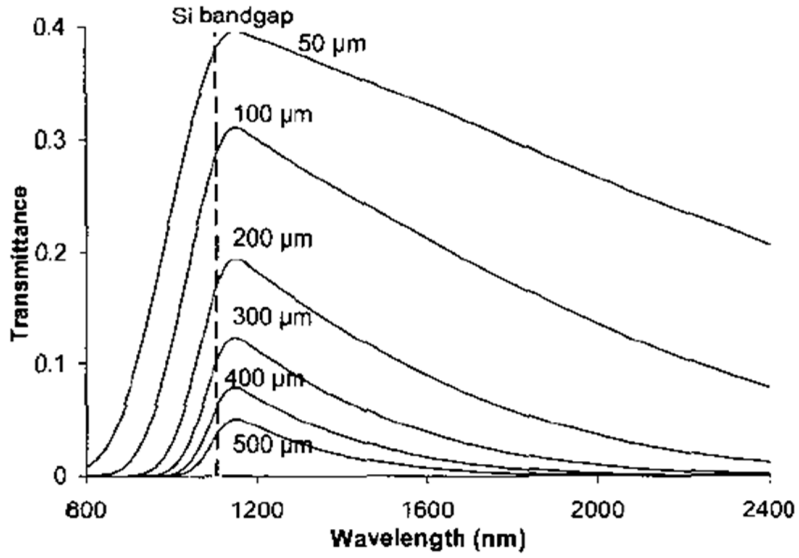

Figure 1 (b) – Light transmittance through different thicknesses of p-doped silicon with a doping concentration of $10^{19}cm^{-3}$ [12, 13]

The results presented in Fig.1 indicate that the highest level of transmission takes place at approximately 1.1µm where it then decreases significantly with increased doping concentrations. Therefore, if a device is lightly doped then there is no requirement for device substrate thinning. Yet, substrate thinning is a major requirement when considering heavily doped silicon substrates. Note here that in general it is necessary for the silicon substrate to have an optically flat surface in order to maintain a uniform laser power delivery during transmission, so great care must be taken if substrate polishing is needed. Furthermore, note also that although an anti-reflection coating is not always compulsory it will further improve the transmission of the laser beam by reducing the large Fresnel reflection encountered at the silicon surface – the Fresnel reflection (approximately 30%) is significant since the refractive index mismatch between air and silicon is large.

The IR microscope can interrogate a microelectronic semiconductor sample for an almost identical set of failure modes to that obtained from the conventional optical microscope, for example delamination of metalisation layers, corrosion, interconnect quality, etc, but offers the advantage of exposing these potential weaknesses and defects under the surface of the otherwise impenetrable silicon substrate [14]. However, although this approach provides another solution in FA analysis, its ability to resolve sub-micron feature sizes is still restricted by the incident wavelength. Furthermore, this arrangement is typically constructed to facilitate optical acquisition in a reflective mode.

Transmission IR microscopy requires an additional level of sample preparation which is excessively destructive. Consequently, reflection IR microscopy is a non-destructive yet ultimately limited FA tool.

1.2.3 The Confocal Microscope

One method to overcome this barrier in spatial resolution is to utilise a confocal microscope – confocal literally translates to “twice focused”. With the invention of confocal imaging in 1961 by M. Minsky [15, 16], the ability to perform optical sectioning within a sample could finally be achieved to generate 3D images through a reduced depth-of-field [17]. In order to do this, a spatial filter (pinhole) is positioned directly in front of a detector in a confocal arrangement with respect to the illumination point source. In this configuration (Fig.2), only the light that emanates from the focal plane will be collected at the detector plane. Any light that originates from above or below this plane will be rejected by the pinhole and will not influence the signal collected by the detector.

Confocal imaging has been successfully used in many applications from the study of biological samples [18, 19] to the more relevant investigation of surface analysis on semiconductor ICs [20, 21], and has addressed some of the issues associated with conventional light microscopy. For example, in the confocal regime, because the depth-of-field is so small the light that emanates from regions immediately above and below the focal plane will be heavily attenuated due to their different primary image focal planes which will result in the isolation of a number of interesting features per image. As a result, this reveals a lot of important information about a sample and alleviates traditionally long inspection times.

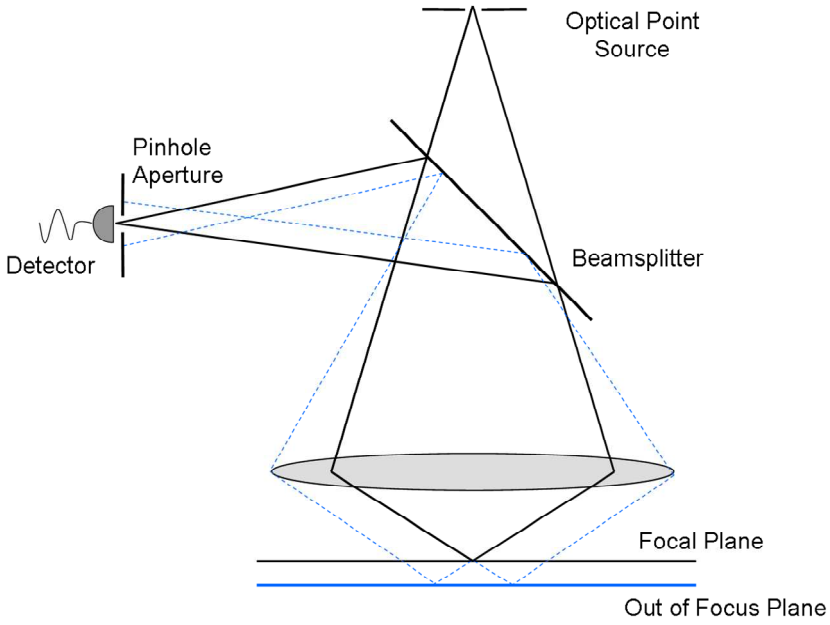

Figure 2 – A Confocal Microscope Arrangement. The detector pinhole is confocal with the optical point source. The pinhole accepts the in-focus light (black), but rejects the out-of-focus light (dotted blue)

In addition, a confocal laser scanning microscope (CLSM) can be used to acquire a point-by-point image of an object by raster scanning a laser beam over its surface, or sub-surface, and collecting the reflected light that is focused onto a suitably located large-area detector. Theoretically, the CLSM can be configured to manage a scanned beam (through the use of a single galvanometer mirror or mirror pair) or a scanned objective lens to redistribute the focus of a stationary beam laterally across a sample. The theory of the LSM was introduced by Wilson and Sheppard [22, 23]; however, it was Sheppard [24] who discussed its relevance in semiconductor device and material applications.

IR confocal laser scanning microscopy combines the advantages of sample penetration in conventional IR microscopy with the improved spatial resolution capabilities of the confocal system. In addition, this technique can be configured to facilitate fully automated acquisition of images for enhanced system performance; however, the most powerful FA tool for obtaining the highest spatial resolution in a scanned configuration is the scanning electron microscope.

1.2.4 The Scanning Electron Microscope (SEM)

The SEM alleviates the reduced spatial resolution examination demands of FA due to the ever-decreasing dimensions and increased physical complexity of modern day microelectronic devices. This technique requires no additional sample preparation to that expected for the optical microscope and is relatively simple to operate.

The original construction of an electron microscope (Fig.3) was the transmission electron microscope (TEM) in which a high voltage electron beam, emanating from a tungsten filament cathode, would be accelerated to incredibly high velocities by an anode before being focused by a pair of electrostatic and electromagnetic lenses onto a transmitting sample below. The electron beam that emerges from the sample carrying certain spatial information about it is then magnified by an objective lens before striking a fluorescent viewing screen that is coated in a phosphor such as zinc sulphide. This imaging screen can be later viewed on a monitor by coupling the phosphors response to a charge-coupled device (CCD) camera. Once these images have been corrected for spherical aberration they can produce highly detailed images on the order of approximately 100pm in silicon [25]. The electron microscope has the capability to resolve features to this level of spatial resolution due to their associated de Broglie wavelength, which is a consequence of wave-particle duality. Since electrons carry more momentum than photons [26], their de Broglie wavelength is smaller. This results in a greatly improved spatial resolution.

In the scanning electron microscope (SEM), an electron beam is scanned across a 2D area of a sample and, unlike the TEM, an image is generated by recording the varying intensity (loss of energy) of the scanned beam as a function of position on the sample.

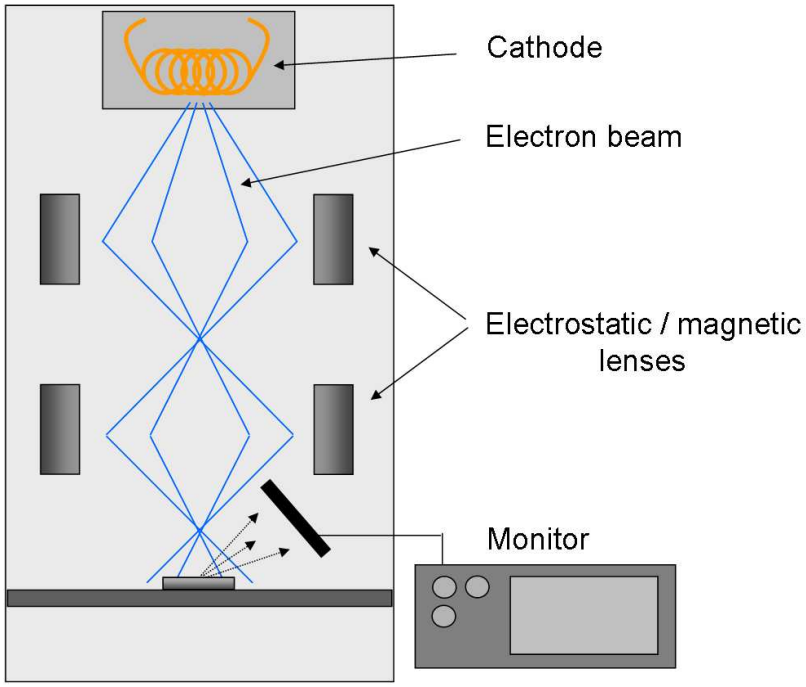

Figure 3 – The Scanning Electron Microscope (SEM)

This loss of energy may result in an emission of x-rays, optical radiation (cathodeluminescence), or even secondary low-energy electrons. It is this varying electron beam intensity, and consequent emission, which must be captured at a different location to that located below the sample. Since a SEM image depends on surface reflection instead of sample transmission it is able to image bulk samples up to several centimetres in all three dimensions and has a much larger depth-of-field. Therefore, it can produce high quality, high resolution 3D structural images of the sample; however, SEM image resolutions generally suffer by an order of magnitude when compared against those obtained from a TEM.

Generally speaking, there are three main issues that affect SEM implementation in an ideal FA environment. The first is that the limited penetration depths achieved by the SEM result in a lack of valid sub-surface investigation. Secondly, the electrical charge of an incident electron may alter device performance and distort the acquired images from one which portrays an accurate representation of the failure mode to that which maps an erroneous device performance. Finally, since an electron beam may permanently alter the electronic characteristics of a device, this technique can be considered to be destructive in nature and therefore unsuitable for FA analysis.

1.2.5 Electron Beam Induced Current (EBIC) Microscope

Electron beam induced current (EBIC) imaging utilises the electron beam of the SEM to inject charge carriers into a material. The physical mechanism adopted to facilitate this phenomenon is the promotion of an electron residing in a lower energy level to a higher energy level within the material. In a direct-bandgap semiconductor, where the lowest energy in the conduction band is aligned directly above the peak energy level of the valence band, this transfer of energy can result in spontaneous emission of a photon through radiative recombination. This recombination is the principal behind cathodeluminescence [27]; however, if an internal electric-field is present across this material, for example if the material comprised of a fabricated p-n junction, then the charge carriers that have been injected into the material will be swept away according to the junction's potential difference. The constant flow of injected carriers can result in a measurable EBIC signal which, when the electron beam is scanned across the surface of a material, will generate an electronic activity map of that particular area.

This technique has been successfully used to identify a wide variety of semiconductor FA defects [28], examples of which include evaluating minority carrier properties, defect populations and inspecting physical deformations. EBIC has also been extended to study local defects in insulators; however, the principal imaging characteristic behind this approach is its downfall since an electronically stimulated device can suffer from excessive charge build-up which can either distort the imaging conditions to reveal a false representation of the inspection, or can permanently alter the device properties. Therefore, an optical signal injection approach is an alternative that can overcome this limitation by avoiding the build up of charge on the sample surface.

1.2.6 Laser Signal Injection Microscopy (OBIC, TOBIC, OBIRCH, TIVA, LIVA)

Laser signal injection microscopy [12] covers an extensive range of possible device probing configurations and technologies. Recent developments in this regime of semiconductor device FA have exploited the use of laser scanning IR microscopy for the purposes of surface and sub-surface fault localisation and defect characterisation. Fault localisation techniques rely on either laser induced thermal or power alteration schemes such as optical beam induced resistance change (OBIRCH) [29] and thermally induced voltage alteration (TIVA) [30-32]. Defect characterisation is based on laser induced

carrier generation techniques such as optical beam induced current (OBIC) [33] and light induced voltage alteration (LIVA) [32].

Although the above mentioned stimulated FA techniques provide a large level of device information and inhibit a range of similar advantages and disadvantages, an exhaustive description of each imaging modality is not required for this review. However, since the nonlinear OBIC approach was adopted throughout this work its characteristics and performance capabilities will be discussed in detail below.

OBIC imaging in silicon ICs was first demonstrated in the 1970s [34] and is a complimentary technique to the common EBIC imaging method [35], with the exception that no charge build up is associated with OBIC imaging. In the OBIC effect, optical radiation with a photon energy greater than the material's bandgap energy is absorbed in a semiconductor sample, generating carriers. In bulk silicon, these carriers diffuse over time and eventually recombine through non-radiative processes. The presence of a junction in the irradiation region presents the carriers with a space–charge region whose internal field can sweep the carriers out to a suitable external circuit where an optically created photocurrent can be detected [36]. When this photocurrent is mapped as a function of scanned beam position, a topological image of the circuit can be acquired which exhibits contrast according to the electrical properties of the device. The OBIC technique has also been configured in a hybrid arrangement along with the laser-scanning confocal IR microscope to investigate semiconductor and metal sites in an IC [20].

OBIC imaging is particularly suited to the inspection of semiconductor devices [14, 37] due to the fact that it is a non-contact, non-destructive testing method. This created a great interest in this technique throughout the 1980s [38-42]; however, there are limitations associated with this imaging mode. OBIC imaging cannot perform depth-resolved analysis because absorption takes place throughout the entire volume of the beam within the sample. This effectively generates carriers over a large axial range. In addition, the fact that the beam generates carriers throughout its entire irradiation volume limits the contrast of the resulting images and attenuates the optical beam as it travels through the sample's substrate to the device layer of interest. This is important in sub-surface imaging when one is wishes to image a structure that is buried several hundreds of microns below the surface of the sample.

Modern flip-chip IC architectures highlight this issue since they are designed in a manner that does not allow front-side optical access to the circuit because of the numerous metallisation and interconnecting layers that occupy the top surface of the chip. For this reason, optical microscopy of flip-chips must be performed by backside imaging through the silicon substrate. This procedure presents the contradictory requirements of achieving high bulk transmission of the illuminating wavelength, yet also sufficient absorption at the same wavelength to generate carriers at the circuit features. These two requirements involve a delicate compromise between generated signal level, penetration depth, illumination wavelength and image contrast.

OBIC imaging is a linear technique and therefore suffers from the same limitations in resolution and contrast as laser fluorescence microscopy, including signal saturation and limited depth-resolution. For these reasons a nonlinear variant of the technique can be used, therefore a two-photon OBIC method was devised. The two-photon absorption process required for this technique is discussed in detail in Section 1.4 of this chapter.

Two-photon absorption is a nonlinear effect and, although it is difficult to measure using continuous-wave (CW) laser sources it can be easily demonstrated with a few milliwatts of light using femtosecond pulses from a modelocked laser – the details of which will be discussed later. Two-photon optical beam induced current (TOBIC) imaging was first demonstrated by Xu [43, 44] using a 1.3µm femtosecond optical parametric oscillator, and addressed the contradictory requirements encountered using linear techniques of focusing through thick substrates while maintaining sufficient absorption at the beam focus of a laser beam to produce a strong OBIC signal. Later, Xu utilised the compact nature of a modelocked fibre laser to investigate vertical cavity surface emitting lasers (VCSELs) through two-photon photocurrent imaging [45]. TOBIC imaging also has the attraction of producing an intrinsic increase in resolution for any given illuminating wavelength due to the nonlinear nature of the excitation. Two-photon absorption depends on the square of the optical intensity that arrives at the focus of the beam and therefore produces a reduction in the effective spot radius by a factor of $\sqrt{2}$, assuming an incident Gaussian transverse profile – i.e. the full width at half maximum (FWHM) of a Gaussian distribution will decrease by a factor of $\sqrt{2}$ when squared.

1.2.7 The Thermal Imaging Microscope

An extremely important parameter in semiconductor IC FA is the investigation of excessive thermal accumulation, whether it be distributed throughout the entire chip volume or localised into a confined 'hot-spot' on a particular device layer. This thermal activity must be efficiently managed in order to avoid device malfunction and improve component performance. Therefore, a non-invasive optical imaging technique is required to detect these device hot-spots quickly and at high spatial resolution.

One solution is to utilise the thermal imaging microscope to acquire thermographic maps of certain device features. This can be achieved using a number of varying configurations and processes. One example is to obtain simple spectral reflectance images from the sample since any thermal activity will alter the reflecting properties of the imaging layers of the device [46]. These images can be obtained using short wavelength excitation and so benefit from high-resolution.

Another alternative is to pursue IR lock-in thermography to improve signal-to-noise (S/N) ratios. This has been used to expose both surface and sub-surface defects caused by surplus thermal action [47, 48].

An additional method, which returns to the laser signal injection regime, is differential thermography [49]. This technique utilises the benefits of monitoring OBIC generation as a function of temperature since resistive structures will be sensitive to thermal activity and hence alter the resulting OBIC output. This methodology uses a feedback detection scheme that can generate a thermal gradient map by filtering out any pre-recorded conventional circuit response and only map out the anomalous fluctuations when interrogating semiconductor ICs.

1.2.8 Atomic Force Microscope (AFM)

The atomic force microscope (AFM) was invented by Binnig in 1986 and since then has become one of the most widely used, and well known, surface scanning-probe microscopy (SPM) technique in the material and biological sciences [50]. It offers spatial resolution performance comparable to that exhibited by the SEM and will almost certainly be found in every serious microelectronic FA lab.

The principal component in this microscope is a scanning cantilever which has a sharp conical probe, or tip, located at its end (Fig.4) The tip is used to scan or 'feel' the surface of the sample in a typically non-contact configuration. When the tip is brought close to the sample surface it experiences either direct contact or Van der Waals forces (the attractive and repulsive force between molecules in a sample) which cause the cantilever to become displaced from its initial position. These forces arise due to physical and/or chemical interactions between the sample and the tip, ultimately causing it to deflect; however, the tip can also simply be brought into contact with the material in order to map its physical profile. Therefore, when the tip is scanned across a two-dimensional (2D) area it will map the surface profile of the sample with atomic precision. Typically, a laser beam is incident on the back surface of the cantilever to monitor the deflection of the tip and the resulting laser deflection distribution. The redistribution of the laser beam position, as it is scanned across the sample, is collected by a quadrant photodiode array.

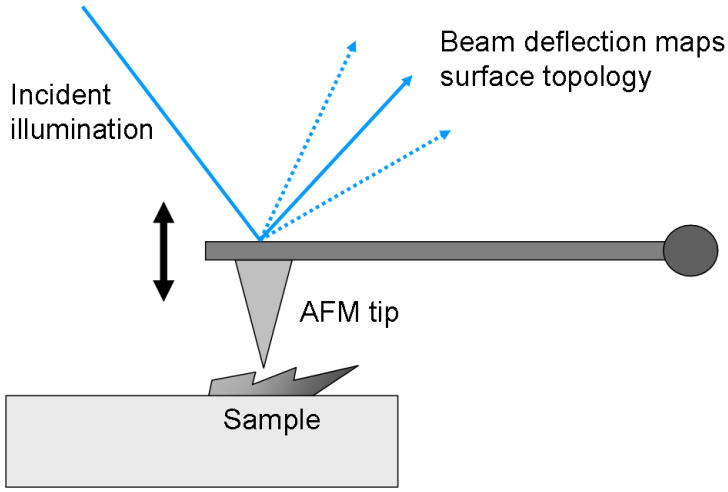

Figure 4 – The Atomic Force Microscope (AFM). A scanned cantilever and conical tip can map out the surface profile of a sample in either a contact or non-contact arrangement

Although an AFM offers nanometre profiling performance and is relatively simple to use, it suffers from several limitations, an example of which is the restricted physical movement of the tip. This limits the dimensions of an AFM image to around a few hundred micrometres both laterally and axially. Furthermore, the poor scan rate and therefore image acquisition time is a major hindrance to the semiconductor failure analyst since sample interrogation must be performed quickly for rapid diagnosis. In

addition, during the time taken to record an image, the sample and tip may suffer from thermal drift – e.g. up to 2µm over 5 hours [51]. This will result in an imperfect evaluation; however, this thermal drift issue may become obsolete through the development of video-rate and feature recognition AFM [52].

1.3 Nonlinear Effects and Techniques

Nonlinear effects and techniques have played an important role in the advance of several scientific industries and have enhanced a number of technical inspection applications. The ability to utilise an intensity dependent response within a sample is a common characteristic of all nonlinear techniques and permits the ability to improve spatial resolution, provide optical sectioning throughout thick materials and offer non-destructive 3D imaging. There are several nonlinear imaging techniques available. These include multi-photon absorption imaging [53], two-photon fluorescence [54], second harmonic generation (SHG) [55] and third harmonic generation (THG) [56]. It is important that these nonlinear imaging modes are reviewed and understood since they offer advanced evaluation opportunities that are simple not available in the linear regime.

In order to understand Sections 1.3.1 and 1.3.2 below, one must review the polarisation response of a medium in the presence of an incident electromagnetic field. This response states that radiation propagating through a medium exerts a force on the loosely bound valence or conduction band electrons. Typically, this force is small and in an isotropic medium the resulting electric polarisation is both parallel and proportional to the applied field. The polarisation response, *P*, is defined by,

$$P = \varepsilon_0 \chi E \tag{1}$$

Where ε_0 is the permittivity of free-space, χ is the electric susceptibility of the medium and E is the applied electric-field. In the presence of extremely high electric-fields, the polarisation response can no longer increase on a linear scale. We can now express the polarisation response more effectively as a power series expansion:

$$P = \varepsilon_0 \chi E = \varepsilon_0 \left(\chi^{(1)} + \chi^{(2)} E + \chi^{(3)} E^2 \right) E = \varepsilon_0 \left(\chi^{(1)} E + \chi^{(2)} E^2 + \chi^{(3)} E^3 + ... \right) \tag{2}$$

Typically, the value of the linear susceptibility, $\chi^{(1)}$, is much larger than the nonlinear susceptibility coefficients, $\chi^{(2)}, \chi^{(3)}$, etc, so it is only in the presence of intense electric fields that these nonlinear parameters begin to contribute to the polarisation response of the medium.

If an optical wave of the form,

$$E = E_0 \sin \omega t \tag{3}$$

is incident on the medium, then the resulting polarisation response becomes,

$$P = \varepsilon_0 \chi^{(1)} E_0 \sin \omega t + \varepsilon_0 \chi^{(2)} E_0^2 \sin^2 \omega t + \varepsilon_0 \chi^{(3)} E_0^3 \sin^3 \omega t + ... \tag{4}$$

This expression can also be written as,

$$P = \varepsilon_0 \chi^{(1)} E_0 \sin \omega t + \frac{\varepsilon_0 \chi^{(2)}}{2} E_0^2 (1 - \cos 2\omega t) + \frac{\varepsilon_0 \chi^{(3)}}{4} E_0^3 (3 \sin \omega t - \sin 3\omega t) + ... \tag{5}$$

It is the presence of the higher harmonics in terms 2 and 3 of equation (5) which lead to optical harmonic generation, which is important in a variety of applications.

1.3.1 Second Harmonic Generation (SHG)

SHG is a consequence of the $\cos 2\omega t$ term in equation (5). This corresponds to the polarisation response of the medium oscillating at twice the incident fundamental frequency. In terms of photons, this process can be thought of as having two identical incident photons of energy $\hbar\omega$ interact within the medium to combine and form a photon of energy $\hbar 2\omega$. The intensity of the emitted SHG is proportional to the square of the fundamental incident wave and, since the emissions are added coherently, the intensity of the SHG is also proportional to the square of the interaction length.

SHG can be utilised in many applications and configuration where the sample has a non-centrosymmetric crystal structure (second-order effects rely on a non-centrosymmetric crystal structure [57]). Examples include SHG in bulk crystals [58, 59], in engineered glass optical fibres [60], and within the cavity of a laser diode [61-64].

The process of SHG imaging [55, 65-68] is similar to fluorescence imaging (discussed later) with the main difference being that whereas the fluorescent light has an isotropic distribution, SHG emission propagates in the same direction as the incident light. For this reason, the detector must be positioned along the beam axis, as shown in Fig.5.

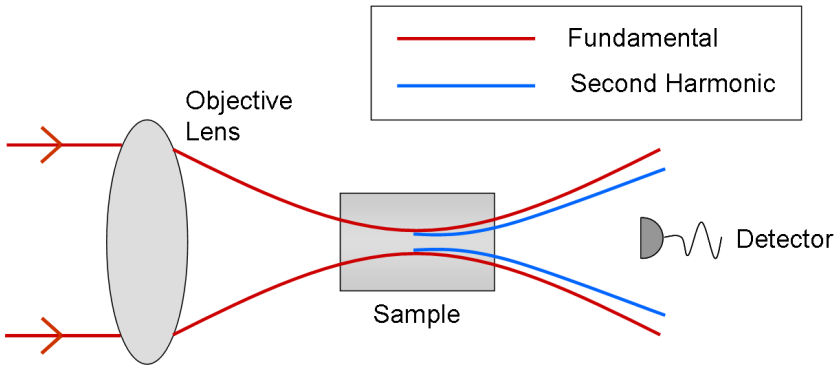

Figure 5 – Second-harmonic generation (SHG)

SHG is an extremely useful, 3D, second-order imaging technique that can be used to detect defects in silicon ICs. In general, SHG is not possible in silicon since it has a symmetric crystal structure; however, if a defect were present to disrupt the material configuration then SHG can take advantage of this. This could be used to assess the quality of wafers for failure analysis.

In addition, a unique process known as electric-field induced second-harmonic generation (EFISHG) can be exploited in semiconductor device imaging. Materials that do not possess inversion symmetry, or that have a symmetry-breaking interface, can produce second-harmonic generation through the use of a second-order effect; however, it is known that in the presence of an electric field a medium can create second-harmonic generation through a third-order process. This EFISHG signal can be observed in all materials, even those with inversion symmetry.

Since third-order susceptibilities, $\chi^{(3)}$, are typically small, it is required that peak laser powers and large voltages are used in order to observe this effect. Therefore, due to the large electric-fields present across confined semiconductor devices and the value of the third-order susceptibility in semiconductors, this otherwise weak effect can be observed.

EFISHG techniques have been used in many applications, examples of which include metal-semiconductor (silicon) junctions [69], at silicon-silicon oxide interfaces [70], in GaAs / AlGaAs quantum wells [71], in the measurement of $\chi^{(3)}$ in glasses [72], and in the tracking of electronic waveforms [73]. It was also been used in the investigation of wave propagation in silicon waveguides [74].

1.3.2 Third Harmonic Generation (THG)

Whereas second-harmonic generation microscopy is reliant on the second-order nonlinearity and non-centrosymmetric materials, third-harmonic generation (THG) imaging [56, 75] originates from the third-order nonlinearity which is present in all materials. Therefore, THG is ideally suited to the imaging of liquids and biological samples [76, 77].

THG occurs when a medium produces a third-order polarisation response to an incident optical field which is dependent on the cube of the optical field. The induced polarisation response oscillates at three times the fundamental frequency. THG is similar to SHG in that the emitted light propagates in the direction of the fundamental light.

It is important to note that the observation conditions for THG microscopy, under tight focusing conditions, generally rely on achieving a state of perfect, or slightly positive, phase-matching. This is achieved when $k_3 - 3k_1 = 0$, where k_3 and k_1 represent the wavevectors of the third-harmonic field and the fundamental field, respectively. Yet, it has been demonstrated that THG can vanish under these conditions when the incident laser beam is focused into a homogeneous bulk material. This can be explained by considering the Gouy phase shift [78] acquired during beam propagation through the focal-plane of the incident beam. A Gouy phase shift is the phase shift difference between a propagating Gaussian beam and a plane-wave in passing through a focal region. Typically, this value is π- there is a phase shift of $\pm\pi/2$ on either side of the beam waist.

In this situation, the THG generated by the homogeneous material before the focal-plane is re-absorbed by the material after the focal-plane due to destructive interference caused by the π phase shift; however, if there exists an inhomogeneous surface near the focal plane, e.g. a dielectric interface, then the symmetry along the optical axis will be broken and a detectable level of THG can be observed under tight focusing conditions [56, 75].

Therefore, THG microscopy is an ideal imaging tool for resolving hidden interfaces located within the probing focal volume.

1.3.3 Two-Photon Absorption (TPA)

Two-photon absorption (TPA) – the original example of multi-photon absorption - was not considered until several years after it was discovered that there exists a series of discrete energy levels in which the electrons associated with a particular atom must lie. Niels Bohr made the initial hypothesis in 1913 that radiation could be emitted by an atom when an electron sitting in a higher energy level, E_2 (larger radius orbit), returns to its ground state, E_1 (smallest radius orbit). This emitted radiation is characterised by the formula:

$$h\omega = E_2 - E_1 \tag{6}$$

where h is Plank's constant (h = 6.63 x 10^{-34}) and ω is the frequency at which the radiation is emitted/absorbed.

TPA was later introduced by a PhD student named Maria Goppert-Mayer who challenged the idea that there exists only a single discrete transition between adjacent energy levels. She argued that there was a finite probability that an atom may absorb or emit radiation in a process that exploits the use of an intermediate virtual state within a single quantum transition, although this probability is very small indeed [79, 80].

For a qualitative interpretation into how this idea can be understood, one can consider the Heisenberg Uncertainty Principle. This implies that an electron has the potential to remain in a virtual state (i.e. not real), after it has acquired a given amount of energy, for a finite length of time so long as the condition

$$\Delta E \Delta t \approx \hbar \tag{7}$$

is satisfied. In equation (7), ΔE is the energy obtained by the system and Δt is the time over which the energy may remain in the system. What this representation suggests is that no matter where the virtual energy state is located within the material's bandgap, it will be allocated a finite period of time over which this state may 'exist'.

One may consider a two-photon interaction to consist of two energy level intervals that occupy exactly one half of the single photon energy gap (Fig.6). Classically, this double transition is forbidden; however, the electron may 'exist' in this approximately half-way (virtual) state for a short period of time according to the energy-time uncertainty principal assumption discussed above. Therefore, if another photon of suitable energy were to arrive at this intermediate state before the electron fell back down to its initial energy level (the ground state) it may indeed be possible for the second photon to stimulate the electron to a higher energy level.

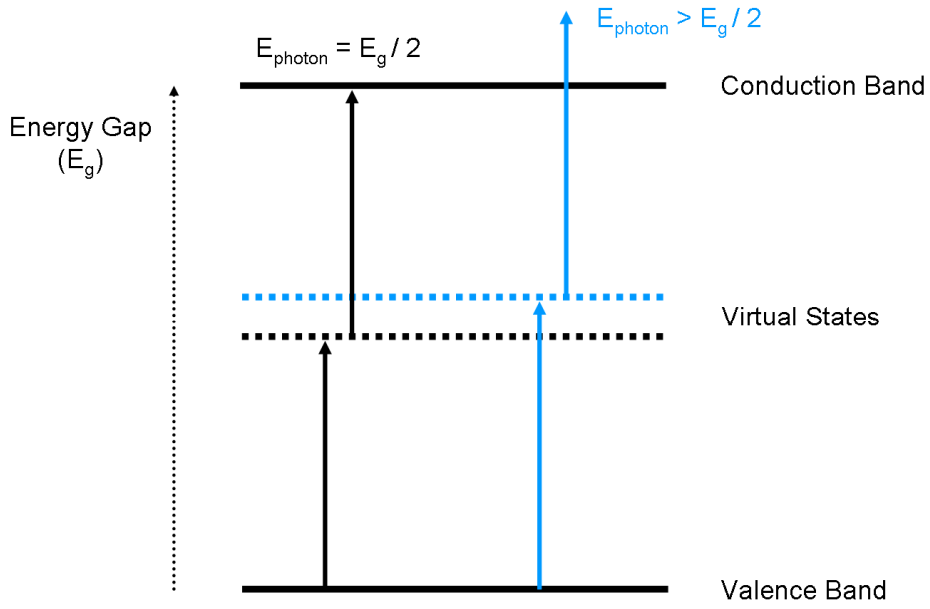

Figure 6 – Two-Photon Absorption (TPA) [81]. TPA in a semiconductor material can take place if the sum of the incident photon energy is exactly equal to, or greater than, half the material bandgap energy. This is unlike molecular TPA where the sum of the incident photon energy must exactly equal the bandgap transition

Although one has visualised this process in two equal energy steps, in truth the virtual state does not have to be positioned at the half-way energy level. It is also possible for the virtual state to be positioned in a manner that would require two different energy photons to interact with each other in order to obtain TPA. In principal, the only condition is that the two photons arrive near contemporaneously at the same position in space; however, due to the incredibly low probability of this event ever taking place [82] - it was calculated that the chance of a two-photon transition compared to a single photon transition ever happening would be around 1 in 10^8 - and the fact that the light

sources at the time of its initial contemplation produced intensities that were considerably lower than what was required, it was difficult for anyone to justify pursuing research in this field. In addition, even with modern ultrafast sources, this 'two-colour' arrangement is difficult to achieve in practice since it requires the spatiotemporal overlap of two different pulses from two different sources in the focal plane of the co-propagating beams in order to be successful.

It was not until the 1960s, and the invention of the laser, that the appropriate light intensities could be produced and this theory could finally be investigated. This initiated a variety of experimental and theoretical work which involved multi-photon processes in a wide range of materials [83-90]; however it must be stated that multi-photon absorption and emission was not initially considered to be a tool for the purposes of imaging but was instead used an alternative method of performing spectroscopy [91-96].

Today, the main light sources utilised for multi-photon purposes are those used in ultrafast laser technology. A key source in this field is the erbium-doped fibre laser and is discussed in detail in the following chapter.

1.3.4 Two-Photon Absorption in Semiconductor Integrated-Circuits

In order to facilitate two-photon absorption in a semiconductor sample, the laser wavelength must be chosen to be less than the bandgap of the semiconductor substrate material which has to be traversed. This is characteristic of TPA since no carriers will be generated at these wavelengths at low intensities – i.e. no optical absorption. The absorption spectrum of silicon exhibits extremely low absorption values at sub-bandgap (<1.1eV) energies; however, the semiconductor material can absorb two, or more, photons simultaneously at sufficiently high optical intensities. When this event takes place a single electron-hole pair is generated within the material [80]. This unique multi-photon absorption characteristic has been utilised in several non-semiconductor studies, including the development of spectroscopic techniques [97, 98] and in 3D multi-photon excitation microscopy of biological systems [53, 54, 99]. The exploitation of TPA in silicon is a critical feature of the work described within this thesis, and in various IC failure analysis modes, and therefore it will be discussed in detail.

There are several important parameters in the TPA process that are of particular relevance to IC characterisation instruments. Since silicon is transparent to the incident

laser radiation in the linear regime, the conventional single-photon exponential attenuation within the sample (Beer's Law) due to such a condition can no longer be applied. The generation of electron-hole pairs (carriers) through the TPA process is proportional to an intensity-squared relationship with the incident laser pulse. This indicates that there will only be significant nonlinear absorption within the high-intensity focal-volume of the focused beam [100-102]. This unique property allows for the injection of carriers to occupy any region within the sample, ultimately providing the option to generate a 3D map of absorption sensitivity sites on a device through the backside illumination of ICs which have been fabricated using silicon, gallium arsenide (GaAs) or indium phosphide (InP) wafers. In addition, the generated charge trail – i.e. the level of carriers generated as a function of laser intensity – that is produced through the TPA process differs in appearance to that generated through single-photon absorption. This interesting attribute can be understood by considering the theoretical analysis of beam propagation and carrier generation in a semiconductor material [103]:

$$\frac{dI(r,z)}{dz} = -\alpha I(r,z) - \beta_2 I^2(r,z) - \sigma_{ex} N I(r,z) \tag{8}$$

$$\frac{d\Phi(r,z)}{dz} = \beta_1 I(r,z) - \gamma_1 N(r,z) \tag{9}$$

$$\frac{dN(r,z)}{dt} = \frac{\alpha I(r,z)}{\hbar\omega} + \frac{\beta_2 I^2(r,z)}{2\hbar\omega} \tag{10}$$

where I is the beam irradiance, N is the density of free-carriers, Φ is the phase, α is the linear absorption coefficient, r is the radial distribution of the optical beam, ω is the optical frequency, β_2 is the TPA coefficient that is proportional to the imaginary part of $\chi^{(3)}$ (the third-order nonlinear-optical susceptibility), σ_{ex} is the absorptivity of laser-generated free carriers, β_1 is proportional to the real part of $\chi^{(3)}$, γ_1 describes the refraction due to free carriers, and z is the axial depth of the material.

Equation (8) describes the optical absorption experienced by a laser beam propagating in the material, (9) the phase change induced by the free carriers and the beam itself and (10) the carrier generation for both one- and two-photon absorption. In equation (10), $\hbar\omega$ represents the photon energy, where $\hbar$ is Planck's constant and the factor of two in

the denominator of the second term accounts for the generation of carriers for every TPA event that takes place.

The radial dependence of the laser beam irradiance, assuming a Gaussian distribution, is given by,

$$I(r,z) = \frac{2P}{\pi w(z)^2} \exp\left(\frac{-2r^2}{w(z)^2}\right) \tag{11}$$

where the longitudinal dependence of the beam radius $w(z)$ is,

$$w(z) = w_0 \left[1 + \left(\frac{\lambda z}{\pi w_0^2 n}\right)^2\right]^{\frac{1}{2}} \tag{12}$$

In these expressions, z is the longitudinal position relative to w_0 (the beam waist – i.e. focal position radius), P is the beam power, n is the refractive index and λ is the wavelength of the incident radiation. The confocal parameter of a Gaussian beam (z_0) is defined as the spatial region emanating from the beam waist over which the 1/e radius of the electric-field amplitude is less than or equal to $\sqrt{2}w_0$, and is expressed as,

$$z_0 = \pm \frac{\pi n w^2}{\lambda} \tag{13}$$

The propagation distance over which the beam is reasonably well collimated in the vicinity of w_0 is given by the parameter $2z_0$. As an example, in silicon (n~3.5), when λ=1.55µm and the beam waist is 0.8µm, this confocal parameter traverses approximately 9µm.

According to equations (8)-(10), it can be seen that a complete description of carrier generation in a semiconductor material is a fairly complex function of both laser pulse intensity and phase. In general, (8)-(10) can be solved simultaneously using equations (11) and (12) to describe the spatial dependence of the pulse irradiance, as well as an expression for describing the temporal behaviour of the pulse corresponding to (11); however, in order to illustrate the characteristics of TPA in semiconductor materials, only the carrier generation process, described by (10), will be discussed here.

In conventional single-photon absorption carrier generation, the I^2 term in equation (10) is small and can be neglected [104]. This situation is therefore governed by Beer's Law and allows one to express the laser beam irradiance as a function of depth within the semiconductor material easily. In addition, the density of beam induced carriers as a function of depth can also be calculated by considering the first term on the right-hand side of equation (10),

$$N_{1P}(z) = \frac{\alpha}{\hbar\omega}\exp(-\alpha z)\int_{-\infty}^{\infty} I_0(z,t)dt \tag{14}$$

In equation (14), the radial dependence of the pulse irradiance (11) has been suppressed for simplicity.

However, as we have seen already, TPA is proportional to the square of the pulse irradiance and therefore is not subject to exponential attenuation – refer to the right-hand side of equation (10). In addition, it is common for nonlinear refraction (equation (9) at the air-semiconductor boundary to alter the beam's propagation properties (equation (12)), and as a result amend the beam irradiance along *z*. Since TPA induced carrier generation is given by,

$$\frac{dN_{2P}(z)}{dt} = \frac{\beta_2}{2\hbar\omega} I^2(z,t) \tag{15}$$

the relative magnitude of the effect in (9) needs to be carefully considered. When nonlinear absorption is the only means of attenuation in a material, the irradiance as a function of depth is expressed as,

$$I(z) = \frac{I_0}{1+\beta_2 I_0 z} \tag{16}$$

From this, the optically induced carrier density can be evaluated by integration of (15) to give,

$$N_{2P}(z) = \frac{\beta_2}{2\hbar\omega}\int_{-\infty}^{\infty} I^2(z,t)dt \tag{17}$$

The integral in equation (17) can be calculated through substitution of *I(z)* from the expression given in (16) which will need to be amended to include an explicit time dependence through $I_0(t)$. For high-purity silicon under sub-bandgap illumination, the linear absorption coefficient is negligible and the generated photo-induced carrier density is expected to echo that expressed by equation (17) [103].

The expressions presented above provide the necessary details required to understand the advantages of TPA in semiconductor device studies. One main property that has been derived is that for single-photon absorption (above-bandgap excitation) there will be an exponential decrease in carrier generation as a function of depth within a material. This property results in an exponential optical absorption throughout the volume of the beam within the sample due to intrinsic optical attenuation that is linear with respect to laser irradiance; however, in a TPA arrangement, the absorption follows an intensity squared relationship which ultimately provides an ability to inject carriers at any given depth within the sample. This approach is analogous to the practice of optical sectioning in confocal fluorescent microscopy [17, 105].

1.3.5 Two-Photon Fluorescence (TPF)

Fluorescence can be achieved through the following process: when a photon is absorbed in a suitable medium, an electron is promoted to a higher energy state. Here it undergoes a process of non-radiative decay before emitting a photon, of lower energy to that of the absorbed photon, in the form of a fluorescent signal. This is a simple process that involves little technological sophistication; however, a fluorescent signal can only be obtained after a number of requirements have been met. First of all, a sample must be either fluorescent in nature or have a fluorescent ‘tag’ attached to it. An example of such a ‘tag’ is the green fluorescent protein [106]. Furthermore, a sample must be absorbing at the incident laser wavelength and contain the energy levels required for excitation and fluorescence.

Single photon fluorescence is the simplest to realise yet has a number of drawbacks. A major drawback of this imaging method is that, because it is a first-order effect, absorption takes place throughout the whole volume of the excitation beam contained within the sample (Fig.7). This can be a problem if one is interested in the levels of absorption at the focal-point of the beam. The beam will have experienced a significant level of attenuation before it reaches its section of importance. Also, another problem

associated with the amount of absorption within a sample is photo-bleaching – destruction of the fluorescent 'tag' due to excessive photochemical damage. If this were to occur the imaging site would be of no more use, unless additional fluorescent 'tag' were to be injected into the sample again.

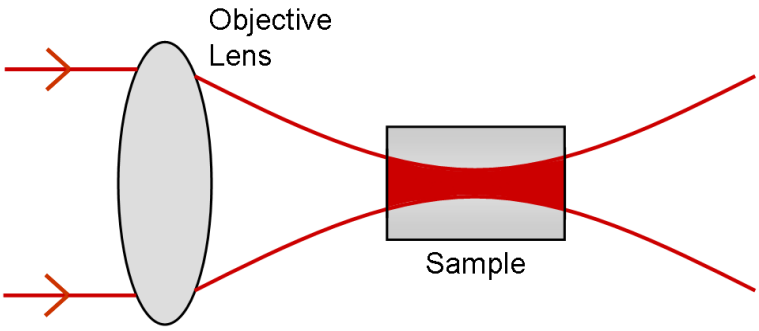

Figure 7 – Single photon absorption fluorescence. Absorption takes place throughout the entire volume of the excitation beam within the sample

Moreover, if one were interested in the study of biological samples, effects known as phototoxicity and chemical toxicity could cause problems due to excessive linear absorption. When imaging biological cells, it is vital that the cells remain alive for as long as possible, and if a large number of cells are being affected by the rate of absorption throughout the sample, the rate of damage to the cell will be higher. Simple heating caused by absorption can also damage the sample.

Finally, single photon fluorescence can be used to produce 3D images through confocal fluorescence laser scanning microscopy [105, 107].

TPF, on the other hand, provides a simple solution to these problems through an intensity-squared fluorescence relationship which alleviates the issues of excessive sample absorption [108], sample damage through photo-bleaching [109] and limited optical probing performance. Therefore, since a signal is only generated throughout the focal-volume of the incident beam, the resulting fluorescence can be detected at any location surrounding the sample due to its isotropic emission (i.e. 3D detection – Fig.8).

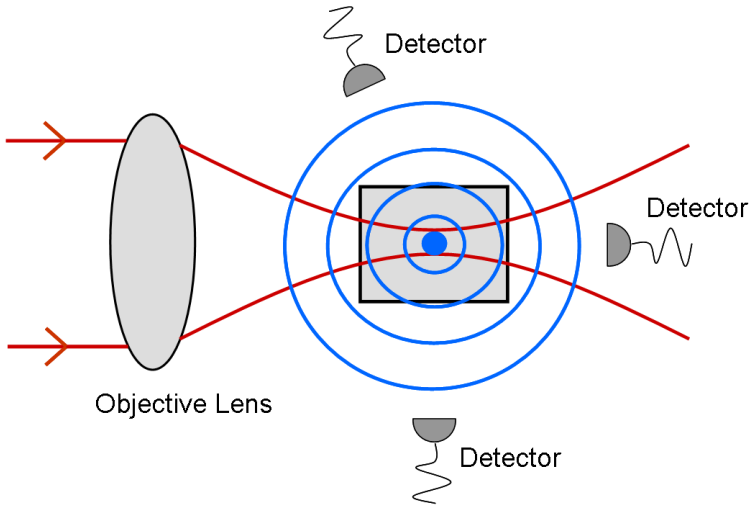

Figure 8 – Two-photon absorption fluorescence. Excitation beam shown in red, fluorescence in blue

This process was first demonstrated by Denk *et al* who utilised a two-photon microscope in the imaging of biological samples [54].

With regard to semiconductor imaging, it is also possible to observe this photo-bleaching effect where the level of TPA within a device becomes saturated and the resulting signal can no longer discriminate between neighbouring features. This was observed during the initial experimental work performed here by recording a high continuous TOBIC signal as the beam was laterally/axially translated across the chip. It was simple to overcome this effect however by limiting the incident optical power at the sample to ~5mW. This preserved TOBIC sensitivity whilst limiting any optically induced damage within the sample. Care must be taken here since photo-bleaching within a semiconductor chip can lead to device malfunction or physical damage.

Typically, TPA is obtained by using photons which originate from the same optical source. These photons therefore have identical energies; however, this condition can be manipulated by considering a combination of any two photons whose energies sum to the required material energy gap. This technique is known as two-colour TPA and has been studied in semiconductor devices [110, 111].

In addition, the ability to select difference photon energies (i.e. wavelengths) leads to the realisation that an optical wavelength may be chosen which requires 3 or more identical photons to satisfy the material's band-gap condition. This requires optical sources that

can produce exceptionally high peak powers, yet the demonstration of three-photon absorption fluorescence has been reported [112-114]. Furthermore, a four-photon absorption process has been demonstrated [115, 116]; however this was used in spectroscopic studies instead of imaging purposes.

1.4 Solid Immersion Techniques for Nanoscale Semiconductor Inspection and Probing

The solid immersion lens (SIL) is a powerful optical component that can enhance a variety of nanophotonic applications. In comparison with liquid immersion methods, "solid immersion" techniques are less well known in the microscopy community and for that reason have received limited attention as enabling tools in the characterisation and development of photonic and electronic devices. Since its invention, the SIL has been exploited in several nanoscale technologies, including semiconductor integrated-circuit (IC) inspection [117-120], nanoscale spectroscopy [121, 122], optical data storage [123, 124] and photolithography [125], yet the benefits the SIL has introduced in these fields have received poor coverage. Therefore, a detailed review of the theoretical aspects of the SIL is discussed and recent demonstrations of SIL-enhanced nanophotonic technologies are reviewed.

The field of nanophotonics, in which optical techniques are applied and developed to facilitate optical experiments with a spatial resolution of a few hundred nanometers or less, covers a wide range of general optics and technologies. These investigations typically involve state-of-the-art equipment and generally reject rudimentary procedures and apparatus in optical arrangements that are subject to increased scrutiny and precision. It is for this reason that the SIL provides a new and refreshing alternative to these complex configurations. It is straightforward to implement a SIL into optical systems and, when this is achieved, a well-defined list of progressive developments can be realised. SIL-enhanced methodologies offer improvements in spatial resolution (resolving power), collection efficiency and magnification, all critical parameters in the investigation of nanoscale devices. These advantages will be discussed in detail later in this chapter.

It is because of the reasons described above that the development of high resolution optical imaging techniques play a key role in the characterisation of semiconductor nanostructures.

1.4.1 Optical Resolution in the Far-Field

Nanophotonic experiments that involve optical coupling between a nanoscale object and a larger light source or detector normally employ either scanning near-field optical microscopy (SNOM) techniques [126] or high-*NA* conventional far-field microscopy. In far-field imaging, the resolution is determined by the angular spectrum and the spatial irradiance distribution of the light, in contrast to SNOM in which the resolution is primarily a function of the physical size of the near-field optical aperture used. An important consideration in far-field microscopy or spectroscopy of nanophotonics materials is therefore the resolving power of the microscope that is used. When considering an object positioned in the far-field, the limiting factor is the diffraction of the incident light. This prevents a conventional optical microscope from resolving any feature whose physical dimensions are less than approximately half the free-space illuminating wavelength of the optical system; however, when one considers the issue of imaging a structure which is buried at a given depth beneath a substrate, then the issues regarding resolving power become more complex, as the following sub-sections illustrate.

1.4.1.1 Surface Microscopy

The far-field diffraction of light, assuming the absence of any aberrations, states that the spatial resolution of any conventional optical microscope is subject to a lateral limit of,

$$\Delta x = \Delta y = 0.51\lambda / NA \tag{18}$$

(Sparrow's resolution criterion [127]) and a longitudinal limit of,

$$\Delta z = 0.44\lambda / n\sin^2(\alpha/2) \tag{19}$$

[128], where λ is the free-space wavelength of light, n is the refractive index of the object space, and α is the angular semi-aperture in the object space. The numerical aperture, $NA = n\sin\alpha$, determines the optical resolution through an inverse relationship with the diffraction limited lateral spatial resolving power. From this, there are essentially two parameters which can be manipulated to improve resolution. The first is to increase the angular semi-aperture of the system. This can improve the spatial resolution and also increase the amount of light collected from the focal plane, which can be of benefit in fluorescence collection. The second parameter is the local

wavelength. This can be reduced to improve the resolving power either by using a light source operating at shorter wavelength or by increasing the refractive index of the medium surrounding the focal plane.

Imaging in a medium of high refractive index increases the maximum *NA* to a value of *n*, resulting in an improvement in the lateral spatial resolution to $\Delta x = \Delta y = 0.51\lambda / n$, and the longitudinal spatial resolution limit to $\Delta z = 0.88\lambda / n$. Liquid immersion techniques can be ideal for this imaging configuration since a number of high-refractive-index liquids are readily available (e.g. many oils) and are simple to introduce into an optical arrangement. These liquids can have refractive index values of as high as 1.74 (methylene iodide) and under such conditions the immersed object space can provide a useful improvement in *NA* and spatial resolution; however, this arrangement can also introduce deleterious effects. An example of this is an increased probability of dirt and debris in the liquid entering the object space which can contaminate both the immersion liquid and the sample under inspection.

1.4.1.2 Sub-Surface Microscopy

When the object space is located at a given depth below the surface of a material then a range of issues are encountered that determine whether these buried structures can be adequately resolved by an optical microscope. The first consideration concerns the optical transparency of the surrounding medium. This parameter will determine the range of illumination wavelengths that are suitable to use, since light must be able to travel through the bulk material with sufficiently low loss in order to reach the buried features, and (in reflectance microscopy) to travel back through the sample towards the objective lens. Another parameter of critical importance is the refractive index, and its value determines how the incident light will be reflected and refracted at the surface of the medium.

In the commonly encountered case of a planar air-medium interface, reflection from the surface will reduce the amount of light which can be coupled into the material, limiting the amount of light that can be collected by a microscope objective to rays propagating at angles of incidence below the critical angle, $\alpha_c = \sin^{-1}(1/n)$. For these rays, Snell's Law informs us that the angular semi-aperture in the medium is reduced by a factor of *n* in a sub-surface configuration. Despite this reduction in the local value of $\sin\alpha$, the

overall *NA* of the imaging system remains unchanged because the refractive index in the object space is proportionately greater than that of air.

Another effect that refraction has on limiting optimum resolution achievable below a planar air-medium interface is that it introduces a significant amount of spherical aberration. This has a considerable impact on the diffraction limited performance of the microscope since spherical aberration increases linearly with angle and it is exactly these high-*NA* rays which one must include to obtain optimum resolving power.

Historically, liquid immersion techniques have been applied to circumvent some of these limiting factors by mitigating the effect of the planar geometry of the air-medium interface in order to improve the sub-surface resolving power of a microscope. Without any correction, the refractive effects described above ultimately mean a sub-surface imaging arrangement will always produce poorer performance than an imaging arrangement at the surface unless the planar interface geometry can be suitably modified.

1.4.2 The Solid Immersion Lens

Solid immersion microscopy was invented by Mansfield and Kino in 1990 [129, 130] and since then there has been a lot of interest in its use. It is based on the previously mentioned idea of liquid immersion microscopy [131] but improves on this technique by including the light that is located beyond the critical angle in the system to enhance the spatial resolution and beam-collection efficiency.

SIL methods are well suited to the imaging, characterisation and even the fabrication of many semiconductor nanophotonic devices [132-134] since it is not possible to obtain any immersion oils that have refractive indices approaching those of common semiconductors, nor is it possible to physically immerse the objective lens into solid samples.

Two types of SIL design are available and are discussed in detail below.

1.4.2.1 Hemispherical Solid Immersion Lens (h-SIL)

The SIL concept comes from the theory described by Born and Wolf [128]. This theory states that light can be focused without aberrations at only two points within a high-index sphere. These focal points are known as the “aplanatic” points of the sphere.

The first of these focal positions is located at the centre of the sphere (Fig.9). The incoming rays arrive at normal incidence to the surface of the sphere and do not encounter refraction at the air-SIL interface. This condition forms the basis for the design of a hemispherical SIL (h-SIL – Fig.10). Such elements are commonly used to image structures that lie close to the surface of a sample because these structures will be positioned at a focal plane lying immediately below the planar surface of the h-SIL. An h-SIL is a valuable component in the analysis of semiconductor quantum dots (QD) since it provides an opportunity to enhance the collection efficiency as well as improve the spatial profiling resolution of the sample under investigation - discussed later. An h-SIL also introduces magnification into an imaging system by a factor of *n*. The only limiting factor of the h-SIL, with regard to improved *NA*, is the maximum *NA* available from the objective lens.

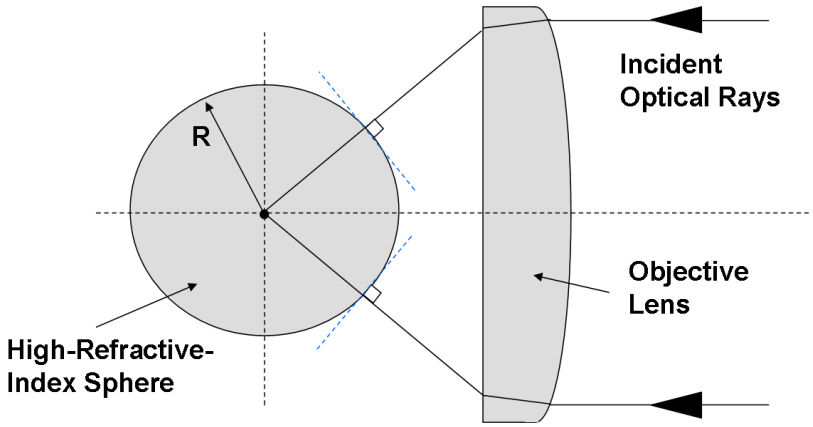

Figure 9 - Diagram illustrating the first aplanatic point within a sphere

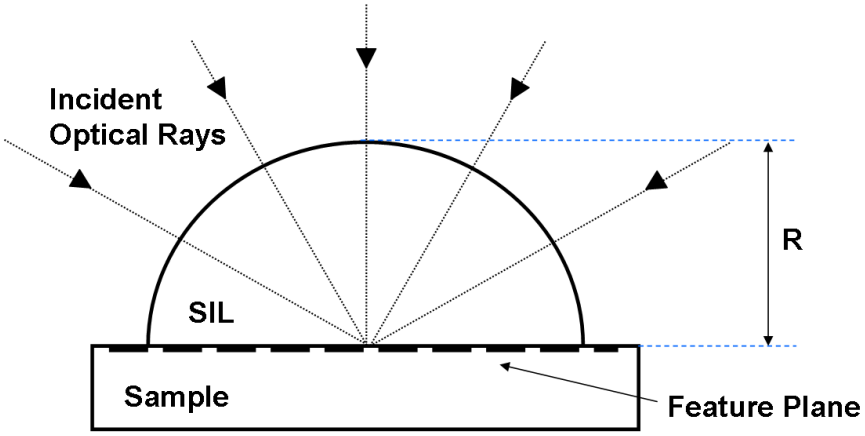

Figure 10 - A Standard Hemispherical Solid Immersion Lens (h-SIL)

1.4.2.2 Super Solid Immersion Lens (s-SIL)

Super solid immersion lenses exploit the second aplanatic focal position, which is located at a distance $z_0 = (n_1 / n_0)R$ from the centre of the sphere, where R is the radius of curvature of the sphere and n_0 and n_1 are the refractive indices of the sphere and the air respectively (Fig.11). Light focused to this point, whose incident rays will be refracted at the air-SIL interface, has a virtual focus located outside the sphere at a distance $z_1 = (n_0 / n_1)R$ from its centre. It is this condition that informs the design of a super-SIL (s-SIL) – also known as a Weierstrass Optic [132]. A major benefit of using an s-SIL stems from its improved magnification properties – compared to the h-SIL - which will be discussed later.

When one wishes to use a SIL to investigate sub-surface features in a given medium, care must be taken to ensure that there is a good index match between the SIL and the substrate. We note here that both an h-SIL and an s-SIL can be used for either surface or sub-surface interrogation. The key factor here is the design of the SIL itself which will be discussed below.

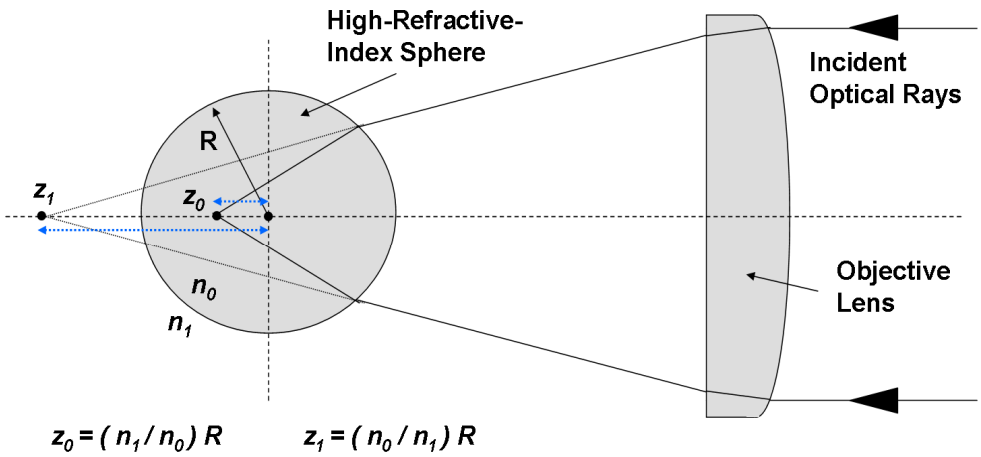

Figure 11 - Diagram illustrating the second aplanatic point within a sphere

Due to the geometry of the SIL, the generated focal spot size will be smaller because of the increase in the *NA* the SIL has on the system. The *NA* is defined by the expression $NA = n\sin\alpha$, as described previously. In sub-surface imaging, the best conventional microscopes can only achieve a value approaching unity since the solid angle in the medium reduces by a factor of *n*; however, if an s-SIL is used the solid angle increases by a factor of *n*. This indicates that the *NA* can be increased by a factor of n^2, up to the value were the *NA* is approximately equal to *n*. The maximum possible *NA* cannot ever realistically be achieved since it requires the rays of the focused laser beam to arrive at 90º. Nevertheless, the $\sin\alpha$ term in the expression for *NA* remains high for angles significantly below 90º, e.g. *NA* = 0.95*n* corresponds to θ = 70º. Using the information, one can calculate resolution values by considering Sparrow's criterion, $\Delta x = 0.51\lambda / NA$.

At this point it must be stated that in order for an s-SIL to operate effectively it must be designed following a standard process for achieving the maximum possible *NA* [128, 130, 135]. By considering the aplanatic points of a sphere, and by knowing the radius of the sphere, *R*, the refractive index of the components, *n*, and the depth at which the area of interest is located, *X*, then the distance *D*, which is the physical height of the s-SIL, can be calculated by using the following expression:

$$D = R\left(1 + \frac{1}{n}\right) - X \qquad (20)$$

Therefore, the focal position of an s-SIL (Fig.12) is wavelength dependent since *n* depends on the wavelength of the incident light. In contrast, the use of an h-SIL is universal for any wavelength.

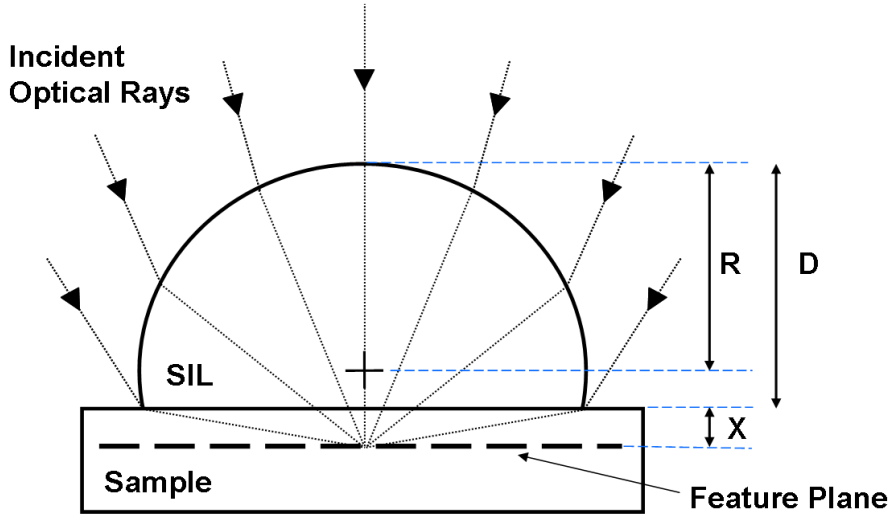

Figure 12 - A Super-Solid Immersion Lens (s-SIL)

Table 1 highlights a list of recent experimental techniques that have benefited from the enhanced spatial resolution of either an h-SIL or an s-SIL.

Table 1 - Recent demonstrations of SIL-enhanced spatial resolution

SIL Material	SIL Refractive Index	SIL Type	Free-space λ (nm)	Resolution (nm)	Refs
Glass	2	h-SIL	950	~350	[122]
Glass	1.845	s-SIL	633	178	[136]
Silicon	3.48	h-SIL	1064	230	[117]
Silicon	3.48	s-SIL	1530	~70*	[120]
GaAs	3.48	h-SIL	1050	350	[137]
Sapphire	1.76	s-SIL	736	243	[138]

* This performance will be discussed in Chapter 4

1.4.2.3 *Magnification Effects in Solid Immersion Lenses*

It has been stated already that an h-SIL introduces magnification to an imaging system (magnification ~ n). In contrast, an s-SIL adds significantly more magnification (~n^2). These increases in magnification can be best understood as an "optical lever" effect. When a focused laser beam is offset laterally from the optic axis by some distance on

the top surface of a SIL the resulting focal position moves by a smaller related distance. The beam offset and the resulting focal offset factors are different for both the h-SIL and the s-SIL. It has been stated previously throughout the literature that for the case of an h-SIL this factor is $\Delta x / n$, and for an s-SIL the factor is $\Delta x / n^2$, where Δx indicates the beam offset on the top of the SIL and n is the refractive index [139].

We have investigated this optical lever effect in detail for both the h-SIL and the s-SIL [118, 140], not only because it plays an extremely important role in the imaging system as a whole, but because it was suggested and confirmed that there is an optical lever effect in the axial direction as well – although initially the axial dependency was not fully understood [139]. We carried out a detailed analysis on both types of SIL, examining the optical lever effect in the axial and lateral directions by using the ray tracing software ASAP (Breault Research Organization).

The magnification analysis was performed and reviewed as part of the research efforts comprising Chapter 3, therefore they will be excluded from this discussion at present.

In order to effectively summarise all of the important features discussed to this point, the following table is presented to illustrate the main SIL imaging benefits [139]:

Table 2 - Important SIL parameters

	Magnification	**Resolution Gain**	**Max defined by:**
h-SIL	n	$1/n$	$NA_{objective\ lens}$
s-SIL	n^2	$1/n^2$	$1/n_{SIL}$

Solid immersion lenses can play a vital role in several aspects of nanophotonic characterisation and imaging applications. The following section reviews and discusses the recent literature with regard to practical SIL applications and considers current and future novel imaging architectures where SILs are at the forefront of these enabling technologies.

1.4.3 Non-Integrated-Circuit Applications of SILs

1.4.3.1 Optical Data Storage

The advance of optical data storage applications such as DVDs and BlueRay™ depends on the delivery of ever-increasing storage capacity per unit volume – just as Moore's Law [1] decrees a continuous rise in the density of transistors in semiconductor ICs. As the size of the individual storage elements shrinks, researchers face the challenge of overcoming the far-field diffraction limitations of recording and reading optically-encoded information which puts restrictions on the maximum capacity of an optical storage device. One solution to overcome this issue is to utilize evanescent near-fields that can be produced by fabricating optical read/write heads that consist of high-refractive-index SILs [124, 141]. Researchers and engineers have demonstrated a recording density of more than 40Gb/cm^2 when operated along with novel materials, including diamond [142], that have a potential capacity of up to 120Gb/cm^2; however, due to the use of evanescent near-fields in this approach, these technologies require a spacing between the read/write pickups and the storage media of approximately 10-25nm. This creates a range of problematic issues for optical data storage since the small spacing introduces difficulties in the removal of the medium and an enhanced probability in device contamination; however, this application is not only limited to the near-field. Mansfield *et al* [143] described a far-field configuration that can tolerate variations in media thickness and a certain degree of skew as the disc wobbles during rotation.

Alternatively, it has been shown that the SIL geometry can be manipulated slightly to develop a novel imaging technique know as the solid immersion mirror [144-147]. In this arrangement, the illumination source is coupled into an optical waveguide and brought to a focus by a 2D parabolic mirror which has been fabricated in the waveguide (Fig.13). The waveguides reported here were fabricated by thin-film deposition on commonly used materials for recording head sliders in the magnetic data storage industry. These studies demonstrate an optical mode confinement of ~180nm under ~640nm illumination.

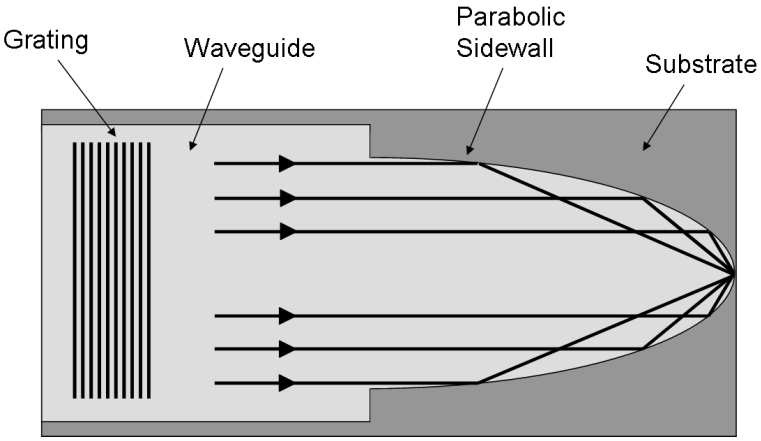

Figure 13 - Planar Solid Immersion Mirror [144-147]

1.4.3.2 Photoresponse Mapping

A novel technique which exploits the reduced spatial profiling benefits of a SIL is in the sub-micrometre photoresponse mapping of nanowire superconducting single-photon detectors (SSPD). SSPDs that are based on superconducting nanowires are a new form of high-speed, high-sensitivity single-photon detector that has a broad spectral range covering the visible well out to the infrared (IR). The basic SSPD consists of a 100nm wide wire which follows a serpentine route patterned onto an ultrathin Niobium Nitride (NbN) superconductor. The limitations of these devices arise from defects or other forms of contamination or processing errors, resulting in a poor device yield. Electrical current and/or inductance measurements are typically employed to investigate these issues; however the minimum achievable focal spot size in optical characterisation overwhelms the device area itself. Hadfield *et al* [148] have utilised a hemispherical SIL to reduce the focal spot-size to dimensions smaller than the actual device area to generate an improved photoresponse map. The results are illustrated in Fig.14 below.

Fig.14 (a) shows a scanning electron micrograph of a meander type SNSPD. Fig.14 (b) shows a photoresponse map of a device with high detection efficiency where no SIL has been used to obtain a uniform response across the entire area efficiency. In contrast, Fig.14 (c) shows a photoresponse map of a device with low detection efficiency where an h-SIL has been utilised. The sensitive area in Fig.14 (c) is much smaller than the focal spot, indicating the presence of a localised constriction in the nanowire.

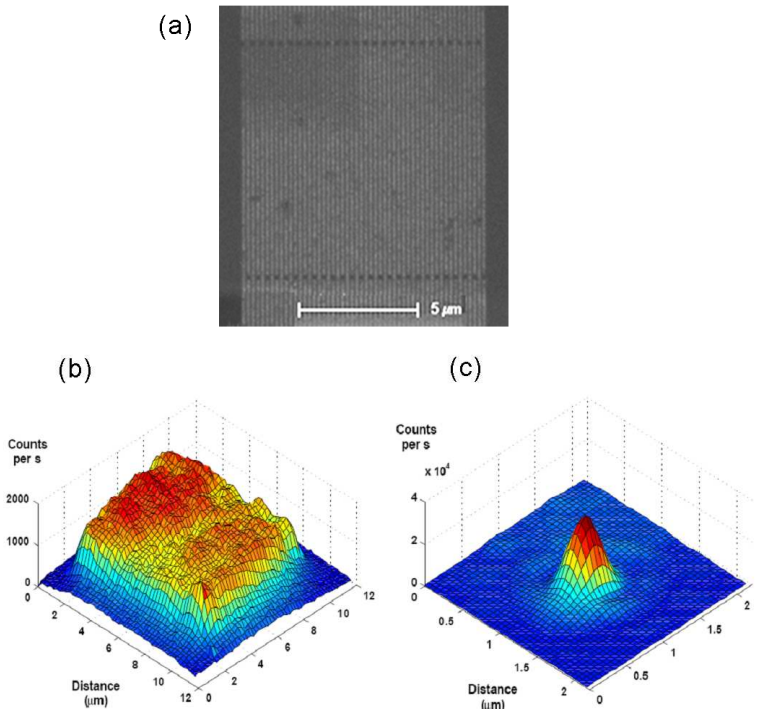

Figure 14 - Nano-optical studies of superconducting nanowire single-photon detectors (SNSPD). (a) Scanning electron micrograph of a meander type SNSPD (linewidth 100nm, pitch 200nm, total area 10mm x 10mm). (b) Photoresponse map of uniform high efficiency device, (*NA* = 0.4, no SIL, λ = 470nm FWHM spot size 620nm). (c) Photoresponse map of constricted low efficiency device (*NA* = 0.36, n = 2 SIL, λ = 470nm, FWHM spot size 313nm) [141]

1.4.3.3 Spectroscopic Studies of Semiconductor Nanostructures

Nano-photoluminescence is one of the most critical characterisation techniques that can be used to investigate the electronic energy levels in semiconductors nanostructures. The fabrication and development of semiconductor nanostructures occupy a large volume of state-of-the-art optoelectronic applications, therefore photoluminescence (PL) has been developed into a local spectroscopy method to cover such structures as quantum wells [149, 150] and QDs [151]. As previously mentioned, the diffractive far-field limitations on spatial resolution restrict the performance of local excitation/detection techniques. This can be overcome by working in the near-field regime with SNOM for example; however, far-field investigations need not be completely excluded. By positioning a suitable SIL on the surface of a given sample, semiconductor spectroscopy can be enhanced since a SIL is simple to work with and reduces the risk of sample contamination. Furthermore, SIL experiments can be performed at low temperature.

As we will see, PL experiments cover a wide range of semiconductor materials due to the endeavours of researchers and material scientists in their search for innovative

photonic devices that exhibit novel characteristics. For this reason, a wide range of semiconductor materials have been considered for SIL manufacture since the refractive index between SIL and sample must be accurately matched. To date, SILs made from a wide variety of different materials to suit particular applications have been successfully fabricated and demonstrated. Some of these SILs will be discussed later within this review.

In a far-field PL system using a SIL [152], not only is there an improvement in the spatial resolution, there is also an increase in the collection efficiency. The collection efficiency of a spectroscopic system is of enormous importance, especially if there exists a low level of excitation intensity or a low signal level. Various SNOM experiments do not offer a useful solution here since there is a trade-off between spot size and collection efficiency. Therefore, by introducing a SIL into a far-field PL arrangement the collection efficiency can be greatly enhanced [153-156]. Comparison shows that SIL and non-SIL collection efficiencies can differ by about a factor of 6 [137]; however this value may vary, by approximately 20%, simply due to the cleanliness of both the sample and the SIL.

Typical SIL experiments exploit the force of gravity to retain the SIL in position on the sample; however, in some cases the experimental arrangement is altered to configure the sample and SIL planar surfaces normal to the surface of the optical bench. This results in a need to fix the SIL in place on the sample which raises the question of the potential air gap influence on system performance. The evaluation of *NA* in a SIL-enhanced nano-PL arrangement is no different to any other far-field system. The *NA* is defined as $NA_{obj} \cdot n_{SIL}$ for a h-SIL and $NA_{obj} \cdot n_{SIL}^2$ (up to a maximum value of n_{SIL}) for a s-SIL. The influence an air gap has on resolution is heavily dependent on whether the effective *NA* approaches n_{SIL} or not. When this condition is satisfied a near-field description is necessary. It has been shown theoretically that even an interface roughness of λ/5 can affect the resolution [135]; however, an effective $NA << n_{SIL}$ remains in the far-field regime and has been theoretically demonstrated to have a low impact on system resolution even with an air gap of several microns [157]. This may be explained by considering the effects of total internal reflection between the SIL planar surface and the sample surface under both high- and low-*NA* conditions.

Generally speaking, a SIL-enhanced nano-PL arrangement can be incorporated into any semiconductor spectroscopy experiment when there is a requirement for high spatial resolution, high collection efficiency and the planar surfaces of the materials are optically flat. From here we present a range of applications where the SIL-enhanced nano-PL arrangement has demonstrated its benefits.

As an introduction, the improved spatial resolution from a SIL-enhanced system has been demonstrated in the evaluation of QD densities on a semiconductor sample [121, 158]. Fig.15 illustrates the effect a SIL has on PL measurements of single dots. Two QD samples, each with similar dot densities have been measured under identical experimental condition. Therefore, these two graphs are comparable to each other, where only the introduction of a SIL has taken place. With no SIL we see many spectral lines - these are all from different dots; however, in the SIL sample we see three lines which emanate from the same dot. The SIL has decreased the number of dots studied by decreasing the focal spot size. With no SIL the calculated diffraction limited spot size was 760nm and with a SIL it was 380nm. This decreases the spot area by a factor of 4 which effectively reduces the number of dots studied by a factor of 4 as well. In this example we can see that the SIL has also increased the collection efficiency by a factor of 4. The increase in counts lets us see these extra lines in the PL spectrum. Figure 15 is reproduced by kind permission by Dr. P. Dalgarno.

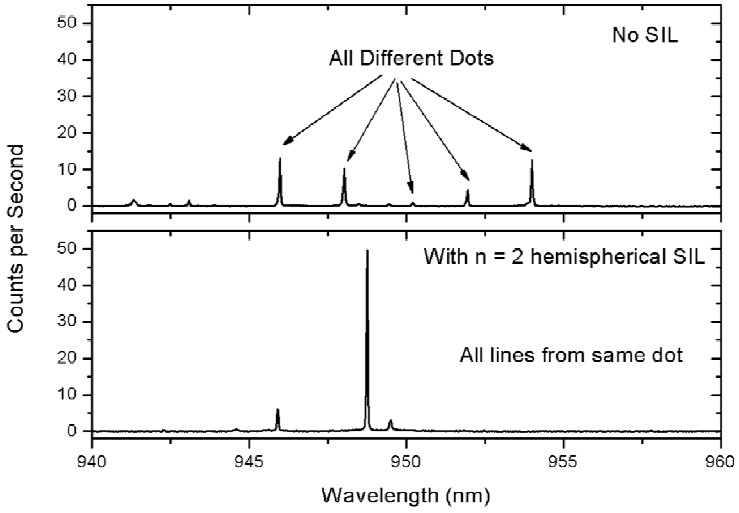

Figure 15 - SIL-enhanced PL experiments highlighting the improvement on spatial resolution. The figure presents spectra from two samples, one recorded with a SIL and one without a SIL. The two samples had similar quantum dot densities and experienced the same excitation powers

In other nano-PL experiments glass and GaAs SIL techniques have been utilised to study single InAs/GaAs QDs [137, 154]. In addition, a SIL has been applied to high-resolution spectroscopic analysis of GaAs quantum wells [159] to study carrier transfer/diffusion at low temperatures [160-164]. Furthermore, the in-plane transport of excitons in quantum wells by nano-PL investigations through the use of a confocal microscope and a SIL has been demonstrated in ZnSe quantum wells [165].

Another interesting application which has a complimentary experimental approach to nano-PL studies, and utilises the benefits of a SIL, is the investigation of contrast in transmission spectroscopy of a single QD [122]. Laser spectroscopy has two main advantages over nano-PL: sub-μeV resolution capabilities and an improved ability to prepare the states in the QD - the latter enables the spin characteristics of the dot to be unravelled and understood. The contrast observed here, in the ideal limit, is proportional to the scattering cross-section divided by the laser spot area. Therefore, due to the SIL-enhanced spatial resolution improvement, the contrast is improved by a factor of 5. The result is illustrated below in Fig.16. This figure is reproduced by kind permission of Dr. B. Gerardot.

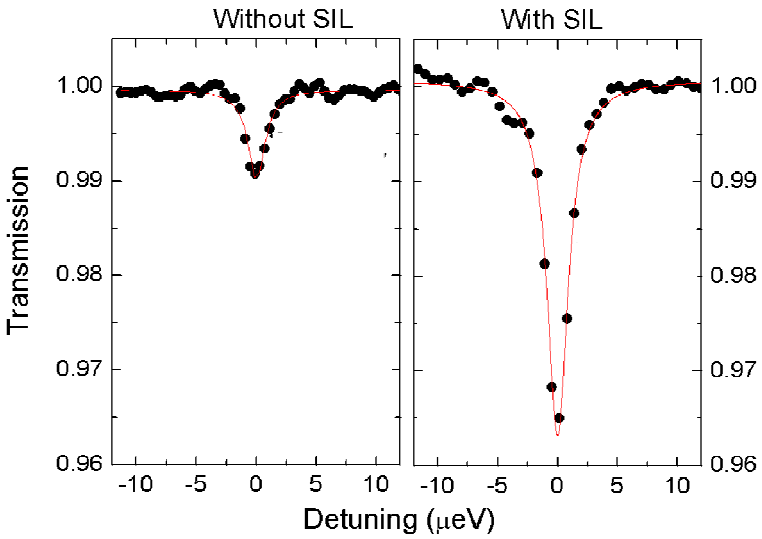

Figure 16 – Contrast-enhanced transmission spectroscopy of a single quantum dot [122]

1.4.4 Applications of SILs in Semiconductor Integrated-Circuit Failure Analysis

The main body of this work concerns the development of various SIL-enhanced TOBIC microscopy techniques to image silicon ICs, and therefore the details and performance of such procedures will be discussed in subsequent Sections. These include the use of a SIL in a backside imaging configuration to profile, in both two and three-dimensions, the internal microstructure of a silicon flip-chip with ultra-high-resolution performance, utilising SIL-enhanced polarisation-dependent imaging to obtain maximum and minimum lateral resolution values ranging from 240nm to 120nm, respectively, depending on the direction of the incident polarisation vector, and employing pupil function engineering along with polarisation-dependent microscope to resolve features with an unprecedented resolution of 70nm. The above mentioned experiments were performed using 1550nm illumination from a femtosecond Er:fibre laser.

There are several other important SIL-enhanced applications in semiconductor IC FA and these will be reviewed below.

1.4.4.1 SIL-Enhanced Confocal Imaging

Confocal laser scanning microscopy is currently the method of choice for sub-surface optical microscopy, and combined with solid immersion techniques, demonstrations have shown a capability to resolve feature sizes of ~230nm under 1064nm free-space illumination [117]. This configuration was the first experimental demonstration of the powerful imaging capabilities exhibited by the s-SIL in high-resolution semiconductor IC inspection in the near-IR. In [114] the authors of the work describe an s-SIL as a numerical aperture increasing lens (NAIL); however the geometry and mathematical treatment of an s-SIL and NAIL are identical.

The experimental approach here is no different to the conventional laser-scanning confocal arrangement described above, yet with the simple addition of an s-SIL the system performance has been greatly improved which reveals the powerful influence an appropriate SIL can create. The only experimental concern in this arrangement is the effective transmission of the illumination wavelength through the additional silicon introduced by the inclusion of the SIL. Optical absorption in silicon limits the transmission through the silicon substrate to wavelengths above or equal to approximately 1µm, therefore this issue is easily remedied by the use of a near-IR optical source. In addition, the sample substrate can be suitably thinned in order to

reduce the penetration length which must be double-passed in a confocal arrangement to further reduce the level of absorption within the silicon substrate.

1.4.4.2 SIL-Enhanced Angular Spectrum Tailoring for IC Characterisation

Ippolito *et al* have expanded the conventional ideas of IC characterisation by demonstrating an angular spectrum dependence on the performance of a silicon IC microscope [166]. This technique utilises a simple spatial light modulator to isolate the supercritical components, only accessible with a SIL, of a focused optical field to induce evanescent coupling beyond the substrate/dielectric interface - sub-critical fields are affected by the dielectric interconnected layer, of refractive index ~1-2, fabricated on the front side of transistors found on modern IC chips. This technique improved on the ability to image the transistor layer of a silicon IC by avoiding light being collected from the first metallisation layer through this supercritical beam isolation (Fig. 17). The low-*NA* rays in the system were able to penetrate the SiO_2 layer and be strongly reflected by the metalisation layer below, whereas the high-*NA* rays were unable to penetrate the SiO_2 layer due to total internal reflection at this interface. Spatial filtering to remove the low-*NA* rays means that the low-contrast image of the device layer is not obscured by the intense reflected rays from the first metalisation layer.

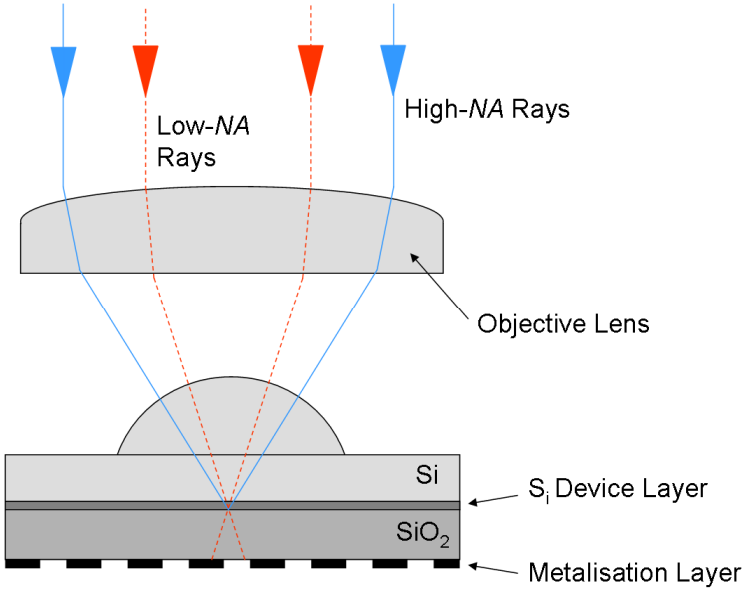

Figure 17 - Angular spectrum tailoring for improved IC characterisation [60]

1.4.4.3 SIL-Enhanced Widefield Microscopy of ICs

In addition to the IC characterisation techniques discussed above, Köklü *et al* have demonstrated that the improvement in spatial resolution provided by a SIL can be exploited to gain significant benefits in IR widefield microscopy of silicon ICs [167]. By utilising the tight focusing characteristics of a SIL, and by removing the blurred contribution from the out-of-focus background signal, it was demonstrated that the widefield microscope can selectively focus on the different axial layers of an IC when performing imaging from the backside through the silicon substrate. This result reported a lateral and longitudinal resolution, which is comparable to the performance of a confocal microscope, of 0.26µm and 1.24µm, respectively.

1.4.4.4 SIL Substrates for Enhanced IC Failure Analysis

The positioning of a SIL on a sample is conventionally controlled by hand or by using a mechanically controlled cantilever approach [141]. These methods offer reduced accuracy and suffer from the issue of repeatability; however, a recent technique, available to IC fault isolation and characterisation engineers, which circumvents these problems by directly "forming the silicon substrate into a SIL" (FOSSIL) [168]. This was achieved by forming the SIL into the substrate using a computer controlled lathe; however, this is also possible by using a focused ion beam (FIB). Through implementation of the FOSSIL technique it has been demonstrated that not only does it improve optical resolution but it also enhances detection sensitivity and potential waveform analysis for future devices. The FOSSIL approach can be implemented at the device fabrication stage in order to alleviate SIL positioning tolerances.

Zachariasse *et al* reported a novel solid immersion blazed-phase diffractive lens for high-resolution laser based FA of silicon ICs [169]. The technique used a general design algorithm using computer generated holography to calculate the structure required for reconstruction of a spherical wavefront through a silicon substrate into any user-defined pattern. This diffractive SIL technique also investigated the reconstruction of multiple focal points and a ring pattern from the same diffractive optic. Fabrication of this device was achieved using a combination of FIB technology and reactive-ion etching. Reactive-ion etching has also been used in the development of a silicon phase Fresnel lens [170] – an imaging mode which is related to that employed by Zachariasse. These progressive techniques are illustrated in Fig.18.

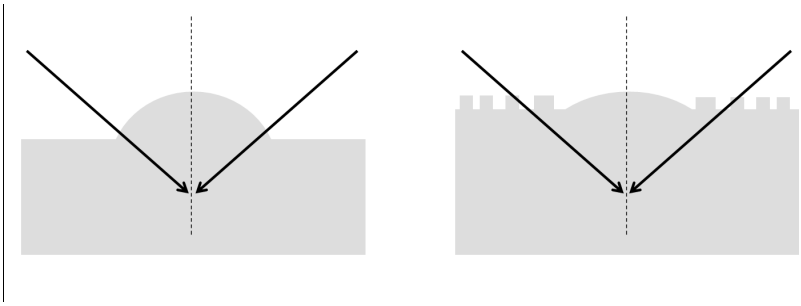

Figure 18 - Solid immersion substrates. Progression from a SIL etched into a substrate [73] to a binary approximation of the ideal solution [169, 170]

1.4.4.5 Other Potential Applications of SILs in IC Characterisation

The ability to image local hot-spots in ICs is a mature technology and there are several reports of SIL-enhanced thermal imaging [48, 171-173] available. In addition, there are several other laser signal injection microscopy techniques deployed in IC research and development that are based on a comparable stimulus. Examples of these include OBIC and TOBIC (discussed above), Optical Beam Induced Resistance Change (OBIRCH), Laser Aided Device Alteration (LADA) and Laser Induced Voltage Alteration (LIVA) to name but a few [12]. All of these above mentioned techniques are compatible with SIL imaging and could benefit from this. Evidence of which has been demonstrated by Goh *et al*. [174] who successfully implemented a SIL into a Thermally Induced Voltage Alteration (TIVA) IC FA scheme to obtain an enhancement in the TIVA signal of up to 15 times. This work also discussed the practical design considerations for optimum SIL-enhanced laser induced techniques for IC characterisation.

An alternative FA technique that exploits optical methods to probe on-chip waveforms as part of the design cycle is the novel EFISHG mode [73]. This approach uses mid-IR femtosecond optical pulses to measure EFISHG conversion efficiencies and can be used to enable high-bandwidth sub-surface optical probing of complementary metal-oxide semiconductor (CMOS) silicon devices in a similar way to that which has been demonstrated using silicon coplanar transmission lines [74]. The EFISHG signal generated is extremely weak and therefore could benefit from the use of a SIL to substantially improve the signal levels recorded. The SIL-enhanced *NA* would create an improved optical resolution as well as increase the capability to generate a higher efficiency conversion due to the larger component of the incident polarization located at normal incidence to the junction plane in a CMOS circuit.

Furthermore, it was recently demonstrated that a SIL-enhanced terahertz (THz) emission microscope had been developed as an alternative inspection tool for semiconductor ICs [175]. This configuration facilitated THz emission and collection in a transmission geometry which utilised three hemispherical SILs – one for focusing the incident laser beam onto the sample (located on the frontside of the sample), the second for improved THz collection efficiency from the device under test (located on the backside) and a third for enhanced THz collection by a suitable detector. This work demonstrated a spatial resolution of less than 1.5µm with an n_{SIL}=1.98 at 780nm.

1.4.5 SIL Modifications

As an aside to using the conventional SIL designs and analysis presented earlier, researchers have investigated two types of novel SIL design which have been analysed theoretically using vector diffraction theory. The advantages of these so-called high-performance super-sphere solid immersion lenses (HPSILs) [176] are that they can improve the Strehl ratio of the focused spot and increase the focal depth of near-field optical systems. This can be achieved by either increasing the radius of the HPSIL so that it is a little larger than that of the common s-SIL or by reducing the distance between the planar surface and the centre of the sphere so that it is slightly smaller than that of the standard s-SIL. These HPSILs can improve the development of near-field optical data storage and photolithography.

Continuing the idea of SIL modification, a near-field optical storage system utilising a left-handed material (LHM) has also been reported by attaching a LHM slab to the lower surface of a conventional SIL [177]. The performance of this novel approach improves on that obtained using conventional storage techniques since it can image the focused spot at the lower surface of the SIL to the surface of a disc with improved accuracy. It also allows a large air-gap to exist for operational convenience while maintaining a large signal contrast and a high storage density.

In addition to the above SIL modifications, an interesting SIL design which breaks from the typical 3D geometry is the silicon-based planar waveguide SIL [178]. In this geometry, the SIL can be positioned in the written sample by photolithography, which remedies common alignment, tilt and packaging problems that occur when using free-space optics. These planar-SILs were simulated using the ray-tracing software Zemax

and the experimental results compared against beam propagation methods. The planar waveguides and the SILs were fabricated from silica and silicon nitride, respectively.

1.4.6 Microfabricated SILs

Fletcher and Crozier *et al* have presented both a microfabricated silicon and silicon nitride SIL for deployment in scanning microscopy applications [179, 180]. Both SILs were fabricated onto individual cantilevers for scanning, and a tip was fabricated opposite the SIL to localise SIL-sample contact. The results from this approach demonstrate sub-diffraction limited performance in both cases. This technique echoes that demonstrated by Lerman *et al* who applied SIL near-field optics to Raman analysis of strained silicon thin films [181]; however, instead of the SIL fabrication taking place on a cantilever, the SIL was positioned on the end of an optical fibre. These scanning microscopy methods that utilise AFM style cantilevers provide an important tool for the investigation of microelectronic devices.

1.5 Conclusions

This chapter has introduced the many important challenges associated with semiconductor IC FA, and has reviewed the diverse microscopical surface and sub-surface investigative methodologies available to the microelectronic failure analyst in an attempt to remedy these issues. Key concepts in this field include illumination penetration, device stimulation and spatial profiling resolution. All of these parameters, and more, have been exposed and discussed in detail. The ability to identify and correctly resolve many possible microchip fabrication defects and operational malfunctions demands the capability to coordinate and employ a large number of mechanical and electronic interrogation techniques. Such modalities range from simple surface optical microscopy to advanced sub-surface laser signal injection schemes such as the TOBIC approach adopted throughout this work.

Furthermore, the theoretical aspects associated with the design and characterisation of a SIL was introduced and a detailed review of experimentally demonstrated and potential SIL-enhanced microscopy applications was presented. Such applications range from the sub-surface examination of the complex 3D microstructures fabricated in silicon ICs, to quantum PL and transmission measurements in semiconductor QD nanostructures. SIL microscopy combines the advantages of conventional microscopy with those of near-field techniques, and is being increasingly adopted across a diverse range of

technologies and applications. Important benefits are enabled by SIL-focusing, including an improved lateral and axial spatial profiling resolution when a SIL is used in laser-scanning microscopy or excitation, and an improved collection efficiency when a SIL is used in a light-collection mode, for example in fluorescence micro-spectroscopy. These advantages arise from the increase in *NA* that is provided by a SIL. Other SIL-enhanced improvements, for example spherical-aberration-free sub-surface imaging, are a fundamental consequence of the aplanatic imaging condition that results from the spherical geometry of the SIL.

1.6 Thesis Structure

The remainder of this thesis is sectioned into 5 chapters:

Chapter 2 introduces the design and construction of the optical sources that are utilised throughout the entirety of this work. These include a stretched-pulse erbium-doped fibre laser and an erbium-doped fibre amplifier (EDFA). The fibre laser was used to permit sufficient silicon substrate transmission and induce nonlinear absorption at the device layer of a silicon flip-chip to create a measureable TOBIC photocurrent. This nonlinear photocurrent was used as the basis of the images displayed in later chapters. The fibre amplifier was used to generate an almost octave spanning supercontinuum to be used in an optical coherence tomography (OCT) arrangement for investigating ultra-high-resolution imaging in silicon microchips and artwork.

Chapter 3 presents results revealing the benefits available to laser signal injection microscopy procedures through the use of a suitably designed SIL by demonstrating ultra-high-resolution 2D and 3D imaging of a silicon flip-chip. The results attained in this section report diffraction-limited optical resolution under near-IR illumination. The chapter includes a discussion of the SIL-induced optical lever effect, an effect which is of enormous importance in the calibration of s-SILs, and an experimentally implemented peak-detection algorithm for optimisation and generation of 3D images that were captured.

Chapter 4 introduces the efforts made towards achieving optical super-resolution performance from our nonlinear microscope by manipulating both the shape and orientation of the focal plane PSF through pupil-function engineering and polarisation-sensitive imaging in the vectorial focusing regime. These techniques are first treated

individually, and their performance characterised and discussed before results from a hybrid arrangement are presented. The work documented here was able to measure sub-100nm feature sizes (~70nm) and set an unprecedented benchmark in the area of far-field optical imaging of silicon ICs.

Chapter 5 discusses the progress made in ultra-broadband supercontinuum generation for application in an ultra-high-resolution high-dynamic-range OCT imaging system. The continuum was generated using a 100m length of polarisation-maintaining highly nonlinear optical fibre which was coupled into a Michelson interferometer to perform imaging of various samples, including a silicon IC, a business card, a selection of artwork and a banknote. The continual optimisation and post-processing of any new captured data from our system is discussed and exposes the wide variety of differing OCT configurations and analytical enhancements which can be implemented to improve the quality of a final image. Such analysis includes Fourier transformations and Hilbert transformations, single photodiode detection and balanced-detection schemes, and the role of polarisation-dependence on manipulating the width of the resulting interferogram.

Chapter 6 will present an overall technical discussion of the impact of the results presented in the earlier chapters. It will also propose potential future developments, improvements and applications.

References

[1] *International Technology Roadmap for Semiconductors - Executive Summary*. 2007.

[2] G.E. Moore, "Craming More Components onto Integrated Circuits", *Electronics Magazine* **38**, 114-117 (1965)

[3] B.P. Richards and P.K. Footner, "Failure Analysis in Semiconductor-Devices - Rationale, Methodology and Practice", *Gec Journal of Research* **1**, 74-91 (1983)

[4] W. Osten, *Optical Inspection of Microsystems - Optical Science and Engineering*. Florida: Taylor and Francis Group (2007)

[5] B. Jalali and S. Fathpour, "Silicon photonics", *Journal of Lightwave Technology* **24**, 4600-4615 (2006)

[6] A.W. Fang, E. Lively, H. Kuo, D. Liang, and J.E. Bowers, "A distributed feedback silicon evanescent laser", *Optics Express* **16**, 4413-4419 (2008)

[7] H.S. Rong, R. Jones, A.S. Liu, O. Cohen, D. Hak, A. Fang, and M. Paniccia, "A continuous-wave Raman silicon laser", *Nature* **433**, 725-728 (2005)

[8] R.E. Warburton, A. McCarthy, A.M. Wallace, S. Hernandez-Marin, S. Cova, R.A. Lamb, and G.S. Buller, "Enhanced performance photon-counting time-of-flight sensor", *Optics Express* **15**, 423-429 (2007)

[9] A.S. Liu, H.S. Rong, R. Jones, O. Cohen, D. Hak, and M. Paniccia, "Optical amplification and lasing by stimulated Raman scattering in silicon waveguides", *Journal of Lightwave Technology* **24**, 1440-1455 (2006)

[10] R.A. Soref, "Silicon-Based Optoelectronics", *Proceedings of the IEEE* **81**, 1687-1706 (1993)

[11] J. Brown, P.K. Footner, and B.P. Richards, "Failure Analysis of Plastic Encapsulated Components - the Advantages of Ir Microscopy", *Journal of Microscopy-Oxford* **148**, 179-194 (1987)

[12] J.C.H. Phang, D.S.H. Chan, M. Palaniappan, J.M. Chin, B. Davis, M. Bruce, J. Wilcox, G. Gilfeather, C.M. Chua, L.S. Koh, H.Y. Ng, and S.H. Tan, "A review of laser induced techniques for microelectronic failure analysis", *Ipfa 2004: Proceedings of the 11th International Symposium on the Physical & Failure Analysis of Integrated Circuits*, 255-261 (2004)

[13] S.E. Aw, H.S. Tan, and C.K. Ong, "Optical-Absorption Measurements of Band-Gap Shrinkage in Moderately and Heavily Doped Silicon", *Journal of Physics-Condensed Matter* **3**, 8213-8223 (1991)

[14] B.P. Richards and P.K. Footner, *The Role of Microscopy in Semiconductor Failure Analysis*: Oxford University Press (1992)

[15] M. Minsky, *Microscopy Apparatus - US Patent Number 3,013,467*. 1961: United States.

[16] T. Wilson, *Confocal Microscopy*. London: Academic Press (1990)

[17] T. Wilson, "Optical Sectioning in Confocal Fluorescent Microscopes", *Journal of Microscopy-Oxford* **154**, 143-156 (1989)

[18] W.B. Amos, J.G. White, and M. Fordham, "Use of Confocal Imaging in the Study of Biological Structures", *Applied Optics* **26**, 3239-3243 (1987)

[19] C.H. Lee and J.P. Wang, "Noninterferometric differential confocal microscopy with 2-nm depth resolution", *Optics Communications* **135**, 233-237 (1997)

[20] V.J. Cemine, B. Buenaobra, C.M. Blanca, and C. Saloma, "High-contrast microscopy of semiconductor and metal sites in integrated circuits by detection of optical feedback", *Optics Letters* **29**, 2479-2481 (2004)

[21] M. Pfennigbauer and W.R. Leeb, "Optical satellite communications with Erbium doped fiber amplifiers", *Space Communications* **19**, 59-67 (2003)

[22] C.J.R. Sheppard and D.M. Shotton, *Confocal Laser Scanning Microscopy*: Bios (1997)

[23] T. Wilson, "Confocal Light-Microscopy", *Annals of the New York Academy of Sciences* **483**, 416-427 (1986)

[24] C.J.R. Sheppard, "Scanning Optical Microscopy of Semiconductor-Materials and Devices", *Scanning Microscopy* **3**, 15-24 (1989)

[25] P.D. Nellist, M.F. Chisholm, N. Dellby, O.L. Krivanek, M.F. Murfitt, Z.S. Szilagyi, A.R. Lupini, A. Borisevich, W.H. Sides, and S.J. Pennycook, "Direct sub-angstrom imaging of a crystal lattice", *Science* **305**, 1741-1741 (2004)

[26] E. Hecht, *Optics*: Addison-Wesley (1987)

[27] J.M. Bonard, J.D. Ganiere, B. Akamatsu, D. Araujo, and F.K. Reinhart, "Cathodoluminescence study of the spatial distribution of electron-hole pairs generated by an electron beam in Al0.4Ga0.6As", *Journal of Applied Physics* **79**, 8693-8703 (1996)

[28] H.J. Leamy, "Charge Collection Scanning Electron-Microscopy", *Journal of Applied Physics* **53**, R51-R80 (1982)

[29] K. Nikawa and S. Inoue, "New laser beam nesting methods applicable to fault localization and defect detection in VLSI devices", *1996 IEEE International Reliability Physics Proceedings, 34th Annual*, 346-354 (1996)

[30] E.I. Cole, "Global fault localization using induced voltage alteration", *Microelectronics Reliability* **41**, 1145-1159 (2001)

[31] P. Tangyunyong, D. Benson, and E.I. Cole, "Thermal modeling of a polysilicon-metal test structure used for thermally induced voltage alteration characterization", *Journal of Vacuum Science & Technology B* **18**, 2820-2825 (2000)

[32] E.I. Cole, "Electron and optical beam testing of integrated circuits using CIVA, LIVA, and LECIVA", *Microelectronic Engineering* **31**, 13-24 (1996)

[33] E.I. Cole, J.M. Soden, J.L. Rife, D.L. Barton, and C.L. Henderson, "Novel Failure Analysis Techniques Using Photon Probing with a Scanning Optical Microscope", *1994 IEEE International Reliability Physics Proceedings - 32nd Annual*, 388-398 (1994)

[34] T. Wilson and J.N. Gannaway, "Examination of grain boundaries in polycrystalline solar cells using a scanning optical microscope", *Electronics Letters* **14**, 507-508 (1978)

[35] P.S.D. Lin, *Method and apparatus for analyzing semiconductor devices using charge-sensitive electronbeam-injected-carrier microscopy*, United States patent 4, 755, Editor. 1988.

[36] K. Kano, *Semiconductor Devices*: Prentice Hall (1998)

[37] C. Werner, D. Reuter, and A.D. Wieck, "Optical beam-induced current in planar two-dimensional n-p-n devices", *Physica E-Low-Dimensional Systems & Nanostructures* **32**, 508-511 (2006)

[38] T. Wilson and E.M. McCabe, "Optical Beam Induced Current Imaging of Dislocations in Semiconductors", *Optik* **75**, 11-15 (1986)

[39] T. Wilson and E.M. McCabe, "Photoluminescence and Optical Beam Induced Current Images of Defects in Semiconductors", *Physica Status Solidi a-Applied Research* **103**, 107-113 (1987)

[40] T. Wilson and E.M. McCabe, "Theory of Optical Beam Induced Current Images of Defects in Semiconductors", *Journal of Applied Physics* **61**, 191-195 (1987)

[41] T. Wilson and E.M. McCabe, "The Effect of Bias on Optical Beam Induced Current Imaging of Defects in Planar and Schottky Junction Devices", *Optik* **78**, 59-63 (1988)

[42] T. Wilson and P.D. Pester, "Theory of Scan Speed Dependent Optical Beam Induced Current Images in Semiconductors", *Optik* **76**, 18-22 (1987)

[43] C. Xu and W. Denk, "Two-photon optical beam induced current imaging through the backside of integrated circuits", *Applied Physics Letters* **71**, 2578-2580 (1997)

[44] C. Xu and W. Denk, "Comparison of one- and two-photon optical beam-induced current imaging", *Journal of Applied Physics* **86**, 2226-2231 (1999)

[45] C. Xu, L.M.F. Chirovsky, W.S. Hobson, J. Lopata, W.H. Knox, J.E. Cunningham, W.Y. Jan, and L.A. D'Asaro, "Two-photon photocurrent imaging of vertical cavity surface emitting lasers", *Applied Physics Letters* **76**, 1510-1512 (2000)

[46] J. Christofferson and A. Shakouri, "Thermoreflectance based thermal microscope", *Review of Scientific Instruments* **76** (2005)

[47] O. Breitenstein, M. Langenkamp, F. Altmann, D. Katzer, A. Lindner, and H. Eggers, "Microscopic lock-in thermography investigation of leakage sites in integrated circuits", *Review of Scientific Instruments* **71**, 4155-4160 (2000)

[48] S.B. Ippolito, S.A. Thorne, M.G. Eraslan, B.B. Goldberg, M.S. Unlu, and Y. Leblebici, "High spatial resolution subsurface thermal emission microscopy", *Applied Physics Letters* **84**, 4529-4531 (2004)

[49] C.M. Blanca, V.J. Cemine, V.M. Sastine, and C. Saloma, "High-resolution differential thermography of integrated circuits with optical feedback laser scanning microscopy", *Applied Physics Letters* **87** (2005)

[50] G. Binnig, C.F. Quate, and C. Gerber, "Atomic Force Microscope", *Physical Review Letters* **56**, 930-933 (1986)

[51] Z.K. Zhan, Y.L. Yang, W.J. Li, Z.L. Dong, Y.L. Qu, Y. Wangland, and L. Zhou, "AFM Operating-Drift Detection and Analyses based on Automated Sequential Image Processing", *2007 7th IEEE Conference on Nanotechnology, Vol 1-3*, 752-757 (2007)

[52] R.V. Lapshin, "Automatic drift elimination in probe microscope images based on techniques of counter-scanning and topography feature recognition", *Measurement Science & Technology* **18**, 907-927 (2007)

[53] W. Denk, "Multiphoton microscopy: Imaging with nonlinear optics", *Photonics Spectra* **31**, 125-& (1997)

[54] W. Denk, J.H. Strickler, and W.W. Webb, "2-Photon Laser Scanning Fluorescence Microscopy", *Science* **248**, 73-76 (1990)

[55] A.C. Millard, P.J. Campagnola, W. Mohler, A. Lewis, and L.M. Loew, *Second harmonic imaging microscopy*, in *Biophotonics, Pt B*. 2003. p. 47-69.

[56] J.A. Squier, M. Muller, G.J. Brakenhoff, and K.R. Wilson, "Third harmonic generation microscopy", *Optics Express* **3**, 315-324 (1998)

[57] A. Yariv, *Quantum Electronics*. New York: Wiley (1989)

[58] Y. Fujii and T. Sakudo, "Electric-field induced optical second-harmonic generation in $KTaO_3$ and $SrTiO_3$", *Physical Review B* **13**, 1161-1167 (1976)

[59] P. Loza-Alvarez, D.T. Reid, P. Faller, M. Ebrahimzadeh, and W. Sibbett, "Simultaneous second-harmonic generation and femtosecond-pulse compression in aperiodically poled KTiOPO4 with a RbTiOAsO4- based optical parametric oscillator", *Journal of the Optical Society of America B-Optical Physics* **16**, 1553-1560 (1999)

[60] T. Mizunami, Y. Sadakane, and Y. Tatsumoto, "Second-harmonic generation from thermally-poled twin-hole silica-glass optical fiber and enhancement by quasi phase matching", *Thin Solid Films* **516**, 5890-5893 (2008)

[61] D. Paboeuf, G. Lucas-Leclin, P. Georges, B. Sumpf, G. Erbert, C. Varona, P. Loiseau, G. Aka, and B. Ferrand, "Blue laser emission by intracavity second harmonic generation in Nd : ASL

pumped by a tapered amplifier laser diode stabilized by a volume Bragg grating", *Applied Physics B-Lasers and Optics* **92**, 189-193 (2008)

[62] F. Jia, Q. Xue, Q. Zheng, Y. Bu, and L. Qian, "5.3 W deep-blue light generation by intra-cavity frequency doubling of Nd : GdVO4", *Applied Physics B-Lasers and Optics* **83**, 245-247 (2006)

[63] M. Thorhauge, J.L. Mortensen, P. Tidemand-Lichtenberg, and P. Buchhave, "Tunable intra-cavity SHG of CWTi : Sapphire lasers around 785 nm and 810 nm in BiBO-crystals", *Optics Express* **14**, 2283-2288 (2006)

[64] Z. Zhang, H.M. Tan, L.L. Gao, B.S. Wang, J.G. Miao, and J.Y. Peng, "Intra-cavity second harmonic generation with Nd : YVO4/BIBO laser at 542 nm", *Optics Communications* **267**, 487-490 (2006)

[65] J.N. Gannaway and C.J.R. Sheppard, "2nd-Harmonic Imaging In Scanning Optical Microscope", *Optical and Quantum Electronics* **10**, 435-439 (1978)

[66] L. Moreaux, O. Sandre, M. Blanchard-Desce, and J. Mertz, "Membrane imaging by simultaneous second-harmonic generation and two-photon microscopy", *Optics Letters* **25**, 320-322 (2000)

[67] L. Moreaux, O. Sandre, and J. Mertz, "Membrane imaging by second-harmonic generation microscopy", *Journal of the Optical Society of America B-Optical Physics* **17**, 1685-1694 (2000)

[68] C.J.R. Sheppard, J.N. Gannaway, R. Kompfner, and D. Walsh, "Scanning Harmonic Optical Microscope", *IEEE Journal of Quantum Electronics* **13**, D100-D100 (1977)

[69] G. Lupke, C. Meyer, C. Ohlhoff, H. Kurz, S. Lehmann, and G. Marowsky, "Optical 2nd-Harmonic Generation as a Probe of Electric-Field-Induced Perturbation of Centrosymmetric Media", *Optics Letters* **20**, 1997-1999 (1995)

[70] P. Godefroy, W. deJong, C.W. vanHasselt, M.A.C. Devillers, and T. Rasing, "Electric field induced second harmonic generation spectroscopy on a metal-oxide-silicon structure", *Applied Physics Letters* **68**, 1981-1983 (1996)

[71] A. Fiore, E. Rosencher, V. Berger, and J. Nagle, "Electric field induced interband second harmonic generation in GaAs/AlGaAs quantum wells", *Applied Physics Letters* **67**, 3765-3767 (1995)

[72] H.G. de Chatellus and E. Freysz, "Measurement of the third-order susceptibility of glasses by EFISH of femtosecond pulses", *Optics Express* **9**, 586-591 (2001)

[73] D. Xiao, E. Ramsay, D.T. Reid, B. Offenbeck, and N. Weber, "Optical probing of a silicon integrated circuit using electric-field-induced second-harmonic generation", *Applied Physics Letters* **88** (2006)

[74] A. Nahata, T.F. Heinz, and J.A. Misewich, "High-speed electrical sampling using optical second-harmonic generation", *Applied Physics Letters* **69**, 746-748 (1996)

[75] Y. Barad, H. Eisenberg, M. Horowitz, and Y. Silberberg, "Nonlinear scanning laser microscopy by third harmonic generation", *Applied Physics Letters* **70**, 922-924 (1997)

[76] A.C. Millard, D.N. Fittinghoff, P.W. Wiseman, M. Muller, G.J. Brakenhoff, J.A. Squier, and K.R. Wilson, "Three dimensional, third harmonic microscopy of living systems", *Biophysical Journal* **78**, 800Plat (2000)

[77] C.-K. Sun, S.-W. Chu, S.-Y. Chen, T.-H. Tsai, T.-Z. Liu, C.-Y. Lin, and H.-J. Tsai, "Higher harmonic generation microscopy for developmental boilogy", *Journal of Structural Biology* **147**, 19-30 (2004)

[78] A.E. Siegman, *Lasers*. Sausalito, California: University Science Books (1986)

[79] M. Goppert-Mayer, "Uber die Wahrscheinlichkeit des Zusammenwirkens zweier Lichtquanten in einem Elementarakt", *Naturwissenschaften* **17**, 932 (1929)

[80] M. Goppert-Mayer, "Uber Elementarakte mit zwei Quantensprungen", *Annalen der Physik* **9**, 273-295 (1931)

[81] M. Brune, J.M. Raimond, P. Goy, L. Davidovich, and S. Haroche, "Realization Of A 2-Photon Maser Oscillator", *Physical Review Letters* **59**, 1899-1902 (1987)

[82] W. Denk and K. Svoboda, "Photon upmanship: Why multiphoton imaging is more than a gimmick", *Neuron* **18**, 351-357 (1997)

[83] T.R. Bader and A. Gold, "Polarization Dependence of Two-Photon Absorption in Solids", *Physical Review* **171**, 997-1003 (1968)

[84] H.B. Bebb, "Quantitative theory of the two-photon ionization of the alkali atoms", *Physical Review* **149**, 25-32 (1966)

[85] H.B. Bebb, "Theory of three-photon ionization of the alkali atoms", *Physical Review* **153**, 23-28 (1967)

[86] R. Braunstein and O. Ockman, "Optical double-photon absorption in CdS", *Physical Review* **134**, A499-A507 (1964)

[87] A. Gold and J.P. Hernandez, "One- and two-photon transitions of atoms in solids", *Physical Review* **139**, A2002-A2007 (1965)

[88] W. Kaiser and C.G.B. Garrett, "Two-Photon Excitation in CaF_2:Eu^{2+}", *Physical Review Letters* **7**, 229-231 (1961)

[89] D.A. Kleinman, "Laser and two-photon processes", *Physical Review* **125**, 87-88 (1962)

[90] W. Zernik, "Two-photon ionization of atomic hydrogen", *Physical Review* **135**, A51-A57 (1964)

[91] I.D. Abella, "Optical double-photon absorption in cesium vapor", *Physical Review Letters* **9**, 453-455 (1962)

[92] J.A. Giordmaine and J.A. Howe, "Intensity-induced optical absorption in CS2", *Physical Review Letters* **11**, 207-209 (1963)

[93] T.W. Hansch, S.A. Lee, R. Wallenstein, and C. Wieman, "Doppler-free two-photon spectroscopy of hydrogen 1S-2S", *Physical Review Letters* **34**, 307-309 (1975)

[94] G.D. Mahan, "Theory of Two-Photon Spectroscopy in Solids", *Physical Review* **170**, 825-838 (1968)

[95] W.L. Peticolas, J.P. Goldsborough, and K.E. Rieckhoff, "Double photon excitation in organic crystals", *Physical Review Letters* **10**, 43-45 (1963)

[96] P.J. Regensburger and E. Panizza, "Two-photon absorption spectrum of CdS", *Physical Review Letters* **18**, 113-114 (1967)

[97] Y.W. Liu and P.E.G. Baird, "Two-photon spectroscopy in potassium", *Measurement Science and Technology* **12**, 740-743 (2001)

[98] D.M. Friedrich, "2-Photon Molecular-Spectroscopy", *Journal of Chemical Education* **59**, 472-481 (1982)

[99] M. Gu and C.J.R. Sheppard, "Effects of a Finite-Sized Pinhole on 3d Image-Formation in Confocal 2-Photon Fluorescence Microscopy", *Journal of Modern Optics* **40**, 2009-2024 (1993)

[100] T.F. Boggess, K.M. Bohnert, K. Mansour, S.C. Moss, I.W. Boyd, and A.L. Smirl, "Simultaneous Measurement of the 2-Photon Coefficient and Free-Carrier Cross-Section above the Bandgap of Crystalline Silicon", *IEEE Journal of Quantum Electronics* **22**, 360-368 (1986)

[101] E.W. Vanstryland, H. Vanherzeele, M.A. Woodall, M.J. Soileau, A.L. Smirl, S. Guha, and T.F. Boggess, "2 Photon-Absorption, Nonlinear Refraction, and Optical Limiting in Semiconductors", *Optical Engineering* **24**, 613-623 (1985)

[102] E.W. Vanstryland, M.A. Woodall, H. Vanherzeele, and M.J. Soileau, "Energy Band-Gap Dependence of 2-Photon Absorption", *Optics Letters* **10**, 490-492 (1985)

[103] D. McMorrow, W.T. Lotshaw, J.S. Melinger, S. Buchner, and R.L. Pease, "Subbandgap laser-induced single event effects: Carrier generation via two-photon absorption", *IEEE Transactions on Nuclear Science* **49**, 3002-3008 (2002)

[104] J.S. Melinger, S. Buchner, D. McMorrow, W.J. Stapor, T.R. Weatherford, and A.B. Campbell, "Critical-Evaluation of the Pulsed-Laser Method for Single Event Effects Testing and Fundamental-Studies", *IEEE Transactions on Nuclear Science* **41**, 2574-2584 (1994)

[105] E.H.K. Stelzer, S. Hell, S. Lindek, R. Stricker, R. Pick, C. Storz, G. Ritter, and N. Salmon, "Nonlinear Absorption Extends Confocal Fluorescence Microscopy into the Ultra-Violet Regime and Confines the Illumination Volume", *Optics Communications* **104**, 223-228 (1994)

[106] R.Y. Tsien, "The Green Fluorescent Protein", *Annual Reviews Biochemistry* **67**, 509-544 (1998)

[107] S. Lindek, C. Cremer, and E.H.K. Stelzer, "Confocal theta fluorescence microscopy with annular apertures", *Applied Optics* **35**, 126-130 (1996)

[108] S.M. Potter, "Vital imaging: Two photons are better than one", *Current Biology* **6**, 1595-1598 (1996)

[109] G.H. Patterson and D.W. Piston, "Photobleaching in two-photon excitation microscopy", *Biophysical Journal* **78**, 2159-2162 (2000)

[110] C.A. Alonzo, W. Garcia, and C. Saloma, "Generation of optical-beam induced current via two-color (two-photon) excitation", *Optics Communications* **246**, 117-122 (2005)

[111] C.A. Alonzo, W. Garcia, and C. Saloma, "Crosstalk between two-photon and two-color (two-photon) excitation in optical beam induced current generation with two confocal excitation beams", *Optics Communications* **270**, 139-144 (2007)

[112] M. Gu, "Resolution in three-photon fluorescence scanning microscopy", *Optics Letters* **21**, 988-990 (1996)

[113] R. Naskrecki, M. Menard, P.v.d. Meulen, G. Vigneron, and S. Pommeret, "Three-photon absorption cross-section of simple molecular liquids", *Optics Communications* **153**, 32-38 (1998)

[114] Y.S. Wang, O.Y.-H. Tai, C.H. Wang, and A.K.-Y. Jen, "One-, two- and three-photon absorption induced fuorescence of a novel chromophore in chloroform solution", *Journal of Chemical Physics* **121**, 7901-7907 (2004)

[115] F.E. Hernandez, K.D. Belfield, I. Cohanoschi, M. Balu, and K.J. Schafer, "Three- and four-photon absorption of a multiphoton absorbing fluorescent probe", *Applied Optics* **43**, 5394-5398 (2004)

[116] H. Shim, M. Liu, C. Hwangbo, and G.I. Stegeman, "Four-photon absorption in the single-crystal polymer bis(paratoluene) sulfonate", *Optics Letters* **23**, 430-432 (1998)

[117] S.B. Ippolito, B.B. Goldberg, and M.S. Unlu, "High spatial resolution subsurface microscopy", *Applied Physics Letters* **78**, 4071-4073 (2001)

[118] E. Ramsay, K.A. Serrels, M.J. Thomson, A.J. Waddie, M.R. Taghizadeh, R.J. Warburton, and D.T. Reid, "Three-dimensional nanoscale subsurface optical imaging of silicon circuits", *Applied Physics Letters* **90**, 131101 (2007)

[119] K.A. Serrels, E. Ramsay, R.J. Warburton, and D.T. Reid, "Nanoscale optical microscopy in the vectorial focusing regime", *Nature Photonics* **2**, 311-314 (2008)

[120] K.A. Serrels, E. Ramsay, D.T. Reid, "70 nm resolution in subsurface optical imaging of silicon integrated-circuits using pupil-function engineering", *Applied Physics Letters* **94**, 073113 (2009)

[121] P.A. Dalgarno, J. McFarlane, D. Brunner, R.W. Lambert, B.D. Gerardot, R.J. Warburton, K. Karrai, A. Badolato, and P.M. Petroff, "Hole recapture limited single photon generation from a single n-type charge-tunable quantum dot", *Applied Physics Letters* **92**, 193103 (2008)

[122] B.D. Gerardot, S. Seidl, P.A. Dalgarno, R.J. Warburton, M. Kroner, K. Karrai, A. Badolato, and P.M. Petroff, "Contrast in transmission spectroscopy of a single quantum dot", *Applied Physics Letters* **90**, 221106 (2007)

[123] I. Ichimura, S. Hayashi, and G.S. Kino, "High-density optical recording using a solid immersion lens", *Applied Optics* **36**, 4339-4348 (1997)

[124] B.D. Terris, H.J. Mamin, and D. Rugar, "Optical-Data Storage Using a Solid Immersion Lens", *Optoelectronics-Devices and Technologies* **10**, 303-310 (1995)

[125] L.P. Ghislain, V.B. Elings, K.B. Crozier, S.R. Manalis, S.C. Minne, K. Wilder, G.S. Kino, and C.F. Quate, "Near-field photolithography with a solid immersion lens", *Applied Physics Letters* **74**, 501-503 (1999)

[126] B. Hecht, B. Sick, U.P. Wild, V. Deckert, R. Zenobi, O.J.F. Martin, and D.W. Pohl, "Scanning near-field optical microscopy with aperture probes: Fundamentals and applications", *Journal of Chemical Physics* **112**, 7761-7774 (2000)

[127] C.M. Sparrow, "On Spectroscopic Resolving Power", *Astrophysical Journal* **44**, 76 (1916)

[128] M. Born and E. Wolf, *Principles of Optics*. 7th ed. Cambridge: Cambridge University Press (2002)

[129] G.S. Kino and S.M. Mansfield, *Near field and solid immersion optical microscope - US Patent Number 5,004,307*. 1991: United States of America.

[130] S.M. Mansfield and G.S. Kino, "Solid Immersion Microscope", *Applied Physics Letters* **57**, 2615-2616 (1990)

[131] K.R. Spring, M.J. Parry-Hill, and M.W. Davidson, *Molecular Expressions Microscopy Primer: Anatomy of the Microscope - Oil Immersion: Interactive Java Tutorial*. 2004.

[132] B.B. Goldberg, S.B. Ippolito, L. Novotny, Z. Liu, and M.S. Unlu, "Immersion Lens Microscopy of Photonic Nanostructures and Quantum Dots", *IEEE Journal of Selected Topics in Quantum Electronics* **8**, 1051-1059 (2002)

[133] Z.H. Liu, B.B. Goldberg, S.B. Ippolito, A.N. Vamivakas, M.S. Unlu, and R. Mirin, "High resolution, high collection efficiency in numerical aperture increasing lens microscopy of individual quantum dots", *Applied Physics Letters* **87** (2005)

[134] E. Ramsay, N. Pleynet, D. Xiao, R.J. Warburton, and D.T. Reid, "Two-photon optical-beam-induced current solid-immersion imaging of a silicon flip chip with a resolution of 325 nm", *Optics Letters* **30**, 26-28 (2005)

[135] M. Baba, T. Sasaki, M. Yoshita, and H. Akiyama, "Aberrations and allowances for errors in a hemisphere solid immersion lens for submicron-resolution photoluminescence microscopy", *Journal of Applied Physics* **85**, 6923-6925 (1999)

[136] K. Karrai, X. Lorenz, and L. Novotny, "Enhanced reflectivity contrast in confocal solid immersion lens microscopy", *Applied Physics Letters* **77**, 3459-3461 (2000)

[137] Z.H. Liu, B.B. Goldberg, S.B. Ippolito, A.N. Vamivakas, M.S. Unlu, and R. Mirin, "High resolution, high collection efficiency in numerical aperture increasing lens microscopy of individual quantum dots", *Applied Physics Letters* **87**, 071905 (2005)

[138] Q. Wu, R.D. Grober, D. Gammon, and D.S. Katzer, "Imaging spectroscopy of two-dimensional excitons in a narrow GaAs/AlGaAs quantum well", *Physical Review Letters* **83**, 2652-2655 (1999)

[139] S.B. Ippolito, B.B. Goldberg, and M.S. Unlu, "Theoretical analysis of numerical aperture increasing lens microscopy", *Journal of Applied Physics* **97**, 053105 (2005)

[140] E. Ramsay, K.A. Serrels, M.J. Thomson, A.J. Waddle, R.J. Warburton, M.R. Taghizadeh, and D.T. Reid, "Three-dimensional nanometric sub-surface imaging of a silicon flip-chip using the two-photon optical beam induced current method", *Microelectronics Reliability* **47**, 1534-1538 (2007)

[141] B.D. Terris, H.J. Mamin, D. Rugar, W.R. Studenmund, and G.S. Kino, "Near-Field Optical-Data Storage Using a Solid Immersion Lens", *Applied Physics Letters* **65**, 388-390 (1994)

[142] M. Shinoda, K. Saito, T. Kondo, A. Nakaoki, M. Furuki, M. Takeda, M. Yamamoto, T.J. Schaich, B.M. Van Oerle, H.P. Godfried, P.A.C. Kriele, E.P. Houwman, W.H.M. Nelissen, G.J. Pels, and P.G.M. Spaaij, "High-density near-field readout using diamond solid immersion lens", *Japanese Journal of Applied Physics Part 1-Regular Papers Brief Communications & Review Papers* **45**, 1311-1313 (2006)

[143] S.M. Mansfield, W.R. Studenmund, G.S. Kino, and K. Osato, "High-Numerical-Aperture Lens System for Optical Storage", *Optics Letters* **18**, 305-307 (1993)

[144] Y.J. Zhang, "Optical intensity distribution of a plano-convex solid immersion mirror", *Journal of the Optical Society of America a-Optics Image Science and Vision* **24**, 211-214 (2007)

[145] C.B. Peng, C. Mihalcea, D. Buchel, W.A. Challener, and E.C. Gage, "Near-field optical recording using a planar solid immersion mirror", *Applied Physics Letters* **87**, 151105 (2005)

[146] W.A. Challener, C. Mihalcea, C.B. Peng, and K. Pelhos, "Miniature planar solid immersion mirror with focused spot less than a quarter wavelength", *Optics Express* **13**, 7189-7197 (2005)

[147] Y.J. Zhang, "Optical data storage system with a planoellipsoidal solid immersion mirror illuminated directly by a point light source", *Applied Optics* **45**, 8653-8658 (2006)

[148] R.H. Hadfield, P.A. Dalgarno, J.A. O'Connor, E. Ramsay, R.J. Warburton, E.J. Gansen, B. Baek, M.J. Stevens, R.P. Mirin, and S.W. Nam, "Submicrometer photoresponse mapping of nanowire superconducting single-photon detectors", *Applied Physics Letters* **91**, 241108 (2007)

[149] G.K. Rurimo, M. Schardt, S. Quabis, S. Malzer, C. Dotzler, A. Winkler, G. Leuchs, G.H. Dohler, D. Driscoll, M. Hanson, A.C. Gossard, and S.F. Pereira, "Using a quantum well heterostructure

to study the longitudinal and transverse electric field components of a strongly focused laser beam", *Journal of Applied Physics* **100**, 023112 (2006)

[150] Q. Wu, R.D. Grober, D. Gammon, and D.S. Katzer, "Spectroscopic imaging in a narrow GaAs quantum well", *Physica Status Solidi B-Basic Research* **221**, 505-509 (2000)

[151] R.J. Warburton, C. Schaflein, D. Haft, F. Bickel, A. Lorke, K. Karrai, J.M. Garcia, W. Schoenfeld, and P.M. Petroff, "Optical emission from a charge-tunable quantum ring", *Nature* **405**, 926-929 (2000)

[152] S. Moehl, H. Zhao, B.D. Don, S. Wachter, and H. Kalt, "Solid immersion lens-enhanced nano-photoluminescence: Principle and applications", *Journal of Applied Physics* **93**, 6265-6272 (2003)

[153] M. Yoshita, K. Koyama, Y. Hayamizu, M. Baba, and H. Akiyama, "Improved high collection efficiency in fluorescence microscopy with a Weierstrass-sphere solid immersion lens", *Japanese Journal of Applied Physics Part 2-Letters* **41**, L858-L860 (2002)

[154] V. Zwiller and G. Bjork, "Improved light extraction from emitters in high refractive index materials using solid immersion lenses", *Journal of Applied Physics* **92**, 660-665 (2002)

[155] M. Yoshita, K. Koyama, M. Baba, and H. Akiyama, "Fourier imaging study of efficient near-field optical coupling in solid immersion fluorescence microscopy", *Journal of Applied Physics* **92**, 862-865 (2002)

[156] K. Koyama, M. Yoshita, M. Baba, T. Suemoto, and H. Akiyama, "High collection efficiency in fluorescence microscopy with a solid immersion lens", *Applied Physics Letters* **75**, 1667-1669 (1999)

[157] G.S. Kino, "Applications and theory of the solid immersion lens", *Optical Pulse and Beam Propagation* **3609**, 56-66 (1999)

[158] P.A. Dalgarno, J.M. Smith, J. McFarlane, B.D. Gerardot, K. Karrai, A. Badolato, P.M. Petroff, and R.J. Warburton, *Physical Review B (Condensed Matter and Materials Physics)* **77**, 245311-245318 (2008)

[159] M. Baba, M. Yoshita, T. Sasaki, and H. Akiyama, "Application of solid immersion lens to submicron resolution imaging of nano-scale quantum wells", *Optical Review* **6**, 257-260 (1999)

[160] M. Schardt, A. Winkler, G. Rurimo, M. Hanson, D. Driscoll, S. Quabis, S. Malzer, G. Leuchs, G.H. Doehler, and A.C. Gossard, "TE- and TM-polarization-resolved spectroscopy on quantum wells under normal incidence", *Physica E-Low-Dimensional Systems & Nanostructures* **32**, 241-244 (2006)

[161] M. Yoshita, T. Sasaki, M. Baba, and H. Akiyama, "Application of solid immersion lens to high-spatial resolution photoluminescence imaging of GaAs quantum wells at low temperatures", *Applied Physics Letters* **73**, 635-637 (1998)

[162] M. Yoshita, M. Baba, S. Koshiba, H. Sakaki, and H. Akiyama, "Solid-immersion photoluminescence microscopy of carrier diffusion and drift in facet-growth GaAs quantum wells", *Applied Physics Letters* **73**, 2965-2967 (1998)

[163] T. Sasaki, M. Baba, M. Yoshita, and H. Akiyama, "Application of solid immersion lens to high-resolution photoluminescence imaging of patterned GaAs quantum wells", *Japanese Journal of Applied Physics Part 2-Letters* **36**, L962-L964 (1997)

[164] M. Yoshita, T. Sasaki, M. Baba, S. Koshiba, H. Sakaki, and H. Akiyama, *Carrier transfer in facet-growth GaAs quantum wells studied by solid immersion photoluminescence microscopy*, in *Compound Semiconductors 1998*. 1999. p. 143-148.

[165] B.D. Don, H. Zhao, G. Schwartz, T. Unkelbach, and H. Kalt, "Coherence length and time of excitons in ZnSe quantum wells", *8th Conference on Optics of Excitons in Confined Systems (Oecs-8)*, 462-465 (2004)

[166] S.B. Ippolito, P. Song, D.L. Miles, and J.D. Sylvestri, "Angular spectrum tailoring in solid immersion microscopy for circuit analysis", *Applied Physics Letters* **92** (2008)

[167] F.H. Koklu, J.I. Quesnel, A.N. Vamivakas, S.B. Ippolito, B.B. Goldberg, and M.S. Unlu, "Widefield subsurface microscopy of integrated circuits", *Opt Express* **16**, 9501-6 (2008)

[168] T. Koyama, E. Yoshida, J. Komori, Y. Mashiko, T. Nakasuji, and H. Katoh, "High resolution backside fault isolation technique using directly forming Si substrate into solid immersion lens", *41st Annual Proceedings: International Reliability Physics Symposium*, 529-535 (2003)

[169] F. Zachariasse and M. Goossens, "Diffractive lenses for high resolution laser based failure analysis", *IPFA 2006: Proceedings of the 13th International Symposium on the Physical & Failure Analysis of Integrated Circuits*, 95-96 (2006)

[170] B. Morgan, C.M. Waits, J. Krizmanic, and R. Ghodssi, "Development of a deep silicon phase Fresnel lens using gray-scale lithography and deep reactive ion etching", *Journal of Microelectromechanical Systems* **13**, 113-120 (2004)

[171] G. Tessier, M. Bardoux, C. Boue, and D. Fournier, "Back side thermal imaging of integrated circuits at high spatial resolution", *Applied Physics Letters* **90** (2007)

[172] O. Breitenstein, F. Altmann, T. Riediger, D. Karg, and V. Gottschalk, "Lock-in thermal IR imaging using a solid immersion lens", *Microelectronics Reliability* **46**, 1508-1513 (2006)

[173] D.A. Fletcher, G.S. Kino, and K.E. Goodson, "Thermal microscopy with a microfabricated solid immersion lens", *Microscale Thermophysical Engineering* **7**, 267-273 (2003)

[174] S.H. Goh, C.J.R. Sheppard, A.C.T. Quah, C.M. Chua, L.S. Koh, and J.C.H. Phang, "Design considerations for refractive solid immersion lens: Application to subsurface integrated circuit fault localization using laser induced techniques", *Review of Scientific Instruments* **80** (2009)

[175] S. Kim, H. Murakami, and M. Tonouchi, "Transmission-type laser THz emission microscope using a solid immersion lens", *IEEE Journal of Selected Topics in Quantum Electronics* **14**, 498-504 (2008)

[176] Y.J. Zhang, "Design of high-performance supersphere solid immersion lenses", *Applied Optics* **45**, 4540-4546 (2006)

[177] L. Liu and S.L. He, "Near-field optical storage system using a solid immersion lens with a left-handed material slab", *Optics Express* **12**, 4835-4840 (2004)

[178] D.H. Chien, C.H. Tsai, S.S. Lo, C.C. Chen, and J.Y. Chang, "Solid immersion lenses in planar waveguides", *Journal of Lightwave Technology* **23**, 2746-2748 (2005)

[179] D.A. Fletcher, K.B. Crozier, K.W. Guarini, S.C. Minne, G.S. Kino, C.F. Quate, and K.E. Goodson, "Microfabricated silicon solid immersion lens", *Journal of Microelectromechanical Systems* **10**, 450-459 (2001)

[180] K.B. Crozier, D.A. Fletcher, G.S. Kino, and C.F. Quate, "Micromachined silicon nitride solid immersion lens", *Journal of Microelectromechanical Systems* **11**, 470-478 (2002)

[181] G.M. Lerman, A. Israel, and A. Lewis, "Applying solid immersion near-field optics to Raman analysis of strained silicon thin films", *Applied Physics Letters* **89**, 223122 (2006)

Chapter 2

Mode-locked Er:Fibre Laser and Erbium-Doped Fibre Amplifier (EDFA) Development for Infrared Sub-Surface Imaging

---

2.1 Introduction

Ultrafast fibre lasers and amplifiers have been the subject of intense research and development in recent years where the focus has been on the optimisation and characterisation of these devices in order to offer practical and efficient optical sources for applications including telecommunications [1], optoelectronic devices [2], supercontinuum generation [3], and even satellite communications [4]. Fibre laser development can be traced back to the 1960s with the incorporation of trivalent rare-earth ions such as neodymium, erbium and thulium into a bulk glass host [5]. This initial demonstration prompted much interest in the area and soon after it was reported that neodymium had been doped into the core of a silica fibre [6]. Since it was already well known that the Nd^{3+} ion provided a high efficiency laser gain medium, where the operation wavelength of these lasers is at 1.06µm, it was clear that the focus was going to remain on Nd^{3+}-doped silica fibre lasers. These lasers proved to be extremely successful, yet it was not until the 1980s and the doping of silica fibre with Er^{3+} ions was reported that significant efforts were made in an attempt to utilise the optical properties of this new development. Er^{3+}-doped fibre lasers operate at a wavelength of 1.55µm which falls within the low attenuation window of silica optical fibres and are therefore ideal sources for the telecommunications industry. A lot of progress has been made in this field and has resulted in the advance of long-haul networks over global distances with minimum attenuation. In addition, other rare-earth ions such as holmium (Ho^{3+}), thulium (Tm^{3+}) and ytterbium (Yb^{3+}) have also been investigated and demonstrated as dopants or co-dopants in silica or fluoride optical fibres in an attempt to generate new laser wavelengths and pump sources for a wide variety of optical applications [7-10]. The praseodymium (Pr^{3+}) ion for example has been incorporated into a fluoride fibre to offer an optical source at the other important telecommunication band which occupies 1.3µm [11].

There are several important advantages of fibre laser sources. The fabrication of low loss, rare-earth doped optical fibre is a simple and mature technology, the fibre itself provides the waveguide, and the current availability of fibre-based components such as wavelength division multiplexers (WDMs), fibre Bragg gratings (FBGs), polarisation controllers, etc, reduce the complexity and the dependency on bulk optical and mechanical alignment and manipulation components. Furthermore, these laser sources benefit from good pump source overlap and good heat dissipation. In addition, when operating at 1.3µm or 1.5µm, these systems can be configured using standard telecommunication components which reduce cost. Also, an entirely fibre-based system offers the possibility of adopting different cavity configurations such as simple ring cavities, linear Fabry-Perot, or a combination of both. These long cavity lengths and the strong intensities due to the confined optical radiation within the fibre core can enhance fibre nonlinearity which enhances the possibility of ultrafast mode-locked operation; however, note that these schemes are passive mode-locking schemes only. Ultimately, fibre laser systems offer a compact, portable, inexpensive, diode-pumped optical source which can be utilised in either a free-space or entirely fibre-based configuration.

The main reason behind the demand for fibre lasers is that these sources have the ability to operate in either a stable continuous wave (CW) or mode-locked operation. Mode-locked fibre lasers have the potential to influence a large number of applications. Through careful consideration of the emission wavelength and the optical pulse duration suitable for the particular application, fibre lasers can be used as sources for time division multiplexing (TDM) and WDM in the telecommunications industry [12, 13], medical applications [14, 15], supercontinuum generation [3], frequency metrology [16-18], light detection and ranging (LIDAR) applications [19], and provide seed pulses for solid-states amplifiers such as Nd:glass [20] or titanium sapphire sources [21].

Ultrafast pulses from a modelocked fibre laser operating at 1.5µm are also ideal for imaging inside a silicon integrated-circuit (IC) since they can traverse the silicon substrate of the IC with minimum attenuation as well as provide nonlinear absorption at the device layer of the chip to generate a photocurrent map of a particular area of interest. The ability to gain optical access to sub-surface features provides a platform to develop semiconductor IC inspection techniques beyond those available using conventional methodologies. As a result, this nonlinear laser microscopy technique has

been utilised to great effect in this work and has been expanded upon to achieve unprecedented resolution performance.

Moreover, the large nonlinearity in some fibres can be used to create the large bandwidths required to generate ultrafast optical pulses which can be utilised in the exciting area of optical coherence tomography (OCT). The broad bandwidth contained within each pulse reduces its temporal profile due to the reciprocal relationship between pulse duration and bandwidth [22, 23]. This can be used to great effect when one wishes to investigate the buried structural configuration of certain materials which contain feature sizes in the range of several microns.

These applications will be discussed and exploited in subsequent chapters; however the source development for that work will be examined within this chapter.

2.2 The Er^{3+} Ion

The erbium atom has an electronic configuration of [Xe] $4f^{12}$ $6s^2$, where [Xe] represents the closed shell electronic configuration of xenon. When erbium ions are doped into a glass host material a number of interesting chemical and electronic re-configurations take place [24]. Initially, ionic bonds form between the erbium ions and the surrounding host lattice. This takes place through the removal of two electrons from the 6s shell and one electron from the 4f shell. This process amends the electronic structure to [Xe] $4f^{11}$ $5s^2$ $5p^6$ $6s^0$ and changes the erbium atoms into trivalent Er^{3+} ions. Typically, the electronic energy levels associated with an individual ion are quantised; however these energy levels can spread out and broaden when ions are incorporated into a dielectric host due to the Stark effect caused by the surrounding electric-field. This broadening can be both homogeneous (uniform) and inhomogeneous (non-uniform), but in the case of erbium ions the latter is dominant. It is through accessing the intra 4f – 4f transitions within the Er^{3+} ion that allows the optical stimulation and amplification at particular wavelengths to take place. Fig. 1 represents a schematic representation of the first five intra 4f energy levels, with the addition of the important $^4S_{3/2}$ energy level, of the Er^{3+} ion when doped into a silica glass fibre. The levels are labelled according to the Russell-Saunders coupling term $^{2S+1}L_J$, where S, L and J represent to the total spin, the total orbital angular momentum and the total spin angular momentum, respectively, of a particular energy level. The quantum number L can be represented by the letter S, P, D, F, G, H, I…. for L = 0, 1, 2, 3, 4, 5, 6.., respectively.

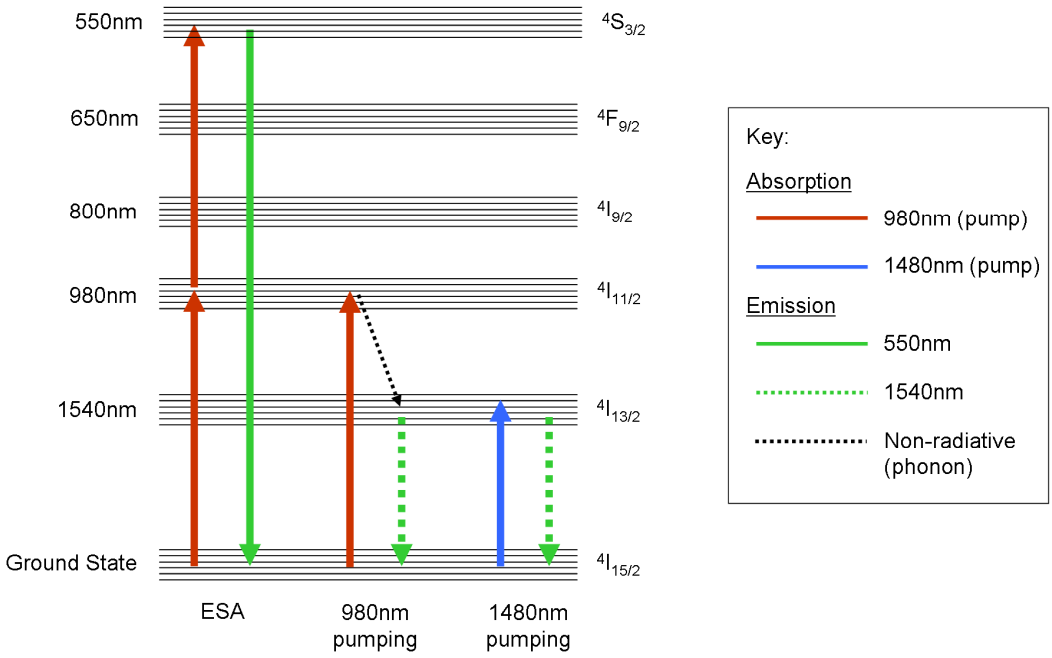

Figure 1 – Schematic representation of some important Er^{3+} ion energy levels in a silica-glass fibre host material

In order to observe laser action at 1550nm it is necessary to obtain a population inversion between the $^4I_{13/2}$ state and the $^4I_{15/2}$ (ground) state. This is typically achieved through optical pumping at either 980nm to the short lived $^4I_{11/2}$ state or by directly pumping at 1480nm to the $^4I_{13/2}$ state.

When the erbium energy levels are pumped at 980nm a three-level system is created between the $^4I_{11/2}$ state, the $^4I_{13/2}$ state, and the ground state. The 980nm pump is absorbed in the $^4I_{11/2}$ state where it then quickly decays non-radiatively down to the $^4I_{13/2}$ state. It is at this stage that the 1550nm output light is generated through the transition between the $^4I_{13/2}$ state and the ground state. Efficient optical pumping at 980nm can be achieved by stable, high power laser diodes. This allows for strong pumping to take place which results in an intense optical output.

However, when the erbium energy levels are pumped at 1480nm (this can be achieved using Indium Phosphide / Indium Gallium Arsenide Phosphide (InP/InGaAsP) semiconductor diode lasers), it is essentially a two-level system which is created between the $^4I_{13/2}$ state and the ground state. This process also has its benefits in that since no significant non-radiative decay takes place there is no additional heating of the host material through phonon generation. Furthermore, the quantum efficiency of such a

system is higher than its 980nm counterpart since the spectral absorption and emission cross-sections are closer together. Yet, there are a number of disadvantages to this particular pumping scheme. The main issue is that 1480nm pump sources suffer from limited versatility and performance which results in lower efficiency and increased power consumption and thermal management. Also, the quality and availability of fibre-coupled optical components (e.g. WDMs) are restricted when operating at 1480nm. Ultimately, it is 980nm pumping that offers Er:fibre laser designers and engineers added flexibility.

Finally, it is a requirement that the host material has a substantial doping concentration (approximately 10^{20} ions/cm^3) since the pump absorption and the signal emission cross-sections are relatively small (~10^{-20}cm^2). This condition is of considerable importance when working with short lengths of fibre. Furthermore, due to these small cross-sectional areas it is necessary to provide high pump powers in order to generate and maintain a state of population inversion; however, at 980nm this is remedied through the reliable, high power pump laser diode sources available at present.

2.2.1 Energy Transfer Between Ions

An important characteristic of the erbium energy level diagram is that it is possible for neighbouring ions to transfer energy between themselves. The energy transfer between ions has been discussed by Hehlen *et al* [25] who state that the probability that energy transfer will occur between two ions will increase at a rate which is proportional to $1/R^6$, where R is the inter-ion spacing. When a medium is highly doped this creates a situation were the inter-ion spatial displacement is reduced and, as a result, encourages these transitions. Such energy transfer mechanisms can play an important role in the system performance. For example, by introducing ytterbium ions (Yb^{3+}) into an erbium-doped material efficient energy transfer can take place between the Yb^{3+} ions in their $^2F_{5/2}$ level and the Er^{3+} ions which occupy their $^4I_{11/2}$ level when pumped at 980nm. Since the absorption cross-section of the Yb^{3+} ion is almost a factor of ten times larger than the Er^{3+} ion equivalent, the pump radiation can be efficiently absorbed and transferred to the Er^{3+} ions. This results in increased system quantum efficiency since the absorption and emission cross-sections are more effectively overlapped. Co-doping within host materials is common practice in modern components.

2.2.2 Excited State Absorption (ESA)

Excited state absorption is mainly considered to be a detrimental process whereby pump light at a particular frequency is not absorbed by an ion which is situated in the ground state, but by an ion which is located in a higher energy state. This effect can take place if there exists a third energy level which resides at an even higher energy state to the second where the energy difference between state three and state two equals the energy of the incident pump photon exactly. ESA has the potential to occur at any energy level so long as the state contains a finite population. With respect to erbium, ESA is generally considered to take place at the $^4I_{13/2}$ state due to its long lifetime (~10ms) [24]. The result of ESA ultimately increases the threshold pump power while reducing the device gain.

Nevertheless, when erbium ions are doped into a silica glass host the process of ESA does not exhibit any deleterious effects. The energy levels of erbium within silica, except from the $^4I_{13/2}$ level, are characterised by their short lifetimes, therefore, pumping at 980nm has a negligible effect on system performance since the $^4I_{15/2}$ and $^4I_{13/2}$ states remain unchanged and the $^4I_{11/2}$ state already has a short lifetime [26]. ESA in this regime only introduces an increase in the pump absorption.

ESA can also explain why, when the erbium-doped fibre is optically pumped at 980nm, it exhibits fluorescence in the green region of the visible spectrum [27]. If an electron is promoted from the ground state to an upper energy level through absorption then is further excited to another upper energy level through ESA, the total energy difference it has attained between the ground state and its final excited state exactly matches that which, when released as a photon, would emit in the green (~550nm or ~2.3eV). ESA is the main process behind this green fluorescence; however, it may also be possible for an ion-ion energy transfer process to stimulate this effect - if the ion-ion energy transfer at the first excited state is large enough to induce a further energy transition. Nonetheless, the probability of this event taking place is lower than that for ESA.

2.3 Ultrafast Fibre Laser Mode-locking Schemes

Ultrafast lasers produce pulses of light that can have a duration between 10^{-12} seconds (1 picosecond) and 10^{-15} seconds (1 femtosecond) – although pulse durations of 170 attoseconds (10^{-18} seconds) have been demonstrated [28]. This can be achieved through a process known as mode-locking. Mode-locking is an optical technique which supports

the coherent oscillation of multiple cavity modes [29]. The resonant frequencies within a laser cavity arise through the requirement that the resonator length be equal to an integer number of half wavelengths. This situation supports the formation of a standing wave within the resonator. The separation of these resonant frequencies can be expressed as,

$$\Delta\omega = 2\pi c / l \tag{1}$$

where l is the optical roundtrip length of the resonator and c is the speed of light. It is when these modes are connected by a fixed phase relationship that a regular sequence of ultrafast pulses is created.

$$E(t) = \sum_n E_n \exp i\left[(\omega_0 + n\Delta\omega)t + n\Delta\varphi\right] \tag{2}$$

The expression above describes the total optical field if the nth longitudinal mode has an amplitude of E_n, where ω_0 is the centre frequency of the output, t represents time, and $\Delta\varphi$ is the phase difference between adjacent modes. In order to induce this fixed phase relationship between the cavity modes and, as a result, achieve mode-locking, $\Delta\varphi$ must be set to a constant value.

The mode-locking of ultrafast fibre lasers can be separated into two main categories: active and passive mode-locking [29].

Active mode-locking can be achieved by applying an external drive to a laser cavity. There are two methods in which this may be accomplished [30]: either by modulating the intracavity loss - Amplitude Modulation (AM) mode-locking, or by modulating the intracavity phase - Frequency Modulation (FM) mode-locking. These techniques are commonplace in a number of laser systems used today, especially semiconductor and solid-state lasers.

In passive mode-locking, it is not necessary to apply an external drive to the cavity. Instead, the laser cavity is designed to contain an element whose optical loss decreases as the power that is incident on it increases [30] i.e. nonlinear loss. It is because of this nonlinear effect that it is possible to generate additional cavity frequencies that were not initially present in the system. This in turn can increase the strength of the resultant

mode-locking since these additional cavity modes can now be included in the mode-locking process.

The following sections will discuss the three main passive fibre laser mode-locking techniques which have been demonstrated to produce sub-picosecond pulse durations. These include semiconductor saturable absorbers, the nonlinear amplifying loop mirror (NALM), and nonlinear polarisation rotation (this technique is also known as polarisation additive pulse mode-locking or Kerr mode-locking). It is the latter scheme which has been exploited during the erbium fibre laser source development stage of this work.

2.3.1 Semiconductor Saturable Absorption

A saturable absorber makes use of an intense pump wave within a cavity, tuned to resonance (i.e. $\hbar\omega = E_2 - E_1$), to induce significant levels of absorption within a medium (which is placed inside the laser system) that will create a state of equilibrium between the population of the upper and lower energy states within that medium [31, 32]. At this point the absorption becomes zero and the transmission through the sample will be high. The saturable absorption effect therefore leads to an intensity-dependent (i.e. nonlinear) transmission. It is the time taken for the saturable absorber to recover that determines its classification – fast (picosecond) or slow (nanosecond).

An intense resonant signal within a laser cavity can also induce high levels of stimulated emission as well, so much so that the rate of emission can saturate the population difference between the upper and lower energy levels.

$$k = (N_2 - N_1)\frac{n\hbar\omega_{21}B_{21}}{c} \tag{3}$$

The expression above describes the small-signal gain coefficient, where B_{21} is a constant proportional to the absorption transition rate between energy levels 1 and 2, and N_i represents the population of energy levels i, where i = 1, 2. When the intense resonant signal depletes the upper energy level to the degree that $N_2 \approx N_1$ and $k = 0$, gain saturation occurs.

For the generation of ultrashort optical pulses one can either use the combination of a slow saturable absorber and gain saturation, or simply use a single fast saturable

absorber. When an optical pulse is incident on a slow saturable absorber, its leading edge is absorbed and creates an excited state which is relatively transparent to the trailing edge. This effect in isolation is insufficient to generate ultrashort (i.e. femtosecond) pulses and therefore must be combined with dynamic gain saturation to achieve mode-locking. A laser medium with a gain relaxation time faster than the cavity round-trip time, but slower than the absorber recovery time, must be used to ensure that the gain recovers in time to amplify the next round-trip pulse and the absorber recovers in time to be fully saturated by it. The pulse therefore, when travelling through a saturable absorber first then the gain medium, experiences a gain window with a finite duration which strongly shapes the pulse. Yet, when a fast saturable absorber is used, the dynamics of the absorber and the gain medium no longer represent the limiting factor influencing pulse duration, and other effects such as linear and nonlinear dispersion become the dominant pulse shaping mechanisms.

It is commonplace at present to create a saturable absorber by using thin semiconductor quantum-well structures, where the bandgap is similar to the laser wavelength. In this technology, electrons are excited to higher energy levels through the energy delivered by incident photons, and because the wells are thin only a small number of unoccupied states are required to be filled before no further absorption can take place. These structures are typically supported on top of a Bragg mirror arrangement [33].

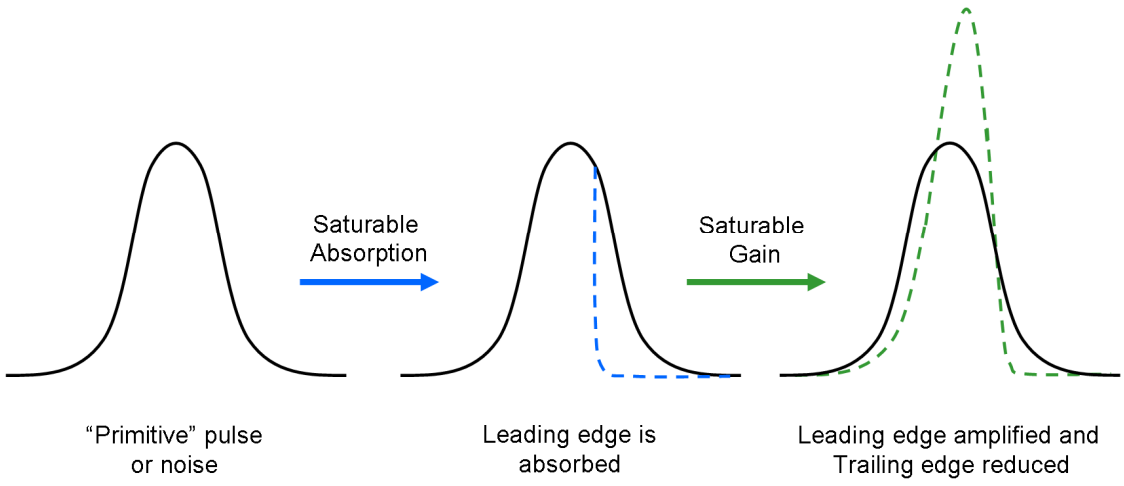

Figure 2 – A general representation of the saturable absorption / gain process used to generate ultrafast pulses

2.3.2 Nonlinear Amplifying Loop Mirror (NALM)

The NALM depends on the optical Kerr effect (explained later), along with polarisation control, taking place within a length of optical fibre to cause artificial saturable absorption to generate a state of pulse shortening. The optical Kerr effect is an instantaneous optical effect in which the refractive index of a material is modified due to the intensity dependence of its electric polarisation response.

The Kerr effect can be used to induce a nonlinear phase shift of a wave which has been exploited in the NALM to achieve modelocked operation through interference between this wave and an unperturbed original wave within the fibre. The NALM (Fig. 3) is based on a fibre Sagnac interferometer which has a fibre amplifier placed asymmetrically in the loop [34]. Optical pulses are coupled into the loop and split by a 50/50 fibre splitter to generate counter-propagating pulses within the Sagnac ring. For small optical input powers, the loop operates in the linear regime and the two counter propagating pulses experience the same phase delay and are therefore directed back out of the input after recombination at the 50/50 splitter; however, at high optical input powers, the loop will operate in the nonlinear regime and become intensity-dependent. Here, the two pulses obtain a net phase difference after propagation in the loop. In this regime there is a clear distinction between whether the input pulse is strong or weak when it enters the nonlinear sections, therefore the amplified pulse is rejected out from the loop via an output port. This scheme is similar to the principles of additive pulse mode-locking (APM). APM uses the interference between two counter propagating nonlinear optical pulses to induce the effect of a fast saturable absorber. This technique has been adopted in many fibre laser configurations to generate ultrafast optical pulses [35, 36].

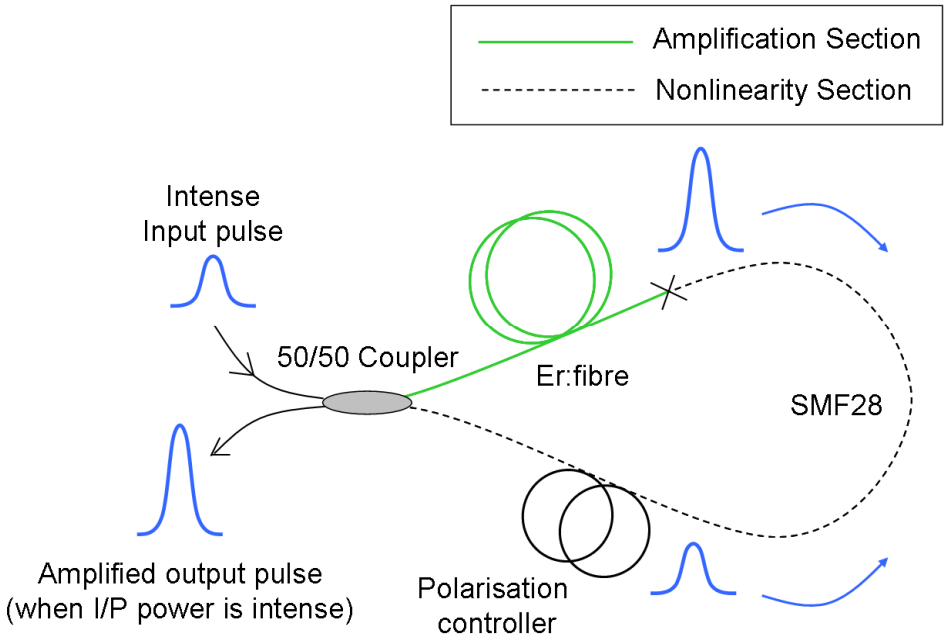

Figure 3 – The Nonlinear Amplifying Loop Mirror (NALM). A weak input pulse will be reflected back out of the input port at the 50/50 coupler; however when the input pulse is intense then the amplified output is rejected from the coupler

The NALM can be fibre coupled into a unidirectional fibre ring. This creates a laser which has a figure-of-8 cavity shape where pulses of amplified intensity remain within the cavity and any reflected low intensity pulses are rejected by an isolator which forces the unidirectional operation [37] (Fig. 4).

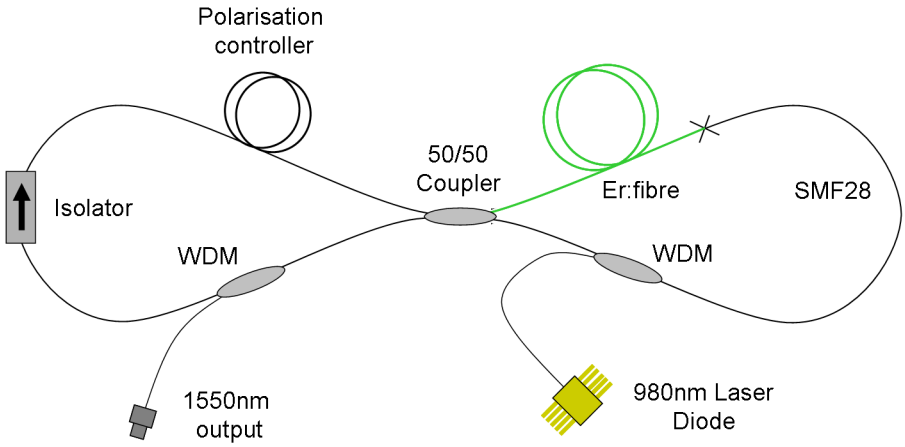

Figure 4 – Figure-of-8 Er:fibre laser configuration. This system utilises the intensity-dependent operational effects of the NALM described above

2.3.3 Nonlinear Polarisation Rotation (NPR)

NPR is a passive mode-locking technique that can be utilised within an optical fibre [38, 39] and is the mode-locking technique deployed during the construction of the stretched-pulse Er:fibre laser used in this work. The main requirement is that an intensity-dependent polarisation state is created within the fibre in order to obtain a net phase difference between strong and weak circulating pulses. Typically, this can be achieved through counter propagating two independent pulses within a fibre – as is the case with the NALM describe above; however, the trick to NPR relies on the generation of a net phase difference from only a single pulse.

When an intense elliptically-polarised optical pulse propagates along a length of non-polarisation maintaining fibre, it is possible for a nonlinear rotation of its polarisation state to take place. This rotation occurs due to the intensity-dependent Kerr effect (i.e. self-phase modulation (SPM) – described later – as well as some birefringence within the fibre) which acts upon the two orthogonal components of the elliptical polarisation state causing them to slip out of phase. The induced rotation within the fibre can be manipulated and controlled through the use of wave plates (polarisation controllers) in order to stimulate mode-locking action in a fibre ring cavity. In this configuration, the wave plates are adjusted to allow maximum transmission of the pulse when the pulse intensity is highest; however, the transmission only becomes intensity-dependent after propagation through a polarisation-sensitive beamsplitter, which acts as a low intensity rejection port – i.e. an artificial saturable absorber. As a result, mode-locking through NPR is an ideal technique since the absorption process is extremely fast and can be controlled by the polarisation controllers.

For a typical Gaussian shaped pulse profile, the effects of NPR only occurs at the centre of the pulse since the intensity is too low at the wings for NPR to take place. Therefore, a propagating Gaussian pulse will experience a polarisation rotation within its central portion (highest intensity) whereas the polarisation state across the wings of the pulse (lowest intensity) will remain unchanged (Fig. 5). As a result, a polarisation-sensitive beamsplitter within a laser cavity will transmit the centre of the pulse and reject the wings, shortening the pulse per round trip.

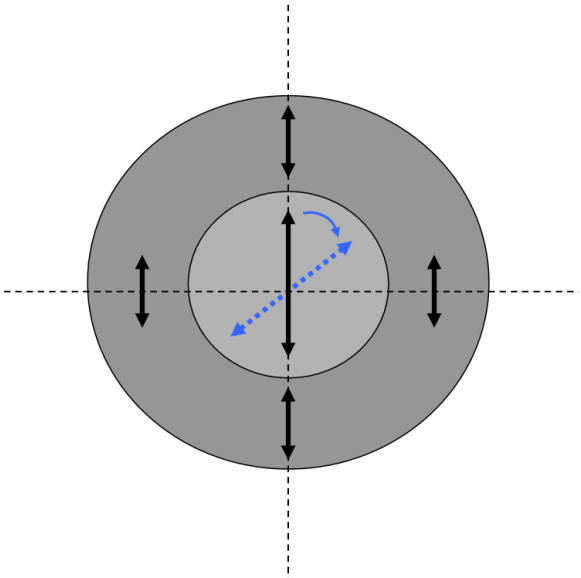

Figure 5 – Nonlinear Polarisation Rotation. The polarisation state at the centre of the pulse is rotated due to the intensity-dependent Kerr effect, whereas the polarisation state at the lower intensity wings remain unchanged

NPR suffers from two main environmental factors which have to be considered. The first is that the optimum polarisation settings of the wave-plates can drift with temperature. This requires that the system be frequently readjusted which is detrimental to an experimental configuration since it may be difficult to reproduce identical saturable absorption modulation depths and power – an important set of parameters that define the mode-locking process. Furthermore, air currents or acoustic noise may cause optical fibres to move slightly. This will result in an amended state of birefringence within the fibre which will alter the mode-locking characteristics.

NPR is a powerful mode-locking technique which can generate ultrafast pulses with significant output power (tens of milliwatts). An illustration of such a mode-locking scheme which utilises NPR, and used in the stretched-pulse erbium-doped fibre laser constructed and described later, is given in Fig. 6; however, note that this scheme can suffer in an uncontrolled environment. Therefore, it is recommended that fibre lasers which are mode-locked in this particular regime are constructed within a suitable enclosure and operated in a temperature regulated location in order to minimise potential difficulties.

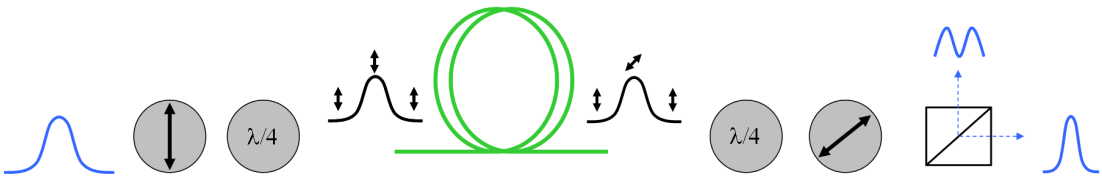

Figure 6 – NPR mode-locking scheme. The low intensity wings of the pulse are rejected out of the cavity by a polarisation-sensitive beamsplitter whereas the high intensity centre of the pulse remains within the cavity

2.3.4 Harmonic Mode-locking

An interesting mode-locking technique that can be adopted in erbium-doped fibre lasers is to lock together the resonant modes of the cavity at the *n*th harmonic with respect to the fundamental mode [40-42]. In this approach a passive, fast intensity-dependent loss mechanism is utilised as an intra-cavity nonlinear element which can cause an intense optical pulse to experience a high loss. The main requirement here is that the nonlinearity of this element can recover to its initial state before the arrival of the next pulse. If this is achieved then the pulse intensities are forced to become fixed to a certain value.

This technique has been demonstrated in an erbium-doped fibre laser which used NPR – it was also observed and reproduced using the fibre laser constructed for this work. Here, the APM mode-locking scheme used NPR as a source of artificial saturable absorption. Through careful alignment of the polarisation controllers it is possible to bias the output of the laser into a regime of increased transmission through the polariser with increased intensity (APM) or decreased transmission with increased intensity. The latter describes the process of additive pulse limiting (APL) [41] and is the mechanism behind this harmonic mode-locking procedure. Typically, during APM an intense pulse experiences less loss so is able to accumulate greater pulse energy per round trip; however, APL restricts this energy build up and, as a result, forces the laser to distribute the energy among additional pulses which oscillate at the cavity's harmonic frequencies.

This process has its advantage in obtaining high pulse repetition rates from such long cavity laser systems since more pulses are forced to oscillate periodically within the cavity; however, when the laser is made to operate in such a regime, it has been demonstrated that the pulse energies can fluctuate from pulse to pulse [43]. This

mechanism can be explained by examining the relaxation time of the erbium gain medium. Since this duration is longer than the pulse repetition rate the saturated state of the gain limits the intensity of the subsequent pulse. This can be seen in Fig. 7. Fig. 7 was obtained by directing the output of our fibre laser, which was mode-locked at the second harmonic, onto the detector surface of a fast indium gallium arsenide (InGaAs) photodiode. It is clear that there exists a periodic fluctuation in intensity per pulse; however, note that this would not disrupt any TOBIC experimental observations since the repetition rate of 64GHz and the low modulation depth would be averaged out during a continuous raster scan, or point-by-point acquisition system, due to the relative differences in time-scale – the point-by-point acquisition system used in this work would stop at each position for approximately 0.25 seconds.

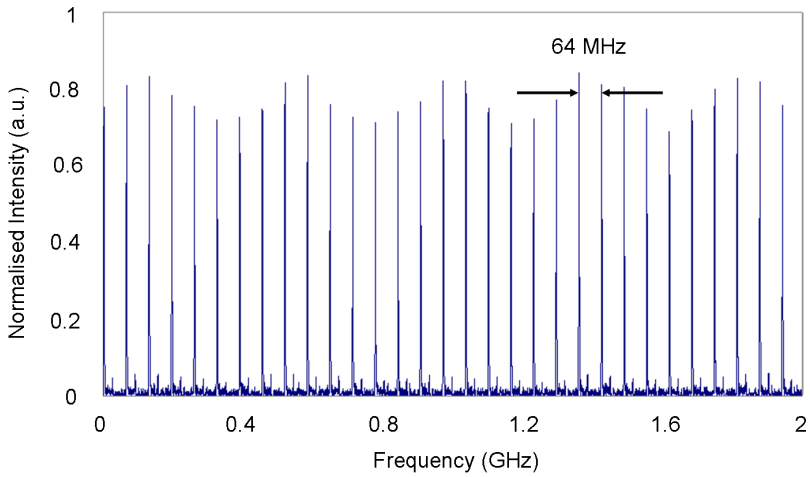

Figure 7 – Harmonic Mode-locking. The fundamental repetition rate of the laser is 32MHz; however our fibre laser has been modelocked at the second harmonic (64MHz). This results in intensity fluctuations from pulse to pulse due to gain saturation

2.4 Ultrafast Pulse Properties

Ultrashort pulses require large bandwidths since pulse durations are proportional to the reciprocal of the source bandwidth [44]. This initially appears to be a relatively simple condition to satisfy, however the generation of ultrashort pulses requires the management of a number of linear and nonlinear effects encountered by the pulse as they propagate through optical materials. These considerations are particularly important in fibre lasers because of the long path lengths in the fibre material.

2.4.1 Linear Material Dispersion

When an ultrashort pulse propagates through an optical material it experiences chromatic dispersion [5]. This process can be described as the variation of refractive index with wavelength. Chromatic dispersion in materials originates from the frequency-dependent linear dielectric susceptibility, $\chi^{(1)}$, which relates the induced electric polarisation, $P(\omega)$, to the applied optical field, $E(\omega)$:

$$P(\omega) = \varepsilon_0 \chi^{(1)}(\omega) E(\omega) \tag{4}$$

This linear dispersion causes pulse broadening and is a consequence of the real part of the $\chi^{(1)}$ term, namely, $n_0 = \sqrt{1 + \mathrm{Re}\{\chi^{(1)}\}}$.

Dispersive effects are best analysed in terms of optical phase. This parameter is related to the refractive index by,

$$\phi(\omega) = \frac{n_0(\omega)\omega L}{c} \tag{5}$$

where L is the length of the medium and c is the speed of light in a vacuum. The local variation of the spectral phase due to an optical medium can be represented as the Taylor expansion:

$$\phi(\omega) = \phi(\omega_0) + (\omega - \omega_0)\frac{\partial \phi}{\partial \omega} + \frac{1}{2}(\omega - \omega_0)^2 \frac{\partial^2 \phi}{\partial \omega^2} + \frac{1}{6}(\omega - \omega_0)^3 \frac{\partial^3 \phi}{\partial \omega^3} + ... \tag{6}$$

where ω_0 is the pulse centre frequency. Each term in (6) corresponds to individual dispersive effects.

The first term, $\phi(\omega_0)$, describes the change in carrier phase. This term has no effect upon the pulse.

The linear term, $\frac{\partial \phi}{\partial \omega}$, describes the *group delay* of the pulse – i.e. a linear phase ramp in frequency. This is responsible for the delay of the pulse in time and dictates the length of time the pulse will spend in the medium.

The quadratic term, $\frac{\partial^2\phi}{\partial\omega^2}$, as well as the additional higher order terms, describe the *group delay dispersion* of the pulse – i.e. a variation of group delay with frequency. This is responsible for the resulting pulse shape after propagation through the medium. The term $(\omega-\omega_0)^2$ is responsible for adding *linear chirp* to the pulse. This is essentially a time-varying linear increase or decrease in the instantaneous optical frequency across the pulse.

The cubic spectral phase term results in the pulse compression at one edge of the pulse and pulse broadening at the other edge. As a consequence this leads to pulse break-up.

In bulk optical materials, for example BK7 glass (n=1.5) or silicon (n~3.48), material dispersion is a key issue since all dielectric materials exhibit dispersive qualities due to their frequency-dependent optical response. The group velocity in such components is related to the refractive index by,

$$v_g = \frac{d\omega}{dk} = \frac{c}{n-\lambda\frac{dn}{d\lambda}} \tag{7}$$

where $k = 2\pi n/\lambda$ and $\omega = 2\pi c/\lambda$.

The group-delay is the time taken for a pulse travelling at its group velocity to cover a given distance, *l*, and is expressed as,

$$\tau_g = \frac{d\phi}{d\omega} = \frac{l}{v_g} \tag{8}$$

The group delay dispersion (GDD), i.e. the change of group delay with frequency, is given by the expression,

$$GDD = \frac{d\tau_g}{d\omega} = \frac{d^2\phi}{d\omega^2} = \frac{d\left(l/v_g\right)}{d\omega} \tag{9}$$

When the GDD is zero then the pulse experiences no broadening and is unchanged; however, when the GDD is positive longer wavelengths will travel faster. The

dispersion in this regime is considered to be “normal” or positive. In addition, when the GDD is negative, shorter wavelengths travel faster, and the dispersion is considered to be “anomalous” or negative.

2.4.2 Group Delay Dispersion Compensation

If an ultrashort pulse experiences a significant amount of GDD when propagating through an optical system its duration will increase due to the distribution of different group velocities across the bandwidth of the pulse. This can have a deleterious effect on the overall pulse quality and, as a result, any experimental process undertaken prior to beam delivery. Therefore, it is of critical importance that the initial ultrashort pulse duration is maintained throughout the optical system.

There are several GDD compensation techniques available which have been demonstrated both theoretically and experimentally. All of these methods are successful by considering the levels and/or locations of GDD experienced by the pulse during propagation.

Two prisms can be used to provide a source of negative GDD which is located externally to the laser resonator cavity (extra-cavity) [45]. The initial description of such a technique discussed the use of four prisms in a single-pass arrangement; however, this method can be amended to facilitate a prism pair in a symmetrical reflection configuration. This technique can be adopted intra-cavity where the prisms are located near one of the laser cavity end mirrors. The negative (anomalous) GDD of the prism pair compensates for the positive GDD created by the laser through geometrical dispersion since a prism will have a wavelength dependent angular response. In this technique the prisms are set to Brewster’s angle to optimise the transmission of the incident optical beam and to minimise Fresnel reflections.

This prism pair arrangement compensates for GDD since the different wavelengths contained within the optical pulse have different transit times as they propagate through the prism pair. The resultant geometrical dispersion can be adjusted by controlling the apex separation, l, between the prisms and the angular deviation, β, of the refracted rays. These parameters are of critical importance since the GDD will change from being positive to negative if the separation length is allowed to extend too far.

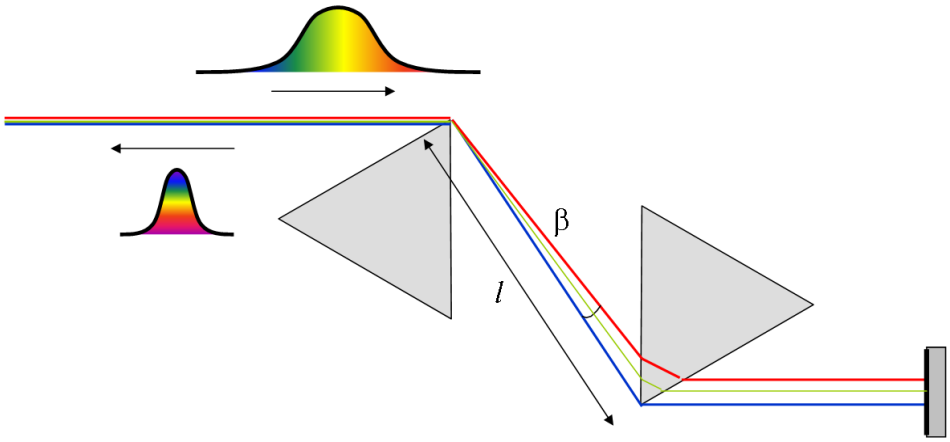

Figure 8 – Group delay dispersion compensation through the use of a double-pass prism pair arrangement

Another GDD compensation technique is available which can remove the complexity of critical beam alignment within a laser cavity by simply replacing one of the cavity end mirrors with a chirped mirror [46]. A chirped mirror is fabricated as a multilayer dielectric stack of increasing layer periodicity and alternating material layer composition (typically TiO_2 and SiO_2). This incremental stack period provides a controlled reflection parameter which is a function of wavelength and layer period (i.e. different wavelengths will be reflected at different depths within the dielectric stack). Since the longer wavelengths contained within the incident pulse are allowed to travel further into the dispersive mirror it results in an increased optical path length which effectively balances the negative GDD of the pulse. The use of a chirped mirror for GDD compensation is simple to incorporate into an optical system; however it is often the case that these components are unable to provide enough dispersion compensation to that which is required.

An additional source for GDD compensation remains to be discussed which takes into consideration the appeal of entirely fibre based systems. The above examples are standard free-space solutions yet it is the periodic material properties of the dielectric mirror which suggests that a similar configuration can be fabricated into an optical fibre.

A fibre Bragg grating (FBG) is essentially a distributed Bragg reflector which has been fabricated into a short section of optical fibre that can be used to reflect a particular range of wavelengths in order to transmit the others. This process is accomplished by

generating a periodic variation of the refractive index in the fibre core. This is where the comparison can be made between the chirped free-space mirror. FBG's were first reported by Hill in 1978 who was investigating photosensitivity in germanium-doped fibres [47].

The simplest solution to remedy the limiting effects of GDD in an all-fibre-based system exists in a single-pass arrangement. This requires no more than the inclusion of an additional section of standard silica telecommunications fibre into the system. For example, the negative GDD in an appropriate length of silica fibre can effectively balance the positive GDD imposed on the optical pulses within a length of erbium-doped fibre. This technique has not only been used to balance the net cavity GDD in a stretched-pulse erbium-doped fibre laser systems [39, 48], but also provides a solution to balance the GDD in amplified fibre laser pulses from an EDFA (these ideas will be discussed later in this Chapter).

The magnitude of GDD in optical materials essentially depends on the variation of refractive index with wavelength. Therefore, by controlling the refractive index against wavelength response of a material it is possible to tailor the level of GDD it will exhibit. In an erbium-doped fibre, this can be achieved by increasing or decreasing the doping concentration of erbium ions within the fibre core; however, standard silica fibres have limited flexibility for managing GDD (i.e. tailored refractive index profiles within the fibre core – dispersion-shifted fibres) when compared to state-of-the-art engineered micro-structured fibres.

Photonic Crystal Fibre (PCF), initially demonstrated in the early 1990s by J. C. Knight *et al* [49], is an optical waveguide that has the ability to guide light along its core due to a periodic modulation in its radial refractive index profile. This radial distribution can consist of a solid core that is surrounded by an array of air holes, or even a hollow core surrounded by an array of air holes. The latter arrangement is know as a Photonic Bandgap (PBG) Fibre [50]. These fibres can be configured using a wide variety of different materials, periodic radial geometries and dimensions. As a result, micro-structured fibre offers a large number of amendable parameters that can be modified during the fabrication process in order to tailor the fibre's optical properties. This results in the availability of optical fibre that can exhibit a completely customised GDD profile across a given spectral range. If the GDD of a fibre can be set to zero at a particular

wavelength, or even fixed at zero across a broad bandwidth, the need for GDD compensation would be completely eliminated.

It is important to note here that, when working with optical fibres, it is not only the dispersion arising from a materials frequency dependent refractive index (material dispersion) that is the only factor to consider. Modal dispersion is only relevant to waveguides and takes place because the optical wave that propagates in the guide is divided into two components: a forward travelling wavevector and a stationary transverse wavevector. The transverse component will increase in magnitude if the fibre core size is reduced whereas the magnitude of the travelling component will reduce. This results in a lower group velocity compared to that experienced during propagation through an equivalent bulk material. Since these different propagation modes travel along the fibre with different group velocities it is possible for a single input pulse to be observed as a series of individually spaced pulses (i.e. a smooth envelope) at the output. However, this modal dispersion can be reduced through the implementation of graded-index fibres compared to step-index fibres since the group velocities are then matched and the differences between delay times of the propagating wavevectors are reduced.

2.4.3 Self-phase Modulation

Self-phase modulation (SPM) [5] is a product of the optical Kerr effect in which a high-intensity optical field propagating through a material induces a change in the refractive index of the medium and can be understood by considering the expression for the polarisation in an isotropic media (centrosymmetric material - $\chi^{(2)} = 0$):

$$P = \varepsilon_0\left(\chi^{(1)}E + \chi^{(3)}E^3\right) = \varepsilon_0\left(\chi^{(1)} + \chi^{(3)}E^2\right)E = \varepsilon_0\chi E \tag{10}$$

where ε_0 is the permittivity of free-space and χ is the susceptibility of the material where $\chi = \chi^{(1)} + \chi^{(3)}E^2$ and $n = \sqrt{1+\chi}$.

Here, we can write the linear refractive index $n_0 = \sqrt{1+\chi^{(1)}}$, so by using a Taylor series approximation, one can state that:

$$n \approx n_0 + \frac{\chi^{(3)}}{2n_0}E^2 \tag{11}$$

The field amplitude *E* can be converted into intensity by using $I = n_0 c\varepsilon_0 |E|^2 / 2$ to give,

$$n = n_o + n_2 I \tag{12}$$

where $n_2 = \frac{\chi^{(3)}}{n_0^2 c\varepsilon_0}$

This reveals that the refractive index is intensity-dependent due to the role of the third-order nonlinearity.

The phase shift experienced by an optical beam of length *l*, refractive index *n* and wavelength λ is given by,

$$\phi = \frac{-2\pi n l}{\lambda} \tag{13}$$

Therefore, for an optical pulse (whose intensity is a function of time), the time dependent phase shift is,

$$\phi(t) = \frac{-2\pi n_2 I(t) l}{\lambda} \tag{14}$$

where *I* is the intensity and the Kerr effect states that $n = n_o + n_2 I$.

This results in a change of the instantaneous frequency as,

$$\Delta\omega = \frac{d\phi}{dt} = \frac{-2\pi n_2 l}{\lambda}\frac{dI}{dt} \tag{15}$$

This results in the leading edge of the pulse, where *dI/dt* is positive, being red-shifted ($\Delta\omega$ is negative) and the trailing edge of the pulse, where *dI/dt* is negative, being blue-shifted. This process is known as self-phase modulation and can result in the generation of new frequencies that were not originally present in the pulse. This can be utilised in ultrashort pulse generation since when this effect is balanced with significant levels of negative dispersion it is possible to use SPM to reduce the pulse duration.

A spatial-domain equivalent to this time-domain process leads to an effect known as Kerr-lensing in which a Gaussian-profiled plane wave experiences larger phase

retardation at the centre of the beam than at its edges when it propagates through a thin sheet of nonlinear material. This results in wavefront curvature and self-focussing [5]. Kerr-lensing can be used in combination with a suitable aperture to induce mode-locking action in a laser cavity [51]. Here, an aperture is placed after the medium so that self-focused (i.e. high-power) light is transmitted more efficiently than unfocused light (i.e. low-power).

2.4.4 Optical Solitons

An interesting phenomenon in nonlinear optics is the generation of an optical soliton. A soliton is an optical pulse that reproduces its temporal or spectral shape as it propagates through a transparent medium as a function of propagation length – except from the N = 1 soliton (explained later). Typically, an ultrashort pulse will be reshaped during propagation in a medium by SPM (temporal) and linear dispersion (spectral). It is possible to exactly balance these two effects within a medium in order to allow a pulse to propagate indefinitely without broadening – assuming no attenuation of the pulse over time.

The propagation of an optical pulse in a lossless material can be described by the nonlinear Schrödinger equation (NLSE) [5]:

$$i\frac{\partial A}{\partial z} = \frac{\beta_2}{2}\frac{\partial^2 A}{\partial T^2} - \gamma|A|^2 A \tag{16}$$

where A represents the amplitude of the pulse envelope, β_2 is the parameter responsible for dispersion, and the nonlinear parameter γ describes the effects of SPM.

It is useful here to normalise (16) by introducing three dimensionless variables,

$$U = \frac{A}{\sqrt{P_0}} \qquad \xi = \frac{z}{L_D} \qquad \tau = \frac{T}{T_0} \tag{17}$$

where P_0 is the pulse peak power, T_0 is the pulse duration, and L_D is the dispersion length.

From here it is possible to express the NLSE as,

$$i\frac{\partial U}{\partial \xi} = \pm(\beta_2)\frac{1}{2}\frac{\partial^2 U}{\partial \tau^2} - N^2|U|^2 U \tag{18}$$

A new parameter *N* has been introduced in (15) and can be described by,

$$N^2 = \frac{\gamma P_0 T_0^2}{|\beta_2|} \tag{19}$$

The parameter *N* can be removed from (18) by the introduction of $u = NU = \sqrt{\gamma L_d A}$.

Equation (18) can now be expressed in its standard normalised form:

$$i\frac{\partial u}{\partial \xi} + \frac{1}{2}\frac{\partial^2 u}{\partial \tau^2} + |u|^2 u = 0 \tag{20}$$

The first term in equation (20) describes the pulse propagation through the material, the second term describes dispersion, and the third term describes SPM.

The parameter *N* is called the 'soliton number' and is used to describe the multiple solutions of the NLSE that exist. These solutions are determined by the power and duration of the optical pulse and the dispersion and nonlinearity of the medium. The *N*=1 soliton propagates within the medium without changing its shape; however, higher-order solitons are characterised by a periodic pulse reshaping over a given length known as the soliton 'period'.

Soliton formation has been the subject of intense investigation over a number of years due to the critical role it has in ultrafast nonlinear optical systems; however in erbium-doped fibre lasers, soliton formation can have a detrimental effect on optimum system performance. Entirely fibre-based laser systems have utilised soliton propagation and their resulting shapes to induce ultrashort pulse formation through additive pulse mode-locking schemes (APM) [36]. Nonetheless, this approach puts a limit on the maximum possible pulse width and energy. This limit can also result in multiple-pulsing within the

cavity and the coupling of significant energy into frequency sidebands that diminish the pulse peak power [38].

2.4.5 Pulse Measurement

In order to measure the duration of an ultrashort optical pulse, an event in time is required which is shorter than the pulse duration to be measured. This presents a problem when using electronics since electronic detection is simply not fast enough to cope with the characterisation requirements necessary in the ultrafast regime. As a result, various optical solutions have been developed which can measure a wide range of important optical pulse parameters.

The simplest approach to measure ultrafast optical pulses is in the time-domain by using a technique called autocorrelation. An autocorrelation provides an estimate of the actual pulse duration by recording the electric-field response of a pulse against a variable time-delayed replica of itself. This response will depend on both the pulse duration and the separation of the two identical pulses at a particular time.

An autocorrelation is typically obtained using a Michelson interferometer. In this arrangement, the pulse is separated into two arms, one with a fixed optical path length and the other with a periodically varying optical path length, and then recombined again at a suitable detector. The first-order autocorrelation is insensitive to pulse duration, so it is common for a second-order response to be recorded at the detector so either a second-harmonic generation crystal is positioned immediately before the detector and its nonlinear signal recorded, or a simple two-photon photodiode can be used which uses two-photon absorption to generate a signal. Fig. 9 illustrates these two experimental arrangements.

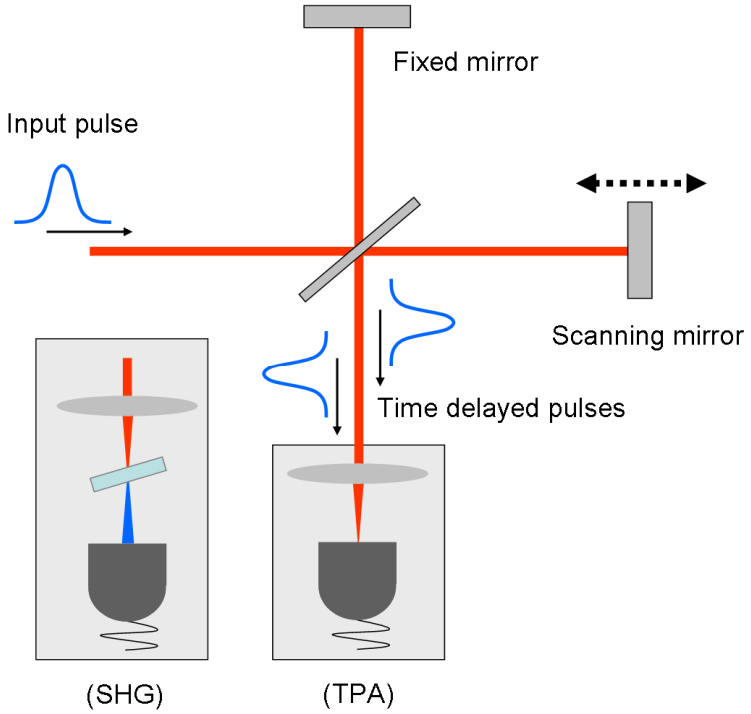

Figure 9 – Autocorrelations. In the time-domain, either a second-harmonic generation (SHG) crystal or a two-photon absorption (TPA) photodiode can be used to record the second order response autocorrelation function

The second-order response leads to what is known as an *interferometric* autocorrelation, and it takes the form [52],

$$g_2(\tau) = \frac{\int_{-\infty}^{\infty} \left| \{E(t) + E(t-\tau)\}^2 \right|^2 dt}{2\int_{-\infty}^{\infty} \left| \{E(t)\}^2 \right|^2 dt} \tag{21}$$

When the detection system used is not fast enough to resolve all the fringes in the autocorrelation, an average response is measured and this describes an *intensity* autocorrelation. This amended profile takes the form,

$$G_2(\tau) = 1 + \frac{2\int_{-\infty}^{\infty} I(t) I(t-\tau) dt}{\int_{-\infty}^{\infty} I(t)^2 dt} \tag{22}$$

A common characteristic of these interferometric autocorrelation functions when measuring pulse duration, regardless of input pulse shape, is that they always display a peak-to-background contrast ratio of 8:1. Intensity autocorrelation functions on the other hand exhibit a 3:1 contrast ratio.

Furthermore, it is not possible to simply calculate the pulse duration from the autocorrelation function alone. Since the autocorrelation full width at half maximum (FWHM) is only proportional to the actual pulse FWHM, a calibration factor must be taken into consideration. For a Gaussian pulse shape it is 1.414 ($\sqrt{2}$) and for a $\text{sech}^2(t)$ pulse shape it is 1.543 [52].

All of the autocorrelations recorded throughout this work were obtained using a silicon photodiode to measure the two-photon autocorrelation response.

2.5 Erbium-Doped Fibre Soliton Laser

Aside from the original work on ultrafast figure-of-8 soliton fibre lasers by Duling *et al* beginning in the late 1980s [37, 53, 54], the first erbium-doped fibre soliton ring laser constructed to produce stable femtosecond optical pulses at the fundamental repetition rate of the cavity was achieved by Tamura *et al* [36]. This laser operated in the soliton regime due to the average negative dispersion of -19ps^2/km for the fibre ring, was mode-locked using polarisation-APM and generated 450fs pulses with an average output power of ~50mW.

These fibre laser configurations utilise the formation of an optical soliton within the fibre in order to accommodate ultrashort pulse operation. Optical solitons are generated through balancing chromatic dispersion with the Kerr effect. Standard silica fibres have negative group delay dispersion at 1.55µm which can be used to compensate for the positive effects of the induced Kerr nonlinearity within a fibre. When these variable parameters reach a state of equilibrium, an optical pulse may oscillate within the cavity that maintains its temporal and spectral shape over long propagation distances. This describes the formation of a first order optical soliton; however, it is possible to generate solitions of higher orders. These solitions do not retain continuous temporal and spectral characteristics but will repeat their shape over a periodic interval.

Fibre soliton lasers can be made to produce sub-picosecond pulses on a routine basis; however, these systems suffer from important characteristic limitations.

2.5.1 Additive Pulse Mode-locking (APM) Saturation

Additive pulse mode-locking (described earlier) is a technique which essentially mimics the role of a saturable absorber in an artificial manner. Therefore, APM is used to shape an oscillating pulse within a laser cavity in order to induce ultrashort pulse operation; however, APM deployed in an all-fibre based soliton laser can lead to an intrinsic limitation in the soliton regime. It is common for these lasers to operate with multiple pulses supported within the cavity when under high pump powers. This is a consequence of the quantisation of the soliton pulse energy with excessive gain [55]. Since the peak power of a soliton is capped due to the theoretical expression for soliton pulse area, if the pump power is increased to a higher value then the peak power of the reshaped soliton will reach a maximum value through saturation of the APM mechanism. This results in a breakdown of the soliton that once oscillated at the fundamental repetition rate of the cavity into a non-periodic redistribution of multiple-pulses.

It is possible to overcome this limitation however through cavity length and gain management. Construction of a short laser cavity and fine tuning of the gain within the cavity will permit stable, single pulse per round-trip operation since the system is tailored to allow a single oscillating soliton to consume all the gain that is available [38].

2.5.3 Spectral Sidebands

The spectral distribution of a mode-locked fibre soliton laser can exhibit characteristic non-uniform sidebands (Kelly sidebands [56]) which are related to the soliton pulses oscillating within the cavity. These sidebands are located around the central peak of the spectrum and are a consequence of soliton filtering. Since a soliton experiences periodic perturbations in gain (erbium fibre) and loss (output coupling) as it propagates within a fibre laser, it is forced to dispense a portion of its spectral content. The resulting frequency packet which has been removed will then propagate within the fibre according to the phase velocity of its constituent frequencies. It is upon each cavity round trip that this, now dispersed, frequency packet will experience destructive interference except at the frequencies which are phase-matched – phase-matching means that there exists a fixed phase relationship (more accurately, the phase mismatch must be zero) between interacting waves maintained along the propagation direction. It is at

these phase-matched frequencies that constructive interference takes place which results in the generation of these non-uniform sidebands. In this case, the linearly dispersed frequency packet's propagation vector, k_{lin}, and the propagation vector of the periodic perturbations, k_p, sum to equal the propagation vector of the soliton, k_s (i.e. $k_s = k_{lin} + k_p$)

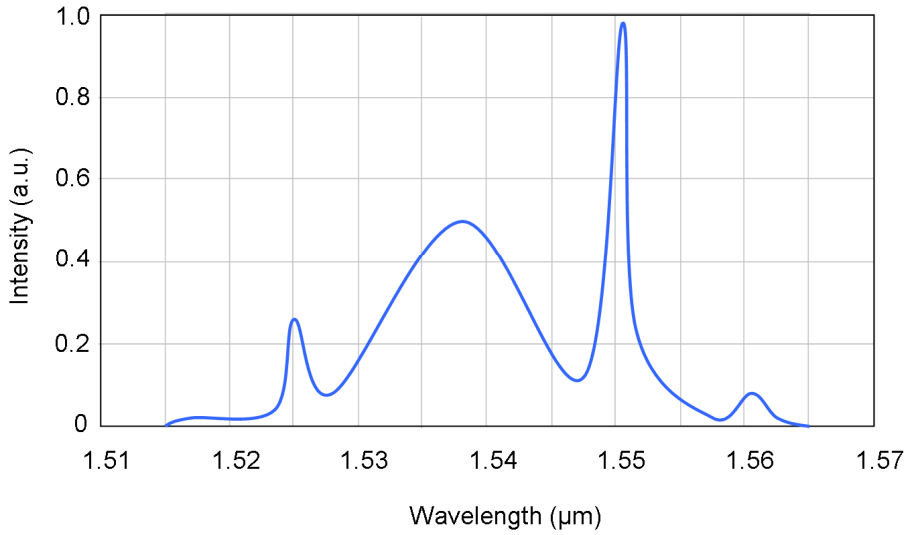

Figure 10 – The spectral distribution of a mode-locked fibre soliton laser can exhibit characteristic non-uniform Kelly sidebands (after [36])

The distribution of Kelly sidebands around the central peak of the spectral output is determined by the soliton pulse width, the dispersion within the cavity, and the cavity length. As a rough guide, and as a general example, it is satisfactory to state that these sidebands will be located closer to the central peak if one were able to reduce the duration of the soliton pulse within the cavity, or be displaced from the central peak to a higher degree through pulse expansion, since the other parameters are typically fixed. Furthermore, care must be taken when inferring the resulting pulse duration from this, or any other, strongly non-Gaussian spectral distribution. The use of the FWHM is clearly inappropriate since the peak in the above spectrum is offset from the centre of the spectrum which would generate in an invalid result.

It is important to note that appropriate balancing of the above mentioned parameters can minimise the generation of these sidebands; however, it is the overall limitations of the fibre soliton laser which are undesirable for convenient system performance and experimental implementation. Therefore, an alternative all-fibre based configuration was conceived in order to remedy these deleterious effects.

2.6 Stretched-Pulse Erbium-Doped Fibre Laser

The stretched-pulse erbium-doped fibre laser is a powerful solution to the detrimental operational and practical effects induced through operation in the soliton regime. These issues include limitations on output pulse width and energy due to the generation of Kelly sidebands in the optical spectrum and also saturation of the APM mechanism. The stretched-pulse fibre laser addresses these problems by employing almost perfectly balanced lengths of both largely negatively and positively dispersive fibre within the cavity, where the net cavity dispersion is slightly positive.

In a stretched-pulse erbium-doped fibre laser, which is the arrangement employed for the construction of our fibre laser source, the alternative sections of large positive- and negative-dispersion fibre result in a pulse that stretches in the positive segment (erbium-doped fibre) and then compresses as it propagates through the negative segment (standard SMF28 fibre).

In this mode of operation, the pulses that circulate within the cavity have a significantly lower peak output power since the pulse widths can change by an order of magnitude as they make one round trip. This therefore reduces the net nonlinear phase shift that is induced per pass which, as a result, circumvents the possibility of APM saturation. Furthermore, through the combined effects of SPM and the large positive-dispersion in the erbium fibre, it is possible to achieve significant spectral broadening. Therefore, it is common for the output pulses from these lasers to have a large spectral bandwidth and a high energy.

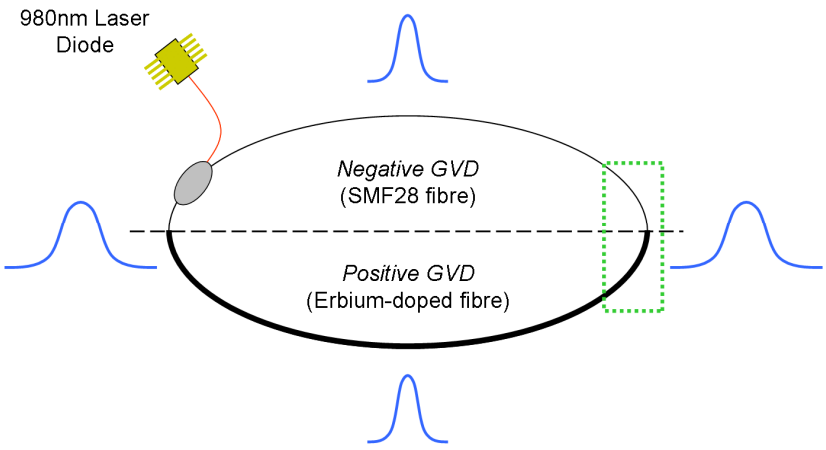

Figure 11 - The stretched-pulse fibre laser employs almost perfectly balanced lengths of both large negative and positive dispersion fibre within the cavity, where the net cavity dispersion is slightly positive. The green dotted box represents the cavity location for free-space optics in the configuration throughout this work

Another benefit of stretched-pulse fibre lasers is that a minimum pulse width is only attained over a small portion of the entire cavity round trip. This puts a limit on the net nonlinear phase shift throughout the cavity and allows the alternating dispersive qualities to become the dominant procedure. It is common for the output of stretched-pulse lasers to be positioned where the peak power within the cavity is low, i.e. located at the boundary where negative and positive-dispersion fibres meet (green dotted box – Fig. 11), therefore, the output pulses will have a large linear chip; yet, this does not create any difficulty in post-cavity pulse management. These pulses can be compressed to compensate for the chirp through the use of standard SMF28 fibre, a prism pair, or a grating (these solutions have been discussed in Section 2.4.2); however, it is possible to avoid the requirement of external chirp compensation by positioning the cavity rejection port at a location where the pulse duration is minimised (i.e. at the mid-point of either the erbium-doped fibre or the standard SMF28 fibre).

Another advantage obtained when using a stretched-pulse erbium-doped fibre laser is that the alternating stretching and compressing of the circulating pulse causes it to have a periodically varying propagation vector. This eliminates the generation of unwanted Kelly sidebands in the output spectrum since there is now a reduced phase-matching condition. Therefore, a cleaner optical spectrum is produced and there is less dispersive structure between consecutive pulses.

2.6.1 Construction

The experimental system configured for the purposes of this work is shown in Fig. 12 and was constructed using only standard telecommunication and optomechanical components. The fibre laser was constructed, modelocked and maintained by the author after the components and initial construction was achieved by a temporary summer student within the Ultrafast Optics Group. The design was taken from [39]; however the main differences from this design were the inclusion of different lengths of erbium-doped fibre and SMF28 fibre (Tamura *et al* used 2.5m of standard Corning SMF28 fibre, 45cm of Corning Flexcor 1060 for the WDM and 1m of erbium-doped fibre) and the use of an external isolator to prevent back-reflections from entering the cavity and cancelling mode-locked operation.

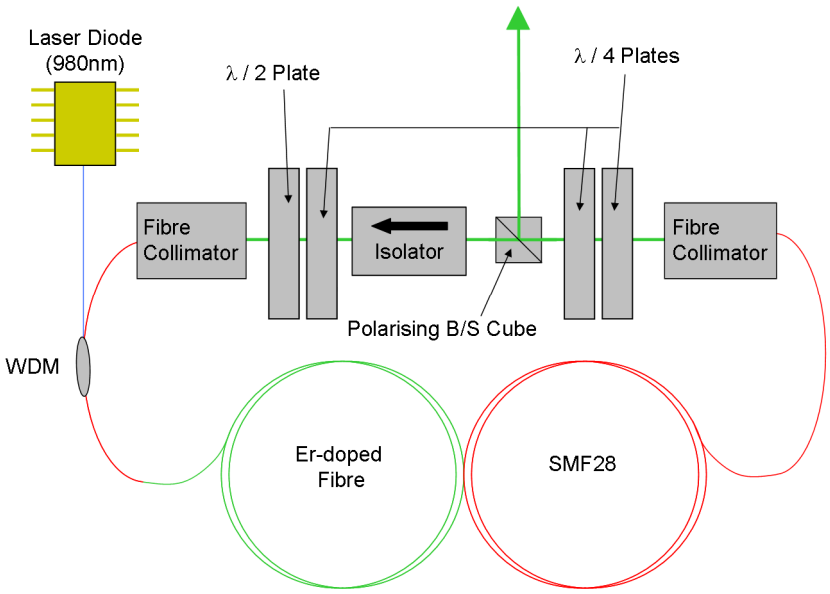

Figure 12 – Experimental configuration of the stretched-pulse erbium-doped fibre laser used through the volume of this work

The ring laser is forced into unidirectional operation through the use of a bulk polarisation-sensitive optical isolator. The input to the isolator is a polarisation-sensitive beamsplitter. The output pulse from the laser is linearly polarised since the polarisation-sensitive beamsplitter acts as a rejection port which couples out the s-state of polarisation. Immediately after the optical isolator, and before the polarisation-sensitive beamsplitter, are positioned pairs of bulk wave plates which are used for polarisation control to induce efficient NPR mode-locking operation. At the exit of the isolator there is a quarter-wave plate then a half-wave plate. These components have the role of creating a state of elliptical polarisation before pulse propagation into the erbium-doped fibre and SMF28 fibre. At the entrance of the polarisation-sensitive beamsplitter is a pair of quarter-wave plates. The first wave plate transforms the rotated elliptical state of polarisation into amplitude modulation. The second wave plate is used to compensate for any remaining linear birefringence in the fibres. Please note here that no fibre-based polarisation controllers are used in his arrangement. It was found, and has been demonstrated, that the use of bulk wave plates provide a higher degree of precision and reproducibility that that obtained through the use of fibre based polarisation controllers [57]. Under this bulk arrangement, once the polarisation controllers were manipulated into producing mode-locked performance, these settings could be recorded and revisited in order to achieve a similar performance to a high degree of accuracy – on condition that the fibre had not been displaced or amended through environmental conditions (as

described previously). These bulk optical components were positioned in a free-space segment of the ring cavity – i.e. the green dotted box in Fig. 11.

The cavity had a total length of 450cm which comprised 286cm of standard Corning SMF28 telecommunications fibre (positive dispersion), 150cm of OFS high-concentration erbium-doped fibre (negative dispersion, peak absorption at 1530nm $\propto$ 45-65dB/m), and 14cm of free-space. The entire cavity was tailored so that the net cavity dispersion was slightly positive. The dispersion of the bulk optical components was estimated to contribute no addition dispersion. The pump source was a 980nm laser diode from Furukawa Electric which provided a maximum pump power of 400mW.

The laser was operated in the forward direction and produced approximately 75mW (15.6kW) of average (peak) output power at a repetition rate of 32MHz. The pulse width was measured using a two-photon autocorrelation and was found to be ~160fs (assuming a Gaussian pulse shape). In order to confirm operation at the fundamental frequency, either a fast InGaAs photodetector could be used to monitor the pulse repetition rate on a suitable oscilloscope, or a radio-frequency (RF) spectrum analyser could be used to validate that the beat frequency between the optical modes matched the fundamental repetition rate. Both of these procedures can also be used to confirm single-pulse operation by observing the output pulses; however, the RF spectrum analyser provides a superior validation since it provides an accurate representation of the frequency content of the periodically-pulsed signal.

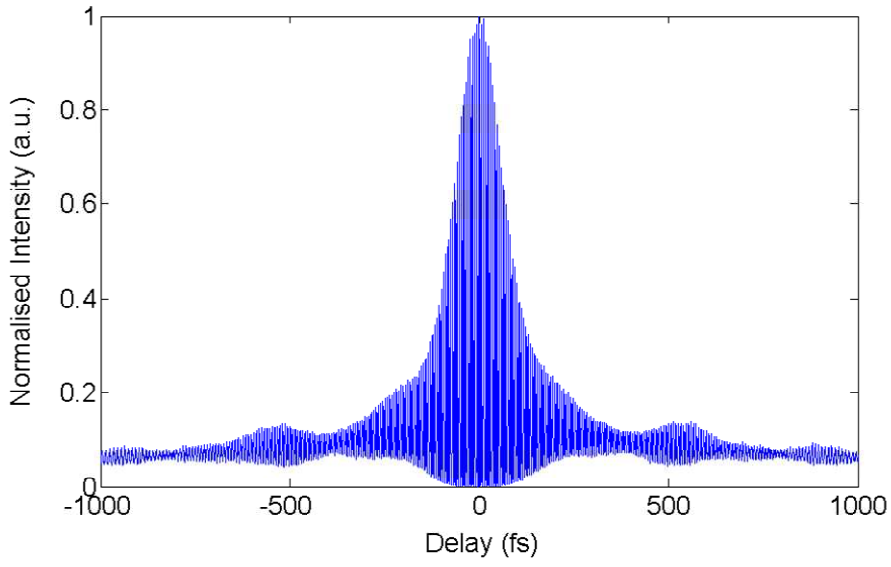

Figure 13 – Stretched-pulse erbium-doped fibre laser autocorrelation. The pulse duration was measured to be ~160fs – assuming a Gaussian pulse shape

The optical spectrum obtained from our arrangement is shown in Fig. 14. This illustrates the general shape of the obtained spectrum; however it has been amended slightly to illustrate the effect of potential multiple-pulsing within the cavity - this was achieved by adjusting the cavity wave plates (polarisation controllers) to alter the optimum NPR conditions. The result is highlighted by the spectral fluctuations located on the back of the main spectral shape at ~1545nm and from 1565-1580nm. Multiple-pulsing must be removed in order to generate high quality output pulses through further manipulation of the polarisation controllers until a stable optical spectrum is achieved.

In addition to the configuration shown in Fig. 12, an additional optical isolator was positioned immediately after the output of the laser to prevent any back-reflections from external experimental optical elements to influence the set mode-locking conditions. It was found that when a strong back-reflection was directed back into the laser cavity the mode-locked output would drop out and the laser would return to its initial state of continuous wave operation.

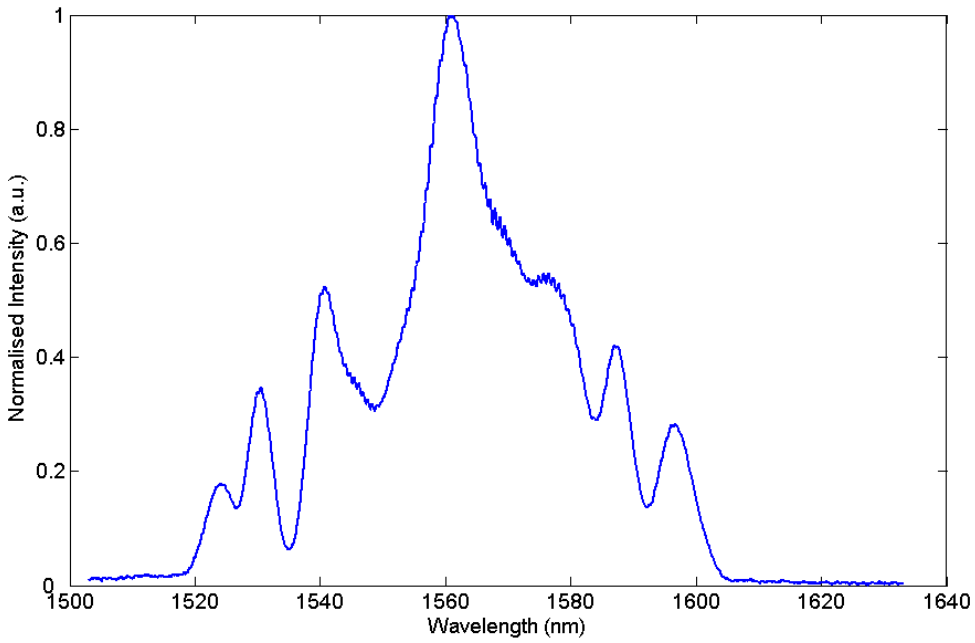

Figure 14 – Optical spectrum of our stretched-pulse erbium-doped fibre laser. The spectral fluctuations located on the back of the main spectral shape at ~1545nm and from 1565-1580nm are a consequence of multiple-pulsing

The polarisation-sensitive beamsplitter has an important role to play in the optimisation of the stretched-pulse fibre laser. Initially, in an all-fibre based arrangement, a fibre output coupler was used which ultimately reduced the efficiency of the laser due to

increased internal losses; however, through the use of bulk optical components, the polarisation-sensitive beamsplitter acts as the laser rejection port which can be tuned to achieve large loss for low intensities. This therefore improves system performance two-fold by reducing the intra-cavity loss and tolerating higher rejected powers through delicate polarisation control. One concern however may be the quality of the rejected 'wings' of the oscillating cavity pulse; however, this is remedied when the net nonlinear phase shift required for mode-locked operation is low ($<\pi/2$) - hence, the use of strain-induced slightly birefringent optical fibres in the laser cavity.

2.6.2 Stretched-Pulse APM – The Master Equation

The optical pulses circulating in both soliton and stretched-pulse fibre lasers can be described using a steady-state theoretical analysis that describes mode-locking in the time-domain. This technique considers the individual effect that each element within the cavity has on the pulse, and demands that these processes repeat themselves every cavity round trip. The analysis described here is governed by the Haus Master Equation [58] which, in the case of a stretched-pulse system, assumes small nonlinear changes per cavity round trip and a chirped Gaussian model [59]. This theory treats the nonlinearity and dispersion imbalance within the cavity as perturbations and can accurately predict the absence of Kelly sidebands from a stretched-pulse configuration. The Master equation can be seen as a generalisation of the NLSE.

The Master Equation for the stretched-pulse system takes the form,

$$\left[(g-l)+\left(\frac{g}{\Omega_g^2}+jD\right)\frac{d}{dt^2}+\gamma_0|A_0|^2\left(1-\mu\frac{t^2}{\tau_0^2}\right)-j\delta_0|A_0|^2\left(1-\mu\frac{t^2}{\tau_0^2}\right)\right]a(t)=-j\psi a(t) \quad (23)$$

where g is the laser gain, l is the linear loss per cavity round trip, Ω_g is the gain bandwidth, D is the average dispersion, t represents time, γ_0 describes self-amplitude modulation (i.e. the saturable absorption action due to nonlinear polarisation rotation), A_0 is the peak amplitude of the pulse, μ is the curvature of the parabolic time-dependent nonlinear phase shift (in a stretched-pulse fibre laser μ <1 due to the average stretching and compressing of the pulse per round trip) τ is the normalised pulse width, δ_0 describes the effects of SPM, and ψ is the net linear phase.

The Master Equation, when considering a stretched-pulse fibre laser, has a chirped Gaussian solution,

$$u(t) = A_0 \exp\left(-Q\frac{t^2}{2}\right) \tag{24}$$

where $u(t)$ represents the complex amplitude of the oscillating electric-field within the cavity and the complex parameter Q is obtained by balancing terms in (23).

This Gaussian solution is in agreement with the simplified Kuizenga-Siegman theory [60, 61] which also models ultrafast pulse propagation and duration. These solutions can be attained by utilising a spit-step Fourier approach [5].

2.7 Erbium-Doped Fibre Amplifier (EDFA)

Erbium-doped fibre amplifiers can be utilised in a wide variety of applications, examples of which include optical frequency metrology, optical supercontinuum generation and in the telecommunications industry as a source of optical signal enhancement across long transmission lines. The latter was the original driving force behind EDFA optimisation and characterisation since it provided an efficient, entirely optical replacement for electrical amplifiers avoiding the need for optical-to-electrical conversion. The spectral output of such devices falls perfectly within the telecommunications C Band (conventionally 1530-1565nm), which can also be tuned to accommodate a small portion of the L Band (long wavelength 1565-1625). Since fibre optical communications require the ability to transfer data over an enormous distance, a major drawback can be signal attenuation and pulse breakdown due to excessive attenuation within the fibre. Therefore, a series of optical amplifiers is used to optically boost the amplitude of the transmitted signal at periodic intervals along a length of single-mode fibre which has been dispersion-shifted to accommodate zero-dispersion at 1550nm.

For many novel applications, the ability to provide high average powers and high pulse energies is incredibly important. It is clear that for particular areas of science and engineering the EDFA is an ideal solution; however, the amplification process within an optical fibre is not a trivial task to facilitate and, in addition, when ultrashort pulses are concerned, a key requirement is the control of nonlinear effects within the fibre core.

This is extremely critical since the desire is to maintain good pulse quality and short pulse durations after the amplification process is complete. The basic solution here is to scale down the peak intensity of an ultrashort pulse within the fibre core, which can be achieved through a variety of different techniques, in order to regulate the nonlinear effects, even at high peak powers.

There are several methods which can be applied to obtain such pulse amplification management. These include chirped pulse amplification (where the pulse is stretched in time prior to amplification and then compressed again afterwards), fibre core-size scaling (a spatial technique where the core of the amplifying fibre is manipulated to accommodate an increased number of modes), and nonlinear pulse amplification, which is the process adopted in this work and is explained in detail below.

2.7.1 Nonlinear Pulse Amplification

Nonlinear pulse amplification is obtained by coupling an optical pulse into a fibre amplification system and allowing the effects of gain, SPM and dispersion to spectrally and temporally influence the propagating pulse in a manner that will result in either a compressed or chirped pulse at the output - depending on the configuration of the amplifier used. The amplified compressed, or chirped, pulses that emerge from the system are a result of the sign of the fibre dispersion. Therefore, if an amplifying negative-dispersion fibre is used then a compressed pulse will be produced, otherwise, if an amplifying positive-dispersion fibre is used then a chirped pulse will result.

In the case of a positive-dispersion fibre, the chirped pulses that are emitted have to be compressed again using a suitable mechanism after the amplification stage. Since erbium-doped fibre is positively dispersive, this is the typical requirement for EDFA configurations; however, it is possible to alleviate this post-amplification compression by temporally stretching the input pulse in a length of standard telecommunication negative-dispersion fibre before entering the amplifier. When this is achieved the pulse will be simultaneously amplified and compressed within the positive-dispersion fibre. By controlling the length of pre-chirping fibre it is possible to accurately tune the peak intensity of the amplified output pulses.

A main advantage of using a positive-dispersion nonlinear amplification process is that is should generate significantly higher pulse energies than the negative-dispersion

alternative. This is because positive dispersion will stretch the pulse within the amplifying fibre, which is also spectrally broadened through SPM, which in turn reduces the pulse peak power and therefore increases the maximum achievable amplified pulse energies.

2.7.2 Construction

The construction of the EDFA was executed entirely by the author and is illustrated in the schematic diagram Fig. 15. The components that were used were all standard telecommunication elements which comprised of two Bookham 980nm laser diodes which provided a maximum continuous wave output power of 400mW each, two WDMs, a 170cm length of erbium-doped fibre (same fibre used for Er:fibre laser), a length of SMF28 optical fibre for dispersion compensation (discussed later), a heat sink, a die-cast box and a fibre collimator. The laser diodes were managed using a pair of temperature controllers and current drivers – a combination of each for each laser diode. A complete system was configured by designing a contained arrangement around the die-cast box and the heat sink. The laser diodes were attached to the heat sink then enclosed in the die-cast box. At opposing end faces of the die-cast box were electrical interfaces for current and temperature control of the laser diodes. On the top surface of the die-cast box was positioned a reel of erbium-doped fibre along with the two WDMs and the fibre collimator. The erbium-doped fibre was double-pumped from both ends by the laser diodes which were fibre coupled out from the die-cast box into a WDM each then spliced to the erbium-doped fibre. The remaining fibre inputs of each WDM were used for either signal input pulse collection from the erbium-doped fibre laser or as the output of the EDFA after pulse dispersion compensation.

The EDFA accepted input pulses from the erbium-doped fibre laser of approximately 75mW average power. These pulses were relay imaged from the output fibre collimator of the fibre laser (located before the polarisation sensitive beamsplitter with respect to the pulse propagation direction) onto the fibre collimator of the EDFA using a suitable 4f arrangement. After nonlinear pulse amplification through the additional length of erbium-doped fibre and pulse compression through the accompanying SMF28 fibre of the EDFA, the resulting average output power was measured to be ~200mW.

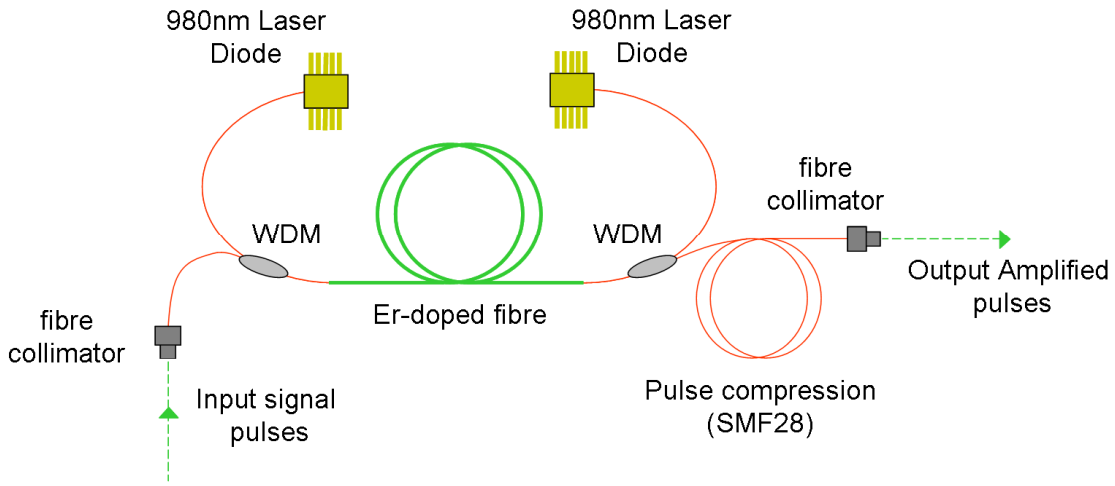

Figure 15 – Erbium-doped fibre amplifier (EDFA) schematic diagram

2.7.3 Dispersion Compensation

As mentioned previously, the nonlinear pulse amplification process within a positive-dispersion fibre (erbium-doped fibre) results in a stretched (chirped) pulse output through the effects of gain, dispersion and SPM. This can be compensated for by either pre-stretching the pulse in a length of SMF28 fibre (negative-dispersion) then observing pulse shortening during amplification, as demonstrated by Tauser *et al* [18], or by compressing the pulse after it has been stretched during the amplification process. The latter approach was adopted here and will be described below.

In order to assess the length of negative-dispersion SMF28 fibre required to produce output pulses from the EDFA that were suitably compressed to observe minimum pulse durations and maximum pulse intensities, a fibre cut-back method was applied. This simple cutback procedure involved splicing in an excessive length of SMF28 after the output of the erbium-doped fibre then recording individual autocorrelation traces over a series of reducing fibre lengths until a minimum pulse duration had elapsed. Once this had been observed, the required length of SMF28 fibre was spliced back into the system to return to the minimum output pulse duration. This procedure is illustrated in Fig. 16 and the two-photon interferometric autocorrelation results obtained are presented in Fig. 17.

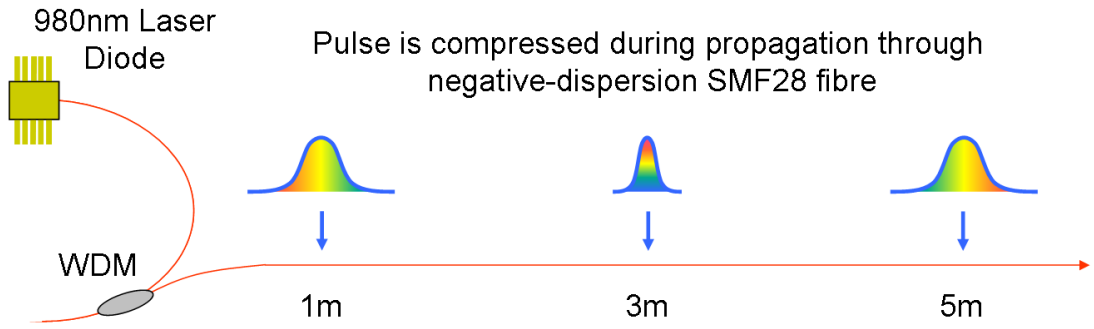

Figure 16 – Fibre cutback measurement for post-amplification pulse dispersion compensation

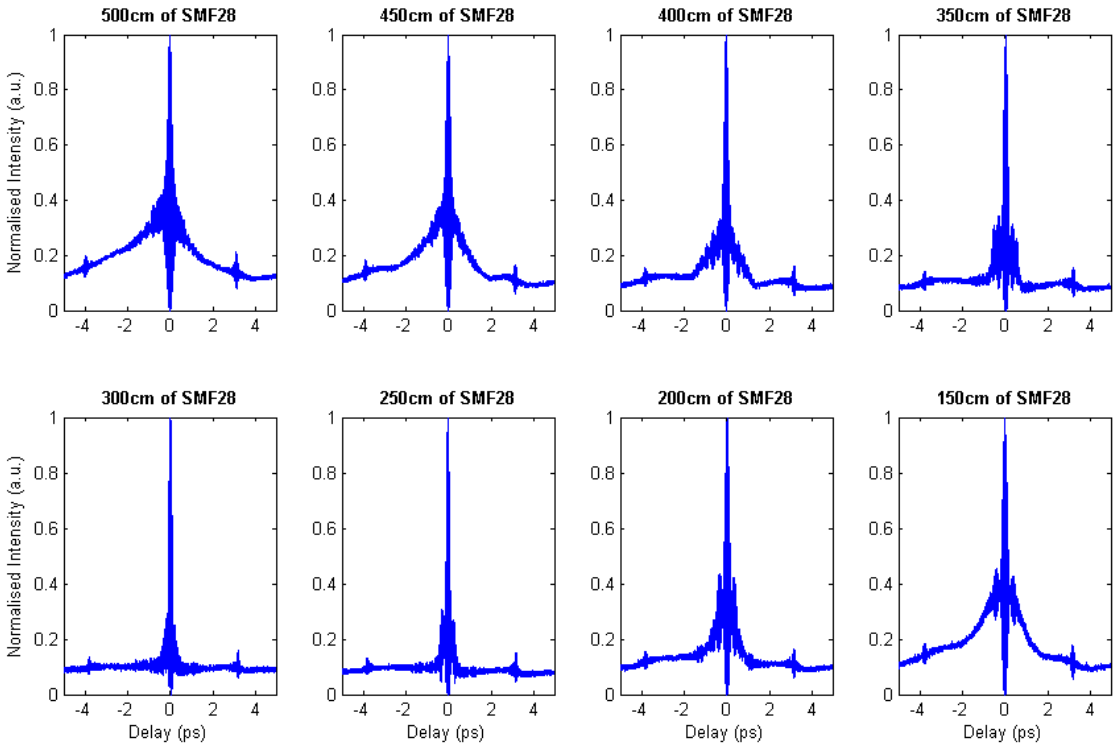

Figure 17 – Fibre cutback measurement results presenting interferometric autocorrelations recorded at different lengths of SMF28 optical fibre. Excessive pulse chirp is represented as a rise in intensity at the wings of certain traces

It can be seen from the autocorrelations shown in Fig. 17 that the pulses are highly chirped when at fibre lengths above and below the optimised length for obtaining the minimum pulse duration. This is highlighted by the large rise in intensity at the wings of

the interferometric autocorrelations. This intensity increase can be explained by considering the locations where the frequency content of two pulses exactly overlaps when one pulse traverses the other. When a monochromatic pulse is interfered with an exact replica of itself then interference will be observed as soon as the two pulses come into contact with each other; however, if two highly-chirped pulses are brought into contact with each other, the location at which there will be interference is where the frequency content of each pulse exactly overlaps – i.e. when the pulse envelopes are matched at zero delay. At every other location there is a frequency mis-match which results in a rise in intensity on the autocorrelation trace. Furthermore, since a chirped pulse is stretched, it will come into contact with the other pulse sooner than when two compressed pulses are brought together. This is why the rise in intensity can begin far out in the wings of the interferometric autocorrelation trace.

For reasons explained above, an interferometric autocorrelation is not an ideal method to use when determining pulse durations by considering the resulting FWHM extent of each trace. A suitable alternative is to record a series of intensity autocorrelations as the SMF28 fibre is cut back from its originally excessive length. In order to avoid having to measure an interferometric/intensity autocorrelation pair at each fibre cut-back length, an analytical approach is to Fourier filter each interferometric autocorrelation trace to reveal its intensity autocorrelation equivalent.

This analytic intensity autocorrelation technique was used to expose a more accurate representation of pulse compression within the SMF28 fibre. The results obtained from this method are presented in Fig. 18. These results were all individual measurements taken from Fig. 17. The measurements are repeatable to approximately ± 5fs with the main source of error arising due to experimental inconsistencies; such as optical alignment, optical power (fibre cleave quality, initial source power), optomechanical or scanning stage calibration issues.

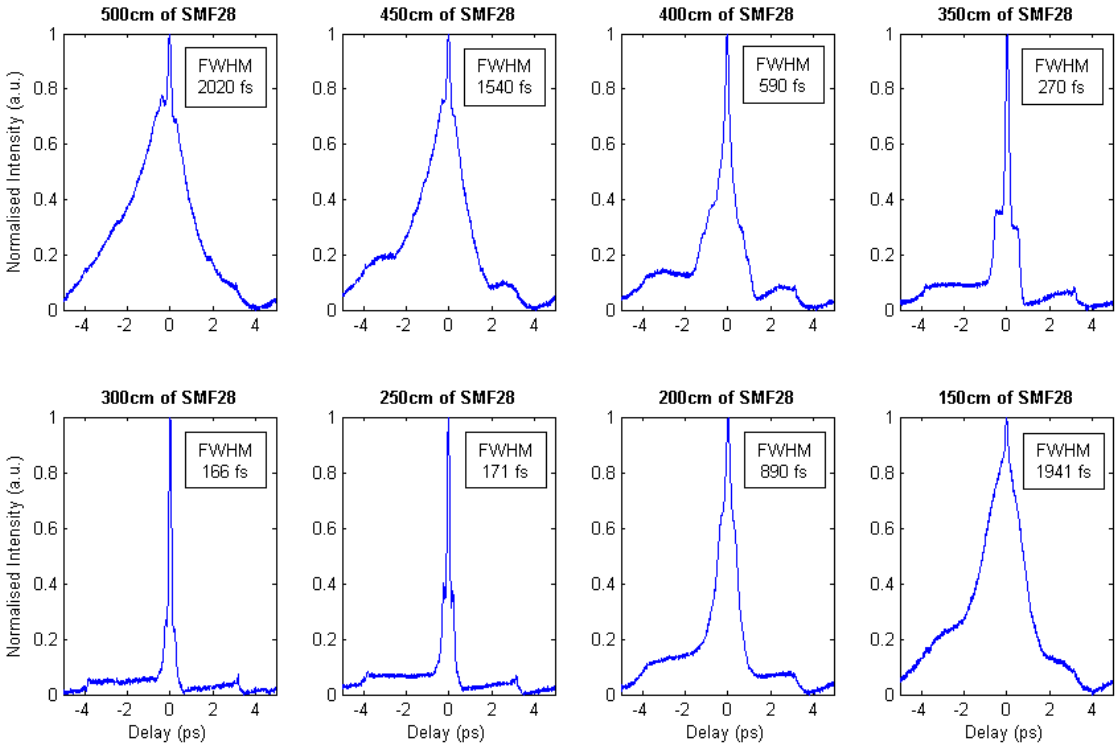

Figure 18 – Fibre cutback measurement results presenting intensity autocorrelations recorded at different lengths of SMF28 optical fibre. The images were obtained by applying an appropriate level of Fourier filtering on each of the traces presented in Fig. 17

The results presented above highlight the striking level of pulse compression that is achieved within the SMF28 fibre. The FWHM values are stated in the insets located at the top right-hand side of each trace. These FWHM values have been collected and compiled in a separate plot which is given in Fig. 19.

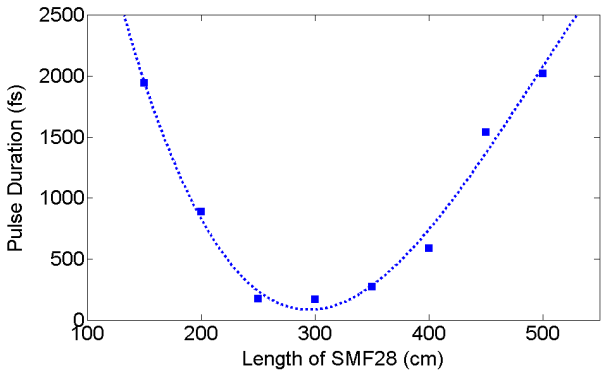

Figure 19 – Plot of FWHM pulse duration against SMF28 fibre length in post-amplification dispersion compensating cutback measurement. The squares represent acquired data points and the dotted line is a cubic fit to the data

Fig. 19 illustrates that a propagating pulse will be compressed and then stretched again quite significantly along a 5m length of negative-dispersion SMF28 after it has exited an amplifying length of positive-dispersion erbium-doped fibre. The measured pulse durations vary from a heavily chirped maximum of ~2ps at 5m down to the compressed minimum value of 166fs at ~3m.

For completeness, our stretched-pulse erbium-doped fibre laser and EDFA configuration is illustrated in Fig. 20.

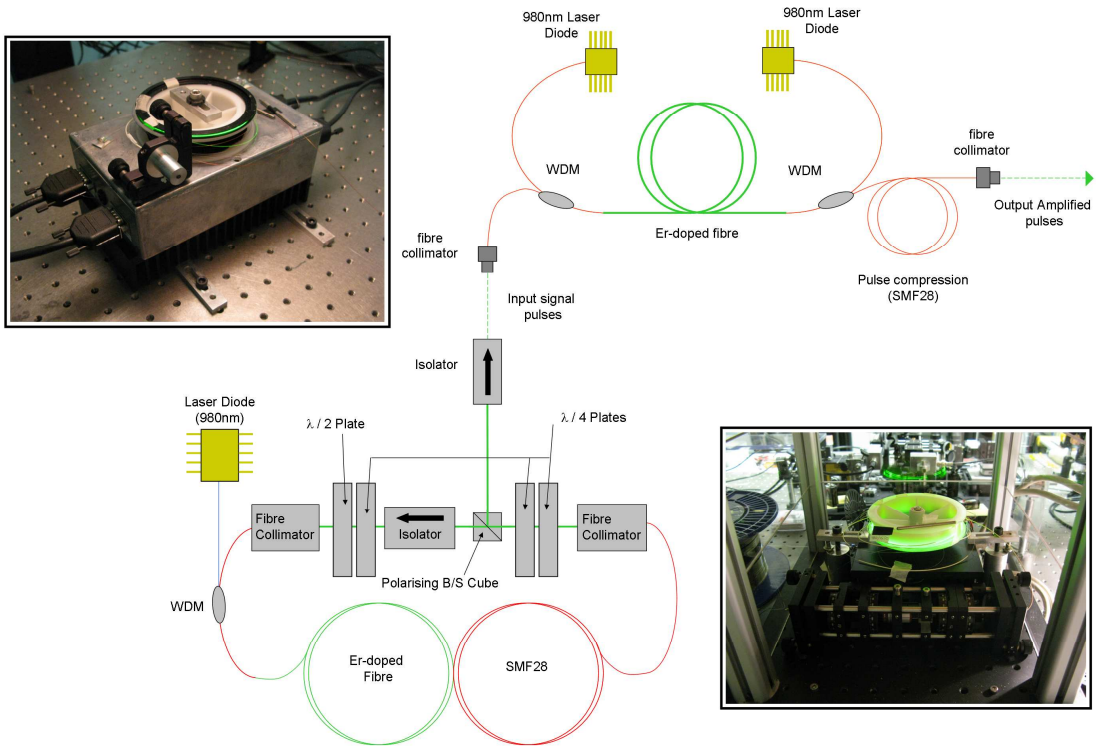

Figure 20 – Complete stretched-pulse erbium-doped fibre laser and EDFA arrangement

2.8 Conclusions

Mode-locked erbium-doped fibre lasers and amplifiers have been the workhorse of the ultrafast optics lab for several years and have generated an intense sustained period of research and development in a wide variety of optical technologies. These lasers not only provide an efficient and reliable optical source but can also be extremely compact, durable and simple to use. Currently, erbium-doped fibre lasers and EDFAs are creating a lot of interest in industrial activities and the flux of commercial products available on the market has increased significantly.

In this chapter I have discussed the physics behind the erbium ion when doped into a dielectric host material and highlighted several important optical processes that take place when it is optically stimulated. In addition, I have reviewed a selection of fibre laser mode-locking techniques and discussed the management of the resulting ultrafast pulses. The erbium-doped fibre soliton laser was then presented and its limiting optical performance discussed. As a solution, the stretched-pulse erbium-doped fibre laser was established and the construction of such a device, for the purposes of this work, was illustrated and reviewed. In addition, an EDFA was also required to compliment the latter stages of this work (OCT) and its construction and properties were discussed and presented.

The final assembled stretched-pulse erbium-doped fibre laser provided approximately 75mW of average output power at a fundamental repetition rate of 32MHz. The pulse width was measured using a two-photon autocorrelation and was found to be ~160fs. Furthermore, I have demonstrated an EDFA with efficient post-amplification pulse compression whose amplified average output power was approximately 200mW and whose pulse width was measured, at the 3m of additional SMF28 point, using a two-photon autocorrelation and found to be 166fs.

References

[1] M. Karasek and M. Menif, "Serial topology of wide-band erbium-doped fiber amplifier for WDM applications", *IEEE Photonics Technology Letters* **13**, 939-941 (2001)

[2] A.J. Kenyon, "Recent developments in rare-earth doped materials for optoelectronics", *Progress in Quantum Electronics* **26**, 225-284 (2002)

[3] J.W. Nicholson, A.D. Yablon, P.S. Westbrook, K.S. Feder, and M.F. Yan, "High power, single mode, all-fiber source of femtosecond pulses at 1550 nm and its use in supercontinuum generation", *Optics Express* **12**, 3025-3034 (2004)

[4] M. Pfennigbauer and W.R. Leeb, "Optical satellite communications with Erbium doped fiber amplifiers", *Space Communications* **19**, 59-67 (2003)

[5] G.P. Agrawal, *Nonlinear Fiber Optics*. 4th ed. New York: Academic Press (2006)

[6] J. Stone and C.A. Burrus, "Neodymium-Doped Silica Lasers in End-Pumped Fiber Geometry", *Applied Physics Letters* **23**, 388-389 (1973)

[7] J.Y. Allain, M. Monerie, and H. Poignant, "High-Efficiency Cw Thulium-Sensitized Holmium-Doped Fluoride Fiber Laser Operating at 2.04 Mu-M", *Electronics Letters* **27**, 1513-1515 (1991)

[8] D.C. Hanna, R.M. Percival, R.G. Smart, and A.C. Tropper, "Efficient and Tunable Operation of a Tm-Doped Fiber Laser", *Optics Communications* **75**, 283-286 (1990)

[9] D.C. Hanna, I.M. Jauncey, R.M. Percival, I.R. Perry, R.G. Smart, P.J. Suni, J.E. Townsend, and A.C. Tropper, "Continuous-Wave Oscillation of a Monomode Thulium-Doped Fiber Laser", *Electronics Letters* **24**, 1222-1223 (1988)

[10] D.C. Hanna, R.M. Percival, I.R. Perry, R.G. Smart, P.J. Suni, J.E. Townsend, and A.C. Tropper, "Continuous-Wave Oscillation of a Monomode Ytterbium-Doped Fiber Laser", *Electronics Letters* **24**, 1111-1113 (1988)

[11] Y. Durteste, M. Monerie, J.Y. Allain, and H. Poignant, "Amplification and Lasing at 1.3-Mu-M in Praseodymium-Doped Fluorozirconate Fibers", *Electronics Letters* **27**, 626-628 (1991)

[12] K. Tamura, E. Yoshida, and M. Nakazawa, "Generation of 10GHz pulse trains at 16 wavelengths by spectrally slicing a high power femtosecond source", *Electronics Letters* **32**, 1691-1693 (1996)

[13] K. Tamura, E. Yoshida, E. Yamada, and M. Nakazawa, "Generation of a 0.5 W average power train of femtosecond pulses at 10 GHz in the 1.55 mu m region", *Electronics Letters* **32**, 835-836 (1996)

[14] C. Bourolias, E. Prokopakis, E. Sobol, J. Moschandreas, G.A. Velegrakis, and E. Helidonis, "Septal cartilage reshaping with the use of an Erbium doped glass fiber laser. Preliminary results", *Rhinology* **46**, 62-65 (2008)

[15] C.C. Neubaur and G. Stevens, "Erbium : YAG laser cataract removal: Role of fiber-optic delivery system", *Journal of Cataract and Refractive Surgery* **25**, 514-520 (1999)

[16] J.L. Peng, H. Ahn, R.H. Shu, H.C. Chui, and J.W. Nicholson, "Highly stable, frequency-controlled mode-locked erbium fiber laser comb", *Applied Physics B-Lasers and Optics* **86**, 49-53 (2007)

[17] F. Adler, K. Moutzouris, A. Leitenstorfer, H. Schnatz, B. Lipphardt, G. Grosche, and F. Tauser, "Phase-locked two-branch erbium-doped fiber laser system for long-term precision measurements of optical frequencies", *Optics Express* **12**, 5872-5880 (2004)

[18] F. Tauser, A. Leitenstorfer, and W. Zinth, "Amplified femtosecond pulses from an Er : fiber system: Nonlinear pulse shortening and self-referencing detection of the carrier-envelope phase evolution", *Optics Express* **11**, 594-600 (2003)

[19] G. Canat, L. Lombard, A. Dolfi, M. Valla, C. Planchat, B. Augere, P. Bourdon, V. Jolivet, C. Besson, Y. Jaouen, S. Jetschke, S. Unger, J. Kirchhof, E. Gueorguiev, and C. Vitre, "High brightness 1.5 mu m pulsed fiber laser for lidar: From fibers to systems", *Fiber and Integrated Optics* **27**, 422-439 (2008)

[20] M. Hofer, M.H. Ober, F. Haberl, M.E. Fermann, E.R. Taylor, and K.P. Jedrzejewski, "Regenerative Nd Glass Amplifier Seeded with a Nd Fiber Laser", *Optics Letters* **17**, 807-809 (1992)

[21] A. Hariharan, D.J. Harter, T.S. Sosnowski, S. Kane, D.T. Du, T.B. Norris, and J. Squier, "Injection of ultrafast regenerative amplifiers with low energy femtosecond pulses from an Er-doped fiber laser", *Optics Communications* **132**, 469-473 (1996)

[22] J.W. Nicholson, R. Bise, J. Alonzo, T. Stockert, D.J. Trevor, F. Dimarcello, E. Monberg, J.M. Fini, P.S. Westbrook, K. Feder, and L. Gruner-Nielsen, "Visible continuum generation using a femtosecond erbium-doped fiber laser and a silica nonlinear fiber", *Optics Letters* **33**, 28-30 (2008)

[23] M.C. Stumpf, S.C. Zeller, A. Schlatter, T. Okuno, T. Sudmeyer, and U. Keller, "Compact Er : Yb : glass-laser-based supercontinuum source for high-resolution optical coherence tomography", *Optics Express* **16**, 10572-10579 (2008)

[24] E. Desurvire, *Erbium-doped fiber amplifiers: Principles and applications*: John Wiley & Sons (2002)

[25] M.P. Hehlen, N.J. Cockroft, T.R. Gosnell, A.J. Bruce, G. Nykolak, and J. Shmulovich, "Uniform upconversion in high-concentration Er3+-doped soda lime silicate and aluminosilicate glasses", *Optics Letters* **22**, 772-774 (1997)

[26] W.J. Miniscalco, "Erbium-Doped Glasses for Fiber Amplifiers at 1500-Nm", *Journal of Lightwave Technology* **9**, 234-250 (1991)

[27] P.A. Krug, M.G. Sceats, G.R. Atkins, S.C. Guy, and S.B. Poole, "Intermediate Excited-State Absorption in Erbium-Doped Fiber Strongly Pumped at 980-Nm", *Optics Letters* **16**, 1976-1978 (1991)

[28] R. Lopez-Martens, K. Varju, P. Johnsson, J. Mauritsson, Y. Mairesse, P. Salieres, M.B. Gaarde, K.J. Schafer, A. Persson, S. Svanberg, C.G. Wahlstrom, and A. L'Huillier, "Amplitude and phase control of attosecond light pulses", *Physical Review Letters* **94** (2005)

[29] A.E. Siegman, *Lasers*. Sausalito, California: University Science Books (1986)

[30] W.T. Silfvast, *Laser Fundamentals*. 2nd ed: Cambridge Univeristy Press (2004)

[31] G.R. Jacobovitzveselka, U. Keller, and M.T. Asom, "Broad-Band Fast Semiconductor Saturable Absorber", *Optics Letters* **17**, 1791-1793 (1992)

[32] E.P. Ippen, C.V. Shank, and A. Dienes, "Passive Mode-Locking of Cw Dye Laser", *Applied Physics Letters* **21**, 348-& (1972)

[33] W.H. Loh, D. Atkinson, P.R. Morkel, M. Hopkinson, A. Rivers, A.J. Seeds, and D.N. Payne, "Passively Mode-Locked Er3+ Fiber Laser Using a Semiconductor Nonlinear Mirror", *IEEE Photonics Technology Letters* **5**, 35-37 (1993)

[34] M. Nakazawa, E. Yoshida, and Y. Kimura, "Low Threshold, 290-Fs Erbium-Doped Fiber Laser with a Nonlinear Amplifying Loop Mirror Pumped by InGaAsP Laser-Diodes", *Applied Physics Letters* **59**, 2073-2075 (1991)

[35] S. Namiki, E.P. Ippen, H.A. Haus, and K. Tamura, "Relaxation oscillation behavior in polarization additive pulse mode-locked fiber ring lasers", *Applied Physics Letters* **69**, 3969-3971 (1996)

[36] K. Tamura, H.A. Haus, and E.P. Ippen, "Self-Starting Additive Pulse Mode-Locked Erbium Fiber Ring Laser", *Electronics Letters* **28**, 2226-2228 (1992)

[37] M.L. Dennis and I.N. Duling, "High Repetition Rate Figure 8 Laser with Extracavity Feedback", *Electronics Letters* **28**, 1894-1896 (1992)

[38] L.E. Nelson, D.J. Jones, K. Tamura, H.A. Haus, and E.P. Ippen, "Ultrashort-pulse fiber ring lasers", *Applied Physics B-Lasers and Optics* **65**, 277-294 (1997)

[39] K. Tamura, C.R. Doerr, L.E. Nelson, H.A. Haus, and E.P. Ippen, "Technique for Obtaining High-Energy Ultrashort Pulses from an Additive-Pulse Mode-Locked Erbium-Doped Fiber Ring Laser", *Optics Letters* **19**, 46-48 (1994)

[40] A. Takada and H. Miyazawa, "30 Ghz Picosecond Pulse Generation from Actively Mode-Locked Erbium-Doped Fiber Laser", *Electronics Letters* **26**, 216-217 (1990)

[41] C.R. Doerr, H.A. Haus, E.P. Ippen, M. Shirasaki, and K. Tamura, "Additive-Pulse Limiting", *Optics Letters* **19**, 31-33 (1994)

[42] A.B. Grudinin, D.J. Richardson, and D.N. Payne, "Passive Harmonic Modelocking of a Fiber Soliton Ring Lasers", *Electronics Letters* **29**, 1860-1861 (1993)

[43] G.T. Harvey and L.F. Mollenauer, "Harmonically Mode-Locked Fiber Ring Laser with an Internal Fabry-Perot Stabilizer for Soliton Transmission", *Optics Letters* **18**, 107-109 (1993)

[44] M.E. Fermann and I. Hartl, "Ultrafast Fiber Laser Technology", *IEEE Journal of Selected Topics in Quantum Electronics* **15**, 191-206 (2009)

[45] R.L. Fork, O.E. Martinez, and J.P. Gordon, "Negative Dispersion Using Pairs of Prisms", *Optics Letters* **9**, 150-152 (1984)

[46] R. Szipocs, K. Ferencz, C. Spielmann, and F. Krausz, "Chirped Multilayer Coatings for Broad-Band Dispersion Control in Femtosecond Lasers", *Optics Letters* **19**, 201-203 (1994)

[47] K.O. Hill, Y. Fujii, D.C. Johnson, and B.S. Kawasaki, "Photosensitivity in Optical Fiber Waveguides - Application to Reflection Filter Fabrication", *Applied Physics Letters* **32**, 647-649 (1978)

[48] K. Tamura, E.P. Ippen, H.A. Haus, and L.E. Nelson, "77-Fs Pulse Generation from a Stretched-Pulse Mode-Locked All-Fiber Ring Laser", *Optics Letters* **18**, 1080-1082 (1993)

[49] J.C. Knight, T.A. Birks, P.S. Russell, and D.M. Atkin, "All-silica single-mode optical fiber with photonic crystal cladding", *Optics Letters* **21**, 1547-1549 (1996)

[50] R.F. Cregan, B.J. Mangan, J.C. Knight, T.A. Birks, P.S. Russell, P.J. Roberts, and D.C. Allan, "Single-mode photonic band gap guidance of light in air", *Science* **285**, 1537-1539 (1999)

[51] D.E. Spence, P.N. Kean, and W. Sibbett, "60 fsec pulse generation from a self-mode-locked Ti:Sapphire laser", *Optics Letters* **16**, 42-44 (1991)

[52] J.C.M. Diels, J.J. Fontaine, I.C. McMichael, and F. Simoni, "Control and Measurement of Ultrashort Pulse Shapes (in Amplitude and Phase) with Femtosecond Accuracy", *Applied Optics* **24**, 1270-1282 (1985)

[53] I.N. Duling, "All-Fiber Ring Soliton Laser Mode-Locked with a Nonlinear Mirror", *Optics Letters* **16**, 539-541 (1991)

[54] I.N. Duling, "Subpicosecond All-Fiber Erbium Laser", *Electronics Letters* **27**, 544-545 (1991)

[55] H.A. Haus, E.P. Ippen, and K. Tamura, "Additive-Pulse Modelocking in Fiber Lasers", *IEEE Journal of Quantum Electronics* **30**, 200-208 (1994)

[56] S.M.J. Kelly, "Characteristic Side-Band Instability of Periodically Amplified Average Soliton", *Electronics Letters* **28**, 806-807 (1992)

[57] H.A. Haus, J.G. Fujimoto, and E.P. Ippen, "Analytic Theory of Additive Pulse and Kerr Lens Mode-Locking", *IEEE Journal of Quantum Electronics* **28**, 2086-2096 (1992)

[58] H.A. Haus, K. Tamura, L.E. Nelson, and E.P. Ippen, "Stretched-Pulse Additive-Pulse Mode-Locking in Fiber Ring Lasers - Theory and Experiment", *IEEE Journal of Quantum Electronics* **31**, 591-598 (1995)

[59] K. Tamura, E.P. Ippen, and H.A. Haus, "Pulse Dynamics in Stretched-Pulse Fiber Lasers", *Applied Physics Letters* **67**, 158-160 (1995)

[60] D.J. Kuizenga and A.E. Siegman, "FM and AM Mode Locking of Homogeneous Laser .1. Theory", *IEEE Journal of Quantum Electronics* **QE 6**, 694-& (1970)

[61] D.J. Kuizenga and A.E. Siegman, "FM and AM Mode Locking of Homogeneous Laser .2. Experimental Results in a Nd-Yag Laser with Internal FM Modulation", *IEEE Journal of Quantum Electronics* **QE 6**, 709-& (1970)

Chapter 3

Ultra-High-Resolution Two- and Three-Dimensional Imaging of a Semiconductor Flip-Chip using a Solid Immersion Lens

3.1 Introduction

In silicon devices, standard optical beam induced current (OBIC) microscopy of silicon integrated-circuits (IC) [1] is hindered by the contradictory requirements of choosing a laser wavelength that allows high bulk transmission, up to several mm of silicon, but is also absorbed sufficiently in the micron-scale device layer to produce high contrast images. The issue of penetration is also encountered in conventional confocal imaging when using light at 1064nm [2]. The proximity of the band-edge at this wavelength means that the absorption coefficient is around $80cm^{-1}$. Furthermore, the light must also make a double-pass through the silicon due to the transmission / reflection nature of the confocal system. In both cases the introduction of a super solid immersion lens (s-SIL) causes further absorption. An elegant solution is to use the two-photon optical beam induced current (TOBIC) effect [3-5] to achieve high absorption of infrared radiation at the beam focus but also high transmission throughout the sample and s-SIL. Using two-photon absorption instead of single photon absorption (examples of single photon solutions are described in [1, 6-11]) the lateral resolution of the microscope is improved, and the ability to implement axially-resolved imaging is provided because two-photon absorption is highly dependent on the optical intensity. In this chapter, two-dimensional (2D) diffraction-limited imaging performance with a resolution of 166nm is described, which extends to three-dimensional (3D) sub-surface imaging with approximately 100nm axial profiling resolution. This result surpasses earlier performance obtained by Ramsay *et al* [12] and is attributed to an enhanced ability to perform systematic axial scanning and thus an improved ability to localise the focus of the beam in the component layer of the chip.

3.2 Solid Immersion Lens Microscopy using TOBIC Imaging

Semiconductor devices have been investigated and analysed for decades now in order to evaluate their operating characteristics. This has led to the development of a wide range of imaging modalities in this interesting area which include OBIC [13] and two-photon techniques [14-16]. Progression in this field suggested that it was natural for these systems to be considered in the implementation of various optical modes for practical defect detection and imaging of silicon ICs [17-19]. SILs provide the ability to improve the resolution of these imaging technologies by increasing the numerical aperture (*NA*) of the system and have been adopted into these schemes now for several years [12, 20]. In previous work, Ippolito *et al* showed that an h-SIL could be used to image a silicon chip to achieve a resolution of 230nm by imaging at 1064nm [21].

Details of the theory of SIL imaging is given by Born and Wolf [22], which is also covered in Section 1.5, and can be used to separate SIL imaging into two modalities, hemispherical (h) SIL imaging and Weiserstrauss / super-SIL (s-SIL) imaging. Imaging using an h-SIL can resolve structures that lie close to the surface of a sample [23] and also features located at a given distance below the surface of the sample. This is also true when imaging using an s-SIL. In this work a s-SIL modality was chosen and designed to resolve circuit features located around 100µm below the backside surface of the silicon die [24-28]. The details of the prescription used to design the correct s-SIL for imaging at a given surface / sub-surface depth are presented in [21] and were presented earlier in Section 1.5.

Common resolution formulae can be used to calculate the resolution expected from using s-SIL imaging. The usual expression for *NA* applies to SIL imaging and is $NA = n\sin\alpha$ where α is the half-angle of the cone formed inside a material of refractive index *n* by the converging rays at the beam focus. The maximum possible *NA* cannot exceed *n* since this corresponds to the rays of the focused laser beam arriving over a cone half-angle of 90° which is difficult to achieve experimentally. Sparrow's criterion [29] states that the smallest resolvable feature size can be calculated from the expression $0.51\lambda/NA$ under linear imaging. In two-photon SIL imaging this becomes $0.51\lambda/n\sqrt{2}$ since the signal obtained under this nonlinear configuration is sensitive to the intensity squared – if one were to square a Gaussian point spread function (PSF) the resulting full width at half maximum (FWHM) will be smaller than the original by a factor of $\sqrt{2}$. Therefore, Sparrow's criterion in this case implies a diffraction-limited resolution limit of 160nm for imaging in silicon when using a free-space wavelength of 1550nm.

To verify this, a program was written in MATLAB which was designed to model the radial point spread function (PSF), under plane-wave illumination, using an analytical result that is valid for high-*NA* [30] and gives the optical field, $\psi(\eta)$, measured at the observation plane as:

$$\psi(\eta) = 2\int_0^1 A(r)\exp[i\Phi(r)]J_0(\eta r)rdr \qquad (1)$$

where $A(r)$ and $\Phi(r)$ are the amplitude and phase profiles of the light before the pupil of the focusing lens, J_0 is a Bessel function of the first kind and r is the normalised radial coordinate at the pupil plane.

The PSF is calculated at the image plane where the lateral position across the image plane is given by the radial coordinate ρ. For the purposes of calculation a dimensionless radial parameter is used,

$$\eta = \frac{\pi D \rho}{\lambda f} = \frac{2\pi \rho NA}{\lambda} \tag{2}$$

which takes account of the *NA* of the focusing system and the illumination wavelength. This approach is illustrated in Fig. 1.

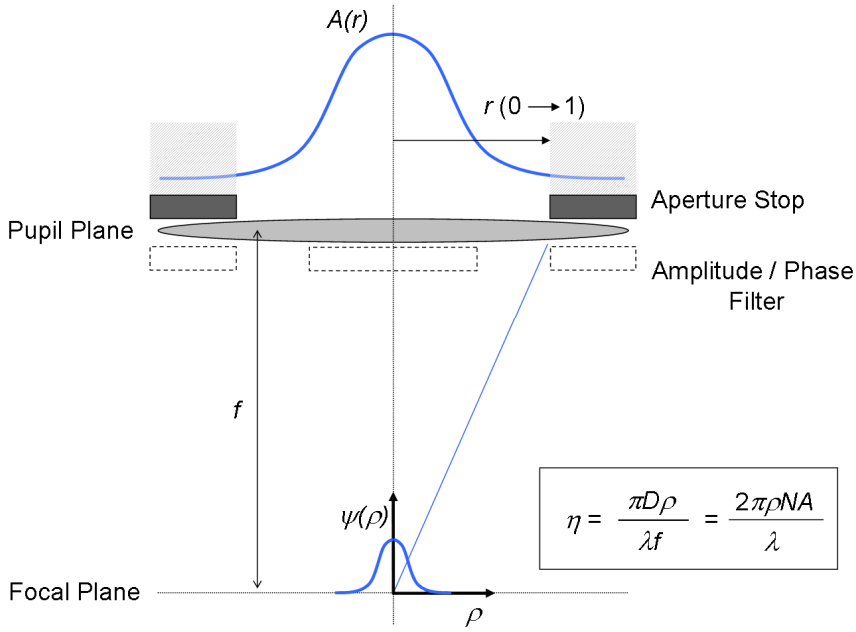

Figure 1 – Illustration of the analytical scalar approach, discussed by Sales and Morris [30], utilised to model both the linear and nonlinear lateral PSFs

A corresponding analytic expression for the axial PSF is given by Sheppard and Hegedus [31] and takes the form:

$$\psi(z) = 2\int_0^1 A(r)\exp\left[\frac{iu(z)r^2}{2}\right]rdr \tag{3}$$

where,

$$u(z) = 4kz\sin^2\left(\frac{\alpha}{2}\right) = \frac{8\pi z}{\lambda}\sin^2\left(\frac{\alpha}{2}\right) \tag{4}$$

Fig. 2 presents plots of the lateral (a) and axial (b) PSF of the light focused inside a silicon sample at *NA* = 3.4 which corresponds to a cone half-angle of 78°. The left side of each plot is the PSF obtained under linear imaging (proportional to $|\psi|^2$) and the right side represents the effective PSF due to two-photon excitation (proportional to $|\psi|^4$).

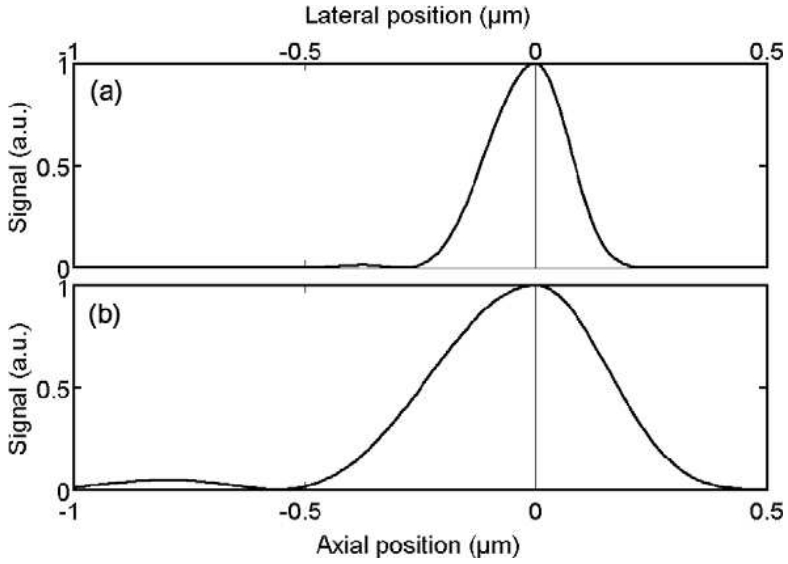

Figure 2 - (a) Lateral and (b) axial point spread functions calculated for linear (left side) and two-photon (right side) excitation imaging under plane-wave illumination, assuming *NA* = 3.4

The models predict diffraction-limited resolutions, under two-photon excitation, of 168nm (lateral) and 350nm (axial). Since there is agreement between the exact lateral resolution calculated by the model and that inferred from Sparrow's criterion this indicates that Sparrow's criterion is a useful expression for predicting the resolution achievable using TOBIC SIL imaging.

I would like to acknowledge Dr Euan Ramsay for his contribution towards preparing the MATLAB code required to present the results given above.

3.3 Spatial Calibration

As well as increasing the *NA* of the imaging system and removing the spherical aberration caused by the index mismatch between the air / silicon interface, a SIL also acts as an 'optical lever'. It is well documented that sample-scanned SIL images (where the SIL rides on top of the sample) are subject to this 'optical lever' effect in which the distance moved by the optical focus inside the sample is smaller than the physical displacement of the sample relative to the illuminating beam [32]. Although this provides some insight into optical control when using a SIL, the standard results from the literature for the lateral and axial scaling factors make the assumption of paraxial rays, but this is clearly not valid under high-*NA* conditions. In order to avoid inappropriate assumptions embedded in the standard analytical results it was decided to analyse the axial and lateral optical lever effect in both h-SIL and s-SIL imaging geometries by using the ray tracing software ASAP (Breault Research Organization) under plane-wave illumination. Fig. 3 illustrates the analytical procedure. A focused beam (initial beam - black rays) is displaced laterally - axial translation was also investigated and will be explained later – on the top surface of a SIL by a physical distance of 500µm (laterally shifted beam - red rays). The 'optical lever' effect within the SIL controls the magnitude of the optical translation of the focal spot which, when using an s-SIL in this case, corresponds to a lateral optical displacement of 41.3µm, shown in Fig. 4. Note here that in Fig. 4 there is also a corresponding vertical shift to the focal spot. This is due to the field curvature and possible off-axis aberrations (i.e. spherical aberration) in the system [24].

In order to be confident that no off-axis aberrations were to distort any experimentally acquired images, a general rule-of-thumb could be to limit the lateral scan of the laser beam above the SIL and sample to $R/2$, where R represents the radius of the SIL. That would define the usable field-of-view for an s-SIL and sample to $(R/2)/n^2$ - or $(R/2)/n$ for an h-SIL. The corresponding field-of-view for a silicon s-SIL of radius of 2mm is ~166µm. This result is further supported by considering the field-of-view of Fig. 13 (introduced later).

The ASAP simulation analysis is given below.

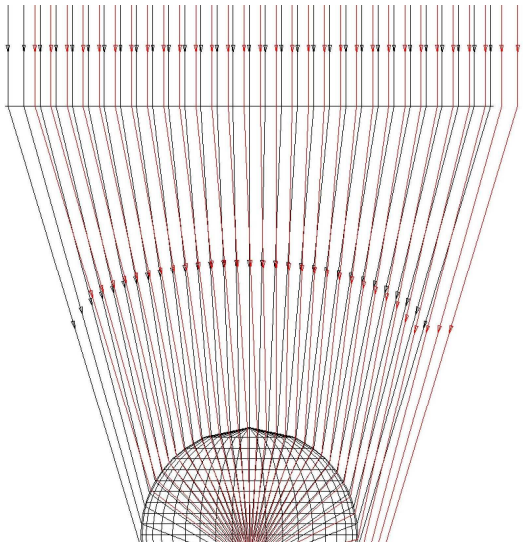

Figure 3 - ASAP image that illustrates the process of the lateral shift of the beam on the top surface of the SIL. The shifted beam (red) has been displaced by 500µm

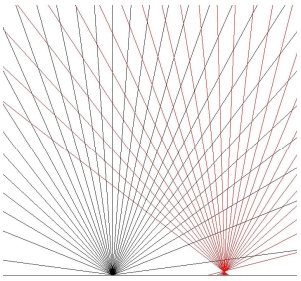

Figure 4 - Magnified imaging at the focal points of the initial and laterally shifted beam within the SIL which are separated by 41.3µm. The small axial shift in the laterally shifted beam is due to the field curvature in the system

Rays focused through both an h-SIL and an s-SIL, which were designed for imaging at 100µm below the surface of a silicon die according to the standard prescription given in the literature [32], were modelled at various lateral displacements of the sample and SIL relative to the illuminating beam. In the model an objective lens with an *NA* = 0.42 was chosen which corresponded to that which was used in the experiment. The optical focus was defined as the region in the sample showing the smallest lateral spread of the ray bundle, and this definition should be consistent with the experimental axial position that yields the highest two-photon signal. A common SIL diameter of 2mm was selected and the refractive index for both the SIL and sample matched that of silicon (3.48). For a given physical displacement of the sample and SIL, the corresponding optical displacement of the focus was given by the model; an example of which is shown in Fig. 5 for a lateral displacement and in Fig. 6 for an axial displacement when imaging through an s-SIL.

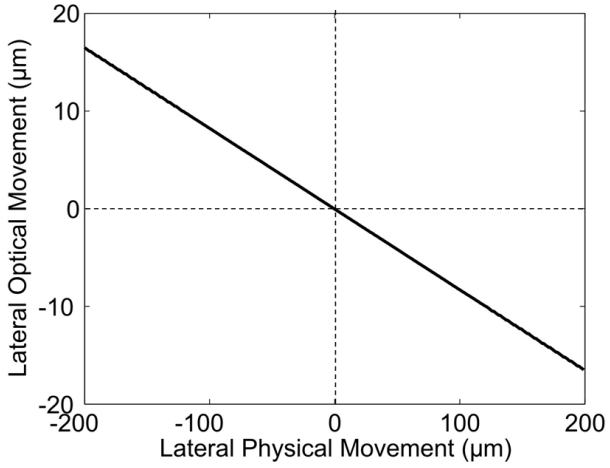

Figure 5 - Lateral physical displacement against lateral optical displacement when imaging using an s-SIL

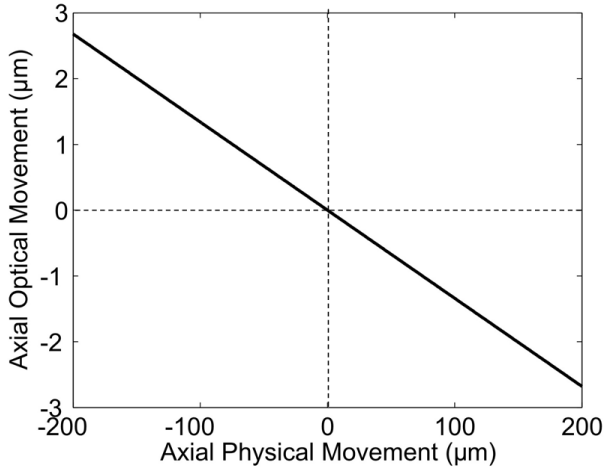

Figure 6 - Axial physical displacement against axial optical displacement when imaging using an s-SIL

By correlating the movement of the focal position with the physical displacement of the sample and SIL we extracted a scaling factor for a range of different values of sample and SIL refractive index. The logarithmic plots in Fig. 7 and Fig. 8 represent the lateral and axial scaling factors for an s-SIL and an h-SIL respectively as a function of the refractive index of the SIL. The circular symbols indicate the s-SIL, and the square symbols indicate the h-SIL**.** For sub-surface imaging (s-SIL geometry) the index of the SIL and the medium are chosen to be equal. Dealing first with the lateral behaviour, the slope of the s-SIL logarithmic plot in Fig. 7 is exactly 2, which confirms the n^2 lateral scaling factor obtained from the literature for the s-SIL, and the slope of the h-SIL plot is exactly 1, which indicates and confirms the scaling factor of n. Therefore,

in both cases this behaviour is consistent with analytic results predicted by paraxial theory [33].

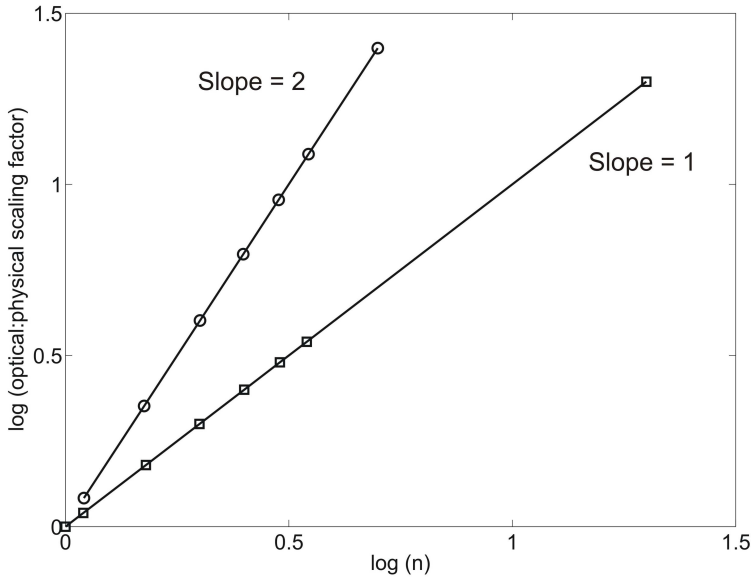

Figure 7 - Plot showing the logarithm of the optical / physical scaling factor against the logarithm of h- and s-SIL refractive indices for lateral motion. The circular symbols indicate the s-SIL, and the square symbols indicate the h-SIL. The slope of the fitted line for the h-SIL is 1, indicating that the movement of the focal spot is a factor of *n* smaller than the physical movement of the sample, whereas the slope of the fitted line for the s-SIL is 2, indicating that the movement of the focal spot is a factor of n^2 smaller than the physical movement of the sample

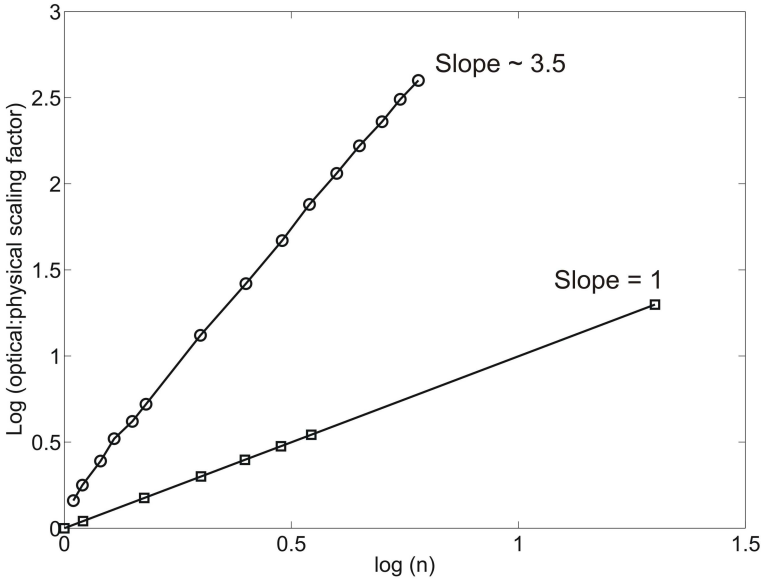

Figure 8 – As for Fig. 9 except that the slope of the fitted line for the h-SIL is 1, indicating that the movement of the focal spot is a factor of *n* smaller than the physical movement of the sample, whereas the data for the s-SIL deviates slightly from the expected linear trend

In the literature [21, 32], the axial scaling factor of an s-SIL is stated as n^3. The results of our model show a non-uniform scaling factor in *n*, and for our particular refractive index (n=3.5) the scaling factor is calculated to be ~75 (approximately $n^{3.5}$), whereas n^3 would imply a factor of 42. The behaviour of a hemispherical solid immersion lens (h-SIL) in the axial direction shows a scaling factor of *n*, although for high refractive indices, even this ceases to be exact. The difference between our axial scaling factor and that quoted in the literature for a s-SIL is due to the fact that the n^3 factor only applies to paraxial rays [34]. In our model, we assume that the light is focused at the point where the bundle of rays propagating through the system has the smallest width, which leads to a non-uniform scaling factor. This method was chosen because the smallest spot size is where the most efficient two-photon absorption occurs. In our simulations, a factor of n^3 (~42) was obtained by propagating only the paraxial rays in the system and looking for the point where those rays cross the optical axis of the objective lens, whereas a factor of 161 was obtained by propagating only the extreme rays. The optical: physical scaling factor of around 75 was used to interpret subsequent experimental results demonstrated in this chapter which used axial scanning to acquire a sub-surface depth-resolved image of the circuit.

I would like to acknowledge Dr Martin Thomson for preparing the ASAP code required to present the results given above.

3.4 The Silicon Flip-Chip

The silicon IC under investigation throughout this volume of work was a 0.35µm feature size silicon flip-chip which was generously provided by Credence Systems, CA, USA (previously known as Schlumberger Test and Transaction). The device has a $1cm^2$ exposed silicon substrate which had been chemically thinned and polished to a thickness of 100µm. The quoted thickness was measured and confirmed using a confocal microscope which is outlined in the next section. The chip contained a standard test circuit which would be used in a commercial application. The images presented throughout this work are believed to be an area which contains a form of proprietary electrostatic protection device at the input to an inverter chain. The TOBIC signal which was recorded from the device was acquired from the photocurrent flowing between the input of the device and ground [35]. The chip remained unpowered throughout the acquisition of the experimental images and a wide bandwidth amplifier with low output impedance was connected immediately after the chip's output pin in

order to improve the time-response of the detection circuit and enable rapidly varying signals to be measured. Since we only had information on the pins which were associated to a certain location on the chip, it was only possible to probe that particular vicinity, which had a detectable footprint of approximately 400µm^2.

Fig. 9 illustrates a series of computer generated schematics which highlight a 150µm^2 area in which a photocurrent image could be obtained and investigated. It draws attention to several interesting features which span a significant lateral region on the chip. These features occupy multiple axial levels as well which provides a third dimension in which to interrogate. This can be seen in Fig. 10 which shows a cross-sectional scanning electron micrograph of a particular location on the chip.

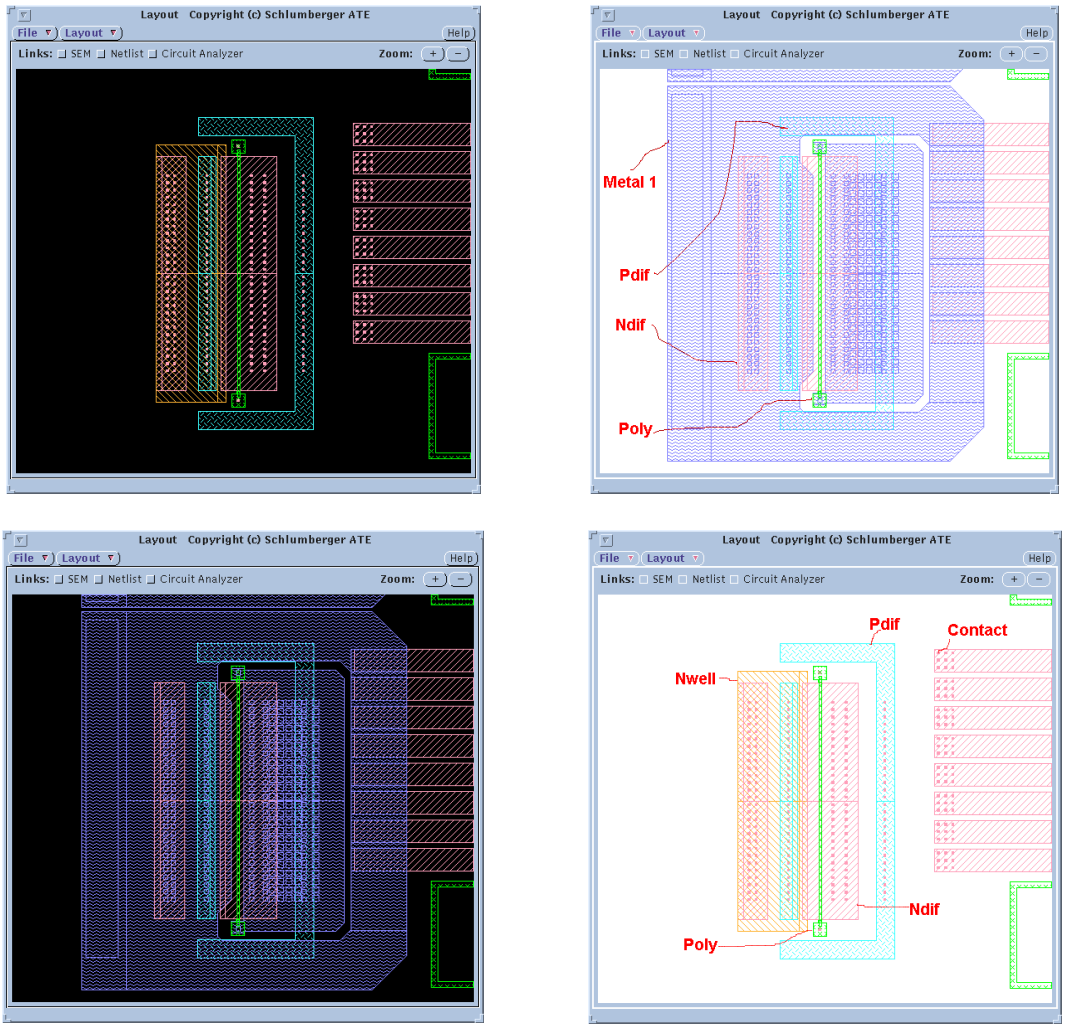

Figure 9 - Computer generated schematics of the probing area under investigation on the silicon flip-chip

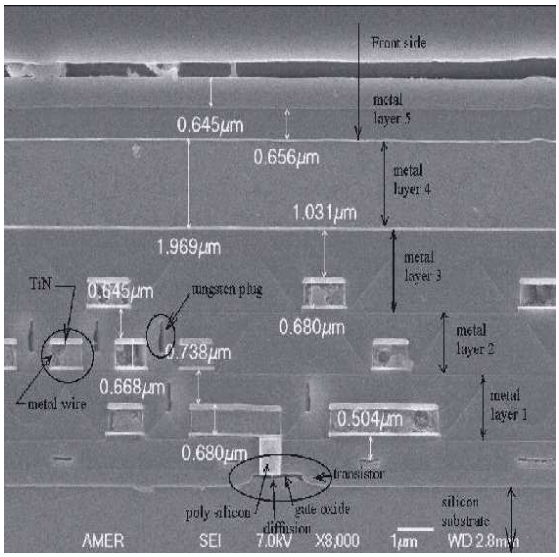

Figure 10 - Computer generated cross-sectional schematic of the probing area under investigation on the silicon flip-chip

The information pack that accompanied the device contained a description on how to pinpoint the exact probing point in which to examine. The instructions stated that there was a corner on the chip's silicon substrate that was marked and that one should investigate along the edge of the device from that position until the correct probe point was found. In order to achieve this, the sample, which was mounted in a three-axis translation stage, was raster scanned laterally and axially across the recommended probe volume until a photocurrent signal was measured on an oscilloscope. A detailed description regarding the acquisition of the probe point is discussed in Section 3.6.

There are several methods to obtain the probe point on the chip both with and without the SIL in place. The simplest idea is to use an infra-red camera to image through the silicon substrate then search for the features that are illustrated on the device schematics by eye. This approach may well work however it ignores all aspects of the photocurrent generating properties required which will ultimately provide an image. A second, and more robust, method is to make use of a frequency-doubled Nd:YAG laser pointer. This can be aligned into the system so that it follows a path which is collinear with the probe beam. The benefit of this scheme is that it conveniently increases the visibility of the beam within the system which aids alignment. Also, since this pilot beam is the output from a doubled near-IR (1064nm) source, one can profit from the leakage of this fundamental wavelength since it will penetrate the silicon substrate and provide a source of single photon absorption to a considerable depth. Due to the fact that this is a linear process there will be no focal dependence throughout the penetrated

volume, therefore removing the use of the objective lens for the time being and allowing for a large stimulated region to be examined. Once the signal is discovered, the final process is to simply introduce the objective lens, performing one last lateral scan for optimisation, then reposition the sample axially to bring the device into focus.

3.5 Solid Immersion Lens Design

The historical details and theoretical analysis associated with the solid immersion lens are discussed in Chapter 1.5.

When one wishes to exploit the use of a SIL great care must be taken during its design and implementation stages in order to achieve the desired level of performance. The SIL is a critical component in an imaging system since it dictates the precise location at which the incident optical beam will come to a focus within the sample under study. For this reason the SIL used in this work was designed carefully in order to calculate the exact depth at which a silicon sphere must be cut during fabrication. In order to determine this, one must refer to equation (20) (discussed in Chapter 1, Section 1.4.2.2) and consider the radius of the original sphere, the refractive index of the sample and the depth at which the device layer is buried within the silicon substrate since all of these parameters are required.

The refractive index of silicon at a wavelength of 1.53µm is relatively simple to calculate and was done so by modelling the Sellmeier equation [36] for silicon out to the wavelength of interest. This was performed in MATLAB and confirmed a refractive index of approximately 3.48. The resulting Sellmeier curve for silicon is illustrated in Fig. 11.

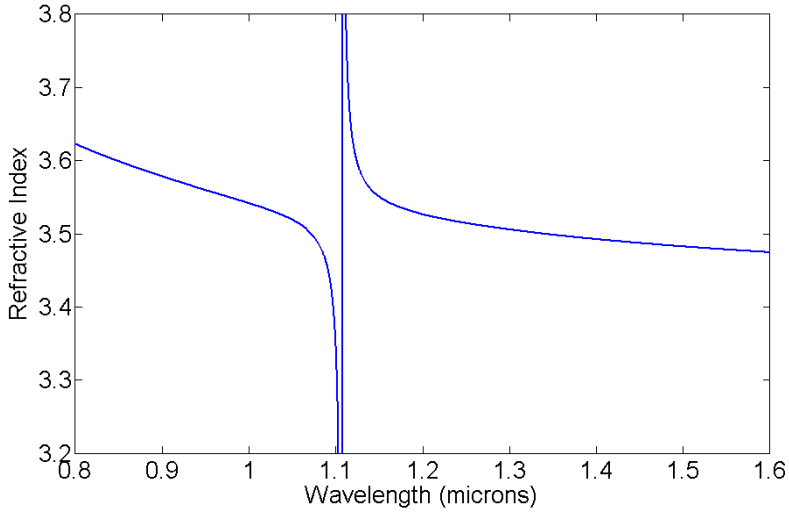

Figure 11 – Sellmeier curve for silicon used to calculate the refractive index at 1.55µm

The depth at which the device layer is buried below the silicon substrate was known to be 100µm [37]; however, this was confirmed by imaging the top surface of the silicon substrate using a mid-IR confocal microscope (which had been configured into our TOBIC microscope for this purpose), translating the sample in the axial direction in order to start imaging through the silicon substrate, and then noting the total translation distance once the device layer came to a perfect focus. The total axial distance traversed came to 30µm. Please note here that this distance represents the *optical* distance that the sample must be displaced, and not the *physical* distance that must be covered. The physical distance, in the paraxial regime, is generally known to be the optical path length multiplied by the index of refraction. Therefore, this corresponds to a circuit depth of 100µm; however, since the objective lens used in this work was of significant *NA* (*NA*=0.42), our system is removed from the paraxial regime and results in a relatively large negative contribution through spherical aberration due to the refractive index mismatch. This does not hinder our approach though since the high-*NA* rays were calculated to only come to a focus an additional 25µm into the silicon substrate. Therefore, for the calculations in the SIL design, the depth at which the device layer is buried below the silicon substrate was chosen to be 100µm.

When designing a SIL, there are basically only two critical issues with regards to end product usability which must be considered before committing to its final size, since technically a SIL design is only dependent on the distance at which the features of interest are located below its surrounding media. This is an outcome from equation

(20) – please refer to Chapter 1, Section 1.4.2.2. The first consideration is whether the SIL will be able to fit between the objective lens and the sample or not. The second consideration is whether the size of the SIL will create difficulty when being used in an experimental arrangement. These two issues create a trade-off between how big and how small a SIL can be within a working system. Clever experimental configurations can be adopted in, for example, the semiconductor industry where the silicon substrate of a chip is lithographically etched away to leave the required embossed SIL top-surface geometry [38], equivalent Fresnel lens [39] or diffractive SIL [40, 41] exposed exactly above the imaging area of interest - as an aside, it has also been known in microfluidic systems for a SIL to be free-floating in a liquid and aligned using laser optical tweezers [42]; however, this fabrication consideration can only be executed during the design stages of the chip itself and requires access to advanced facilities. Therefore, by taking the above points into consideration, the radius of curvature of the SIL was chosen to be 2mm in order to permit delicate SIL manipulation yet flexibility and ease of implementation by hand.

One final aspect of the SIL, when it comes to actually using it, is the ability to position it in the correct location on the sample under investigation. Failure to do so will result in a heavily abberated / distorted final image or, in the worst case scenario, result in the acquisition of no image at all. This condition becomes even more critical when one considers the nonlinear nature of the TOBIC imaging system used in this work. Since two-photon absorption is intensity dependent, the location of the focus plays a key role in the acquisition of a signal from the sample. In the linear regime this situation is considerably simpler since even a sample which is out of focus will generate a little signal, allowing the user to improve on this initial level of detection by scanning around the focal volume in three dimensions in an attempt to locate a peak in the available signal level.

3.6 Data Acquisition

It was critical that one positioned the SIL on the chip's silicon substrate in the exact location in order to generate the maximum photocurrent for acqusition. This was achieved by initially locating the position on the chip which generated the maximum two-photon signal level without the SIL actually being in place. In order to obtain this the sample was raster scanned around the vicinity that had been marked on the device surface in the xz-plane, with equal lateral translations in the y-direction after each plane

had been interrogated, until a signal was detected and then peaked up on. Having completed that stage, the next step was to position the SIL accordingly. This required a considerable translation of the sample in the axial direction towards the objective lens before the SIL could be positioned because the SIL provides an improvement in the system's magnification. Hence, the positioning of the SIL in the vicinity of a non-SIL maximum signal level location would significantly alter the focusing conditions of the system and therefore eradicate the original signal level. To avoid this, one must calculate the axial displacement required to return the focal spot back to the device layer of the chip by revisiting the design geometry of the SIL. It was calculated that a displacement of 6.3mm towards the objective lens was necessary. Once the sample had been elevated to this point then the SIL could be positioned immediately below the focused beam, with the apex of the SIL aligned to the optical axis of the microscope, through the use of carbon-tipped tweezers. The SIL then had to be delicately manoeuvred into the exact position which produced the collection of the largest TOBIC signal. Although this procedure was extremely sensitive and required a great deal of patience, it was fit for purpose and generally only consumed a small amount of time to complete.

With the SIL in the correct position, initial experiments were performed which concentrated on acquiring high-resolution 2D images of the silicon chip. This involved laterally scanning the sample and SIL in a raster fashion under the incident laser beam in order to map out and collect the photocurrent detected over a 2D area. The sample was mounted in a custom built aluminium plate which housed the chip in a three-axis translation stage. Each axis contained a fully automated stepper motor (Newport NewStep actuator) which provided computer control over the mechanical movements of the three-axis stage. These actuators offered a total physical scanning range of 10mm, which, according to the optical lever effect described in Section 3.3 above, results in a total optical scanning range of ~800µm. The minimum scanning pitch was quoted at 100nm, which corresponds to an optical stepping precision of ~8.3nm. These high precision stepper motors were a valuable tool in the acquisition process.

Computer control of the actuators was performed using the Agilent VEE programming environment. The code was configured to laterally raster scan the actuators over a 2D area using a point-by-point translation sequence. The photocurrent generated at each pixel location was collected and visualised using a Tektronix TDS210 digital

oscilloscope and then sent to a personal computer (PC) through an 8-bit electrical bus (General Purpose Interface Bus - GPIB). The PC controlled the three-axis translation stage through an RS232 serial port connection.

The data were collected as a continuous string and stored in the PCs memory until the full 2D area was mapped out. The total length of the string was equal to the total number of pixels that comprised an image since each pixel generated a two-photon photocurrent which was recorded and saved. For example, an image that consisted of 500 pixels by 500 pixels would have a string length containing 250000 elements. The image processing was carried out in the MATLAB programming environment which made it easy to manage data sets which were essentially matrices. The data were saved as an ASCII file which was loaded into MATLAB, reshaped into a 2D area (depending on the shape of the desired probe area), and then calibrated into the appropriate dimensions. Once the 2D matrix was constructed and calibrated the image was visualised as a pseudo-colour plot. This could be amended later using a suitable colourmap to obtain the best quality image for visualisation.

3.7 Experimental Configuration

Observable two-photon absorption requires femtosecond laser illumination at a wavelength longer than the band-edge of silicon. The band-edge of silicon is ~1.05µm and therefore a femtosecond stretched-pulse erbium-doped fibre laser, operating at 1.55µm, was used to image the 0.35µm feature size silicon flip-chip. The laser produced pulses of approximately 160fs duration at a repetition rate of around 32MHz. The average optical power at the sample was measured to be 5mW. The laser used in this work can be readily constructed from standard telecommunication components and its design is described in Chapter 2.3. and [43]. The semiconductor flip-chip which was imaged had a polished silicon substrate that was 100µm thick and the SIL, which was designed to image at this depth, was placed on the backside of the substrate and used in combination with a 0.42*NA* (magnification - x50, corrected for chromatic aberration from 0.48µm to 1.8µm) objective lens. The incident Gaussian laser beam emanating from the output of the erbium-fibre laser was naturally divergent, therefore, in order to overfill the 6mm diameter pupil of the objective lens, the beam was allowed to diverge until a suitable full width at half maximum (FWHM) beam waist value was obtained. A knife-edge beam profiling investigation was completed at several locations after the laser output and a final FWHM value of 6.3mm was accepted as a suitable

beam diameter to overfill the objective lens input pupil (3.3mm diameter). At this location a collimating lens, which had a focal length matching the distance covered from the output coupler of the fibre laser to the position where the 6.3mm FWHM value was recorded, was inserted. Beam steering was controlled by kinematic mirror mounts which contained gold mirrors for maximum reflectivity of the 1.55µm erbium-fibre laser output; however, one gold mirror was replaced with a dichroic mirror in order to enhance the usability of the microscope since a green pilot beam can be introduced to improve visualisation of the beam steering and alignment (described previously in Section 3.4). After the objective lens the beam overfilled the SIL, and a simple ray tracing analysis implied a maximum usable *NA* of 3.4, corresponding to the value taken in the model of the PSF discussed in Section 3.2. The sample and SIL were scanned using Newport NewStep stepper motors with a minimum physical step of 100nm. This corresponded to a lateral optical step of ~8.3nm through the optical lever effect. The two-photon photocurrent was detected using a Tektronix TDS210 digital oscilloscope, and a desktop PC was used to control the scanning and to visualise the data. The experimental configuration is illustrated in Fig. 12.

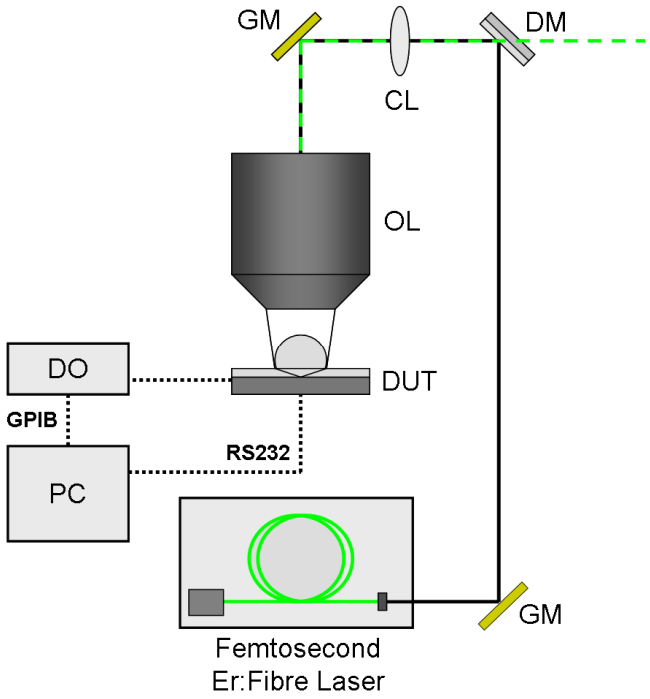

Figure 12 – Sample-scanning TOBIC microscope. The device under test was positioned on XYZ scanning stages. GM – gold mirror, DM – dichroic mirror, CL – collimating lens, OL – objective lens, DUT – device under test, DO – digital oscilloscope

3.8 Ultra-High-Resolution Two-Dimensional (2D) Imaging

The device was imaged initially using a relatively coarse optical stepping pitch of 800nm in order to generate a map suitable for navigation purposes, shown in Fig. 13. An investigation into locating the exact focal position had to be carried out beforehand. It was possible to alter the contrast in each image generated by simply amending the focal position of the illuminating beam within the silicon substrate. This involved the axial translation of the device either towards or away from the objective lens. This proved to be a fascinating property since the differing contrast observed from image to image, observed over a small axial translations, confirms the possibility of acquiring a 3D image using a TOBIC microscope [44, 45]. This is discussed and verified in detail in Section 3.11.

Fig. 13 is approximately 120µm by 120µm and required a total run-time of 15 hours to acquire. This duration proved to be excessive and created a total operating time issue which is addressed in Chapter 4; however, it also demonstrates the stability of the erbium-doped fibre laser source. There are no degrading or random fluctuations of contrast to be found throughout the image at all.

In order to perform ultra-high-resolution imaging of the device a suitable feature had to be selected which was both interesting and challenging to acquire. After an extensive visual interrogation of the coarsely scanned image, an area that contained a particularly appealing structure which would satisfy the criteria imposed was identified and is highlighted by the red circle in Fig. 13. A review of the computer generated schematics provided by Credence Systems was required and it was found that the area contained a 3×3 matrix of tungsten vias, at separations of ~1.25µm, which were grown on an n-doped silicon “finger”. This region, shown in Fig. 14 below, was ideal for ultra-high resolution imaging since it covered an area which is less than $10\mu m^2$ and contained a significant level of detail.

Figure 13 - Medium resolution TOBIC image of the device in the lateral plane. The red circle highlights the matrix of tungsten vias, located at the end of a metal "finger", where ultra-high-resolution imaging was investigated

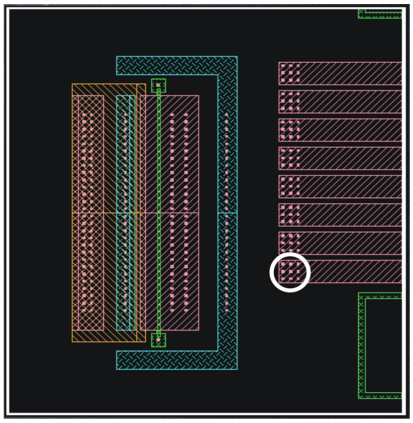

Figure 14 - Computer generated device schematic which maps the various positions occupied by tungsten vias and reconfirms that the area of interest is suitable for ultra-high-resolution imaging

Since the initial image map was acquired using a relatively large optical scanning pitch, in order to obtain an ultra-high-resolution image of the 3×3 matrix of tungsten vias the optical scanning pitch had to be reduced to the smallest available option (100nm physical, ~8.3nm optical) and the inspected area had to be significantly reduced as well. A total scanning area of approximately 32µm^2 was mapped out and the resulting 2D ultra-high-resolution TOBIC image is shown in Fig. 15.

Since the 3×3 matrix of tungsten vias were three-dimensional, it was possible to adjust the location of the focal spot within the structure which would either suppress or

enhance the contrast between the peaks and troughs of the tungsten vias. The best image contrast was obtained when the focus was positioned at the mid-point between the peaks and the troughs. Fig. 15 was acquired and visualised using an identical procedure to that used to obtain the coarse map image which was explained previously.

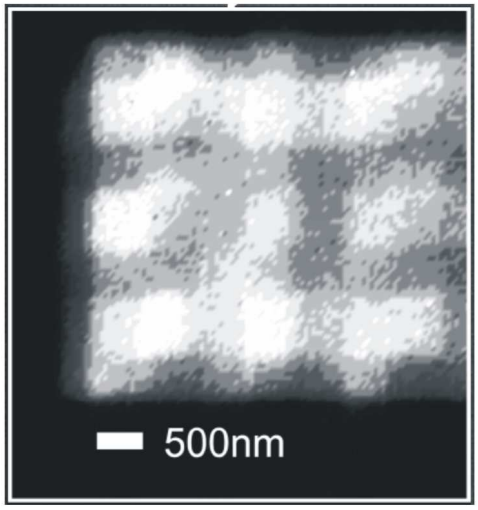

Figure 15 - Ultra-high-resolution TOBIC image of a matrix of tungsten vias on an n-doped silicon "finger"

3.9 Resolution Measurement

The ability to determine the resolution of an optical microscope is a key requirement and one which plays an important role in the evaluation of the capabilities of a microscope. The standard procedure used to evaluate this is to try and resolve structures written onto a resolution target. This target acts as a control sample that contains a set of precise features that have dimensions significantly smaller than the resolution of the microscope. A typical example of a resolution target is the USAF standard resolution target [46]. The resolution of the microscope is defined from the minimum resolvable feature, of known accuracy, on the target. This can be a successful procedure in determining the resolution of a microscope; however no such target existed for the TOBIC microscope use throughout this work. Therefore, the performance of the system had to be assessed using structures fabricated on the device itself.

The adopted procedure echoed work performed by Ippolito *et al* [21] which essentially involved scanning the focused spot over the edge of a particular feature located on the

device. It is because of this approach that the "finger" structure imaged in Fig. 13 and Fig. 15 above, was of particular interest.

In order to ensure that the resolution value obtained from a given line-scan across a feature edge corresponded to the true resolution limit of the TOBIC system, a series of results were recorded consisting of three laterally displaced line-scans which traversed a number of consecutive finger-gap-finger elements and covered an axial range extending throughout the optical focus of the microscope. The lateral displacement of each line-scan was ~5µm (physical). Once the sharpest feature edge was located from the data set, a position which corresponds to the feature being in the focal plane of the incident beam, then a resolution measurement could be taken and evaluated.

The procedure implemented by Ippolito is simple but one which must be reviewed to understand how the resolution of a microscope can be inferred from this technique. The reason that the resolution can be measured is due to the variation in the optical signal as the finite width of the laser beam travels across a semiconductor / metal interface. If the optical signal is high when the beam is focused into the semiconductor, when it moves across the interface towards the metal region the signal level will gradually drop to a lower value. This can be visualised in Fig. 16 (a) and (b) below.

Initially, the incident beam is focused into the semiconductor. This generates a large TOBIC signal since the entire beam contributes to the measured signal – this is represented in Fig. 16 (a) as the blue area under the Gaussian curve. When that particular situation is compared against that shown in Fig. 16 (b) it is clear to see that when the beam is focused at a semiconductor / metal interface the signal will start to fall since a smaller portion of the incident beam contributes to the generated TOBIC signal.

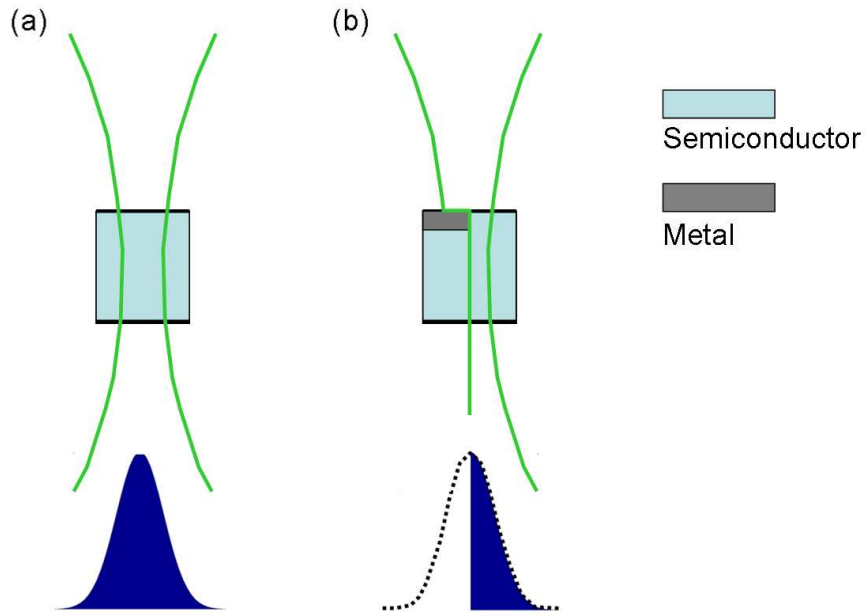

Figure 16 - (a) Focusing in a semiconductor, (b) focusing at a metal / semiconductor interface

The intensity of the TOBIC signal can be expressed as a function of the spatial characteristics of the focused beam. Here, $I(r)$ is the intensity of the beam at a particular radial position. Typically, $I(r)$ is defined as a Gaussian distribution, therefore, if there exists an infinitely sharp interface transition between the semiconductor and the metal regions, then the signal level *S* recorded can be defined as:

$$S = \int_{r=edge}^{r=\infty} I(r)dr \tag{4}$$

The resolution of the microscope can be calculated from the form of the curve that is generated as the focused beam is translated across the interface. This curve has a non-analytic shape but can be described as the integral of a Gaussian function. This can be understood in mathematical term where the curve takes the form $f(x)$ where *x* is the distance traversed and $f(x)$ is the photocurrent obtained. It can then be stated that:

$$f(x) \propto \int \exp(ax^2)dx \tag{5}$$

The previously acquired experimental line-scan series was revisited and the scan displaying the sharpest transition across a finger-gap intersection was chosen to infer a lateral resolution measurement for the 2D results. The experimental data points are separated by optical intervals of ~8.3nm and are plotted together in Fig. 17. A resolution value could be calculated from the data by fitting the numerical integral of a Gaussian PSF to it by using a multi-dimensional least-squares minimisation algorithm that simultaneously optimised the width of the point spread function distribution and its centre position. The theoretical Gaussian generated in Fig. 17 matches the trend of the experimental data to a high degree and is therefore a suitable function to use in calculating the FWHM focal spot size of the system.

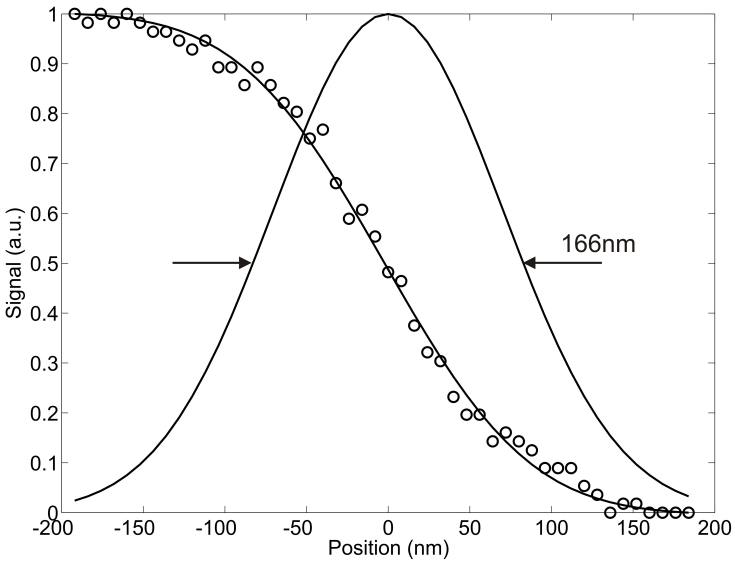

Figure 17 – Lateral resolution measurement across the edge of the "finger" shown in Fig. 13 (above) generating 166nm resolution. The solid fitting line is the integral of the Gaussian PSF shown in the figure

The resolution value calculated from this fit was 166nm and is comparable to the theoretically predicted diffraction-limited resolution value of 168nm described in Section 3.2 earlier in this chapter. In subsequent experiments we have found it straightforward to repeatably obtain very similar resolutions at widely separated points across the sample. At this resolution it was possible to clearly resolve individual features which we believe are tungsten vias arranged in a 3×3 grid at separations of 1.25µm.

3.10 Cubic Interpolation for Three-Dimensional (3D) Profiling

During the investigation into ultra-high-resolution 2D imaging of a 3 × 3 matrix of tungsten vias on n-doped silicon described above, the chosen imaging area and subsequent alterations in image contrast through small axial displacements of the focal spot during the optimisation stage suggested the possibility to obtain a 3D plot. In order to obtain a 3D image the system would have to contain a reliable and repeatable mechanism for precise axial translation. This was already in place through the use of a Newport NewStep actuator in the vertical translation arm of the three-axis translation stage which housed the device under test. All three actuators had identical pitch and total available scanning range.

The process used to acquire a 3D image was similar to that used in confocal microscopy [2] to locate the heights of structures which relies on the technique of peak-detection to be exploited. It was similar to the data collection method used to obtain the 2D image explained previously but instead of initially scanning the axial range to obtain the exact focal position of the incident beam, a series of 2D images were acquired and stacked together in the vertical direction as the beam interrogated a chosen 2D area while the sample was translated through the focal spot in small axial steps.

The generated data-cube was loaded into MATLAB as before but processed in a different manner. The photocurrents generated over the entire axial range at each identical XY pixel on the stacked 2D images were isolated and plotted together. A cubic curve was then fitted to this data – a cubic fitting was chosen since it was the lowest order of polynomial which would display a good fit to the data. From this trace a peak photocurrent depth could be obtained and used as the corresponding 3D voxel for that particular column of pixel points from the 3D data cube. This process was then repeated over every identical XY pixel / axial column position throughout the experimental data-cube and is illustrated in Fig. 18 below. The theoretical understanding behind this ability to map out 3D structures in a silicon chip emanates from the fact that the maximum signal level generated will be found when the focal spot is located exactly in the centre of a p-n junction. It is then possible to produce a map of the data-cube's 'photocurrent maxima' in three-dimensions.

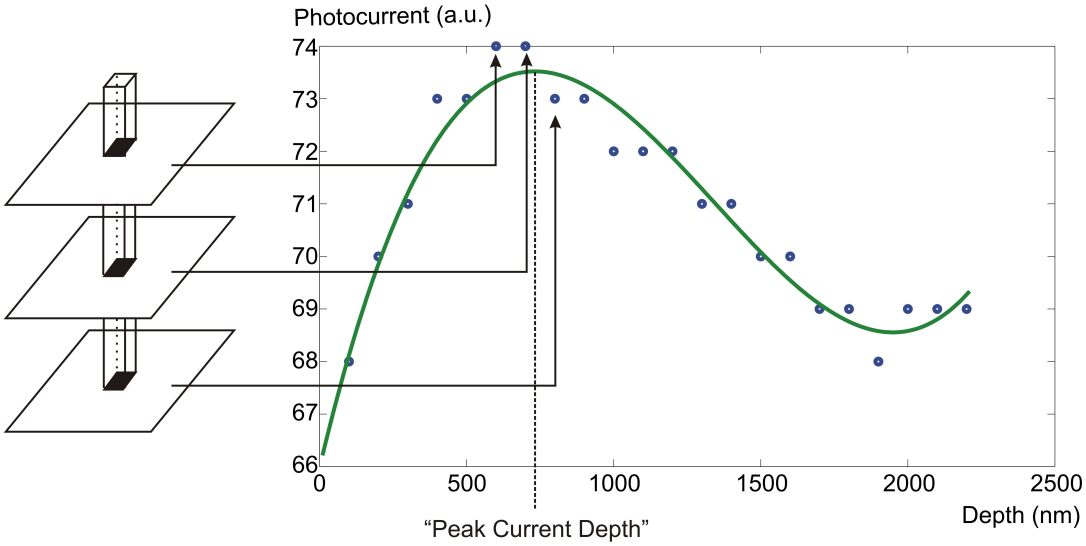

Figure 18 - The peak detection algorithm used to generate 3D images. The axial data column for each XY pixel is plotted and a cubic polynomial interpolated performed in order to obtain the 'peak current depth' for the resulting 3D voxel photocurrent value

3.11 Extension to Nanometric 3D Imaging

Using the peak detection procedure described above it is possible to exploit the focal dependence of the two-photon signal to acquire depth-resolved images that reveal the axial extent of subsurface circuit features [44, 45]. 3D profiling was performed by acquiring a set of 2D images, each one recorded at a different axial position of the sample. In the resulting data-cube, the peak detection algorithm, described in Section 3.10, was then used to find the axial position corresponding to the maximum TOBIC signal at each lateral position in the XY-plane. Since the location of the 2D imaging was already convenient for 3D imaging we profiled the area of the device containing the 3×3 grid of vias with the aim of determining their axial extent, shown in Fig. 19. Fig. 20 shows cross-sections through these data in the X and Y directions of Fig. 19. The axial and lateral scales were calibrated using the results of the ray-tracing model described earlier in Section 3.3. The results indicate that the contacts have an axial extent of ~160nm, based on the difference in the maximum photocurrent measured when the beam is focused either on or between the contacts. The contacts' absolute peak, as inferred from the cross-sectional data (Fig. 20), is consistent to ±60nm. The axial PSF calculation presented in Fig. 2(b) earlier indicates an optimal resolution of 350nm under nonlinear imaging, and experimentally we show approximate profiling resolutions of ~100nm. We note here however that the 3D image generated is not an exact physical representation of the chip's internal topology but is a 3D map of the

maximum photocurrent acquired over a 2D area as the focal volume of the incident beam was traversed.

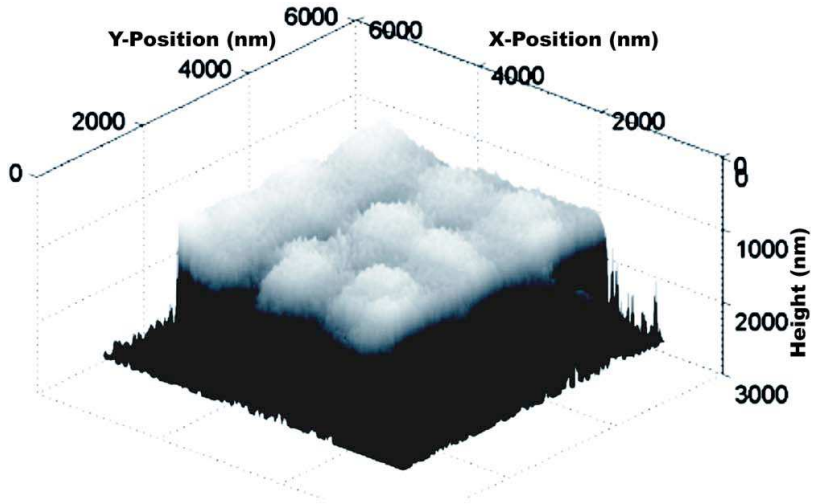

Figure 19 – Three dimensional TOBIC profile of the matrix of tungsten vias on n-doped silicon. The physical lateral separation between bumps is 1.25µm

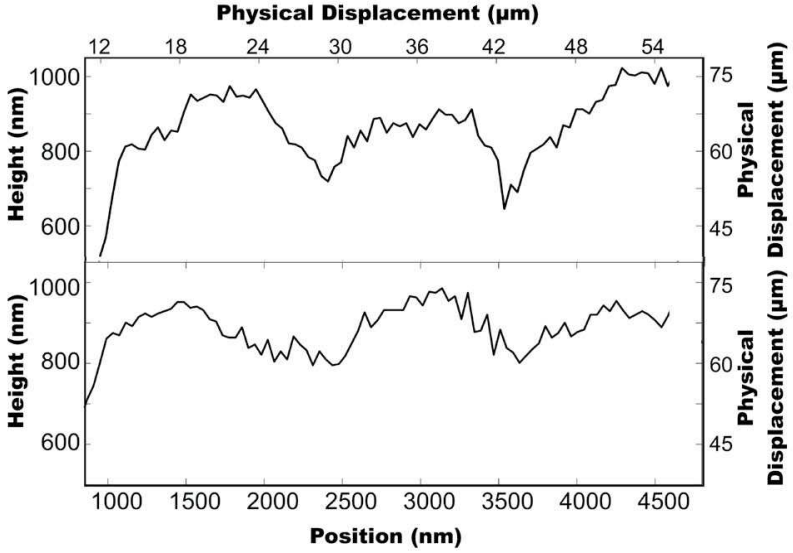

Figure 20 - Cross-sections of the central three contacts shown in Fig. 19

In a separate profiling experiment an image of a different section on the chip, illustrated in Fig. 21, was obtained and investigated. This location corresponded to one end of a poly-silicon wire and the photocurrent image obtained earlier (Fig. 13) suggests that it shows a region which generates a low TOBIC signal. The depth-resolved image, Fig. 22, appears to reveal the presence of a 'hole' in the centre of the feature, while the

surrounding region is uniform in height to around 100nm. The described 'hole' is an area which generated no photocurrent at all and therefore suggests an area that has either been damaged or is the site of a fabrication defect which would ultimately hinder the performance of the device when under test conditions.

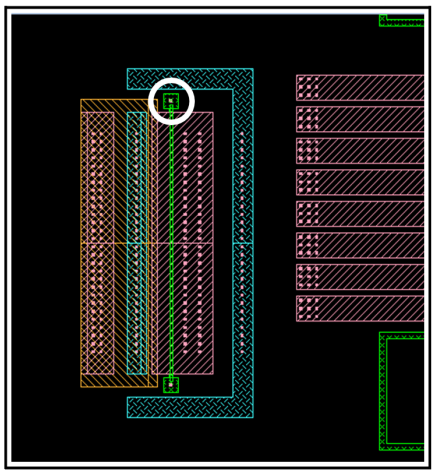

Figure 21 - Computer generated device schematic which highlights the area under investigation during an additional profiling experiment.

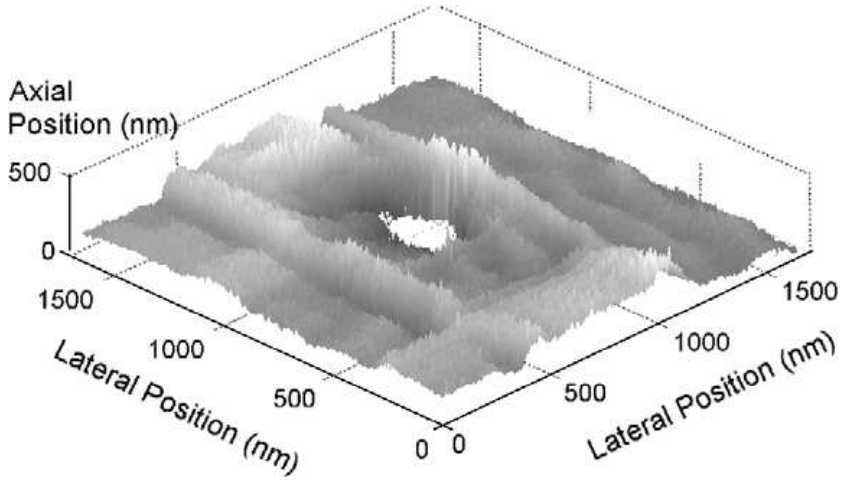

Figure 22 - Depth-resolved image of one end of a poly-silicon wire showing an apparent hole in the centre of the feature.

3.12 Comparison to Theory - Resolution

The experimentally obtained value of 166nm agrees well with the theoretically predicted value of 168nm from the model described in Section 3.2 above. The ability to obtain diffraction-limited performance from the system described in this work is due

to the fact that the motorised axial axis of the three-axis translation stage, in which the silicon sample is housed, provides systematic control of the incident laser beam focal position. This therefore creates an improved ability to localise the focus of the beam in the component layer of the chip. In previous work by Ramsay *et al* [2], this automated focusing ability was not available and resulted in a lateral resolution value of 325nm – approximately double the lateral resolution obtained here.

Another advantage to this system in terms of resolution is its nonlinear imaging characteristics. Since the TOBIC signal generated from the chip is dependent on the square of the incident intensity at the focal volume of the beam, there is a natural reduction of the PSF by a factor of $\sqrt{2}$ - if a Gaussian distribution is squared (i.e. the focal PSF) then the resulting FWHM is narrower by a factor of $\sqrt{2}$.

We have no independent measurement of the axial point spread function, yet the formulae for the lateral and axial point spread functions share the same theoretical basis so we can be confident that the theoretically calculated axial resolution of 350nm is close to that which would be observed experimentally; however, the experimental axial resolution obtained appears to exceed the theoretical diffraction-limited performance. This can be explained by the fact that it is well known that peak detection strategies can allow features much smaller than the axial resolution to be profiled. This result indicates that the contacts had a height of ~160nm. The absolute contact heights, as inferred from the cross-sectional data are consistent to ± 60nm.

3.13 Discussion

Sub-100nm feature sizes are now routine in silicon IC fabrication, and consequently the industry has identified a need for non-destructive wafer / mask level microscopy for measuring the critical dimensions of 3D structures and for defect detection. The ability to resolve the ever reducing feature sizes that are currently being produced on state-of-the-art silicon chips in the lateral plane are of great benefit to the semiconductor industry. The capability of profiling these chips in 3D provides IC test and measurement engineers with an additional degree of freedom when it comes to analysing and navigating the increasingly complex axial structure within a device. A standard contemporary chip contains approximately 5-10 interconnecting layers which exhibit inter-layer separations of sub-µm. Backside imaging through the silicon substrate is typically very poor for longitudinal interrogation since the confocal depth is

approximately equal to the reciprocal of the square of the numerical aperture [47]. This is an extremely important consideration when it comes to profiling silicon IC since out of focus layers will degrade the quality of the resulting image and reduce visibility. Therefore, the results discussed in this chapter with regards to the ability to acquire a topographic representation of a selected circuit volume can play an important role in optical probing and inspection analysis techniques.

The work presented in this chapter addresses this requirement by demonstrating ultra-high-resolution optical imaging of a silicon IC in both two and three dimensions through the use of a silicon s-SIL and the TOBIC effect [48, 49]. This technique shows promise for resolving sub-surface features which are not accessible to inspection methodologies such as electron-beam [50], atomic force microscopy [51] or other high resolution inspection techniques. Resolutions in the 100–200nm range have been recorded and are available in all three dimensions.

It is expected that further improvements in the lateral resolution could be achieved by reducing the imaging wavelength to that which is in close proximity to the silicon band-edge (~1.05µm). This approach is definitely possible; however due to the finite bandwidth of the ultrafast (femtosecond) laser sources used in this arrangement, as well as the fact that the tail of the absorption edge of silicon extends towards longer wavelengths, a single photon signal might dominate a two-photon signal at shorter wavelengths. It would therefore be necessary to increase the shifted wavelength to a value of approximately 1.15µm in order to suppress this effect.

3.14 Conclusions

Ultra-high-resolution optical imaging has been carried out using the TOBIC effect and an s-SIL that shows promise for resolving sub-surface features which are not accessible to common IC debug and high resolution inspection techniques employed within the semiconductor industry. Resolutions in the 100–200nm range are available in all three-dimensions and we expect that further improvements in the lateral resolution could be achieved by reducing the free-space excitation wavelength to that which is closer to the silicon band-edge (~1.15µm) or by employing super-resolution techniques such as pupil-function engineering and / or polarisation-sensitive imaging.

References

[1] B.P. Richards and P.K. Footner, *The Role of Microscopy in Semiconductor Failure Analysis*: Oxford University Press (1992)

[2] C.J.R. Sheppard and D.M. Shotton, *Confocal Laser Scanning Microscopy*: Bios (1997)

[3] C. Xu and W. Denk, "Two-photon optical beam induced current imaging through the backside of integrated circuits", *Applied Physics Letters* **71**, 2578-2580 (1997)

[4] C. Xu and W. Denk, "Comparison of one- and two-photon optical beam-induced current imaging", *Journal of Applied Physics* **86**, 2226-2231 (1999)

[5] D. McMorrow, W.T. Lotshaw, J.S. Melinger, S. Buchner, and R.L. Pease, "Subbandgap laser-induced single event effects: Carrier generation via two-photon absorption", *IEEE Transactions on Nuclear Science* **49**, 3002-3008 (2002)

[6] T. Wilson and J.N. Gannaway, "Examination of grain boundaries in polycrystalline solar cells using a scanning optical microscope", *Electronics Letters* **14**, 507-508 (1978)

[7] T. Wilson and E.M. McCabe, "Optical Beam Induced Current Imaging of Dislocations in Semiconductors", *Optik* **75**, 11-15 (1986)

[8] T. Wilson and E.M. McCabe, "Photoluminescence and Optical Beam Induced Current Images of Defects in Semiconductors", *Physica Status Solidi a-Applied Research* **103**, 107-113 (1987)

[9] T. Wilson and E.M. McCabe, "Theory of Optical Beam Induced Current Images of Defects in Semiconductors", *Journal of Applied Physics* **61**, 191-195 (1987)

[10] T. Wilson and E.M. McCabe, "The Effect of Bias on Optical Beam Induced Current Imaging of Defects in Planar and Schottky Junction Devices", *Optik* **78**, 59-63 (1988)

[11] T. Wilson and P.D. Pester, "Theory of Scan Speed Dependent Optical Beam Induced Current Images in Semiconductors", *Optik* **76**, 18-22 (1987)

[12] E. Ramsay, N. Pleynet, D. Xiao, R.J. Warburton, and D.T. Reid, "Two-photon optical-beam-induced current solid-immersion imaging of a silicon flip chip with a resolution of 325 nm", *Optics Letters* **30**, 26-28 (2005)

[13] C. Werner, D. Reuter, and A.D. Wieck, "Optical beam-induced current in planar two-dimensional n-p-n devices", *Physica E-Low-Dimensional Systems & Nanostructures* **32**, 508-511 (2006)

[14] G. Bautista, C.M. Blanca, and C. Saloma, "Tracking the emergence of defect in light emitting semiconductor diodes with two-photon excitation microscopy and spectral microthermography", *Applied Optics* **46**, 855-860 (2007)

[15] C. Xu, L.M.F. Chirovsky, W.S. Hobson, J. Lopata, W.H. Knox, J.E. Cunningham, W.Y. Jan, and L.A. D'Asaro, "Two-photon photocurrent imaging of vertical cavity surface emitting lasers", *Applied Physics Letters* **76**, 1510-1512 (2000)

[16] F.J. Kao, M.K. Huang, Y.S. Wang, S.L. Huang, M.K. Lee, and C.K. Sun, "Two-photon optical-beam-induced current imaging of indium gallium nitride blue light-emitting diodes", *Optics Letters* **24**, 1407-1409 (1999)

[17] V.J. Cemine, B. Buenaobra, C.M. Blanca, and C. Saloma, "High-contrast microscopy of semiconductor and metal sites in integrated-circuits by detection of optical feedback", *Optics Letters* **29**, 2479-2481 (2004)

[18] C.M. Blanca, V.J. Cemine, V.M. Sastine, and C. Saloma, "High-resolution differential thermography of integrated circuits with optical feedback laser scanning microscopy", *Applied Physics Letters* **87** (2005)

[19] D. Xiao, E. Ramsay, D.T. Reid, B. Offenbeck, and N. Weber, "Optical probing of a silicon integrated circuit using electric-field-induced second-harmonic generation", *Applied Physics Letters* **88** (2006)

[20] R.H. Hadfield, P.A. Dalgarno, J.A. O'Connor, E. Ramsay, R.J. Warburton, E.J. Gansen, B. Baek, M.J. Stevens, R.P. Mirin, and S.W. Nam, "Submicrometer photoresponse mapping of nanowire superconducting single-photon detectors", *Applied Physics Letters* **91**, 241108 (2007)

[21] S.B. Ippolito, B.B. Goldberg, and M.S. Unlu, "High spatial resolution subsurface microscopy", *Applied Physics Letters* **78**, 4071-4073 (2001)

[22] M. Born and E. Wolf, *Principles of Optics*. 7th ed. Cambridge: Cambridge University Press (2002)

[23] B.D. Terris, H.J. Mamin, D. Rugar, W.R. Studenmund, and G.S. Kino, "Near-Field Optical-Data Storage Using a Solid Immersion Lens", *Applied Physics Letters* **65**, 388-390 (1994)

[24] M. Baba, T. Sasaki, M. Yoshita, and H. Akiyama, "Aberrations and allowances for errors in a hemisphere solid immersion lens for submicron-resolution photoluminescence microscopy", *Journal of Applied Physics* **85**, 6923-6925 (1999)

[25] O. Breitenstein, F. Altmann, T. Riediger, D. Karg, and V. Gottschalk, "Lock-in thermal IR imaging using a solid immersion lens", *Microelectronics Reliability* **46**, 1508-1513 (2006)

[26] Q. Wu, G.D. Feke, R.D. Grober, and L.P. Ghislain, "Realization of numerical aperture 2.0 using a gallium phosphide solid immersion lens", *Applied Physics Letters* **75**, 4064-4066 (1999)

[27] Q. Wu, L.P. Ghislain, and V.B. Elings, "Imaging with solid immersion lenses, spatial resolution, and applications", *Proceedings of the IEEE* **88**, 1491-1498 (2000)

[28] D. Lewis, V. Pouget, F. Beaudoin, P. Perdu, H. Lapuyade, P. Fouillat, and A. Touboul, "Backside laser testing of ICs for SET sensitivity evaluation", *IEEE Transactions on Nuclear Science* **48**, 2193-2201 (2001)

[29] C.M. Sparrow, "On Spectroscopic Resolving Power", *Astrophysical Journal* **44**, 76 (1916)

[30] T.R.M. Sales and G.M. Morris, "Fundamental limits of optical superresolution", *Optics Letters* **22**, 582-584 (1997)

[31] C.J.R. Sheppard and Z.S. Hegedus, "Axial Behavior of Pupil-Plane Filters", *Journal of the Optical Society of America a-Optics Image Science and Vision* **5**, 643-647 (1988)

[32] S.B. Ippolito, B.B. Goldberg, and M.S. Unlu, "Theoretical analysis of numerical aperture increasing lens microscopy", *Journal of Applied Physics* **97**, 053105 (2005)

[33] S.B. Ippolito, *High spatial resolution subsurface microscopy*, Boston University, Boston (2004)

[34] M.S. Unlu, M.G. Eraslan, Z. Liu, A.N. Vamivakas, S.A. Thorne, S.B. Ippolito, and B.B. Goldberg, "Application of solid immersion lens techniques to high-resolution subsurface microscopy and thermal imaging", *Abstracts of Papers of the American Chemical Society* **227**, U250-U250 (2004)

[35] K. Kano, *Semiconductor Devices*: Prentice Hall (1998)

[36] INSPEC, *Properties of Silicon*. EMIS datareviews series 4 (1988)

[37] E. Ramsay, *Nonlinear microscopy of semiconductor devices and turbulent fluid flow*, Heriot-Watt University, Edinburgh (2005)

[38] T. Koyama, E. Yoshida, J. Komori, Y. Mashiko, T. Nakasuji, and H. Katoh, "High resolution backside fault isolation technique using directly forming Si substrate into solid immersion lens", *41st Annual Proceedings: International Reliability Physics Symposium*, 529-535 (2003)

[39] B. Morgan, C.M. Waits, J. Krizmanic, and R. Ghodssi, "Development of a deep silicon phase Fresnel lens using gray-scale lithography and deep reactive ion etching", *Journal of Microelectromechanical Systems* **13**, 113-120 (2004)

[40] E. Coyne and F. Zachariasse, "A working method for prototyping solid immersion blazed-phase diffractive optics for near-infrared laser microscopy", *Journal of Micromechanics and Microengineering* **18** (2008)

[41] F. Zachariasse and M. Goossens, "Diffractive lenses for high resolution laser based failure analysis", *IPFA 2006: Proceedings of the 13th International Symposium on the Physical & Failure Analysis of Integrated Circuits*, 95-96 (2006)

[42] A.L. Birkbeck, S. Zlatanovic, S.C. Esener, and M. Ozkan, "Laser-tweezer-controlled solid immersion microscopy in microfluidic systems", *Optics Letters* **30**, 2712-2714 (2005)

[43] K. Tamura, C.R. Doerr, L.E. Nelson, H.A. Haus, and E.P. Ippen, "Technique for Obtaining High-Energy Ultrashort Pulses from an Additive-Pulse Mode-Locked Erbium-Doped Fiber Ring Laser", *Optics Letters* **19**, 46-48 (1994)

[44] E. Ramsay and D.T. Reid, "Investigation of the two-photon optical beam induced current effect in silicon integrated circuits", *Optics Communications* **221**, 427-433 (2003)

[45] E. Ramsay, D.T. Reid, and K. Wilsher, "Three-dimensional imaging of a silicon flip chip using the two-photon optical-beam induced current effect", *Applied Physics Letters* **81**, 7-9 (2002)

[46] USAF, *MIL-STD-150A*.

[47] J.B. Pawley, "Fundamental and Practical Limits in Confocal Light-Microscopy", *Scanning* **13**, 184-198 (1991)

[48] E. Ramsay, K.A. Serrels, M.J. Thomson, A.J. Waddie, M.R. Taghizadeh, R.J. Warburton, and D.T. Reid, "Three-dimensional nanoscale subsurface optical imaging of silicon circuits", *Applied Physics Letters* **90**, 131101 (2007)

[49] E. Ramsay, K.A. Serrels, M.J. Thomson, A.J. Waddle, R.J. Warburton, M.R. Taghizadeh, and D.T. Reid, "Three-dimensional nanometric sub-surface imaging of a silicon flip-chip using the two-photon optical beam induced current method", *Microelectronics Reliability* **47**, 1534-1538 (2007)

[50] E. Ruska, "The Development of the Electron-Microscope and of Electron- Microscopy", *Reviews of Modern Physics* **59**, 627-638 (1987)

[51] F.J. Giessibl, "Advances in atomic force microscopy", *Reviews of Modern Physics* **75**, 949-983 (2003)

Chapter 4

Resolution-Enhancing Techniques in Semiconductor Integrated-Circuit Microscopy

---

4.1 Introduction

Conventional optical resolution is governed by the properties of diffraction [1]. This ultimately restricts the amendable parameters of an imaging system to the illumination wavelength and the numerical aperture (*NA*) of the objective lens. In order to achieve diffraction-limited system performance one can either chose to reduce the wavelength, increase the *NA*, or modify both values simultaneously. Eventually these parameters will reach a limiting value whether as a consequence of optical source wavelength, sample material or the system component tolerances. This situation is deleterious to the progress of several optical technologies, an example of which is the emerging field of nanophotonics, in which optical techniques are applied and developed to facilitate experiments with a spatial resolution of a few hundred nanometers or less. These state-of-the-art experiments require the ability to resolve, interrogate and manipulate optical material on the nanoscale and therefore demand that optical technologies are continuously developed in order to satisfy modern demand / progression. Near-field techniques such as scanning near-field optical microscopy (SNOM) [2] are commonly applied to overcome this constraint; however, there are optical far-field techniques known as 'super-resolution' methods which have made significant progress in recent years and can often extend well established optical methodologies, improving their performance in a way that achieves sub-micron resolution [3]. In the context of imaging, super-resolution refers to any technique that improves the resolution of an imaging system beyond the conventional diffraction-limited value. Such techniques can be attractive because they often provide a simple way to enhance the resolution of an optical system without resorting to more sophisticated near-field methods.

One example of optical super-resolution is the use of pupil-function engineering to manipulate the point-spread function (PSF) at the focal-plane of an imaging system, since the PSF has a radial profile whose shape depends sensitively on the aperture function of the system [4-6]. The PSF is defined as the irradiance distribution at the

focal-plane of an imaging system which is produced when imaging a point source [1], which is equivalent to the focal-plane distribution resulting from focusing a plane-wave (a point source at infinity). Control of the PSF using pupil-function engineering has been applied in several nanophotonic applications, including optical data storage [7], confocal scanning microscopy [8], conventional transmission optical microscopy [9] and fluorescence microscopy [10]. A further advantage in optical data storage can be obtained when using pupil-function engineering since reducing the width of the radial PSF can lead to a corresponding extension of the axial PSF, which, for example, alleviates the requirement of precise control over the distance between the focusing lens and the spinning disc [11].

A second example of optical super-resolution is the ability to manipulate the electromagnetic field distribution in the focal-plane of a high-*NA* imaging system by controlling the polarisation state of the incident illumination. It has been known since 1959 [12] that the focal-plane intensity distribution produced by focusing linearly polarised light under high-*NA* conditions is highly asymmetric. This imaging characteristic can be exploited in a wide variety of nanoscale optoelectronic systems including optical trapping, optical memory and material processing. Although several theoretical models have been demonstrated which advance and uncover the optimum practical conditions for this technique in recent years, only a small volume of experimental results have been published that utilise this effect fully by demonstrating genuine improvements beyond what can be achieved without pupil-function engineering.

In this Chapter I present experimental demonstrations of optical super-resolution in sub-surface solid immersion lens (SIL) enhanced integrated-circuit (IC) imaging using custom annular apertures / obscuration discs, polarisation-dependent focusing techniques and a hybrid configuration of both methods. All of these techniques surpass conventional diffraction-limited performance at 1.55μm.

4.2 Manipulating the Point-Spread Function using Pupil-Function Engineering

For a clear pupil and plane-wave optical illumination, the classical Airy response is obtained whose PSF has a full width half-maximum (FWHM) diameter which can be calculated using $\Delta x \approx 0.51\lambda / \mathrm{NA}$. Custom-engineered aperture functions which modify

either the intensity or phase of the wavefront can reduce the PSF diameter by approximately 30% at the expense of introducing side-lobes into the image. In this section we illustrate this idea by considering a series of annular apertures of differing radii and width.

A scalar analytical result, introduced in Chapter 3, which is valid for high-*NA* [4] gives the optical field, ψ, at the observation plane as,

$$\psi(\eta) = 2\int_0^1 A(r)\exp[i\Phi(r)]J_o(\eta r)rdr \tag{1}$$

where $A(r)$ and $\Phi(r)$ are the amplitude and phase profiles of the light before the pupil of the focusing lens, J_o is a Bessel function of the first kind and *r* is the normalised radial coordinate at the pupil-plane. For typical laser illumination the amplitude $A(r)$ will take the form of a Gaussian profile modulated by the transmission function of the pupil aperture mask. When the aperture mask is an amplitude-only design the phase is zero across the pupil.

The PSF is calculated at the image-plane where the lateral position across the image-plane is given by the radial coordinate ρ. For the purposes of calculation a dimensionless radial parameter is used,

$$\eta = \frac{\pi D\rho}{\lambda f} = \frac{2\pi\rho NA}{\lambda} \tag{2}$$

which takes account of the *NA* of the focusing system and the illumination wavelength.

Various super-resolution techniques have been developed over the years which define, optimise and control the functions $A(r)$ and $\Phi(r)$ in a wide range of differing formats. Basically, this implies that the current state-of-the-art in super-resolution schemes is based on either the control of the illuminating amplitude transmittance or the phase function. With regards to amplitude engineering, methodologies include obscurations [13], annular apertures [14, 15] and continuous-amplitude filters [16]. Phase only technologies include a wide variety of novel diffractive optic elements (DOE) [17-23].

There have also been investigations into accommodating hybrid super-resolution techniques [6, 24-28].

Furthermore, the generation of super-resolution performance need not be limited to the use of diverse optical elements. An intelligent alternative concentrates on post-detection image processing, commonly referred to as super-resolution algorithms [29]. This scheme attempts to provide pass-band restoration as well as some degree of extrapolation of the image spectrum since the image recorded at the output of the imaging system is a low-pass filtered version of the original object due to the finite size of the objective lens; however, this approach is only referred to as an interesting aside to the aforementioned optical techniques described above.

The numerical evaluation of (1) was carried out using MATLAB and considered a selection of differing amplitude transmission functions, under Gaussian illumination, in order to investigate the performance of different filter patterns. The filter patterns are shown in Fig. 1(a), (c), (e) and (g). The calculated conventional (linear) response and the resulting two-photon response (nonlinear - inset) for these filters are illustrated in Fig. 1(b), (d), (f) and (h) respectively. Each filter function is compared against the uniform transmission (clear aperture – dotted line) response which is modeled in Figs. 1(a) and (b).

It can be seen that when the higher spatial frequencies of the system are suppressed there is an increase in the width of the calculated PSF. This is due to the fact that only the paraxial rays of the system are utilised which ultimately reduces the available *NA*. Likewise, when the higher spatial frequencies are isolated and transmitted there can be seen a reduction in the calculated PSF. This is an obvious result since an increase in the *NA* of any imaging system will lead to an improvement in its resolving capabilities given that $NA = n\sin\theta$ and the classical Airy response is obtained whose PSF has a FWHM diameter of $\Delta x \approx 0.51\lambda / \mathrm{NA}$. Fig.1 (g) illustrates a filter which isolates a portion of the system's higher spatial frequencies whilst eliminating the remaining lower order paraxial rays. The filter design and theoretical performance are shown in Fig. 1 (g) and (h).

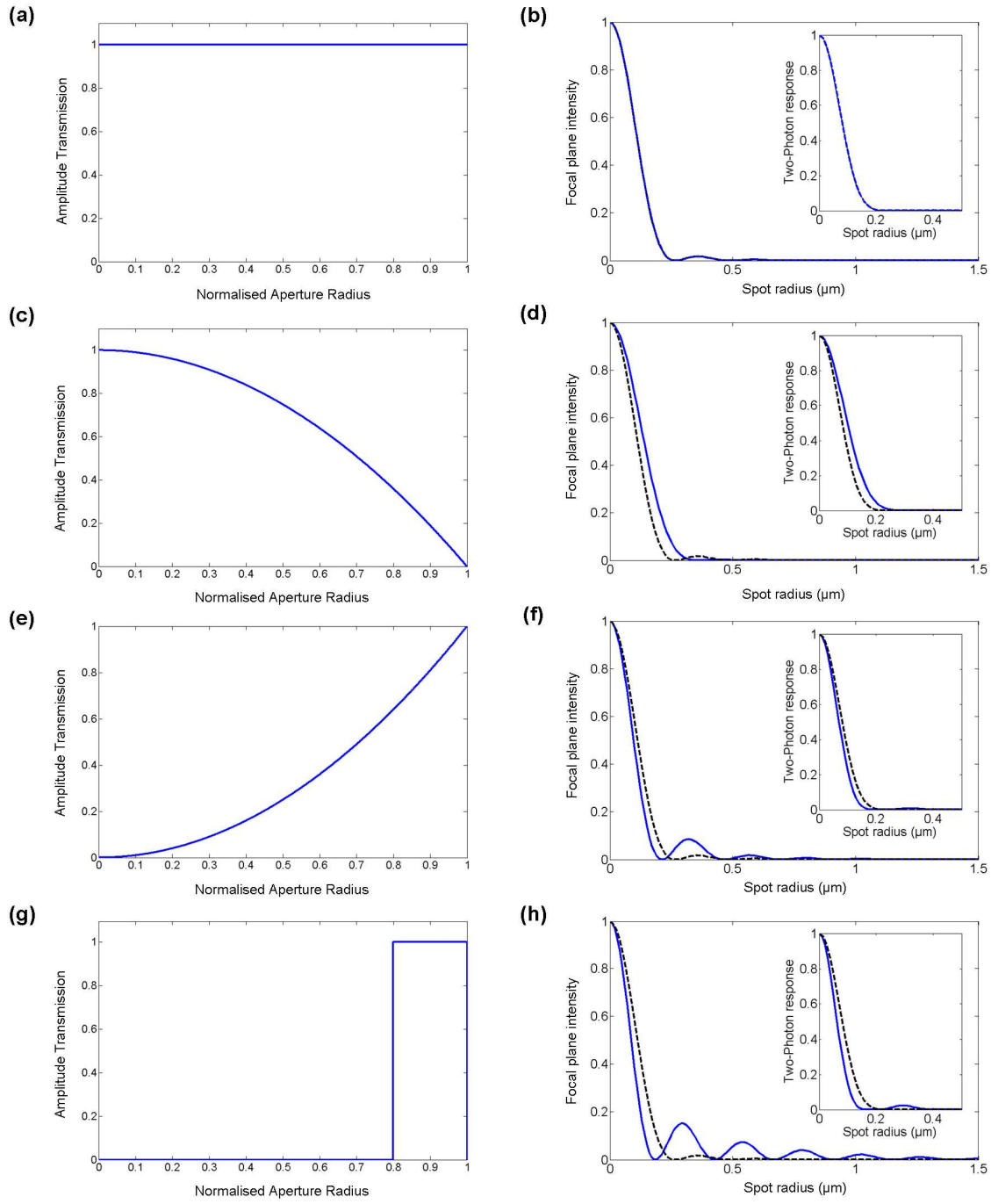

Figure 1 – Aperture filter design (left) and corresponding theoretically calculated PSF performance according to scalar diffraction theory under Gaussian illumination

Another common trend, which is clear from the results, illustrates a narrowing of the PSF through isolation of the higher spatial frequencies at the expense of creating side-lobes of considerable intensity. It is evident that these side-lobes would contribute to the optical performance of a conventional imaging system; however since the work presented here is of a nonlinear nature, it can be seen from the illustrations of the resulting two-photon responses that the central maximum of the PSF dominates under

an intensity-squared relationship. It is the suppression of these generated side-lobes in a nonlinear imaging mode which motivates the use of custom annular apertures in the quest to improve our system's imaging resolution.

Having modeled the resulting PSF profiles from a variety of different aperture amplitude transmission functions we extended this approach to consider a selection of annular amplitude transmission functions. It was expected that these annular apertures could provide a significant reduction in the PSF through the isolation and transmission of the modeled system's higher spatial frequencies. Annular apertures have been applied in transmission microscopy, for example, to obtain resolutions of 90nm [9] and, in general, are suitable in applications where the reduction in power by the aperture is acceptable. Fig. 2 presents further evaluations of (1), again under Gaussian illumination with a beam whose intensity at the edge of the pupil is 13.5% ($1/e^2$) - this corresponds to sufficiently small vignetting of the optical beam in order to avoid side-lobe generation in the open-pupil PSF. For the optical system we considered an illumination wavelength of 633nm, a focal length of 10cm and an *NA* of 0.1; however, now the annular apertures have different radii and widths. The general trends that can be observed are that apertures of greater radii result in sharper PSFs but at the expense of side-lobe formation. In the most extreme case (aperture radius 90% and width 20%) the FWHM diameter of the PSF reduces from 4.0μm to 2.5μm, and this is accompanied by the appearance of side-lobes whose intensity is 15% of the peak PSF intensity; however, this is insignificant under nonlinear excitation - 15% (linear) becomes ~2.25% (nonlinear).

Since an annular aperture only transmits the non-paraxial portions of the illumination beam, only the highest *NA* rays will contribute to the focusing of the beam – the highest spatial frequencies in the PSF. Consequently, a reduction in the PSF corresponds to an increase in the content of the transmitted higher spatial frequencies. It is not surprising therefore that an annular aperture that blocks the low-*NA* (paraxial) rays leads to a reduction in the PSF FWHM value.

It is interesting to note that the side-lobes created when using annular apertures with Gaussian beam illumination have intensities which are considerably smaller than the side-lobes generated when using plane-wave illumination, although the width of the central maximum of the PSF decreases more when using a plane-wave; however, from a

practical applications viewpoint the suppression of the side-lobes when using Gaussian illumination is perhaps more useful than the improvement in the overall spot size.

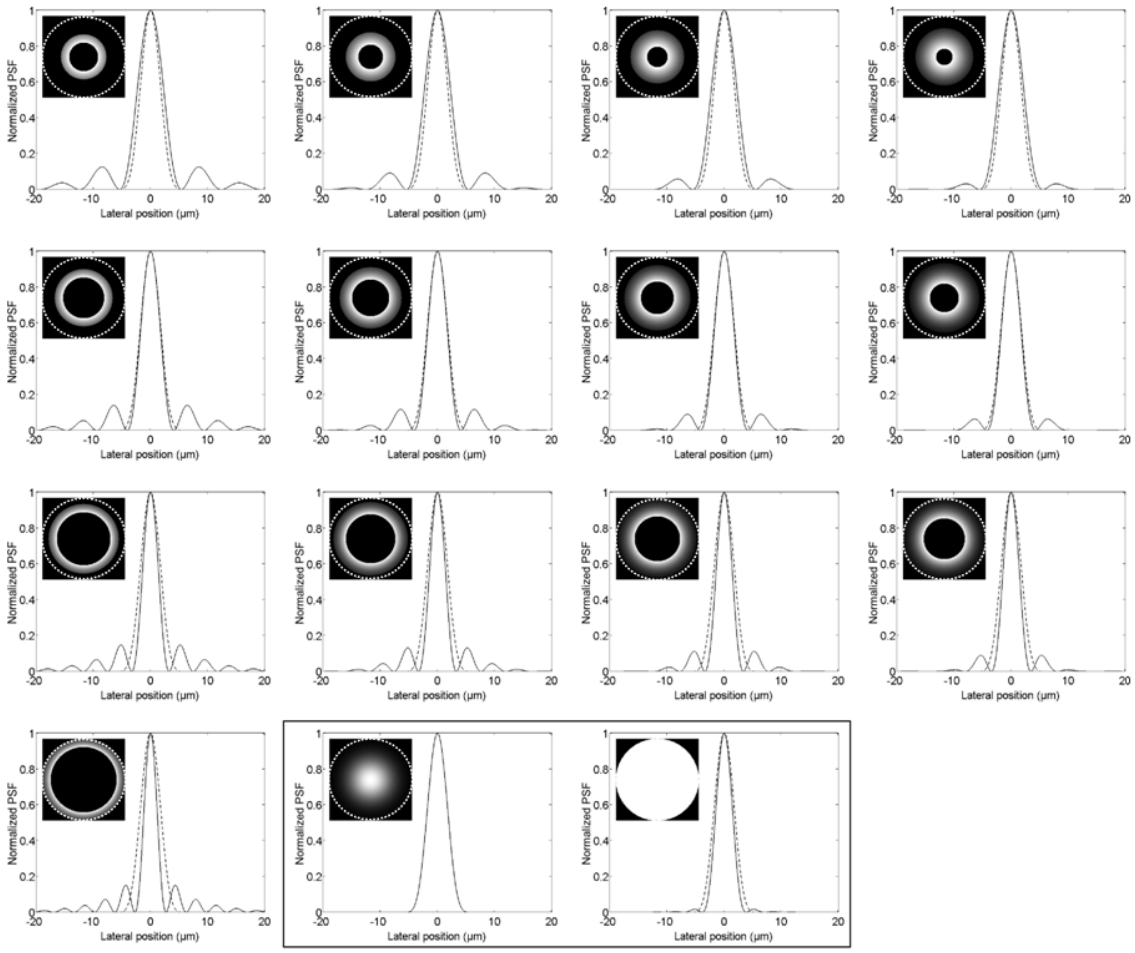

Figure 2 - Calculated lateral PSFs for Gaussian beam illumination of annular apertures with various radii and radial widths. The dashed line in each plot is the PSF obtained with no aperture. The image embedded within each plot shows the normalised intensity of the light transmitted through the pupil of the imaging system, and the pupil extent is shown by the dashed white circle in each image. For each case the illuminating beam had a field intensity that fell to 13.5% at the edge of the pupil. Columns (top to bottom) show results for aperture radii of 45%, 60%, 75% and 90% of the pupil radius. Rows (left to right) show results for aperture widths of 20%, 30%, 40% and 50% of the pupil radius. Inset (boxed): Results for Gaussian illumination with no aperture (left), and uniform illumination with no aperture (right).

I would like to acknowledge Dr Euan Ramsay for his contribution towards preparing the MATLAB code required to present the results given in Fig. 2 (above) and in Fig. 5 (discussed later).

4.3 Optical Super-Resolution Demonstration Using Custom Annular Apertures

It is of primary importance in any imaging system to understand the performance of the components utilised throughout the experimental investigation. Therefore, this section discusses the fabrication and characterisation of a set of custom annular apertures. These apertures were developed in order to advance the imaging resolution capabilities of our two-photon optical beam induced current (TOBIC) microscope beyond that which was achieved in Chapter 3. The performance of the annular apertures was compared against scalar theory.

4.3.1 Experimental Configuration

The optical arrangement used to characterise the effect of the annular apertures is shown in Fig. 4. It consisted of a helium-neon (HeNe) laser, a beam-expanding telescope, a final focusing lens and a charged coupled device (CCD) camera (Basler Vision Technologies A302f – pixels - 782(H) x 582(V), pixel size - 8.3µm^2, max. frame rate - 30 frames/sec, video O/P signal - mono: 8 bits/pixel - colour: 16 bit/pixel). The apertures were placed directly before the final focusing lens. The laser emitted light at a wavelength of 633nm with a power of around 5mW. This light was directed through the beam expanding telescope and collimated such that the FWHM intensity of the beam leaving the telescope was 2.44mm. This collimated beam diameter value was determined by performing a knife-edge measurement perpendicular to the propagation direction immediately after the collimation lens. The final focusing lens was very weak, with a focal length of around 1m. This was chosen to ensure that the focused spot was large enough to illuminate a sufficient number of pixels on the camera's CMOS sensor in order to achieve adequate Nyquist sampling across the image-plane using the available equipment (the Nyquist sampling theorem states that aliasing can be avoided if the Nyquist frequency is greater than the bandwidth, or maximum component frequency, of the signal being sampled). The image from the camera was sent to a personal computer (PC) and visualised using the camera's internal software package. Image characterisation and analysis was performed using MATLAB.

Three annular apertures were characterised in the experiments, each one of which had an annular width (dR) of 0.66mm, and an internal radius (R) with values 1.1mm, 1.6mm and 2.2mm, respectively. The one inch diameter apertures were fabricated from glass substrates and had a central obscuration area, of approximately 100nm thickness,

provided by chromium deposition. The apertures were fabricated using in-house clean-room facilities. In addition, as a reference parameter, analysis was performed on the image that was generated and acquired when no aperture was present. Data acquisition was repeated for different camera gain settings to determine the highest signal possible without saturation. Three images were acquired for each aperture and gain setting, and these images were averaged in MATLAB to reduce random noise in the measurement. The principal noise sources were thermal mode-shape and power fluctuations in the laser. It was discovered that when averaging was performed using more than three captured frames there were no significant advantages to be obtained.

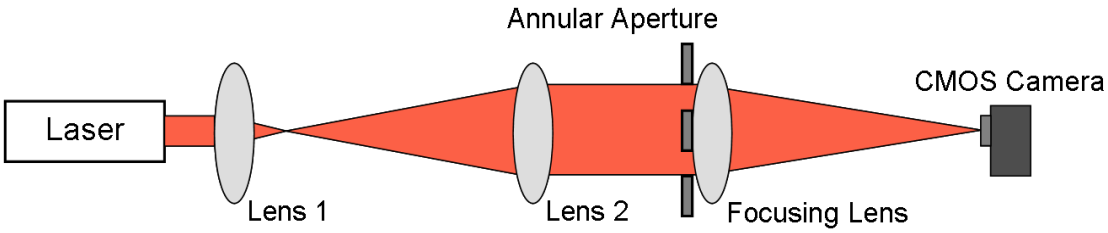

Figure 4 - Experimental configuration. Lenses 1 and 2 form a beam expanding telescope which directs a collimated beam through an annular aperture to a focusing lens. The beam is then focused onto the sensor of a CMOS camera (Basler Vision Technologies A302f – pixels - 782(H) x 582(V), pixel size - 8.3µm2, max. frame rate - 30 frames/sec, video O/P signal - mono: 8 bits/pixel - colour: 16 bit/pixel) and the image from the camera recorded by a PC for analysis. The focal lengths of lenses 1 and 2 in the telescope are 30mm and 100mm respectively, and the focusing lens has a focal length of around 1m.

4.3.2 Analysis and Discussion

When Equation (1) was used to calculate the PSF of our focusing system, it was necessary to accurately determine the system's *NA*. Under plane-wave illumination, the *NA* of an imaging system is defined as $NA = n\sin\theta$, where $\sin\theta = D/2f$, where the lens diameter is *D* and the focal length is *f*. Under Gaussian beam illumination the *NA* is no longer clearly defined since the beam may not fill the entire aperture provided by the lens [30]. Therefore, when interpreting the experimental data using Equation (1), it was necessary to allow the Gaussian beam radius and the system *NA* to both be free fitting parameters.

The analysis of the experimental data and the method to which a theoretical comparison was generated can be described as follows:

To begin we define the parameter $A(r)$ as the input field distribution of our HeNe laser beam. The HeNe produced a Gaussian radial distribution of the form $A(r) = \exp(-qr^2)$, where *r* is the normalised radius across the lens aperture. The Gaussian beam diameter was controlled by varying the parameter *q*. An initial estimate of this Gaussian illumination parameter had to be made based on an experimentally obtained knife-edge beam measurement in order to simulate the PSF in the case of a clear aperture. The value of the FWHM diameter of this simulated PSF was compared to that which was measured experimentally. The value of the *NA* in the simulation was then modified until the simulated and experimental PSF diameters matched. Once this procedure was complete, the next stage was to introduce an annulus into our simulation. The first annulus investigated was the one which transmitted the largest portion of paraxial rays – i.e. the smallest annulus. The values of *q* and *NA* for this annulus were matched to the values used for the clear aperture then the cut-on and cut-off positions for the annulus at the pupil-plane were defined. This was achieved by recalling the experimentally measured beam at the lens pupil, and mapping it onto the normalised radius in the simulation. Through the mapping of the Gaussian distribution at the lens pupil back to the simulation one can determine the intensity profile which is present across the annulus, and hence these can be transferred on to the normalised simulation aperture. The amplitude of the electric-field which falls outside of the transmission window of the annulus was set to be zero, i.e. these radial values were padded with zeros so to concentrate on the effects of the annulus only - on review, it would be ideal at this stage to increase the sampled level of zero padding accordingly in consideration of the Nyquist sampling theorem for improved analytical accuracy. The simulation was then run again to calculate the new PSF, with the inclusion of the annulus, and the result of this was compared with the experimental value achieved. If the FWHM of the PSF calculated with the aperture in place was smaller than that which was measured experimentally then the value of *q* had to be increased. As a result, this required the value of the *NA* to be amended also so that the open-pupil calculation agreed with our experimental value once again. This process was iterated until good agreement was seen between the experimental and the simulated data for both the smallest aperture and the open pupil. Subsequently, when the data for the medium and large apertures were analysed we found that the simulated values of *NA* and *q* did not need to be amended further to obtain good correspondence between the measured and simulated data in these two cases if good correspondence had already been achieved for the smaller pupil.

Fig. 5 shows the experimental results compared against the simulated data obtained using the parameters determined by the above described method. In each figure, the main portion of the figure shows the experimental data (circles) and the simulation (solid line), describing the normalised PSF in the lateral direction. The upper left inset of each figure shows the aperture function that was applied to the Gaussian input beam and the upper right inset of each shows the focal-plane distribution which was recorded on the camera, with the same field size (1mm by 1mm) for each image. Identical gain settings for the camera were used to acquire the data in each sub-figure to provide consistency.

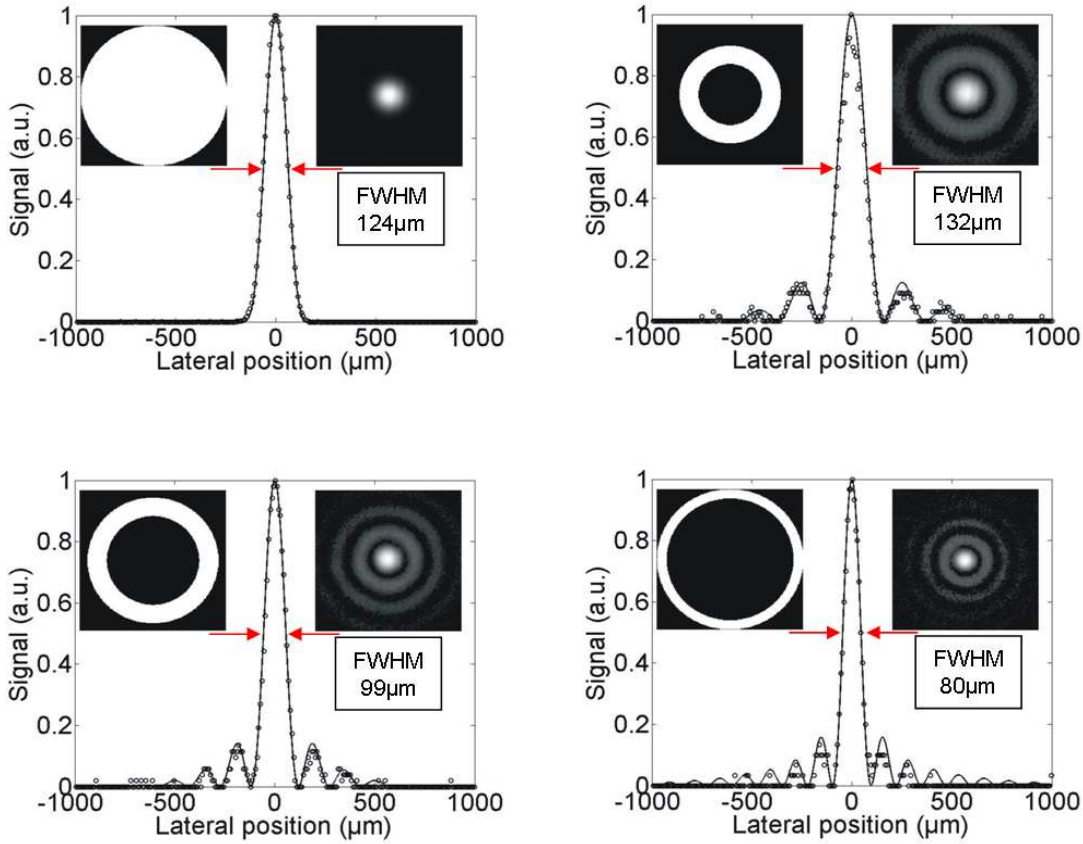

Figure 5 - Theoretical and experimental results obtained for (a) clear aperture; (b) small internal radius annulus; (c) medium internal radius annulus; (d) large internal radius annulus. For each image, the left inset shows the annulus used (white = clear, black = obstructed) on the unit aperture. The right inset shows the image captured on the CMOS camera for a 1 mm by 1mm field of view. The main section of the image shows the theoretical PSF generated using Equation (1) for each given annulus (solid line) and the experimental data generated by taking a line-cut through the centre of each camera image (circles).

Fig. 5 (a) illustrates the results for the open pupil data (no aperture). This was used as a reference for the rest of our experiments. Good agreement can be seen between the

simulated and experimental PSFs, which had a FWHM diameter of 124µm for our long focal length lens and Gaussian input beam. Fig. 5 (b) illustrates the results for an annular aperture whose transmission window cut-on at the normalised pupil radius of 0.434 and cut-off at the normalised pupil radius of 0.695. The FWHM diameter of the central maximum of the PSF increased when using this particular aperture, from 124µm to 132µm. This can be explained however because although the aperture obscured the low-*NA* portion of the pupil function it also obscured a significant portion of the higher *NA* rays as well. This resulted in a net degradation in optical performance. The simulated PSF for this aperture was in good agreement with both the central maximum of the experimental results as well as the position and height of the side-lobes generated as a result of aperturing the beam. Fig. 5 (c) illustrates the results for an annulus which transmits only the portion of the beam falling between the normalised radial values of 0.631 and 0.893. Here we observed a reduction in the FWHM of the PSF from 124µm to 99µm, and again good correspondence can be seen between the simulated and experimental PSFs, both in terms of lateral position, width and heights. Finally, Fig. 5 (d) illustrates the situation where an annulus with a width extending from 0.867 to 1 on the normalised pupil was considered. It is not surprising to discover that this annulus results in the best performance in terms of reducing the FWHM of the PSF, in this case to 80µm, which was around 60% of the width of the open-pupil PSF. Once more, it is shown that good agreement between the experimental and simulated PSFs can be observed; however, we note here that although the higher order side-lobes cannot be seen in the experimental data this can be explained due to the relatively low illumination intensity which has been transmitted by this particular aperture and digitisation quantisation. Also, in order to retain consistency between all experimental results it was necessary to use the same gain settings throughout the data acquisition. Yet again a good agreement is shown with the experimental results for all three annuli and the open pupil. The final values for q and *NA* that were used throughout the simulation were 1.5 and 0.00303, respectively.

4.3.3 Summary and Conclusions

Through the use of obscuration discs and annular apertures it has been shown that the technique of optical super-resolution can be achieved with pupil-plane binary transmission filters. It has been demonstrated experimentally that it is possible to obtain super-resolved focal-spot sizes which are significantly smaller than those obtained under clear-aperture Gaussian illumination through the transmission of only the high-

NA rays of an optical system. A theoretical model, written in MATLAB, for super-resolution has also been introduced and a method of relating the experimental results we obtained to this theory has been explained. The optimum annular aperture used here reduced the PSF FWHM by 60% of its clear aperture value.

In an attempt to improve the performance documented here, one can either investigate the effects of an additional set of annular amplitude apertures which have been designed to transmit an extremely narrow band of high spatial frequencies at the maximum extent of the system *NA*, consider phase only apertures or investigate amplitude / phase hybrid alternatives.

As an aside to the annular aperture work, it is also important to consider the effects of high-*NA* polarisation-dependent focusing. This approach is not only a novel strategy in the pursuit of optical super-resolution, but it can also compliment the results obtained using annular apertures. The next section introduces the theory behind this vectorial focusing approach and presents the first experimental demonstration of such effects.

4.4 Resolution Enhancement Using Polarisation-Dependent Focusing

It has been known since 1959 [12] that the focal-plane intensity distribution produced by focusing linearly-polarised light with a high-*NA* lens will be highly asymmetric. Remarkably, the consequences of this fundamental physical effect in direct image acquisition have remained unexploited, although vectorial focusing effects have previously been observed [31-33]. By using extreme *NA* (*NA* = 3.5) solid-immersion microscopy [34-37] we have obtained images of a silicon IC that show, for the first time, the dramatic influence of polarisation on their spatial resolution, with values ranging from around 100nm to 250nm depending on the polarisation state used. Such imaging is no longer subject to the conventional scalar resolution formulae and we present data showing that polarisation-dependent imaging can, under certain conditions, substantially surpass the classical scalar diffraction-limit embodied by resolution formulae such as Sparrow's criterion.

4.5 Polarisation-Dependent Focusing Theory

The spatial distribution of an optical field at the focus of a high-*NA* lens displays an increasing ellipticity as the *NA* of the system approaches unity. This is because at high-

NA polarisation starts to play a more dominant role in the focal properties of the incident light. In the effort to obtain the smallest focal spot size attainable one must take this into account since polarisation-dependent effects are no longer negligible.

4.5.1 Scalar versus Vectorial Theory

In order to compare the numerical results obtained from calculations involving scalar and vectorial focusing effects one must first discuss the theoretical background of these two conditions.

4.5.1.1 Scalar Theory – Sales and Morris

The scalar diffraction model is based on analysis derived from Sales and Morris [4] and takes into consideration the parameters discussed in Section 4.2. When implementing the model to simulate our optical system, care must be taken to set $A(r)$ to zero where the pupil is obscured when using central-obscuration filters. Note also that the polarisation state of the light field will not affect the shape of the focal spot since the model does not take into account the vectorial nature of the electromagnetic field. In the following figures the results from the scalar model are shown as black, solid lines.

4.5.1.2 Vectorial Theory – Leutenegger

The initial vector diffraction model is based on an analysis derived from Richards and Wolf [12], which investigates the structure of a linearly-polarised electromagnetic field near the focus of a high-*NA* aplanatic lens system which images a point source at infinity. Richards and Wolf adopt an analytical integral representation of the electromagnetic field whereas others have implemented a different methodology to calculate the field near the focus of a high-*NA* objective lens. Instead of applying direct integration, Leutenegger *et al* [38] evaluates the vectorial Debye diffraction integral using a fast Fourier transform (FFT) to calculate the electromagnetic field in the entire focal region. This technique enhances the speed at which these calculations can take place since it employs a sampling grid procedure in combination with the FFT analysis. This work extends that which was initially reported by McCutchen in 1964 who stated that the three-dimensional (3D) diffraction pattern of a point source at the focus of a lens is the 3D Fourier transform of the generalised lens aperture [39, 40].

Others have used the theory presented by Richards and Wolf to calculate the 3D electric energy density distribution at the optical focus [41-43] and some have extended this

further to include spatially variant optical fields [44, 45] along with annular apertures [46, 47] and SILs [48].

The focal-plane energy density distributions presented throughout this chapter are derived from the theory of Leutenegger. This theory is a truly novel and interesting one since it makes use of a sampling grid scheme that allows for the implementation of a direct two-dimensional (2D) FFT of the pupil field. Furthermore, it reduces the problem associated with evaluating the vectorial diffraction integral since it can be now expressed as a modified Fraunhofer diffraction integral. Therefore, I will discuss the important parameters that must be considered in order to implement such a unique approach.

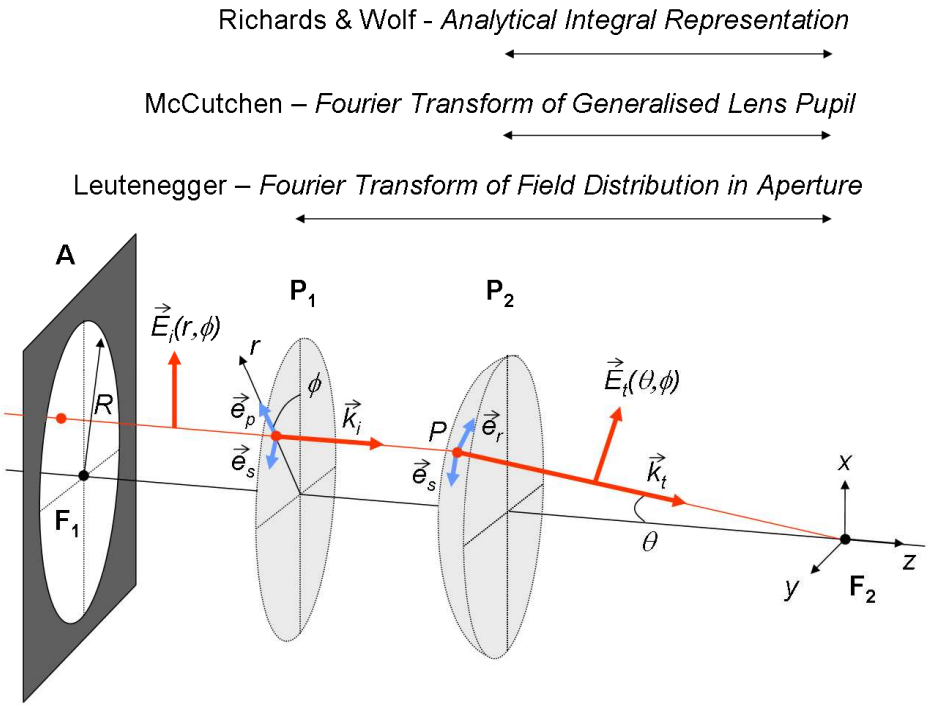

Figure 6 - Optical configuration. The objective lens is represented by the aperture stop *A* of radius *R* and the principal planes P_1 and P_2. The point *P* is the intersection point of a ray with P_2 and highlights the relationship between the position *r* at P_1 of the incident wave $\vec{E}_i$ and the propagation angle at P_2 of the transmitted wave $\vec{E}_t$.

The optical configuration and the respective coordinate systems are illustrated in Fig. 6. A coherent, monochromatic optical wave field parallel to the optical axis crosses the aperture stop *A*, propagates towards the plane P_1 and is transferred to the plane P_2. From here the wave field is refracted and focused towards the focal point F_2. The point *P* is located on the plane P_2 and illustrates the focusing of the ray towards the focal point.

The spherical surface at P_2 is observed from F_2 and the deflection angle θ at the position P is given by,

$$\sin\theta = \frac{r}{R}\frac{NA}{n_t} \tag{3}$$

where r is the off-axis radial component of the incident wave, R is the radius of the aperture stop, NA the numerical aperture of the objective and n_t the refractive index behind the surface P_2.

The incident field $\vec{E}_i(r,\phi)$ at P_1 is decomposed into a radial component (p-polarised) and a tangential component (s-polarised). The unit vectors for p- and s-polarisation are,

$$\vec{e}_p = \begin{pmatrix} \cos\phi \\ \sin\phi \\ 0 \end{pmatrix} \qquad \text{and} \qquad \vec{e}_s = \begin{pmatrix} -\sin\phi \\ \cos\phi \\ 0 \end{pmatrix} \tag{4}$$

where ϕ is the azimuth angle around the optical axis. Upon transmission at point P, the unit vector $\vec{e}_p$ is deflected by θ and becomes,

$$\vec{e}_r = \begin{pmatrix} \cos\phi\cos\theta \\ \sin\phi\cos\theta \\ \sin\theta \end{pmatrix} \tag{5}$$

Therefore, the amplitude, phase and polarisation of the transmitted field at P_2 is,

$$\vec{E}_t(\theta,\phi) = t_p\left(\vec{E}_i \cdot \vec{e}_p\right)\vec{e}_r + t_s\left(\vec{E}_i \cdot \vec{e}_s\right)\vec{e}_s \tag{6}$$

where $t_p(\theta,\phi)$ and $t_s(\theta,\phi)$ are the transmission coefficients for p- and s-polarisation, respectively. These parameters are responsible for expressing the effects of any accumulated phase distortions (i.e. aberrations) as well as amplitude attenuation for both polarisation components upon transmission at point P.

In the Debye approximation, the electric-field $\vec{E}$ at a point (x,y,z) at the focus is obtained by integrating the propagated plane waves that are incident across P_2,

$$\begin{aligned}\vec{E}(x,y,z) &= -\frac{if}{\lambda_0}\iint_{\Omega}\vec{E}_t(\theta,\phi)e^{i\left(k_z z-k_x x-k_y y\right)}d\Omega \\ &= -\frac{if}{\lambda_0}\int_0^{\Theta}\sin\theta\int_0^{2\pi}\vec{E}_t(\theta,\phi)e^{i\left(k_z z-k_x x-k_y y\right)}d\phi d\theta\end{aligned} \tag{7}$$

The phase factor $e^{ik_z z}$ expresses the phase accumulation during propagation along the optical axis (z-axis), whereas the term $e^{-i\left(k_x x+k_y y\right)}$ represents the phase difference of the wavefront at off-axis points (x,y,z) with respect to the on-axis point (0,0,z). The integration in (7) extends over the solid angle within which P_2 is observed at F_2, i.e. $\sin\Theta = NA/n_t$.

The wave vector $\vec{k}_t$ can be expressed in spherical coordinates as,

$$\vec{k}_t(\theta,\phi) = k_0 n_t\begin{pmatrix}-\cos\phi\sin\theta\\ -\sin\phi\sin\theta\\ \cos\theta\end{pmatrix} \qquad \text{where} \qquad k_0 = \frac{2\pi}{\lambda_0} \tag{8}$$

It is at this stage where the evaluation of the Debye diffraction integral, equation (7), is required. Typically, this is performed using direct numerical integration taking into consideration the appropriate coordinate transformations. In doing so one arrives at the Richards and Wolf integral representation [12]; however, this method is computationally laborious and time consuming. Therefore, Leutenegger addressed this issue by demonstrating that the Debye diffraction integral can be expressed as a Fourier transform by splitting the phase factors into a lateral and axial term and by performing the integration over the pupil-plane P_1 instead of the curved surface of P_2. The integration step for a sampling over P_2 can be projected back onto P_1 by using equations (3) and (8) which produces,

$$d\Omega = \left(\frac{NA}{Rn_t}\right)^2\frac{rdrd\phi}{\cos\theta} = \left(\frac{NA}{Rn_t}\right)^2\frac{dxdy}{\cos\theta} = \frac{1}{k_t^2}\frac{dk_x dk_y}{\cos\theta} \tag{9}$$

Implementation of this new projected sampling step into equation (7) yields,

$$\vec{E}(x,y,z) = -\frac{if}{\lambda_0 k_t^2}\iint_{r<R}\left(\frac{\vec{E}_t(\theta,\phi)e^{ik_z z}}{\cos\theta}\right)e^{-i(k_x x+k_y y)}dk_x dk_y \tag{10}$$

By setting $\left|\vec{E}_t\right| = 0$ for $r > R$ one can express the Debye diffraction integral as a Fourier transform of the weighted field $\vec{E}_t$, which finally results in,

$$\vec{E}(x,y,z) = -\frac{if}{\lambda_0 k_t^2}\mathrm{F}_{x,y}\left(\frac{\vec{E}_t(\theta,\phi)e^{ik_z z}}{\cos\theta}\right) \tag{11}$$

Equation (11) now expresses the Debye diffraction integral as a 2D Fourier transform, $\mathrm{F}_{x,y}$, of the field distribution in the aperture *A* that has been projected onto P_2. It can be seen that there is a noticeable similarity between equation (11) and the conventional Fraunhofer diffraction integral (below),

$$\vec{E}(x,y,z) = -\frac{if}{\lambda_0 k^2}\mathrm{F}_{x,y}\left(\vec{E}_A e^{ik_z z}\right) \tag{12}$$

For low-*NA* imaging systems the weighting factor is approximated by $1/\cos\theta \approx 1$ which results in equations (11) and (12) exactly matching.

The numerical implementation of equation (11) is straightforward and can be executed by performing two individual FFTs, one along the x-direction and the other along the y-direction; however, note here that care must be taken to avoid calculation errors. These exist in the form of granular artefacts across the image (Fourier) plane at high frequencies and also image distortion due to aliasing at the aperture rim. These effects can be remedied however by enforcing a minimum sampling step across the aperture pupil and by extending the aperture matrix, by zero-padding, to at lease twice its initial dimensions before performing the FFT, respectively. With respect to the latter solution, once the FFT is performed along the first dimension (e.g. x-axis) it can be cropped back to its initial size before the same procedure is applied to the second dimension (e.g. y-axis). The use of two one-dimensional FFTs with zero-padding and intermediate cropping minimises the effort required for numerical processing.

4.5.1.3 Numerical Aperture Analysis

As an introduction to vectorial effects, we initially considered the results of the model calculating the focal-plane energy density distribution of linearly-polarised plane-wave illumination using the Leutenegger theory presented above [38], as the *NA* of the system is increased from a minimum value of 0 to a maximum of 1 using increments of 0.25. The results are shown in Fig. 7 through Fig. 11 (below – full page) and illustrate the elongation of the PSF along the polarisation direction (red arrow) as the *NA* is increased. The line-sectional plots (circles – x-axis, crosses – y-axis) were compared against the scalar analysis (dashed lines) discussed in Section 4.2. The red arrow indicates the polarisation direction.

4.5.1.4 Annular Aperture Analysis

In an extension to this model, aperture-function engineering effects were investigated in order to reduce the focal spot size further. The obscuration aperture diameter increased from a minimum normalised value of 0 to a maximum normalised value of 0.99. These results are presented in Fig. 12 through Fig. 16 (below – full page). The line-sectional plots (circles – x-axis, crosses – y-axis) were compared against a scalar analysis and highlight an additional reduction in spot size along the x-axis. The red arrow indicates the polarisation direction. The elliptical nature of the focal spot, illustrated in the model, is accessible experimentally in high-*NA* focusing environments such as SIL imaging inside silicon ICs.

I would like to acknowledge Prof. Derryck Reid and Marcel Leutenegger for their contribution towards preparing the MATLAB code required to present the vectorial-field results given below.

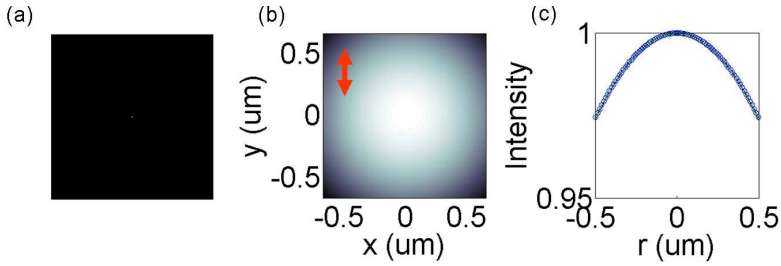

Figure 7 - Theoretical calculations of the focal-plane energy density distribution of linearly-polarised light using the Leutenegger theory presented above [38]. Here we illustrate (a) the aperture function used at *NA*=0, (b) the 2D cross-sectional plot across the xy plane and (c) its accompanying line-sectional plots (circles – x-axis, crosses – y-axis) compared against scalar theory (solid black line). The red arrow indicates the polarisation direction

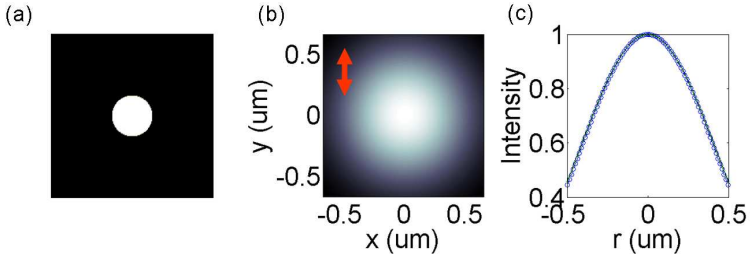

Figure 8 – As for Fig. 7 except with *NA*=0.25

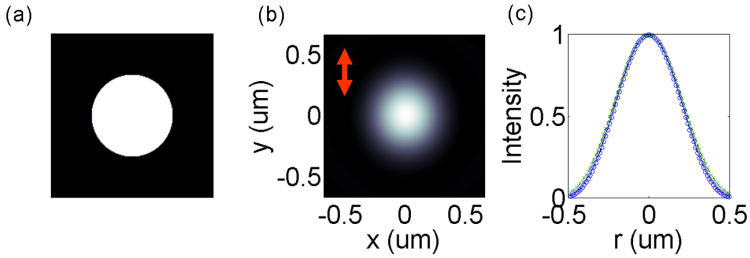

Figure 9 – As for Fig. 7 except with *NA*=0.5

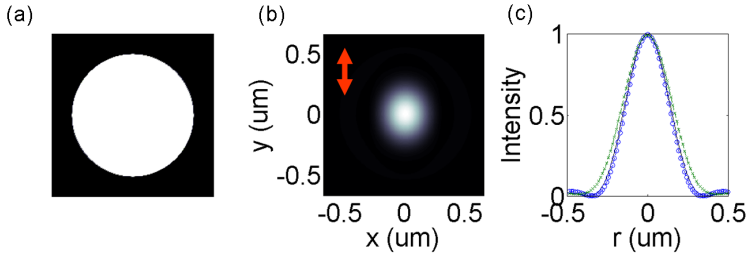

Figure 10 – As for Fig. 7 except with *NA*=0.75

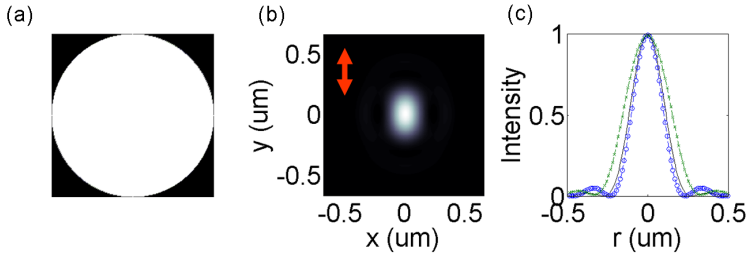

Figure 11 – As for Fig. 7 except with *NA*=1

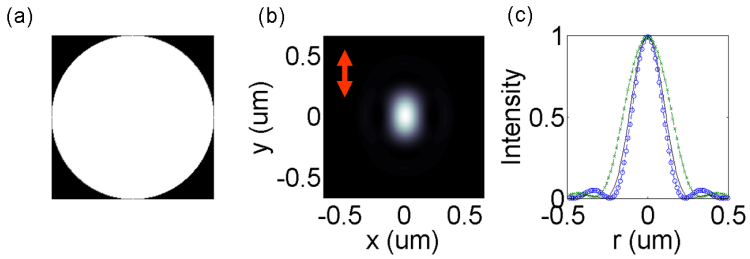

Figure 12 - Theoretical calculations of the focal-plane energy density distribution of linearly-polarised light using the Leutenegger theory presented above [38]. Here we illustrate (a) the aperture function used whose obscuration diameter was 0, (b) the 2D cross-sectional plot across the xy plane and (c) its accompanying line-sectional plots (circles – x-axis, crosses – y-axis) compared against scalar theory (solid black lines). The red arrow indicates the polarisation direction

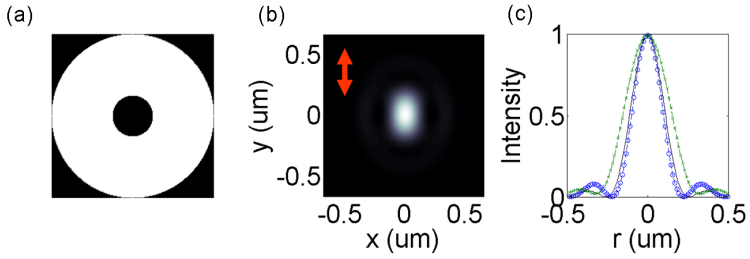

Figure 13 – As for Fig. 12 except with a normalised obscuration diameter of 0.25

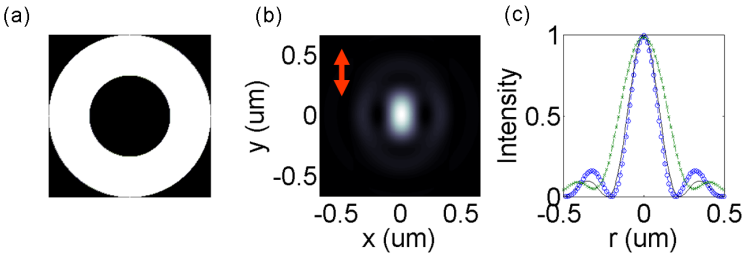

Figure 14 - As for Fig. 12 except with a normalised obscuration diameter of 0.5

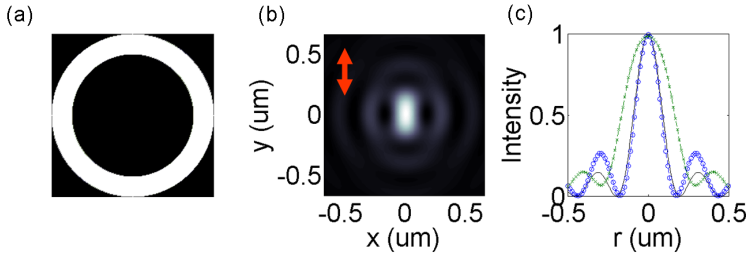

Figure 15 – As for Fig. 12 except with a normalised obscuration diameter of 0.75

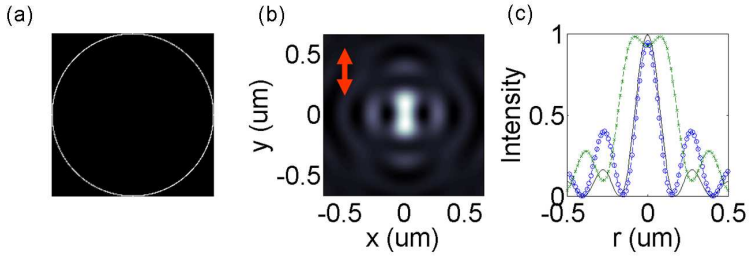

Figure 16 - As for Fig. 12 except with a normalised obscuration diameter of 0.99

Although the above theoretical analysis was investigated under linear polarisation conditions, the incident optical radiation need not be limited to this individual polarisation state. In addition to linear polarisation, it is possible to obtain radial, circular or azimuthal polarisation illumination. All of these polarisation states introduce unique focal-plane electric-field distributions which vary under extreme *NA* conditions and the introduction of annular apertures. These effects are described below.

The focal-plane electric-field distribution contains two components: a transverse (radial) and a longitudinal (axial) field. These components can be controlled (i.e. enhanced or suppressed) through careful consideration of the focusing characteristics of the imaging system. Essentially, under low-*NA* conditions the longitudinal component is negligible when compared against the transverse component; whereas, the longitudinal component becomes more dominant as the *NA* is increased. This longitudinal dominance can be understood through the bending of light rays as they pass through a high-*NA* lens. Immediately before the focusing lens the entire ray bundle across a plane-wave consists of purely transverse components; however, when the wave is influenced by the lens the paraxial components along the optical axis remain unperturbed while the non-paraxial rays are refracted towards the optical axis. This refraction (focusing) becomes stronger as one approaches the edge of the lens and therefore distorts the plane-wave to a larger degree. As a result, the field represented by this modified wavefront is now decomposed into both transverse and longitudinal components, where the magnitude of the longitudinal field component increases with increased refraction. This transverse and longitudinal electric-field description is shown in Fig. 17.

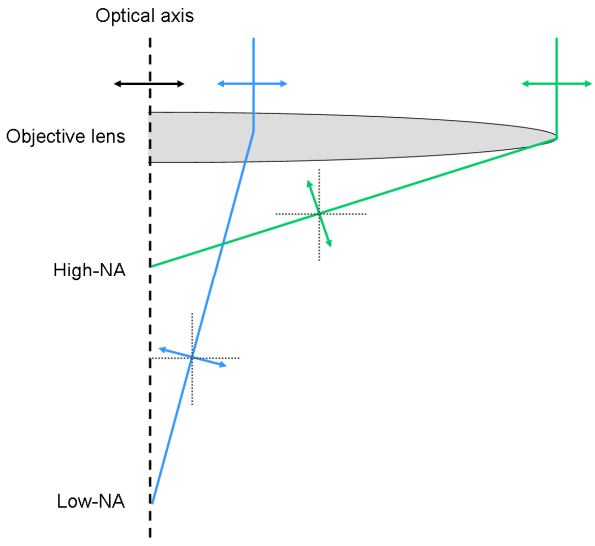

Figure 17 – Transverse and longitudinal components of the focused electric-field as the optical rays extend from low-*NA* to high-*NA*

These effects, along with careful consideration of the polarisation state of the incident illumination, are represented in Fig. 18. This figure illustrates both the transverse and longitudinal components of a focal-plane electric-field distribution for linear, radial and circular polarisation while highlighting the influence of increased *NA* and the introduction of an annular aperture.

For a linearly-polarised beam the longitudinal electric-field component separates into two off-axis side-lobes and is cancelled along the optical axis. For a radially-polarised beam the longitudinal component forms an intense circular spot located on the optical axis. For a circularly polarised beam the longitudinal component forms an annulus which is centred on the optical axis. Under high-*NA* conditions, the longitudinal components of the focal-plane electric-field distribution become dominant and result in an elliptical focal spot for linearly-polarised light and a circular focal spot for both radial and circularly-polarised light. In addition, with the inclusion of an annular aperture only the high-*NA* rays contribute to the electric-field distribution at the focus. Therefore, as the on-axis obscuration is increased, the transverse component is gradually suppressed and the longitudinal component enhanced. This indicates that for the best performance in the search for optical super-resolution, a radially-polarised beam has to be employed along with an annular aperture under high-*NA* conditions. However, for simplicity our work concentrated on linearly-polarised illumination – the generation of spatially non-uniform polarisation distributions is difficult and requires specialist components.

Note here that although an azimuthal polarisation state was also mentioned it was not considered in the above illustration because its electric-field distribution is exclusively transverse, even under high-*NA* conditions. As a result, this arrangement would never result in a performance enhancing super-resolution option and was therefore not discussed.

The resolution enhancing effects of linearly-polarised illumination were studied experimentally, in the absence of aperture-function engineering effects, and in the following section we report ultra-high-resolution sub-surface imaging of a silicon flip-chip using a SIL, obtaining average resolution values from 122 – 240nm, depending on the polarisation state used, and the relative orientation of the features under inspection.

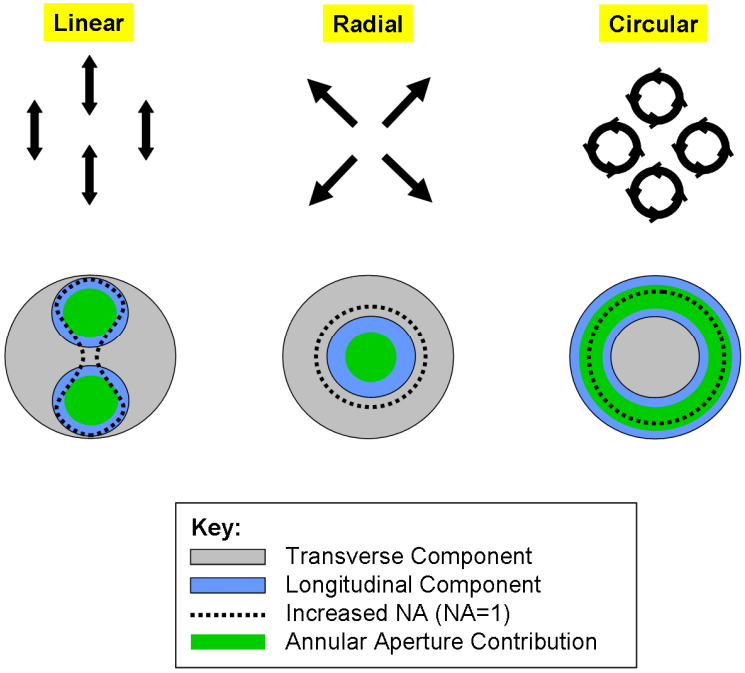

Figure 18 – Illustration for both the transverse and longitudinal components of a focal-plane electric-field distribution for linear, radial and circular polarisation while highlighting the influence of increased *NA* and the introduction of an annular aperture.

4.6 Polarisation-Dependent Imaging Results

4.6.1 Experimental Configuration

To investigate the role of polarisation under high-*NA* conditions we implemented TOBIC imaging using essentially the same experimental configuration described in Chapter 3. This configuration is shown in Fig. 19, where two-photon excitation was achieved through the use of a 1550nm modelocked erbium-fibre laser whose linearly-polarised output beam overfilled an objective lens of *NA* = 0.55. A half-wave plate positioned before the objective lens allowed the polarisation direction of the beam to be controlled. The laser generated 160fs pulses at a repetition frequency of 30MHz with an average (peak) output power of 75mW (15.6kW), and its output was focused by the objective lens through a silicon s-SIL into the device under test. We used a silicon s-SIL based on the prescription described earlier and demonstrated by Ippolito *et al* for aplanatic imaging, which states that a structure buried at a depth, *X*, can be imaged using an s-SIL whose vertical thickness is $R(1+1/n)-X$ where *R* is the SIL radius of curvature and *n* is its refractive index [49]. When this condition is fulfilled, no spherical aberration is introduced into the image. The sample was the same CMOS silicon flip-chip used for the work of Chapter 3, which was fabricated using 0.35µm technology and had an exposed silicon substrate which had been optically polished to a thickness of

100µm. A photo-current was generated and collected at the device terminals through two-photon carrier generation at the device layer of the chip [50] and acquired using narrow-band amplification and lock-in detection via a digital oscilloscope and PC. The device under test was mounted on a computer-controlled motorised three-axis translation stage which had a minimum physical stepping increment along each axis of 100nm, corresponding to a minimum optical stepping interval of around 8.3nm [36].

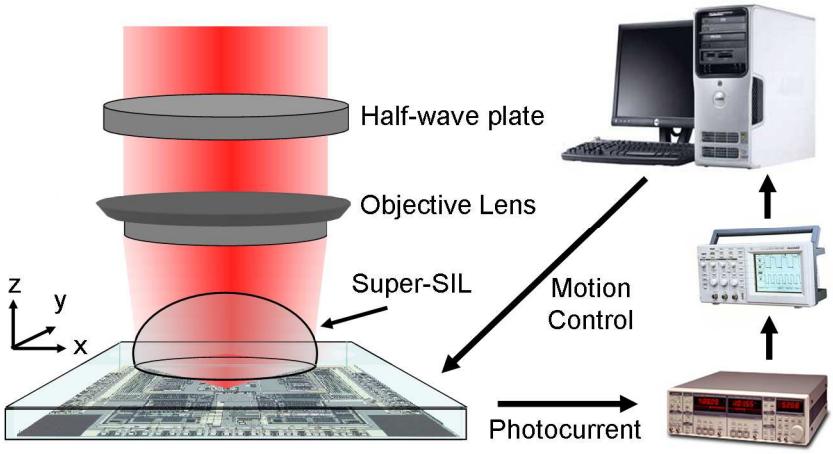

Figure 19 – Experimental arrangement for polarisation-dependent imaging of a silicon flip-chip showing computer-aided control and acquisition.

4.6.2 Qualitative Analysis

It is natural to expect that the experimental results obtained under vectorial focusing would be clear to interpret. The different imaging outcomes obtained by using orthogonal linear polarisation states are illustrated in Fig. 21(a)-(b). We performed high-resolution TOBIC imaging on an interesting section of the chip containing n-type silicon fingers which were bordered by a metallisation region. This area is highlighted by the red box in Fig. 20. The tip of each silicon finger contained a 3×3 matrix of tungsten vias which interconnected the silicon device layer with the first metallisation layer. These tungsten vias are essentially small metal wires that interconnect two layers of the IC. The detailed images shown in Fig. 21(a)-(b) have a $13\mu m \times 6.5\mu m$ field-of-view and a vertical (horizontal) optical sampling interval of 18nm (58nm).

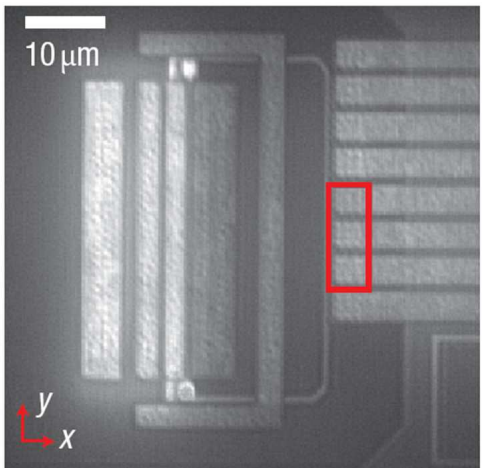

Figure 20 – Wide field-of-view TOBIC image recorded for navigation purposes and indicating the region (red box) at the end of three finger-like structures imaged at maximum resolution

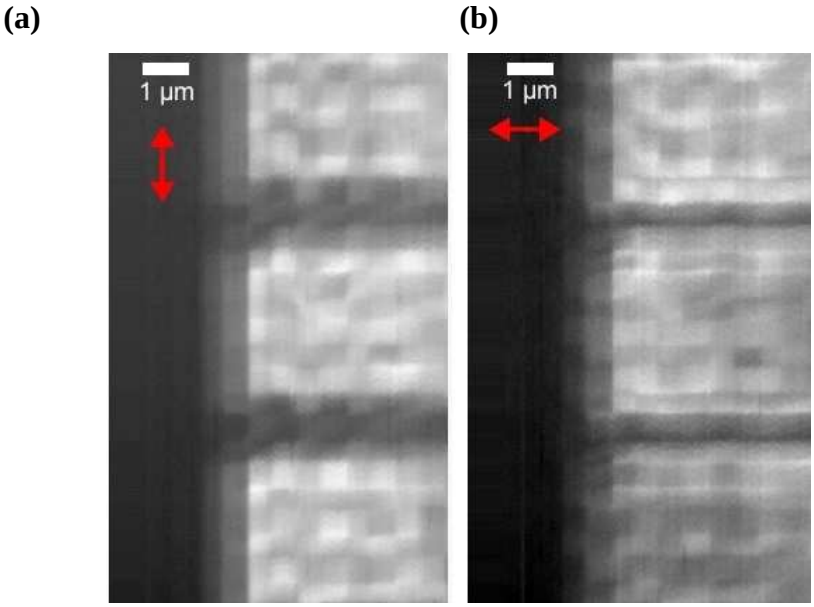

Figure 21 – (a), (b) TOBIC images of the red boxed region showing three 3x3 grids of tungsten vias obtained under the linear polarisations indicated by the red arrows. Lighter image rendering indicates a higher TOBIC photocurrent and the left sides of the detailed finger images have been padded with black to allow the scale bar to appear on a uniform background. The PSF is narrower in the direction normal to the polarisation vector, therefore the gaps between the fingers are better resolved when the polarisation vector lies along the finger edges (b)

The polarisation state used for the image acquisition is indicated in these figures by the red arrow. Lighter image rendering indicates a higher TOBIC photocurrent and the left sides of the detailed finger images have been padded with black to allow the scale bar to appear on a uniform background. The numerical investigations performed earlier inform

us that vectorial focusing theory predicts that the focal spot is elongated along this polarisation direction. The imaging attributes of this focal spot asymmetry are clear to see in the two figures. When the polarisation vector is aligned to be parallel to the gap between the fingers, the feature edges appear sharper and more clearly resolved. In contrast, when the polarisation vector is rotated to become perpendicular to the features under inspection, the edges between the fingers become blurred and the gap between the fingers appears to be wider.

4.6.3 Quantitative Analysis

In order to study this polarisation-dependent effect in a quantitative manner we examined the transition in the acquired image signal as the optical beam was scanned across both the horizontal and vertical edges of the n-doped silicon fingers. The line-cuts through the image data are shown in Fig. 22 (symbols) and were fitted to a Gaussian error function (this process was described in Chapter 3) to determine the width of the PSF in each orthogonal direction and for each polarisation state. The results obtained demonstrate a difference in resolution for data acquired with opposite polarisation states when scanning across the gaps between neighbouring fingers by a factor of two (122nm and 251nm); however, a smaller polarisation-dependent difference (119nm and 172nm) was measured for data obtained by scanning into the tip of a finger. This can be explained by considering the interaction of the focused optical field with the different metal and dielectric environments encountered by the beam in different regions of the device. When a focused beam is scanned into an isolated edge (the finger-tip) it will generate a different result to a beam which is scanned across two or more closely-neighboured edges. This effect takes place since, in the latter condition, the optical near-field will interact with the two edges simultaneously, whereas in the former condition this additional interaction is removed. Ultimately, the numerous optical / material interaction environments to be found within a silicon IC will modify the images obtained as the light interrogates different locations on the chip.

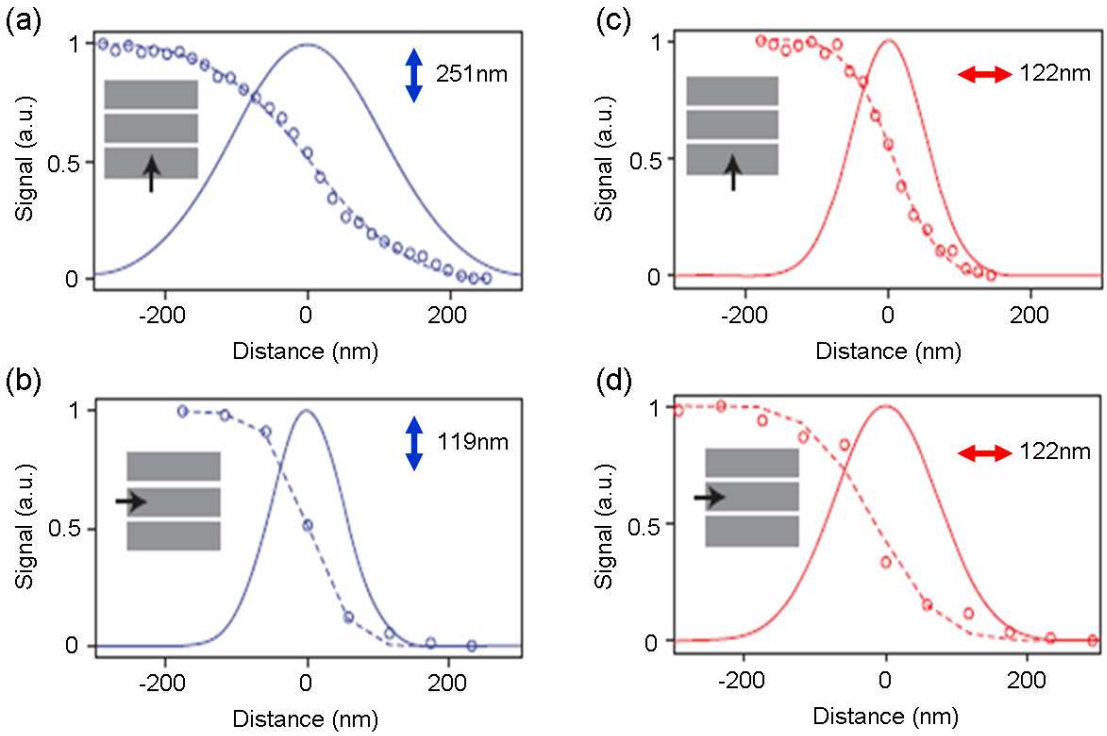

Figure 22 - Resolution measurements obtained under different polarisation conditions. (a), (b) - Line cuts through the detailed image shown in Fig. 21(a), which was recorded for incident light with a wavelength of 1550nm polarised parallel to the y-direction (as defined in Figure 20). (c), (d) - Equivalent data recorded for the image acquired with the orthogonal polarisation state, which was parallel to the x-direction (see Fig. 21(b)). The polarisation direction in each panel is indicated by the blue or red arrows, and the focal-spot shape is inferred by the PSF FWHMs from the Gaussian fits to the data. The scan direction of the beam relative to the sample is indicated by the black arrow

The asymmetry of the tightly-focused spot was also investigated by acquiring multiple resolution measurements over the same edge while the electric-field polarisation vector was rotated. In order to obtain these measurements we rotated the half-wave plate in our experimental system through 360° which corresponded to turning the direction of the electric-field polarisation through 720°. The polarisation direction has a period of 180° (an AC field polarised along an angle ϕ is indistinguishable from one polarised along an angle ϕ+180°). Therefore, the modulation of the measured optical resolution from our results is expected to have a period of 180°. The results, inferred from individual line scans performed across one of the gaps between adjacent fingers, are illustrated in Fig. 23 and confirm this anticipated periodic behaviour. The red curve in the figure is a least-squares fit to the data, and the fitting function is the diameter of an ellipse drawn at a variable angle to one of its principal axes. The upper and lower error bar half-widths represent, respectively, one standard deviation (31nm) between the fit and the data, and the measurement error for each data point was estimated to be ± 17nm.

The presented results reveal random fluctuations in the resolution data. This can be attributed to small variations in the beam-pointing direction which can be introduced by rotating the half-wave plate. The fitted curve implies polarisation-dependent minimum and maximum resolutions of 122nm and 240nm respectively (a ratio of 1.97); however we consistently observed resolutions of approximately 100nm under optical adjustment of the wave plate.

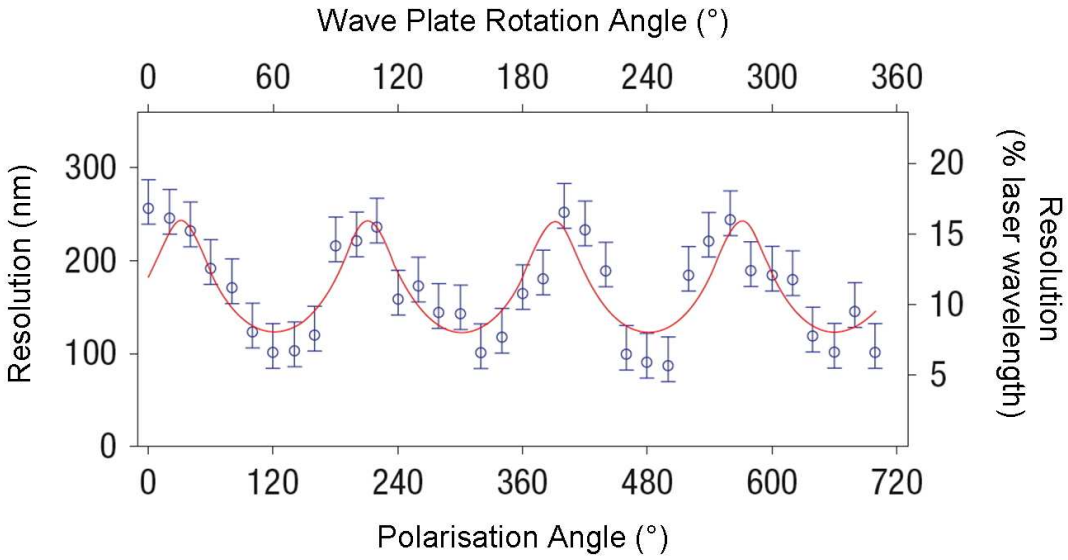

Figure 23 - Dependence of measured resolution values on polarisation direction. The resolution measurements were recorded at half-wave plate angular intervals of 10° and show a 180° period in the electric-field polarisation direction, which is a result of the ellipticity of the focal spot. A least-squares fit to the data (solid curve) implies polarisation-dependent minimum and maximum resolutions of 122nm and 240nm, respectively (a ratio of ~2), with a standard deviation of 31nm (upper error bars) from the fitting function. The measurement error associated with each data point was around +17 nm (lower error bars). The laser wavelength was 1550nm.

4.6.4 Discussion and Summary

The theoretical analysis presented by Leutenegger, which was discussed earlier, and shown in [38], allows us to explain the experimental results obtained. The optical systems used to perform this experiment required an expanded beam to moderately overfill the pupil of the objective lens used to focus light into the s-SIL. The beam diameter (defined at the $1/e^2$ intensity points) was recorded to be 6.2mm at the entrance to the 6 mm diameter objective lens pupil. In our silicon s-SIL imaging configuration the maximum useful *NA* of the objective lens is 0.29. This is because refraction at the s-SIL interface increases the *NA* by a factor of n^2, up to a maximum value of the refractive index of silicon (3.48). Any additional high-*NA* rays from the objective lens will overfill the SIL and not contribute to the optical signal. By overfilling the 0.55*NA* objective lens

we therefore ensured an approximately uniform radial irradiance distribution immediately before the s-SIL. As a result, we are able to interpret and understand the focusing characteristics of the system by assuming that the incident optical beam is composed of linearly-polarised plane-waves.

Through the use of a suitably designed s-SIL we have been able to demonstrate an optical system that can satisfy the conditions required for high-*NA* vectorial focusing. For s-SIL imaging we have *NA*=3.48, corresponding to the near-infrared refractive index of silicon. Fig. 11(b) illustrates the irradiance distributions calculated for this *NA* in the xy focal plane. In this theoretical calculation the incident beam was polarised along the y-axis and the results indicate that the PSF is extended in the direction parallel to the incident polarisation vector by a factor of 1.3. This asymmetry in the focal spot size is consistent with our qualitative results which show that, when scanning over a sharp silicon-metal edge, the best resolution is obtained when the beam is polarised parallel to the edge. When these conditions are achieved, the width of the PSF is minimised in the scanning direction. This results in an improved signal transition rate from a high to a low value, or vice versa, as the spot is scanned over the feature edge, as observed experimentally.

Although the theoretical magnitude and direction in which the focal spot extends is consistent with experiment, a comparison with the resolution values determined from our line scans with the focal-plane irradiance calculated from [38] highlights two discrepancies. The first is the absolute size of the PSF inferred from the resolution measurement, and the second is the ratio between the PSF widths in the x- and y-directions. Both of these differences can be explained by the fact that the presence of an interface near the focal-plane can further increase the ellipticity of the focal spot [51]. It has also been reported, through detailed modelling of light tightly focused by a glass s-SIL [52], that an ellipticity in excess of 1.7 at an air-glass interface can be achieved, and a decrease in the focal spot's FWHM diameter perpendicular to the E-field direction can fall below the conventional diffraction-limited value.

In our experiment the optical beam is focused into the 300nm-thick device layer of a silicon IC which forms an interface with an oxide, poly-silicon or metal layer, depending on the precise location being imaged. It is therefore likely that this interface is responsible for the enhanced ellipticity of the focal spot shape beyond the values

predicted for focusing in bulk silicon; however, 3D details of the device structure were not available at the time of the experiment but would be required to perform a rigorous calculation of the focal-plane electromagnetic field distribution. The minimum experimental PSF width of 120nm is substantially lower than the 181nm FWHM width of the theoretically calculated PSF (note that the effective $\sqrt{2}$ reduction in the PSF width caused by nonlinear excitation has been taken into account). Furthermore, in addition to the effect of a refractive-index interface being present in the vicinity of the focal-plane, the irradiance distribution of the illumination beam may also be responsible for reducing the PSF width to below the expected value. Vector field calculations carried out for tightly focused beams show a strong sensitivity of the focal spot size and shape to the incident spatial irradiance distribution and polarisation state which is capable of reducing the spot size by approximately a additional factor of 0.7 beyond the conventional (scalar) diffraction-limited value [41, 53]. The greater apparent polarisation asymmetry observed experimentally in the PSF may also be a result of the same effect; the analysis presented in [41] indicates that the reduction in spot size is only observed along the direction orthogonal to the polarisation vector, therefore increasing the rotational asymmetry of the focal spot. The incident spatial irradiance distribution and polarisation state can be strongly modified by the significant differences in the Fresnel transmission coefficients for radial and azimuthal polarisations at the spherical surface of the solid immersion lens, and across the gap between the solid immersion lens and the substrate [49]. These effects could also contribute to the polarisation asymmetry reported here. Other physical processes, for example plasmon excitation in the metal edge by the tightly focused rays, may also play contribute to the modification of the apparent focal-plane PSF; however this explanation requires further investigation.

It is anticipated that the vectorial focusing effects explained here may present the option of polarisation-diversity imaging in future applications. Polarisation-diversity imaging is an optical technique where multiple images of the same object are obtained for different polarisation states and combined with suitable image processing techniques to yield images with resolutions in all directions that substantially surpass the conventional diffraction-limited value. In biological imaging the possibility of improving traditional resolutions at longer wavelengths by adopting this approach holds great potential; however, the highest resolutions are usually obtained at visible wavelengths where the spectrum suffers from strong scattering and can also be damaging to the cells under

inspection. Polarisation-diversity imaging is also becoming established as a tool for revealing hidden structure in biological samples [54], and therefore it may be possible to use multiple images acquired under high-*NA* focusing to both improve the imaging resolution and obtain structural information about a sample.

Finally, although polarisation-depenent imaging under nonlinear excitation has been demonstrated in this work, the resolution enhancing properties of vectorial focusing can offer the same benefits to all commonly used variants of linear confocal microscopy also.

4.7 Hybrid Annular Aperture / Polarisation-Dependent Imaging

The results demonstrated in the previous section confirmed that the vectorial nature of the focused field can be of critical importance in an imaging system since the resulting focal spot geometry is a function of increasing *NA*. As the *NA* approaches unity the longitudinal components of the electric-field dominate over the weaker transverse components. This leads to a redistribution of the radial intensity of the PSF in the focal-plane which, at high-*NA*, becomes highly sensitive to the polarisation state of the incident illumination. Various computational methods are now available to allow the focal field to be evaluated efficiently for any known field distribution in the pupil-plane of the lens [38-40, 55]. The theory of Richards and Wolf was the first to discuss the focal properties of linearly-polarised light at high-*NA* and demonstrated that for a system which satisfies these conditions the resulting focal-plane intensity distribution is approximately elliptical, with the ellipse extended along the incident polarisation direction. As discussed already, this asymmetry in the focal spot distribution leads to different resolutions recorded along orthogonal directions in an image [56].

As introduced in Section 4.3, an enhancement in resolution can be achieved by manipulating the irradiance distribution in the pupil-plane of the lens so as to reduce the dimensions of the focal spot below those obtained in the clear-pupil case. In particular, the use of annular pupil-plane apertures in the tight-focusing regime has been the subject of a number of theoretical investigations which collectively highlight the advantages of simple single and multiple-zone annular apertures for improving the lateral resolution as well as manipulating the focal-volume and depth-of-focus through the isolation of the illuminating high spatial frequencies [41, 47, 57-60]. An experimental demonstration of a similar approach by Botcherby *et al* discussed

stereoscopic imaging with an extended depth-of-focus PSF in two-photon fluorescence mode with a lateral resolution of ~200nm [61], corresponding to approximately $\lambda/4$ of the free-space illumination used. Ippolito *et al* used annular illumination to improve the longitudinal localisation of the electrical response of an IC to optical excitation by suppressing the contribution of sub-critical image-bearing rays reflected by the metallisation region of the device [62]. We note that, despite sharing common features with the results we present here, the work in [62] was based on linear confocal microscopy and was not concerned with using annular illumination to improve the lateral resolution of the image.

Although annular illumination achieves a reduction in the central width of the focal spot, this lateral improvement comes at the expense of generating considerable side-lobes that, under linear imaging conditions, tend to diminish the advantages of the technique. Nonlinear imaging however, in the form of two-photon-excitation fluorescence [63] and TOBIC microscopy [50], produces an image-bearing signal that depends quadratically on the focal intensity, suppressing the side-lobes produced by annular illumination. Consequently, combining annular illumination with nonlinear microscopy promises a significant improvement in lateral resolution; however to our knowledge, no experimental study has yet presented a quantitative and qualitative demonstration of this lateral resolution enhancing performance of the magnitude presented in this section (although the accompanying axial effect has been reported in two-photon fluorescence microscopy [61, 64]).

It is clear from a review of the available literature that there exists an extensive range of possible experimental configurations which can be adopted to achieve optical super-resolution when one has available an appropriate SIL, a selection of annular apertures and a means to manipulate the polarisation state of an incident optical field. Many of these super-resolving techniques have been investigated in some form of hybrid arrangement. Some consider a combination of binary annular amplitude and phase apertures [65], others consider annular apertures along with a SIL [66, 67], or have investigated aperture performance under extreme *NA* conditions [68, 69] including novel elliptical apertures [70].

In the work reported in this section, we present high-resolution images of sub-micron structures in a silicon IC, obtained by nonlinear excitation under tight-focusing

conditions using a silicon SIL. These images manifest the asymmetric resolution values expected in this tight-focusing regime, and by employing a series of annular pupil-plane apertures we have demonstrated up to a 64% reduction in the effective area of the focal spot, compared with the values obtained using a clear pupil. In addition, it was found that an increased depth-of-focus creates an extended TOBIC sensitivity regime since nonlinear excitation is dependent on the squared intensity within the focal volume. The integration of the TOBIC signal over a greater depth-of-focus results in a TOBIC image with a reduced contrast.

4.7.1 Experimental Configuration

Our imaging method and apparatus is almost identical to that described in Section 4.6.1 except for the introduction of a set of custom annular apertures positioned immediately before the objective lens. We employ focused light from a 1550nm femtosecond fibre laser to induce two-photon absorption inside a silicon IC. Silicon is normally transparent at wavelengths longer than its band-edge at around 1.05µm; however coincident photons at a longer wavelength can excite carriers via two-photon absorption, causing a measurable photocurrent to flow in an external circuit connected to suitable pins of the device under test. By mapping this photocurrent as a function of focal position it is possible to image the electronic topology of the device in three dimensions [71, 72]. A particular advantage of two-photon excitation is the quadratic dependence of the measured signal as a function of optical intensity. This has the dual effects of confining the signal generation to the focal-plane of the light and of reducing the effective focal spot size below the actual dimensions of the optical focus. An illustration of the experimental configuration is presented in Fig.24.

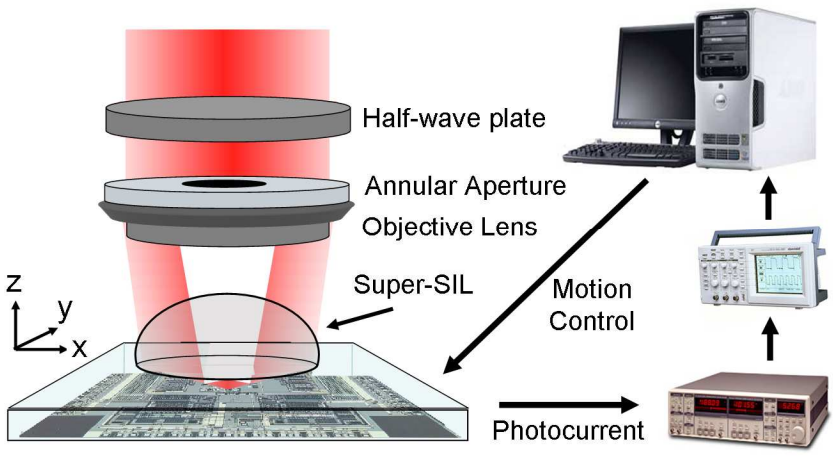

Figure 24 – Experimental configuration of the annular aperture polarisation-dependent TOBIC microscopy arrangement

4.7.2 Analysis and Discussion

Fig. 25 shows a series of images recorded in a region of a CMOS IC comprising eight parallel n-doped silicon-on-metal fingers, the tips of which contain a 3×3 matrix of tungsten vias which interconnect the silicon device layer with the first metallisation layer in the circuit. Fig. 25(c) illustrates the area on the chip that is being imaged - highlighted by the red box. The fingers have widths of 4.5 µm and are separated by gaps of 500nm, while the tungsten vias are spaced at a pitch of 1.25µm and have approximate dimensions of 100 nm (diameter) and 500 nm (depth). Two sets of three images were recorded for incident light with orthogonal linear polarisations, and with the focus positioned to resolve the edges of these fingers to an accuracy which matched previous performance [56]. The images in Fig. 25(a) were acquired using a linear polarisation state lying orthogonal to the fingers, and those shown in Fig. 25(b) were obtained using a polarisation lying parallel to the fingers. Within each set of images, the far-left image was recorded using illumination through a clear pupil, and the remainder (from left to right, respectively) was acquired using pupil-plane annular apertures where the centre 36% and 55% of the aperture was blocked. The polarisation-dependent shape of the focal spot can be seen immediately from the images in Fig. 25. The features in Fig. 25(a) were illuminated with a focal spot that was elongated across the gap between the fingers, causing this gap to be imaged with poorer resolution, but the edges at the finger tips to be more clearly resolved. In the images shown in Fig. 25(b) the opposite is true, with the focal spot resolving the gap between the fingers more clearly but producing a less distinct image of the finger tip edges. Two effects of using an annular irradiance distribution can be seen visually from the results in Fig. 25. The clear aperture results (Fig. 25(a) and (b), left) plainly resolve the 3×3 matrix of tungsten vias. As a greater proportion of the lower *NA* rays are blocked, the gaps between the fingers become more clearly resolved, as expected from theory. Furthermore, the contrast of the 3×3 matrix of tungsten vias becomes poorer because the depth-of-focus increases, resulting in a signal that contains image information integrated throughout a greater depth of the device, reducing the contribution from the image-plane containing the tungsten vias. The improvement in image resolution associated with using the annular illumination can be investigated quantitatively by observing the transition of the signal as the focal spot traverses across an edge in the image. In Fig. 26 we show a series of line-cuts across one of the gaps between two adjacent fingers, with Fig. 26(a) showing these data for an incident polarisation orthogonal to the fingers, and Fig. 26(b) the data for a polarisation lying parallel to the fingers. The effective focal-spot diameters inferred from these

results are shown in the insets of Fig. 26, indicating an average reduction in the focal spot diameter along both directions of around 40%, corresponding to a 64% reduction in the area of the focal spot (measured in the plane containing the edge of the fingers).

It is well known that an annular pupil-plane aperture leads to an extended depth-of-field [20]. Inspection of the images in Fig. 25 shows that the 3×3 matrix of tungsten vias, which occupies an axial extent of 500nm, was imaged with lower contrast when an annular aperture was used; improved lateral resolution is effectively obtained at the expense of poorer depth resolution. This effect can be understood qualitatively by realising that the extended focal depth due to an annular pupil gives a TOBIC signal that is integrated over a greater depth. Depth-localised structures therefore make a proportionately lower contribution to the signal level than in the case of an open pupil.

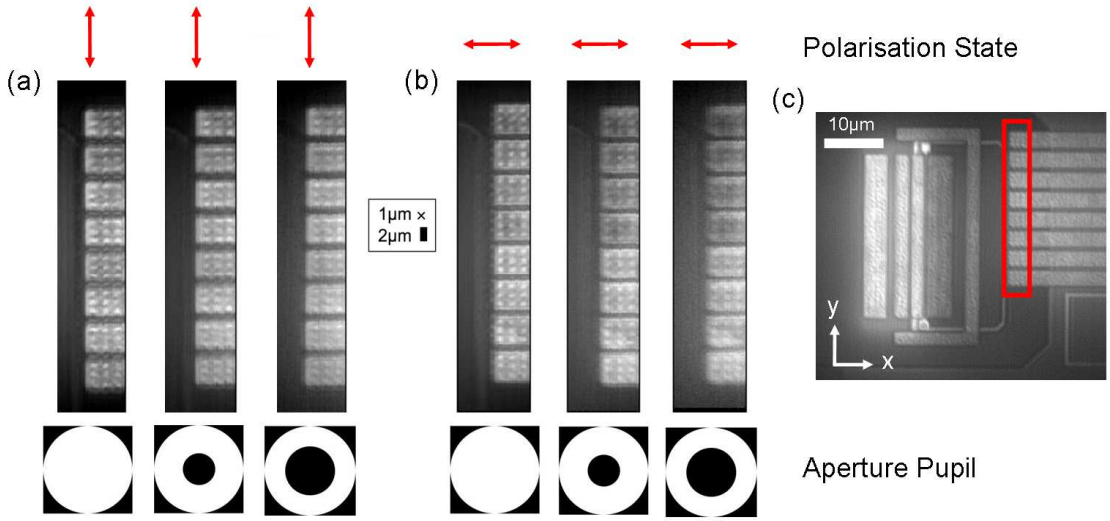

Figure 25 – TOBIC images of the tips of eight parallel silicon-on-metal fingers that form part of a CMOS IC, with the images in (a) acquired with a pupil polarisation oriented orthogonal to the fingers, and those in (b) obtained using an incident polarisation parallel to the fingers. The pupil-plane aperture used in each measurement is indicated schematically below each image. An improvement in resolution is clearly seen as the aperture is adjusted to obscure more of the centre of the pupil. (c) illustrates the area on the chip that is being imaged - highlighted by the red box

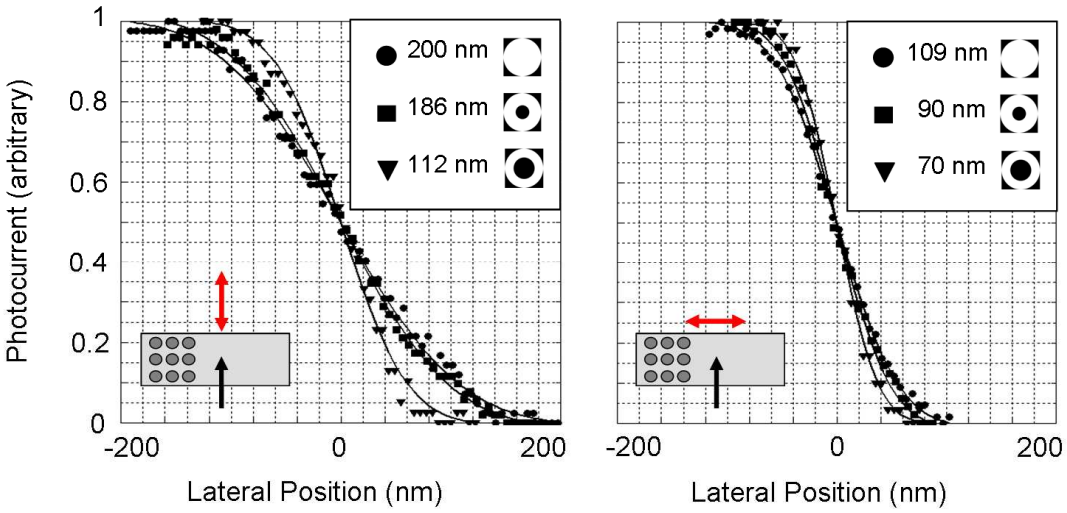

Figure 26 – Line-cuts extracted from the images shown in Fig. 25 and shown for the transition across one of the edges between two adjacent fingers. The results in (a) correspond to a pupil polarisation oriented orthogonal to the finger edges, and those in (b) to an incident polarisation parallel to the finger edges. The experimental data are indicated by symbols. The solid line is the Gaussian error function which is the best-fit to the experimental data, and was used to infer the effective focal-spot diameter in the measurement plane (values shown in the inset). The illustration at the bottom right-hand-side of each image indicates the beam scanning direction (black) and the polarisation orientation (red).

Obtaining exact agreement between experiment and vectorial diffraction theory is difficult in a sample such as a silicon IC in which the dielectric environment is highly non-uniform, and local structure on the scale of the wavelength can significantly influence the field distribution. Nevertheless, it is still possible to obtain a semi-quantitative understanding of the TOBIC contrast mechanism by using vectorial theory to model the size and structure of the optical intensity distribution in the focal region under plane-wave illumination. We configured a simulation which first used the method of Leutenegger [5] to calculate the 3D focal intensity distribution resulting from an open pupil (Fig. 27(a)), and from an annular pupil similar to the largest obscuration one used experimentally (Fig. 27(b)). The darker, smaller volume indicates a contour drawn at the 50% intensity point, and the lighter, larger region a 13% intensity contour, equivalent to the $1/e^2$ radius commonly used in Gaussian optics. The extended depth-of-focus resulting from using an annular pupil is apparent by comparing Fig. 27(a) and (b). The electrical response of the device was modeled by evaluating the two-photon photocurrent generated in a voxel of depth Δz, which is proportional to $I^2\alpha_2\Delta z$ where I is the optical intensity and α_2 is the nonlinear absorption coefficient. A region representing the edge of one of the semiconductor finger structures was modeled as a

3D volume with one quadrant having $\alpha_2 \neq 0$ and the remaining volume having $\alpha_2 = 0$. Within the absorption sensitive quadrant we represented a tungsten plug (see Fig. 3(c)) as a 200nm (diameter) $\times$ 500nm (height) column with $\alpha_2 = 0$. The 3D focal intensity distribution was centered axially within this synthetic environment and the integrated two-photon photocurrent was recorded as the focus was scanned laterally throughout the entire volume. Fig. 27(d) shows the simulated TOBIC image obtained for an annular pupil, with the boundaries of the modeled semiconductor region and the tungsten via indicated by white lines. Sections through the image are shown in the insets of Fig. 27(d) and are compared with similar sections through an image calculated for an open pupil (Fig. 27(d) inset, dashed lines). The sections illustrate that the modeled tungsten via is observed with lower contrast when using an annular pupil-plane aperture, consistent with the experimental images presented in Fig. 25.

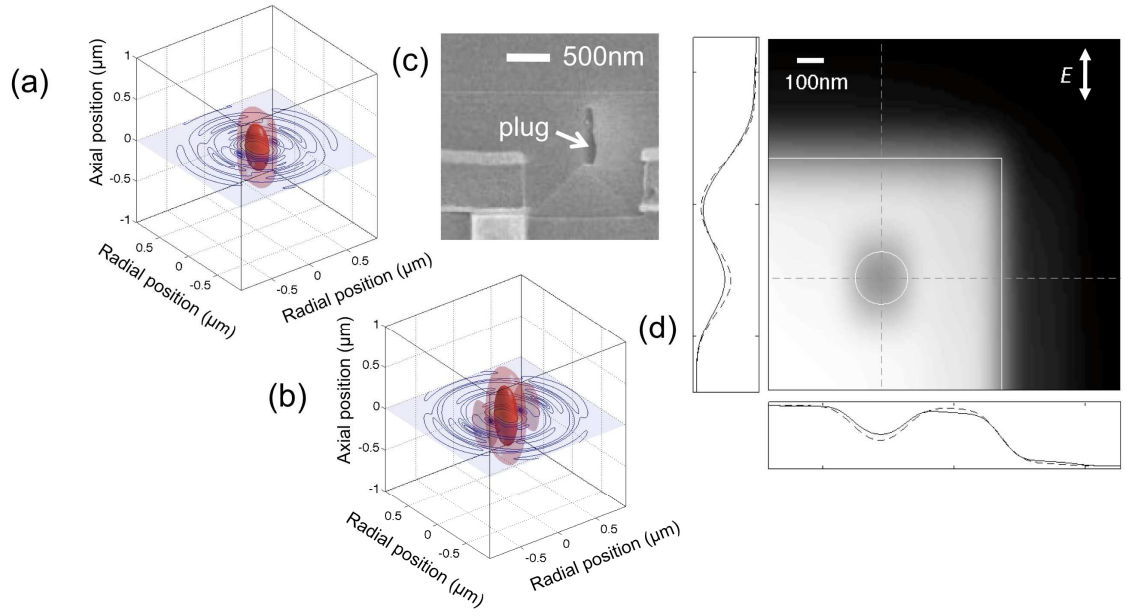

Figure 27 - Simulation results illustrating the decrease in contrast observed using an annular pupil-plane aperture when imaging a region containing narrow metal plug that does not contribute to the two-photon signal. (a, b) 3D PSFs produced by open (a) and annular (b) pupils similar to those used experimentally, with the darker, smaller volume being a contour drawn at the 50% intensity point, and the lighter, larger region a 13% intensity contour, equivalent to the $1/e^2$ radius commonly used in Gaussian optics. (c) Scanning electron microscope image of a section through the experimental device showing a tungsten plug of the kind simulated. (d) Simulated TOBIC image for an annular aperture similar to the largest radius aperture used experimentally. The solid white lines show the boundary of the two-photon absorption region and the circle indicates the diameter of the simulated metal plug. The line-sections along the dashed lines in the main image show the contrast with which the plug is resolved. The solid and dashed cross-sections correspond, respectively, to using annular and open pupils.

I would like to acknowledge Prof. Derryck Reid and Marcel Leutenegger for their contributions towards preparing the MATLAB code required to present the vectorial-field results given above.

4.7.3 Summary and Conclusions

In this Section we have reported results demonstrating how annular pupil-plane apertures can improve the optical resolution obtained in a microscope operating under high *NA* conditions [73]. Under such tight-focusing, and with linearly-polarised illumination, the focal spot is asymmetric, and we showed a lateral resolution enhancement from 200×109nm to 112×70nm, an approximately 64% improvement in terms of the area of the focal spot. Significantly, our results show that, for a nonlinear microscope already operating close to the limits of optical resolution (as indicated by the presence of vectorial effects), pupil-function engineering can usefully enhance the lateral resolution further, but at the expense of poorer axial resolution, as illustrated both by our experimental and simulation results.

4.8 Summary and Conclusions

The combination of SIL imaging with pupil-function engineering offers a potential route to achieving optical super-resolution with unprecedented performance. Such techniques can be attractive because they often provide a simple way to enhance the resolution of an optical system without resorting to more sophisticated near-field methods.

In this work, we have demonstrated a 60% reduction in the focal-plane PSF FWHM when using a particular design of annular amplitude transmission filter. In addition, a theoretical model, written in MATLAB, for predicting the performance of such apertures have been discussed and confirmed against additional experimental results.

A second approach in the pursuit of optical super-resolution is to exploit extreme *NA* focusing, a SIL-induced condition, using linearly-polarised light. Using a model based on the theory of Leutenegger [38], we visualised the electric-field distribution at the focal-plane of a high-*NA* optical system as the *NA* was increased from 0 to 1 and a normalised obscuration parameter was introduced from 0 to 0.99. These results confirmed the extension on the focal-plane PSF in the direction parallel to the polarisation vector as the *NA* was increased and the higher spatial frequencies isolated.

Furthermore, by using extreme *NA* solid-immersion microscopy [34-37] we have obtained images of a silicon IC that showed, for the first time, the dramatic influence of polarisation on spatial resolution, with values ranging from around 100 nm to 250 nm depending on the polarisation state used.

By exploiting the nonlinear suppression of the side-lobes generated by an annular pupil-plane filter we demonstrated how annular pupil-plane apertures can improve the optical resolution obtained in a microscope operating under high-*NA* conditions. We obtained a lateral resolution enhancement from 200×109 nm to 112×70 nm, an approximately 64% improvement in terms of the area of the focal spot. These results demonstrated that, for a nonlinear microscope already operating close to the limits of optical resolution, pupil-function engineering can usefully enhance the lateral resolution further, but at the expense of poorer axial resolution, as illustrated by both our experimental and simulation results.

In addition to this hybrid polarisation-dependent focusing and PSF engineering super-resolution technique, the option remains to investigate the role of spatially non-uniform polarisation distributions – typically radial polarisation – in the search for the smallest focused spot [46, 47, 74-77]. SIL-enhanced super-resolution techniques could have significant advantages in the fields of nanophotonic device imaging and characterisation. The nanoscale diffraction-limited performance enhancement presented here is particularly timely in semiconductor device imaging where the feature sizes of components within silicon ICs continue to be reduced with each new generation of fabrication technology. The combination of nonlinear excitation, solid-immersion focusing and excitation with pupil-function engineering represents a powerful approach to obtaining ultra-high-resolution optical imaging, and may have future applications in the life-sciences, industrial metrology, semiconductor quantum-dot interrogation, optical data storage and high-resolution laser machining.

References

[1] E. Hecht, *Optics*: Addison-Wesley (1987)

[2] B. Hecht, B. Sick, U.P. Wild, V. Deckert, R. Zenobi, O.J.F. Martin, and D.W. Pohl, "Scanning near-field optical microscopy with aperture probes: Fundamentals and applications", *Journal of Chemical Physics* **112**, 7761-7774 (2000)

[3] C.J.R. Sheppard, "Fundamentals of superresolution", *Micron* **38**, 165-169 (2007)

[4] T.R.M. Sales and G.M. Morris, "Fundamental limits of optical superresolution", *Optics Letters* **22**, 582-584 (1997)

[5] C.J.R. Sheppard and Z.S. Hegedus, "Axial Behavior of Pupil-Plane Filters", *Journal of the Optical Society of America A-Optics Image Science and Vision* **5**, 643-647 (1988)

[6] Y.S. Xu, J. Singh, C.J.R. Sheppard, and N.G. Chen, "Ultra long high resolution beam by multi-zone rotationally symmetrical complex pupil filter", *Optics Express* **15**, 6409-6413 (2007)

[7] R. Shinoda and K. Kime, "Focusing characteristics of an optical head with superresolution using a high-aspect-ratio red laser diode", *Japanese Journal of Applied Physics Part 1-Regular Papers Short Notes & Review Papers* **35**, 380-383 (1996)

[8] M. Martinez-Corral, P. Andres, C.J. Zapata-Rodriguez, and C.J.R. Sheppard, "Improvement of three-dimensional resolution in confocal scanning microscopy by combination of two pupil filters", *Optik* **107**, 145-148 (1998)

[9] A. Vainrub, O. Pustovyy, and V. Vodyanoy, "Resolution of 90 nm (lambda/5) in an optical transmission microscope with an annular condenser", *Optics Letters* **31**, 2855-2857 (2006)

[10] S. Lindek, C. Cremer, and E.H.K. Stelzer, "Confocal theta fluorescence microscopy with annular apertures", *Applied Optics* **35**, 126-130 (1996)

[11] H.F. Wang, Z.Y. Chen, and F.X. Gan, "Phase-shifting apodizer for next-generation digital versatile disk", *Optical Engineering* **40**, 991-994 (2001)

[12] B. Richards and E. Wolf, "Electromagnetic diffraction in optical systems II. Structure of the image field in an aplanatic system", *Proc. R. Soc. London Ser. A* **253**, 358-379 (1959)

[13] C.J.R. Sheppard, "Use of Lenses with Annular Aperture in Scanning Optical Microscopy", *Optik* **48**, 329-334 (1977)

[14] Z.S. Hegedus, "Annular Pupil Arrays - Application to Confocal Scanning", *Optica Acta* **32**, 815-826 (1985)

[15] M. Martinez-Corral, M.T. Caballero, E.H.K. Stelzer, and J. Swoger, "Tailoring the axial shape of the point spread function using the Toraldo concept", *Optics Express* **10**, 98-103 (2002)

[16] R. Boivin and A. Boivin, "Optimized Amplitude Filtering for Superresolution over a Restricted Field .1. Achievement of Maximum Central Irradiance under an Energy Constraint", *Optica Acta* **27**, 587-610 (1980)

[17] J. Jia, C.H. Zhou, X.H. Sun, and L.R. Liu, "Superresolution laser beam shaping", *Applied Optics* **43**, 2112-2117 (2004)

[18] H.T. Liu, Y.B. Yan, Q.F. Tan, and G.F. Jin, "Theories for the design of diffractive superresolution elements and limits of optical superresolution", *Journal of the Optical Society of America A-Optics Image Science and Vision* **19**, 2185-2193 (2002)

[19] J.S. Liu, A.J. Waddie, and M.R. Taghizadeh, "Phase-only diffractive optical elements with subdiffraction-limited depth of focus", *Journal of Modern Optics* **50**, 227-237 (2003)

[20] T.R.M. Sales and G.M. Morris, "Diffractive superresolution elements", *Journal of the Optical Society of America A-Optics Image Science and Vision* **14**, 1637-1646 (1997)

[21] T.R.M. Sales and G.M. Morris, "Axial superresolution with phase-only pupil filters", *Optics Communications* **156**, 227-230 (1998)

[22] M.R. Wang and X.G. Huang, "Sub-wavelength-resolvable focused non-Gaussian beam shaped with a binary diffractive optical element", *Applied Optics* **38**, 2171-2176 (1999)

[23] F. Zachariasse and M. Goossens, "Diffractive lenses for high resolution laser based failure analysis", *IPFA 2006: Proceedings of the 13th International Symposium on the Physical & Failure Analysis of Integrated Circuits*, 95-96 (2006)

[24] B.J. Davis, W.C. Karl, A.K. Swan, M.S. Unlu, and B.B. Goldberg, "Capabilities and limitations of pupil-plane filters for superresolution and image enhancement", *Optics Express* **12**, 4150-4156 (2004)

[25] D.M. de Juana, V.F. Canales, P.J. Valle, and M.P. Cagigal, "Focusing properties of annular binary phase filters", *Optics Communications* **229**, 71-77 (2004)

[26] T.G. Jabbour and S.M. Kuebler, "Vector diffraction analysis of high numerical aperture focused beams modified by two- and three-zone annular multi-phase plates", *Optics Express* **14**, 1033-1043 (2006)

[27] F.R. Xiao, J.H. Yuan, G.Y. Wang, and Z.Z. Xu, "Factors in design of optical super-resolving filters", *Chinese Physics Letters* **21**, 70-72 (2004)

[28] X.F. Zhao, C.F. Li, and H. Ruan, "Improvement of three-dimensional resolution in optical data storage by combination of two annular binary phase filters", *Chinese Physics Letters* **21**, 1515-1517 (2004)

[29] M.K. Sundareshan, S. Bhattacharjee, R. Inampudi, and H.Y. Pang, "Image preprocessing for improving computational efficiency in implementation of restoration and superresolution algorithms", *Applied Optics* **41**, 7464-7474 (2002)

[30] N.A. Mortensen, J.R. Folken, P.M.W. Skovgaard, and J. Broeng, "Numerical aperture of single-mode photonic crystal fibers", *IEEE Photonics Technology Letters* **14**, 1094-1096 (2002)

[31] K. Bahlmann and S.W. Hell, "Depolarization by high-aperture focusing", *Three-Demensional and Multidimensional Microscopy: Image Acquisition and Processing IX* **3**, 95-103 (2002)

[32] R. Dorn, S. Quabis, and G. Leuchs, "The focus of light-linear polarization breaks the rotational symmetry of the focal spot", *Journal of Modern Optics* **50**, 1917-1926 (2003)

[33] D.G. Flagello and T.D. Milster, "High-numerical-aperture effects in photoresist", *Applied Optics* **36**, 8944-8951 (1997)

[34] M. Born and E. Wolf, *Principles of Optics*. 7th ed. Cambridge: Cambridge University Press (2002)

[35] I. Ichimura, S. Hayashi, and G.S. Kino, "High-density optical recording using a solid immersion lens", *Applied Optics* **36**, 4339-4348 (1997)

[36] S.B. Ippolito, B.B. Goldberg, and M.S. Unlu, "High spatial resolution subsurface microscopy", *Applied Physics Letters* **78**, 4071-4073 (2001)

[37] B.D. Terris, H.J. Mamin, D. Rugar, W.R. Studenmund, and G.S. Kino, "Near-Field Optical-Data Storage Using a Solid Immersion Lens", *Applied Physics Letters* **65**, 388-390 (1994)

[38] M. Leutenegger, R. Rao, R.A. Leitgeb, and T. Lasser, "Fast focus field calculations", *Optics Express* **14**, 11277-11291 (2006)

[39] C.W. McCutchen, "Generalized aperture and the three-dimensional diffraction image", *Journal of the Optical Society of America* **54**, 240-244 (1964)

[40] C.W. McCutchen, "Generalized aperture and the three-dimensional diffraction image (vol 54, pg 240, 1964)", *Journal of the Optical Society of America A-Optics Image Science and Vision* **19**, 1721-1721 (2002)

[41] S. Quabis, R. Dorn, M. Eberler, O. Glockl, and G. Leuchs, "Focusing light to a tighter spot", *Optics Communications* **179**, 1-7 (2000)

[42] C.J.R. Sheppard, N.K. Balla, and S. Rehman, "Performance parameters for highly-focused electromagnetic waves", *Optics Communications* **282**, 727-734 (2009)

[43] K.S. Youngworth and T.G. Brown, "Focusing of high numerical aperture cylindrical-vector beams", *Optics Express* **7**, 77-87 (2000)

[44] G.M. Lerman and U. Levy, "Tight focusing of spatially variant vector optical fields with elliptical symmetry of linear polarization", *Optics Letters* **32**, 2194-2196 (2007)

[45] N. Lindlein, S. Quabis, U. Peschel, and G. Leuchs, "High numerical aperture imaging with different polarization patterns", *Optics Express* **15**, 5827-5842 (2007)

[46] G.M. Lerman and U. Levy, "Effect of radial polarization and apodization on spot size under tight focusing conditions", *Optics Express* **16**, 4567-4581 (2008)

[47] C.J.R. Sheppard and A. Choudhury, "Annular pupils, radial polarization, and superresolution", *Applied Optics* **43**, 4322-4327 (2004)

[48] S.H. Goh and C.J.R. Sheppard, "High aperture focusing through a spherical interface: Application to refractive solid immersion lens (RSIL) for subsurface imaging", *Optics Communications* **282**, 1036-1041 (2009)

[49] S.B. Ippolito, B.B. Goldberg, and M.S. Unlu, "Theoretical analysis of numerical aperture increasing lens microscopy", *Journal of Applied Physics* **97**, 053105 (2005)

[50] C. Xu and W. Denk, "Two-photon optical beam induced current imaging through the backside of integrated circuits", *Applied Physics Letters* **71**, 2578-2580 (1997)

[51] L. Novotny and B. Hecht, *Principles of Nano-Optics*. New York: Cambridge Univ. Press (2006)

[52] K. Karrai, X. Lorenz, and L. Novotny, "Enhanced reflectivity contrast in confocal solid immersion lens microscopy", *Applied Physics Letters* **77**, 3459-3461 (2000)

[53] T.R.M. Sales, "Smallest focal spot", *Physical Review Letters* **81**, 3844-3847 (1998)

[54] G. Yao and L.V. Wang, "Two-dimensional depth-resolved Mueller matrix characterization of biological tissue by optical coherence tomography", *Optics Letters* **24**, 537-539 (1999)

[55] P. Torok and P. Varga, "Electromagnetic diffraction of light focused through a stratified medium", *Applied Optics* **36**, 2305-2312 (1997)

[56] K.A. Serrels, E. Ramsay, R.J. Warburton, and D.T. Reid, "Nanoscale optical microscopy in the vectorial focusing regime", *Nature Photonics* **2**, 311-314 (2008)

[57] T.G. Jabbour, M. Petrovich, and S.M. Kuebler, "Design of axially super-resolving phase filters using the method of generalized projections", *Optics Communications* **281**, 2002-2011 (2008)

[58] S. Lindek, C. Cremer, and E.H.K. Stelzer, "Confocal theta fluorescence microscopy using two-photon absorption and annular apertures", *Optik* **102**, 131-134 (1996)

[59] N.D. Lai, J.H. Lin, P.W. Chen, J.L. Tang, and C.C. Hsu, "Controlling aspect ratio of focal spots of high numerical aperture objective lens in multi-photon absorption process", *Optics Communications* **258**, 97-102 (2006)

[60] P.P. Mondal and A. Diaspro, "Lateral resolution improvement in two-photon excitation microscopy by aperture engineering", *Optics Communications* **281**, 1855-1859 (2008)

[61] E.J. Botcherby, R. Juskaitis, and T. Wilson, "Scanning two photon fluorescence microscopy with extended depth of field", *Optics Communications* **268**, 253-260 (2006)

[62] S.B. Ippolito, P. Song, D.L. Miles, and J.D. Sylvestri, "Angular spectrum tailoring in solid immersion microscopy for circuit analysis", *Applied Physics Letters* **92**, 101109 (2008)

[63] W. Denk, J.H. Strickler, and W.W. Webb, "2-Photon Laser Scanning Fluorescence Microscopy", *Science* **248**, 73-76 (1990)

[64] S.W. Hell, P.E. Hanninen, A. Kuusisto, M. Schrader, and E. Soini, "Annular Aperture 2-Photon Excitation Microscopy", *Optics Communications* **117**, 20-24 (1995)

[65] H.X. Luo and C.H. Zhou, "Comparison of superresolution effects with annular phase and amplitude filters", *Applied Optics* **43**, 6242-6247 (2004)

[66] C. Liu and S.H. Park, "Numerical analysis of an annular-aperture solid immersion lens", *Optics Letters* **29**, 1742-1744 (2004)

[67] T.D. Milster, F. Akhavan, M. Bailey, J.K. Erwin, D.M. Felix, K. Hirota, S. Koester, K. Shimura, and Y. Zhang, "Super-resolution by combination of a solid immersion lens and an aperture", *Japanese Journal of Applied Physics Part 1-Regular Papers Short Notes & Review Papers* **40**, 1778-1782 (2001)

[68] S.F. Pereira and A.S. van de Nes, "Superresolution by means of polarisation, phase and amplitude pupil masks", *Optics Communications* **234**, 119-124 (2004)

[69] C.J.R. Sheppard and M. Martinez-Corral, "Filter performance parameters for vectorial high-aperture wave fields", *Optics Letters* **33**, 476-478 (2008)

[70] T. Ando, Y. Ohtake, T. Inoue, H. Itoh, N. Matsumoto, and N. Fukuchi, "Shaping tight-focusing patterns of linearly polarized beams through elliptic apertures", *Applied Physics Letters* **92**, 021116 (2008)

[71] E. Ramsay, K.A. Serrels, M.J. Thomson, A.J. Waddie, M.R. Taghizadeh, R.J. Warburton, and D.T. Reid, "Three-dimensional nanoscale subsurface optical imaging of silicon circuits", *Applied Physics Letters* **90**, 131101 (2007)

[72] E. Ramsay, K.A. Serrels, M.J. Thomson, A.J. Waddle, R.J. Warburton, M.R. Taghizadeh, and D.T. Reid, "Three-dimensional nanometric sub-surface imaging of a silicon flip-chip using the two-photon optical beam induced current method", *Microelectronics Reliability* **47**, 1534-1538 (2007)

[73] K.A. Serrels, E. Ramsay, D.T. Reid, "70 nm resolution in subsurface optical imaging of silicon integrated-circuits using pupil-function engineering", *Applied Physics Letters* **94**, 073113 (2009)

[74] S. Quabis, R. Dorn, and G. Leuchs, "Generation of a radially polarized doughnut mode of high quality", *Applied Physics B-Lasers and Optics* **81**, 597-600 (2005)

[75] L.E. Helseth, "Roles of polarization, phase and amplitude in solid immersion lens systems", *Optics Communications* **191**, 161-172 (2001)

[76] R. Dorn, S. Quabis, and G. Leuchs, "Sharper focus for a radially polarized light beam", *Physical Review Letters* **91**, 233901 (2003)

[77] S. Quabis, R. Dorn, O. Glockl, M. Reichle, and M. Eberler, "Reduction of the spot size by using a radially polarized laser beam", *International Seminar on Novel Trends in Nonlinear Laser Spectroscopy and High-Precision Measurements in Optics* **4429**, 105-111 (2000)

Chapter 5

Ultra-High-Resolution Optical Coherence Tomography for the Characterisation of Silicon Integrated-Circuits and Painted and Printed Media

5.1 Introduction and Motivation

Optical coherence tomography (OCT) is a well established high-resolution cross-sectional tomographic imaging technique that can expose the intricate internal microstructures that comprise many biological tissues and materials [1]. OCT utilises the coherent properties of light in order to produce images that are acquired through an interferometric approach which measures the magnitude and time-delay of back-reflected light from a particular sample under investigation. This imaging modality is an extension of the early work performed on white light interferometry that resulted in the development of optical coherence-domain reflectometry (OCDR), a one-dimensional optical ranging technique [2]. OCDR was originally created for fault isolation within optical fibre networks and components; however its unique ability to interrogate materials was soon adopted into the biomedical sciences [3, 4]. This low-coherence heterodyne detection imaging system has since been exploited in a wide variety of biological environments, include the retina [5, 6], human skin [7] and teeth [8].

An outstanding benefit of OCT is that it has the ability to perform non-invasive optical imaging in the sub-micron resolution regime over a profiling depth that can exceed several millimetres. This optical sectioning performance is advantageous in the investigation of embedded microscopic multilayered structures that are located at sample depths beyond those which are accessible through the use of conventional confocal microscopy. Although sub-surface imaging is also possible to access these imaging depths through the use of high-frequency ultrasonic techniques (the acoustic analogy of OCT), ultrasound suffers from reduced performance, higher maintenance costs and operational complexity.

Over the last decade, OCT has developed by incorporating advances in a broad range of different photonic technologies including source development, fibre optics, ultrafast optics, interferometry and Fourier optics [9-14]. It is therefore unsurprising to note that behind the deceptive simplicity of the basic OCT configuration can be found an abundance of state-of-the-art research and development that has led to new technologies for enhancing the capabilities of OCT. Furthermore, the implementation of sophisticated detection schemes are of significant importance during the design stages of practical OCT systems. These provide the ability to measure low-noise interference signals from sub-surface features located at substantial depths [15, 16].

It is useful to compare OCT with the competing technologies of ultrasound and microscopy in order to understand its strengths and weaknesses. The main criteria of interest are resolution performance, imaging depth and ease of implementation.

The resolution of ultrasound imaging is directly associated with the frequency (or wavelength) of the sound waves used [17]. Typically, for clinical applications the frequency is set to approximately 10MHz. This results in a spatial resolution of up to around 150µm. This is advantageous since sound waves at this frequency are easily transmitted into most biological materials and can therefore provide images of structures that are immersed at depths of up to several tens of centimetres deep. By increasing the source frequency it is possible to improve resolution performance further (100MHz results in a spatial resolution of ~15-20µm); however, higher frequencies are strongly attenuated in biological tissue and therefore a trade-off is required between penetration depth and profiling resolution. In addition, since ultrasonic imaging utilises acoustic waves, there is a requirement that direct contact be made between the source and the material under investigation. This condition limits the operation of ultrasonic techniques to only particular applications.

Confocal microscopy is an alternative imaging technique to OCT that can attain sub-micron transverse spatial resolutions. This lateral profiling performance is superior to that which can be obtained through the implementation of ultrasonic or OCT techniques; however, the image penetration of confocal microscopy is limited to only a few hundred microns in biological tissues due to their highly scattering characteristics. Therefore, since it is the evaluation of sub-surface features that is of significant interest, use of this technique is rendered inadequate.

The axial resolution of OCT is determined by the coherence length of the optical source used. This has resulted in OCT systems demonstrating resolutions in the 1-15µm regime - depending on the optical source used (e.g. a superluminescent diode [18], a femtosecond laser [19] or a supercontinuum source [10, 12]). This performance is almost 100 times better than standard ultrasound imaging. This confirms that OCT is the dominant imaging technology for sub-surface interrogation of micro-structured materials. In addition, this non-contact optical technique is ideal for the investigation of a multitude of biological materials due to its low attenuation, non-destructive, high-resolution, and easy access approach. Ultrasound utilises electronic detection to measure

dimensions of approximately 100µm, which corresponds to a time resolution of ~10ns – the speed of sound in water is ~1500m/s. This can be easily acquired using modern electronic devices. In the optical domain, the measurement of a particular structure with a resolution of approximately 10µm corresponds to a time resolution of ~30fs. Direct electronic detection is not possible on this time scale, therefore interferometric time-delayed measurements are required.

OCT can be separated into several distinctive areas: time domain, spectral (Fourier) domain, swept-source OCT and full-field OCT. These are all unique OCT methodologies and have their own advantages and disadvantages.

Time-domain (TD-OCT) operates by varying the optical path length (OPL) in one arm of the interferometer (i.e. reference arm) to produce a reflectivity profile as a function of depth [1]. There are three different methods to acquire an image using this technique. These scanning protocols are known as *depth*, *transverse* and *en face* priorities and will be discussed later in this chapter. Moreover, TD-OCT systems must be efficiently calibrated against a known reference signal in order to remove acquisition errors (also discussed later). TD-OCT was selected as the method of choice for the purposes of this work.

Spectral (Fourier) domain OCT operates by sending the interferometer output signal to an optical spectrometer for evaluation [20]. This technique requires no scanning reference mirror in the interferometer and therefore has no nonlinear reference arm scan rate errors to amend. By taking the Fourier transform of the spectrometer signal it is possible to obtain an interferogram trace that contains topological information about the sample.

Swept source OCT (SS-OCT) is similar to TD-OCT and Fourier domain OCT in that it employs a broadband optical source; however, SS-OCT does not obtain an image by using the entire bandwidth of the source in individual single-point shots [21]. Instead, it builds up the interferogram by capturing individual traces using a small frequency window that is swept throughout the available source bandwidth. SS-OCT has the ability for rapid acquisition rates but in order to obtain a similar depth resolution to that available with TD-OCT or Fourier domain OCT the laser frequency window needs to traverse the entire spectral bandwidth of the source.

Full-field OCT (FF-OCT - also called *en face* OCT) is one of the original embodiments of OCT, based on white-light interference microscopy [22]. Tomographic images are attained by acquiring a series of interferometric images recorded in parallel by an arrayed detector (e.g. a CCD camera). Whereas conventional OCT produces axially-oriented images, FF-OCT acquires images in the *en face* (transverse) orientation. FF-OCT is an alternative method to conventional OCT to provide ultrahigh resolution images by using a simple halogen lamp instead of a complex laser-based source.

OCT is an established medical and biological imaging technique, and continues to be developed within this context; for example, it has already been demonstrated that an OCT systems can be configured using entirely fibre optical components. This results in a compact and robust evaluation unit that is easily transportable and adaptable for a particular application. Endoscopic OCT instruments have also been developed to access and probe internal biological tissue [23, 24]. In contrast to developments driven by applications in the life sciences, the use of OCT in non-biological applications has received considerably less attention and so presents opportunities for novel research. For this reason, the focus of this work will concentrate on ultra-high-resolution near-infrared (IR) TD-OCT imaging in two unique contexts: non-destructive optical inspection of silicon integrated-circuits (IC) and artwork conservation.

OCT imaging as a method of interrogating the structures of 3D architectures encapsulated within state-of-the-art silicon ICs could represent a truly novel inspection and evaluation process. Not only would it offer a complementary procedure for investigating the integrity of semiconductor ICs, it could reveal additional sources of device malfunction; for example, OCT already has the ability to expose stress-induced artefacts within a sample through the use of polarisation-sensitive OCT [25, 26], so could be used to evaluate the effect that packaging-induced stress and strain has on device performance and reliability. FF-OCT imaging of ICs has already been reported [27]; however, this technology has not been fully developed and remains in its infancy.

Furthermore, OCT can be applied as a tool for the non-destructive and non-invasive inspection of sub-surface material deterioration and uniformity. It was reported recently that OCT has attracted the attention of conservation scientists [28-31] but still remains under-developed in this context compared with its dominant clinical applications. OCT has the potential to provide new depth-resolved data, as yet unobtainable by other

methods, which are crucial to understanding physical processes e.g. de-lamination between the paint layers and micro-cracking which eventually lead to the structural failure of vulnerable works of art.

5.2 Theory

OCT is based on a classical linear optical technique known as low-coherence interferometry which was first devised as a measurement tool for characterising optical back-reflections and backscattering in optical fibres and waveguide devices [2]. This interferometric approach offers a precise evaluation of the time delayed back-reflected light with high-dynamic-range and sensitivity.

The theory associated with OCT is far-reaching and can extend to embrace all imaging schemes, optical components, detector performance and arrangements, etc. Therefore, this section aims to address the fundamental features of TD-OCT in order to present a concise treatment of the essential parameters.

5.2.1 Interference and Coherence

Low-coherence interferometry measures the sum of the electric-fields of two incident light beams rather than their intensity. The form of the oscillating electric-field of a light wave can be given by,

$$E(t) = E_o e^{i(\omega t - kz)} \tag{1}$$

where $\omega = 2\pi\upsilon$ and $k = 2\pi/\lambda$, with υ representing frequency and λ representing wavelength.

When two optical beams are combined, their electric-fields are summed together, which may result in constructive or destructive interference, depending on the relative phase of the field oscillations. In order to obtain interference from a single optical source, a simple Michelson interferometer can be used. In the context of OCT, one interferometer arm is empty and serves as a reference, while the other terminates in the sample, as illustrated in Fig. 1.

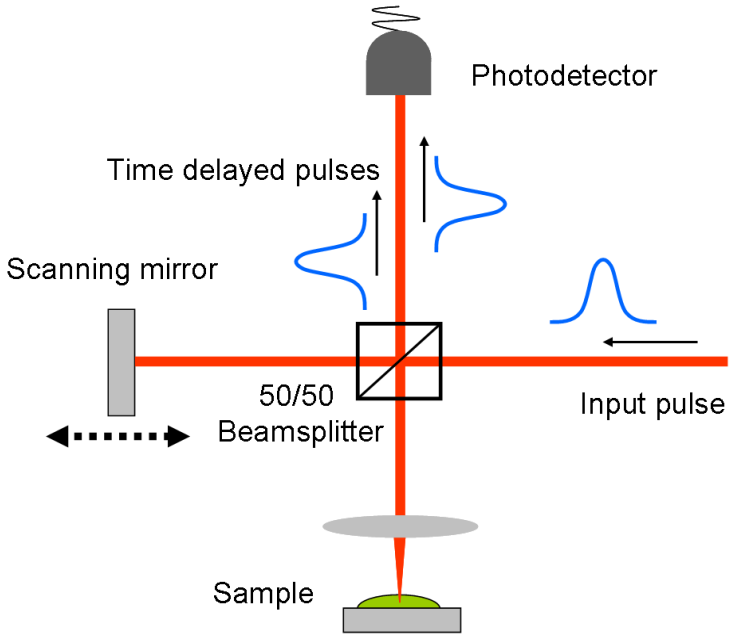

Figure 1 – Experimental Michelson interferometer configuration

The incident beam from the optical source is coupled into the Michelson interferometer and is directed onto a 50/50 beamsplitter. This splits the incident beam into two separate beams, one of which functions as a reference beam and the other of which functions as the signal, or sample, beam. After the beamsplitter, the reference and the sample beams travel given distances in the two arms of the interferometer. The reference beam, $E_r(t-\tau)$, is reflected from a scanning mirror and the signal beam, $E_s(t)$, is reflected back from the sample under investigation. The two beams then combine again at the beamsplitter where they interfere. The output from the interferometer is the sum of the electromagnetic fields from both the reference beam and the sample beam. The measured electric-field at the output is,

$$E_{output}(t) = E_s(t) + E_r(t-\tau) \tag{2}$$

The detector in the interferometer measures the time integrated optical intensity of the output beam that is incident on its surface. This is proportional to the square of the magnitude of the incident electromagnetic field integrated over all time,

$$I_{output}(\tau) = \int_{-\infty}^{\infty} \left| E_s(t) + E_r(t-\tau) \right|^2 dt \tag{3}$$

This can then be expanded to become,

$$I_{output}(\tau) = \int_{-\infty}^{\infty} |E_s(t)|^2 dt + \int_{-\infty}^{\infty} |E_r(t-\tau)|^2 dt + \int_{-\infty}^{\infty} \left(E_s(t) E_r(t-\tau)^* + E_s(t)^* E_r(t-\tau) \right) dt \qquad (4)$$

where $E_s(t)^*$ and $E_r(t-\tau)^*$ are the complex conjugates of the electric-fields in the sample and reference arms respectively.

The first and second term on the right-hand-side of equation (4) represent the DC mean intensities of the returning light from both reference and signal arms, respectively. The third term represents the interference between the light returning from both arms of the interferometer. It is this final term that reveals that one can obtain detailed spectral information about the optical source through the interference between two waves.

By disregarding the first two DC terms in Equation (4), it can be shown that the Fourier transform of $E_{output}(t)$ is the equivalent to the spectral intensity distribution, $I(\omega)$ of the input source; however, this is only the case if $E_r = E_s$. This requires the use of the convolution theorem which states that the convolution ($\otimes$) of two functions $g(t)$ and $h(t)$ is the equivalent to the following integral [32],

$$g(t) \otimes h(t) = \int_{-\infty}^{\infty} g(t) h(\tau - t) dt \qquad (5)$$

where $h(\tau - t)$ is a time delayed and time-reversed version of the function $h(t)$. Spectrally, this convolution integral is the equivalent to the product of the Fourier transforms of $g(t)$ and $h(t)$. Therefore, the integral in equation (5) can be equated to an inverse Fourier transform (FT^{-1}) of the Fourier transformed product of the original functions $g(t)$ and $h(t)$,

$$\int_{-\infty}^{\infty} g(t) h(\tau - t) dt = FT^{-1}\{G(\omega) \cdot H(\omega)\} \qquad (6)$$

where $G(\omega)$ and $H(\omega)$ represent the inverse Fourier transforms of the functions $g(t)$ and $h(t)$ given by the equations below,

$$G(\omega) = \frac{1}{2\pi}\int_{-\infty}^{\infty} g(t)\exp(-i\omega t)dt$$
$$H(\omega) = \frac{1}{2\pi}\int_{-\infty}^{\infty} h(t)\exp(-i\omega t)dt \quad (7)$$

Therefore, in relation to the interferogram signal detected in an OCT system, we can apply the convolution theorem to $E_{output}(t)$ which reduces the cross-terms of Equation (4) to,

$$I_{output}(\tau) = FT^{-1}\left\{e_s(\omega)\cdot e_r(\omega)^*\right\} + c.c. \quad (8)$$

since, due to symmetry, $FT\{E(t)\} = FT\{E(t)^*\} = FT\{E(t-\tau)\} = FT\{E(t-\tau)^*\}$
Therefore,

$$I_{output}(\tau) = FT^{-1}\{I(\omega)\} \quad (9)$$

since, $I(\omega) = |e(\omega)|^2 = e_s(\omega)\cdot e_r(\omega)^*$

Equation (9) informs us that the spectral distribution of the optical source therefore determines the system's sensitivity to the optical path difference between the two interferometer arms. As a result, the degree of coherence is related to the Fourier transform of the source spectrum (and vice versa), implying that the broader the optical spectrum, the narrower the coherence function in the time domain. Therefore, the spatial window within which interference is observed becomes narrower. This optical gating is the phenomenon that determines the axial resolution of the system.

5.2.2 Resolution Performance

The novelty of OCT compared to other light microscopy techniques is that both the lateral and axial resolutions are independent, offering an axial resolution far superior to the confocal parameter of the beam. The axial resolution is indirectly proportional to the spectral bandwidth of the optical source and can therefore be determined by the

coherence length, ℓ_c. The coherence length is the spatial width of the field autocorrelation produced by the interferometer. The envelope of the field autocorrelation is equivalent to the Fourier transform of the power spectrum. For a Gaussian spectral distribution, one can calculate the coherence length, and therefore the axial resolution Δz by the following expression,

$$\ell_c = \Delta z = \frac{2\ln 2}{\pi} \cdot \frac{\lambda_0^2}{\Delta\lambda} \tag{10}$$

where $\Delta\lambda$ is the spectral bandwidth and λ_0 is the central wavelength of the optical source. Although the assumption that the sample under investigation is a plane mirror is a coarse simplification, the derived one-dimensional model of the coherence length gives an appropriate measure of the axial resolution on an OCT system [33]. The treatment of complex highly scattering materials is an advanced issue and is not discussed here.

Since the axial resolution is indirectly proportional to the spectral bandwidth of the optical source, it is clear that broad-bandwidth sources are required to achieve high-axial-resolution. Practically, this can be achieved using a number of different sources and will be discussed later in the chapter.

The lateral resolution of an OCT imaging system is exactly the same as for a conventional optical microscope. This sets the diffraction-limited spot size to be inversely proportional to the numerical aperture (*NA*) of the focused beam. The lateral resolution is determined by the expression,

$$\Delta x = \Delta y = 0.51\lambda / NA \tag{11}$$

High lateral resolution can be achieved by using a high-*NA* objective lens; however, the lateral resolution also influences the confocal parameter, *b*, of the imaging system. The confocal parameter is defined as twice the length of the Raleigh range, z_r, and is expressed as,

$$b = 2z_r = 2\left(\frac{\pi w_o^{\,2}}{\lambda}\right) \tag{12}$$

where w_0 represents the $1/e^2$ beam radius in the focal-plane. Thus, improving the lateral resolution of the system produces a decrease in the depth-of-focus.

In general, OCT imaging is performed using a low-*NA* focusing lens because it is desirable to have a large depth-of-field and use low-coherence interferometry to achieve high-axial-resolution. In this regime, the confocal parameter is much larger than the coherence length, $b > \ell_c$. The image resolution is set by the axial coherence length and the lateral spot size. This arrangement is in contrast to conventional microscopy since it achieves high-axial-resolution independently of the available *NA*. Nonetheless, this configuration is extremely important for particular biomedical applications where the available *NA* is limited.

Fig. 2 provides an illustration of the important resolution and focusing conditions associated with OCT.

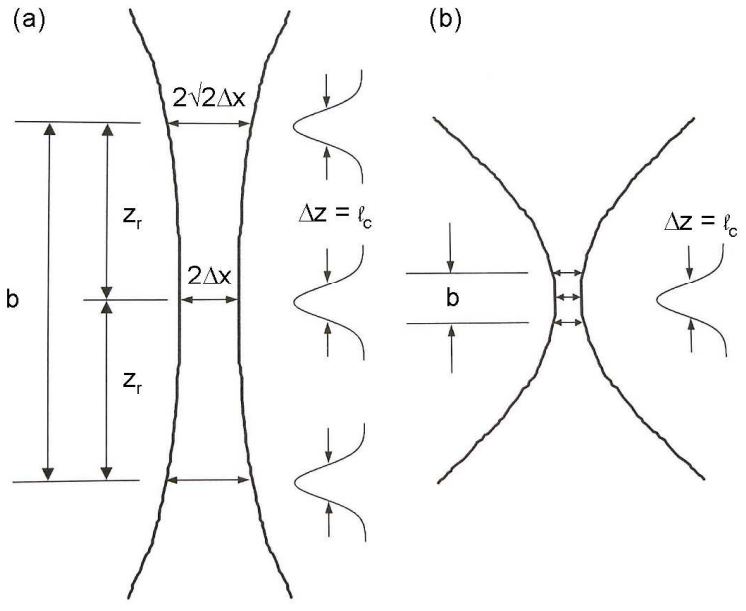

Figure 2 - Illustration of the important OCT resolution parameters associated with (a) low-*NA* and (b) high-*NA* focusing conditions

On the other hand, the possibility of achieving high lateral resolution at the expense of reducing the axial depth-of-focus is not entirely ineffective. Tight lateral and axial focusing is the trademark of confocal imaging and can therefore be combined with OCT techniques to create the field of optical coherence microscopy (OCM) [34]. OCM technologies utilise a depth-of-field that is shorter than the coherence length in order to differentiate between backscattered signals originating from different depths within a sample. This is a useful imaging technique because the coherence gating effect has the ability to remove unwanted contributions from scattering planes located in front and behind the focal-plane better than the confocal gating effect.

5.3 Dispersion Compensation

Pulse broadening due to dispersion is an important parameter which must be considered in any OCT configuration – pulse broadening and various compensation techniques have already been introduced in Chapter 2. If dispersion in the reference arm of the interferometer is not matched with that originating from the sample arm, then the cross-correlation of the reference and sample light will be broadened, reducing the axial resolution of the system. Therefore, it is good design practice to carefully account for dispersion in all elements of the sample and reference arms. The majority of OCT configurations employ a variable dispersion-compensation feature (e.g. a prism pair) in the scanning reference arm for efficient and reliable performance.

There are two main sources of dispersion in a typical OCT system. The first is associated with the imaging objective lens and the second concerns the actual sample.

The dispersion introduced by the focusing lens is relatively simple to compensate for. One solution is to introduce an identical lens, positioned a distance f from the scanning mirror, where f is the focal length of the lens, into the reference arm. Care must be taken here however since the scanning reference mirror will traverse between planes located before and after the exact focal-plane. This will result in the return of a reference arm beam which has alternating degrees of collimation as a function of scanning mirror position. Therefore, both the mirror and the lens must be positioned on the same scanning stage. Another solution would be to introduce a transparent bulk material, positioned at Brewster's angle to minimise back-reflections, of identical refractive index into the reference arm. The thickness of the material can be calculated and matched to

the total bulk material seen by the beam across the focusing lens for accurate compensation.

The second source of dispersion, introduced by the sample itself, is not so easy to balance. Compensation schemes for this situation must consider a number of different sample parameters, including refractive index and thickness. In addition, it is possible for these values to change as a function of beam position on the sample. There is no guarantee that the sample will retain a uniform distribution of physical and material parameters during the acquisition of an image; however, it has been demonstrated that it is possible to calculate the group velocity dispersion (GVD) of an optical material using a simple Michelson interferometer [35]. Hence, it may be possible to integrate the evaluation of GVD with the mechanical translation of a prism pair in the reference arm to accurately balance the fluctuating sample induced dispersion as a function of lateral beam position in real time. This approach would be challenging to implement experimentally, therefore a purely mathematical treatment can be adopted which performs the same task with reduced complexity. By applying a suitable phase term across the acquired interferogram, the dispersion mismatch can be numerically balanced since the accumulated phase distortion has been removed [9, 36]. This can be an effective post-processing technique which can improve image quality with reduced complexity.

5.4 Image Generation

OCT was originally used to generate cross-sectional images by accumulating a number of successive axial measurements of time-delayed backscattered optical echoes at different lateral positions across a sample [1]. This is easy to perform since it involves the simple lateral translation of the incident focused beam. This low-*NA depth* priority technique is the most common method of OCT image generation; however, it is also possible to acquire an image with *transverse* priority. This is achieved by detecting back-reflections or backscattered light at different depths within the sample while laterally scanning the incident beam. This high-*NA* acquisition results in the formation of a cross-sectional image that has acquired optical echoes along a lateral direction (e.g. x-axis) for different axial steps (e.g. z-axis). Furthermore, this transverse technique can be extended to perform OCT imaging with *en-face* priority by acquiring along a specific lateral plane. In this case, the time-delayed optical echoes are detected at a fixed axial depth as beam scanning is initiated along both lateral directions (i.e. x- and y-axis). This

en-face image generation is analogous to the process implemented in confocal microscopy which, in turn, has resulted in the field of OCM – introduced earlier.

Fig. 3 illustrates how OCT image generation is performed under the above mentioned conditions. These three scanning protocols are all unique in their ability to interrogate a sample depending on the imaging conditions and the application.

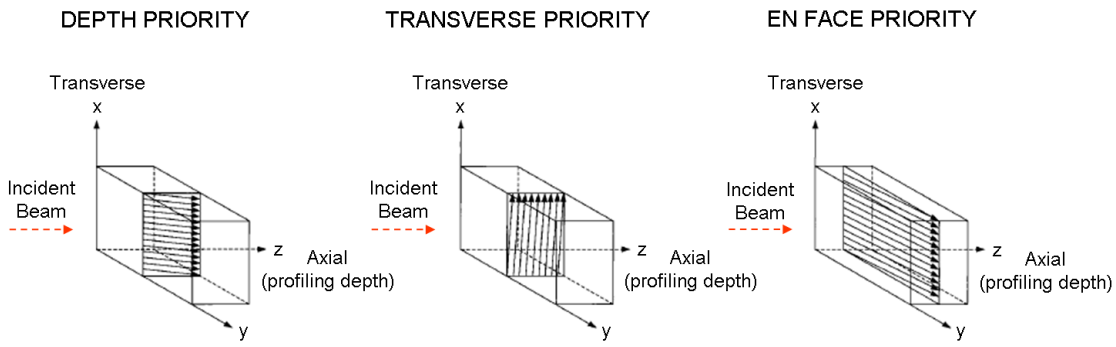

Figure 3 – OCT scanning protocols

A critical aspect of OCT image generation concerns the procedure adopted for efficient envelope extraction from each acquired interferogram. A simple solution is to perform an iterative Fourier-filtering algorithm at every acquisition point; however this can be time consuming. Therefore, an improved alternative is to calculate and plot the analytical Hilbert transform of each input interferogram [37] - a signal that contains no negative frequencies is referred to as an analytical signal. The Hilbert transform provides the interferogram envelope by calculating the fast Fourier transform (FFT) of the interferogram, setting the FFT coefficients that correspond to negative frequencies to zero, then taking the inverse FFT of the result. This algorithm can be described mathematically using the expression,

$$H = \Im^{-1}\left\{\Im\left\{I_{output}(\tau)\right\}\Big|_{\omega>0}\right\} \tag{13}$$

where H represents the Hilbert transform, $\Im$ the Fourier transform, $I_{output}(\tau)$ the detector output signal and ω the spatial frequency in the Fourier domain.

The majority of the OCT images that are presented later in this Chapter used the Hilbert transformations to render images from the raw interferogram data.

After the data to comprise an image have been obtained, a decision has to be made to determine how the image will be viewed. In general, OCT images are displayed in the two-dimensional (2D) linear grayscale format; however, depending on the design, data acquisition and sensitivity of the detectors used, the measured signals may vary over several orders of magnitude. Therefore, it is often appropriate to present the obtained image using a logarithmic scale. This expands the dynamic range of the displayed signal which is useful when the dynamic range of the acquisition system is high.

Colour images can also be presented but are usually restricted to advanced OCT schemes such as OCT elastometry [37, 38], Fourier-domain OCT, SS-OCT or polarisation-sensitive OCT, where a samples flexibility or response to wavelength or polarisation, respectively, must be adequately portrayed.

5.5 Development of a High-Axial-Resolution High-Dynamic-Range OCT interferometer

The following sections discuss the development, implementation and calibration of a high-axial-resolution high-dynamic-range OCT interferometer for non-destructive evaluation and inspection of silicon ICs and artwork conservation. All of the work presented here was undertaken by the author; however, the efforts of Bernd Stark and Michael Renner (both final year MPhys project students) must be acknowledged for their contributions towards the development and calibration of the initial system (Bernd) and enhanced system (Michael).

5.5.1 Initial Configuration

The foundation of the initial, and subsequent, OCT configurations was a free-space Michelson interferometer. This free-space configuration is advantageous due to its experimental versatility since it is straightforward to modify and create different optical arrangements by introducing standard free-space optical components. This is in contrast to the fibre-optical OCT system where the insertion of additional materials and components along the beam path is difficult to implement. An illustration of the initial experimental configuration is given in Fig. 4.

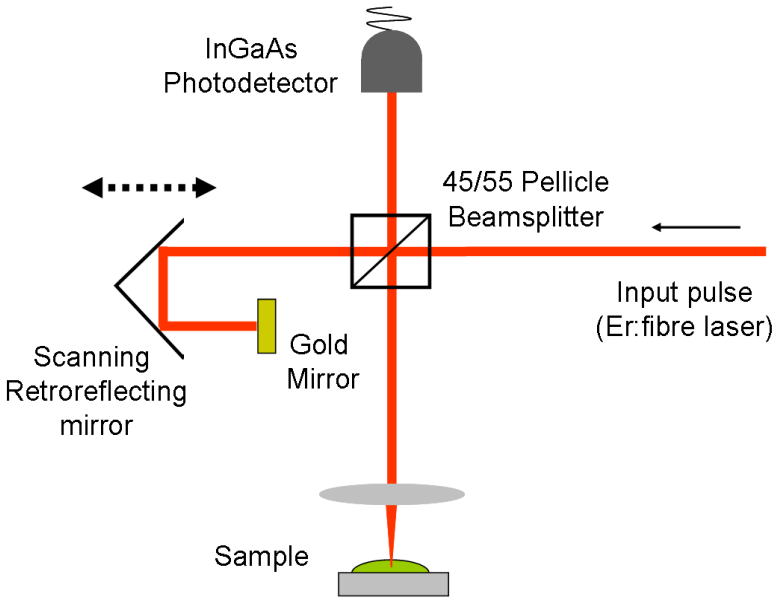

Figure 4 – Initial experimental configuration

The low-coherence optical source adopted was a stretched-pulse erbium-doped fibre laser – this laser has been extensively discussed in Chapter 2. It delivered ~160fs optical pulses at a repetition rate of 32MHz and an average power of ~75mW. The optical bandwidth was approximately 80nm. The fibre laser output beam was collimated and coupled into the Michelson interferometer where it was then split by a 45/55 pellicle beamsplitter (Thorlabs – CM1-BP3). The thickness of the beamsplitter's thin film was ~2µm and its transmission/reflection window was situated in the spectral region between 1-2µm. The transmitted (reflected) light at the beamsplitter then traversed the reference arm (sample arm) where it was reflected by the scanning mirror (sample under investigation) and returned to the beamsplitter. The two interfering beams were then collected by an indium gallium arsenide (InGaAs) photodiode. The resulting interferogram traces were displayed on a Tektronix TDS3032 oscilloscope which was connected to a personal computer (PC) via the GPIB interface. This enabled rapid acquisition and processing of the data in the MATLAB computing environment. The scanning reference arm featured a piezo-driven flexure translation stage which initially contained a standard highly-reflective plane gold mirror and was driven by a high voltage power supply and signal generator. The plane mirror was later replaced with a highly-reflective gold retro-reflector in order to double the available scanning range. The entire flexure-stage scanning unit was then mounted on top of a second standard translation stage and secured to the optical bench. The available scanning range of the flexure-stage was measured to be approximately 300µm. This was calibrated by relating the change of the interferogram peak position on the oscilloscope to a manual offset of

100µm on the translation stage. The total available data range of the oscilloscope (10000 points) was then matched to a half-period of the sinusoidal waveform delivered to the flexure-stage in order to match one oscilloscope screen shot to one full axial scan – the peaks and troughs of the sinusoidal waveform represented the turning points of the flexure-stage. The sample was mounted onto a high-precision automated xyz translation stage (Applied Scientific Instruments – MS2000-XYZ) which was controlled in MATLAB through the RS232 interface.

A key component in the sample arm was the focusing lens. A number of possible options were considered and implemented throughout this work in order to obtain the optimum image generation from the OCT system. The various options investigated are described below.

The first approach was to use a commercially available microscope objective lens. Unfortunately, it became evident that the excessively large glass lens system, with a total length of 12cm, introduced intolerably high loss and dispersion. This resulted in an incredibly broad interferogram trace which had poor signal contrast. An attempt was made to balance the objective lens dispersion by introducing various amounts of glass into the reference arm; however the combined effects of attenuation and dispersion could not be reversed.

The second attempt was the application of a reflective objective lens. The working principle of this lens is based on convex and concave mirrors instead of bulk glass lenses. This arrangement is advantageous since the removal of glass in the sample arm would result in the need for no dispersion compensation in the reference arm. Although this approach appeared promising, this attempt also failed. A deformation in the lens' interior housing caused significant alignment and focusing issues which prevented the formation of an interferogram.

The final option was to investigate the use of aspheric lenses. The minimal dispersion introduced by these relatively thin components could be easily balanced in the reference arm and due to their abundance in the lab it was possible to examine a variety of different materials and focal lengths, etc. Eventually a suitable lens was selected which was made of tantalum crown glass (TAC4), offering high transmission at 1550nm and had a relatively short focal length of 11mm, which resulted in a usable confocal

parameter, b, of ~307µm and a lateral resolution, Δx, of ~17.4µm. The dispersion introduced by this lens was calculated by modelling the group delay dispersion (GDD) introduced by 2.87mm of TAC4 glass. This was achieved through consideration of the appropriate Sellmeier equation. The result (-14fs^2 at 1550nm) demonstrated that the TAC4 induced dispersion could be cancelled out by introducing 800µm of BK7 glass into the Michelson reference arm. 800µm of BK7 corresponds to a thickness which is less than that measured across one microscope slide (~1mm), therefore this almost negligible dispersion was balanced with a single microscope slide in the reference arm.

5.5.2 Calibration

A key feature of any imaging system is its resolution performance, therefore the initial measurement which had to be recorded was the interferogram generated when using the erbium-doped fibre laser. Since the axial resolution of an OCT system is determined by the bandwidth of the optical source it was vital to acquire an accurate measurement of the resulting interferogram. As was reported in Chapter 2, the operation of a stretched-pulse erbium-doped fibre laser can be sensitive to environmental factors such as air currents or vibrations. This proved to be the case during the early stages of this work as the laser's mode-locking mechanism would fail on several occasions, resulting in the need to continually monitor and adjust the lasers intra-cavity wave plates in order to control its mode-locked performance and spectral output. In doing so, the spectral shape of the laser would change slightly at various intervals during the experimental efforts; however, the spectral bandwidth remained approximately constant. The optical spectrum of the erbium-doped fibre laser is presented in Fig. 5. This was acquired using a Rees E200 Series Optical Spectrum Analyser (OSA) - measurement resolution 0.3nm.

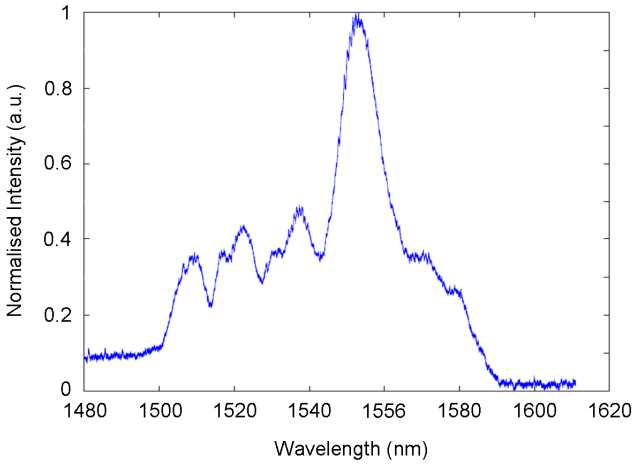

Figure 5 – Stretched-pulse Er:fibre laser optical spectrum acquired using a Rees E200 Series OSA (measurement resolution 0.3nm) . Disregard the offset on the left-hand-side of the spectrum – this was artificially induced by the detection electronics

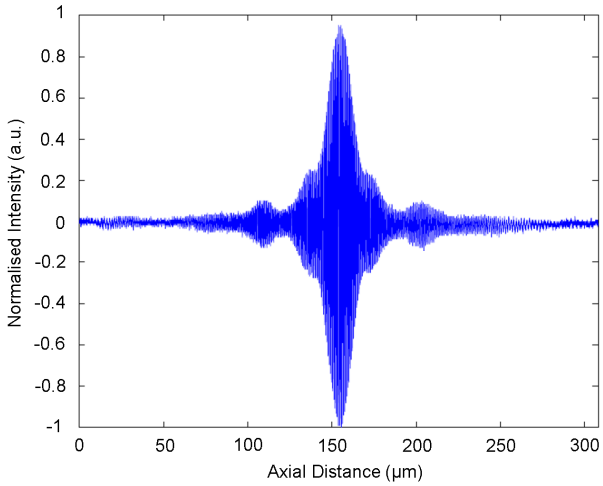

Figure 6 – Interferogram measured with a gold mirror positioned in the sample arm. The FWHM is 18µm

The interferogram recorded using a simple planar gold mirror in the reference arm had a measured full width at half maximum (FWHM) of ~18µm (Fig. 6). The theoretical FWHM value for a Gaussian shaped spectral distribution was calculated to be ~15µm according to equation (10).

5.5.3 Glass Cover-Slide Evaluation

A microscope cover-slide is an ideal source of additional calibration for OCT systems. The basic functionality of an OCT system is to sensitively detect optical echoes from different axially displaced surfaces within a sample, therefore since a cover-slide has only two equally spaced reflecting surfaces it acts as the perfect initial sample under investigation. The thickness of the cover-slide was measured to be ~100µm. This set an accurate axial displacement target to compare against the calibrated cover-slide interferogram trace. If the distance between the two peaks of the optical interferogram matched the 100µm measured in air previously then it would confirm that our system was suitably calibrated. Fig. 7. shows the interferogram trace of the cover-slide measured in glass (n~1.5). It is clear that the peak-to-peak separation distance measured on the interferogram matches the 100µm recorded beforehand, after considering the refractive index of glass, and that our system recorded strong back-reflections each time. Note here that all subsequent interferogram traces or OCT images have their axial distance calibrated for acquisition in air – unless stated otherwise.

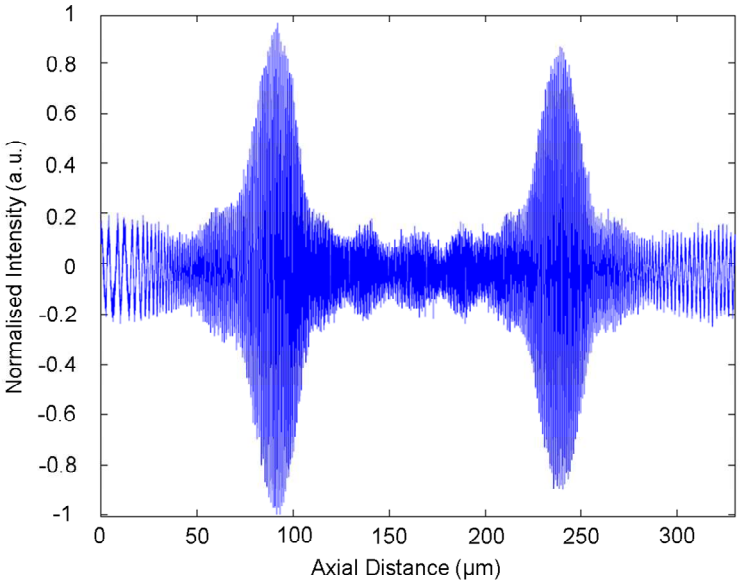

Figure 7 – Acquired interferogram trace of a microscope cover-slide of thickness 100µm – measured in air. The axial distance of the interferogram is that measured in glass (refractive index, n~1.5)

The calibration images acquired above suggested that the initial OCT imaging system was ultimately limited by its axial resolution in its ability to produce high quality sub-surface evaluations of silicon ICs and artwork conservation. Although the results acquired are of a suitable level for basic preliminary examinations of highly reflective simple planer surfaces, the detection of depth-resolved sub-micron features remains to be achieved.

The main limiting factors in this configuration can be separated into two different categories. The most obvious is the relatively large axial resolution performance of 18µm. This value is in good agreement to the theoretically predicted value of 15µm when the erbium-doped fibre laser spectral bandwidth of ~80nm is taken into consideration; however, it is too large for suitable material interrogation. Therefore, an optical source with a larger spectral bandwidth is required since the axial resolution is inversely proportional to this parameter. An ideal solution is to generate a supercontinuum (SC) within a highly nonlinear fibre (HNLF) by spectrally broadening the input optical pulses that traverse the length of the fibre.

Moreover, an additional constraint may be the system's signal-to-noise (S/N) ratio. It is clear that this can be improved by acquiring a heavily averaged signal at each lateral position across a sample; however, this approach is extremely primitive and lacks the

sophistication required to accurately distinguish small signal levels that are concealed beneath large noise levels. A suitable solution is to implement the use of a balanced-detection scheme into the system [39]. This is an efficient source noise rejection technique that can be employed using a wide variety of different OCT configurations.

These two performance-enhancing features will be considered and their implementation into an improved OCT system discussed.

5.5.4 Supercontinuum Generation

A SC source is considered to be that which can generate a high-brightness, broadband continuous spectral distribution. This can be achieved by transmitting an ultrashort optical pulse of high peak power through a nonlinear material which has unique dispersive properties. SC generation therefore is easily implemented in optical fibres due to their confined cross-sectional propagation area and because their dispersive conditions can be tailored with high accuracy during fabrication; examples of such fibres include dispersion-shifted, dispersion flattened and novel photonic crystal fibres (PCF).

There are several nonlinear optical processes which can take place to induce SC generation. These processes fall into four main categories: self-phase modulation (SPM), stimulated Raman scattering (SRS), soliton self-frequency shifting (SSFS) and four-wave mixing (FWM) [40]. These mechanisms can either contribute individually or as a collective mixture to produce a SC. All of these effects are dependent on the magnitude and sign of the fibre dispersion at the central wavelength of the propagating input pump pulse. Moreover, these components are also sensitive to the spectral location(s) of the fibre's zero-dispersion wavelength(s). In order to generate a SC that has the widest spectral range it is a general requirement that the zero-dispersion wavelength is located as close to the centre wavelength of the pump as possible.

The following offers a brief description of the above mentioned principal nonlinear processes responsible for SC generation:

SPM is the primary mechanism for SC generation in optical fibres [41] that exhibit normal dispersion at the pump central wavelength since it is not possible for a soliton to form which would cancel out the SC process. As discussed in Chapter 2, SPM is the

result of an intensity-dependent refractive index change which introduces a phase shift of the propagating pulse that is a function of time. Therefore, a time-dependent frequency shift (chirp) is created which broadens the width of the initial pump spectrum as new spectral components are continuously created as the pump traverses the fibre. Nonetheless, note that SPM in isolation is seldom sufficient for extensive SC generation.

SRS describes an inelastic interaction between the propagating pump pulse and the fibre material where incident photons can excite the fibre material's vibrational states which results in the loss of some photon energy and momentum [42]. This loss of energy red-shifts (shifts to longer wavelengths) the incident pump pulse (this is known as Stokes scattering). A blue-shifted pump pulse can also emerge (known as Anti-Stokes scattering); however this requires the transfer of excited phonon energy to the pump photons. This is less likely to materialise since the probability of this event taking place is very low.

If the pump central wavelength is located close to the zero-dispersion wavelength then the combination of SPM and SRS will broaden the spectrum into the anomalous dispersion regime. This is an ideal situation for soliton formation. Optical solitons generally experience a down-shift of their carrier frequency (a red-shift of their wavelength) which increases with pump power. This effect is called a soliton self-frequency shift (SSFS) [43].

Four-wave mixing (FWM) is a third-order nonlinear effect that can utilise an optical fibre to mediate the interaction of optical frequencies to induce the generation of other frequencies [44]. There is no energy exchange between the wave and the medium (unlike SRS). In this case, energy is transferred to lower and higher frequencies that did not originally exist in the pump spectrum. This process is dependent on the phase-matching and energy conservation conditions,

$$\Delta k = k_3 + k_4 - k_1 - k_2 = \left(n_3\omega_3 + n_4\omega_4 - n_1\omega_1 - n_2\omega_2\right)/c = 0 \qquad (14)$$

which satisfies the need for energy conservation between each frequency. It is generally straight-forward to create a case where $\omega_1=\omega_2$, therefore, if a strong pump wave is

efficiently coupled into an optical fibre it can generate two sidebands located symmetrically at frequencies ω_3 and ω_4, where $\omega_3 > \omega_1 = \omega_2$ and $\omega_4 < \omega_1 = \omega_2$.

For the purposes of this work, it is highly desirable to implement a source with a broad bandwidth in an OCT system since the axial profiling resolution is proportional to the inverse of the source bandwidth. Therefore, SC generation was investigated using several types of highly nonlinear optical fibre.

The initial attempts towards SC generation considered two different types of HNLF: the first was a germanium-doped fibre and the second was a chalcogenide based fibre. Both fibres failed to produce a suitable SC for OCT applications simply because the input pump power from the Er:fibre laser was too low (~75mW average power); however, there were characteristic signs of stimulated nonlinear effects that were observed for both HNLFs – early SSFS and FWM were measured from the germanium-doped fibre and the chalcogenide based fibre, respectively.

Although these nonlinear processes were only starting to develop and broaden the input optical spectrum, these preliminary results suggested that ideal SC generation might still be possible if the input pump power could be increased. We therefore developed an erbium-doped fibre amplifier (EDFA) which could be fibre-coupled onto a length of HNLF for suitable SC generation. The exact details of the EDFA's construction and characterisation were described in Chapter 2; however, the key EDFA parameters to note are that the output pulse duration was measured to be approximately 160fs (after dispersion compensation) and the average output power was ~200mW.

Once the EDFA was implemented and optimised for the OCT configuration the process of investigating SC generation was revisited. The first fibre to be considered was the chalcogenide based fibre since its earlier result showed the greatest promise. This fibre had a length, mode field diameter, chromatic dispersion and chromatic dispersion slope (measured at 1.55µm) of 75cm, 3.78µm, 4.1ps/nm/km, and 0.021ps/nm^2/km. The increased power from the EDFA was coupled into the chalcogenide HNLF by fusion splicing the EDFA's dispersion compensation SMF28 fibre and the HNLF together; however, the direct core mismatch resulted in an unavoidable loss of total available coupling power. The result obtained highlighted an improved performance which was dominated by FWM. This is clearly illustrated by the SC peaks located on both sides of

the 1.55µm pump wavelength (Fig. 15). Although the extremes of this SC extend toward 0.2µm and 1.95µm, there were significant portions of the generated spectrum that contained no intensity at all and therefore was unsuitable for the OCT system.

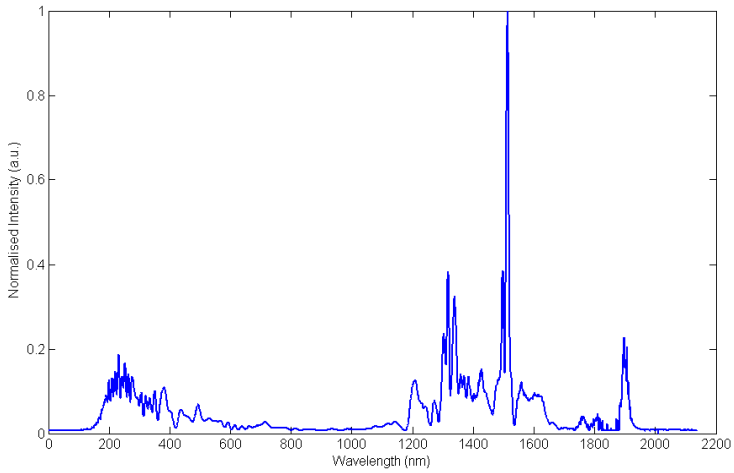

Figure 15 – Supercontinuum Generation – chalcogenide-based fibre result

The second fibre to be examined was a germanium-doped polarisation-maintaining dispersion-shifted HNLF (PM-DS-HNLF) [45]. This was an ideal fibre to use since its characteristics were tailored for efficient SC generation when optically pumped at 1.55µm. This fibre had a length, mode field diameter and chromatic dispersion slope (measured at 1.55µm) of 100m, 3.7µm and -1.3ps/nm^2/km. The resulting SC had a broad bandwidth which was almost octave-spanning (1.25µm to 2.1µm) with a peak intensity located at the pump wavelength of 1.55µm. The spectral distribution observed can be described by the characteristic nonlinear processes SRS and SSFS. An important parameter associated with this fibre is that the polarisation state that enters the fibre is maintained along its entire length. This makes it possible to manipulate the generated SC distribution by controlling the launched input polarisation state through the implementation of stress-induced birefringence fibre polarisation controllers. By changing the launched polarisation state it is possible to redistribute the spectral intensity of the pump beam into either the slow or fast axis of the fibre. The result is a modified SC spectral width and shape. This was investigated and optimised for the OCT system. Fig. 16 illustrates a number of possible spectral distributions under such an arrangement.

I would like to acknowledge Dr. Henry Bookey for providing the PM-DS-HNLF.

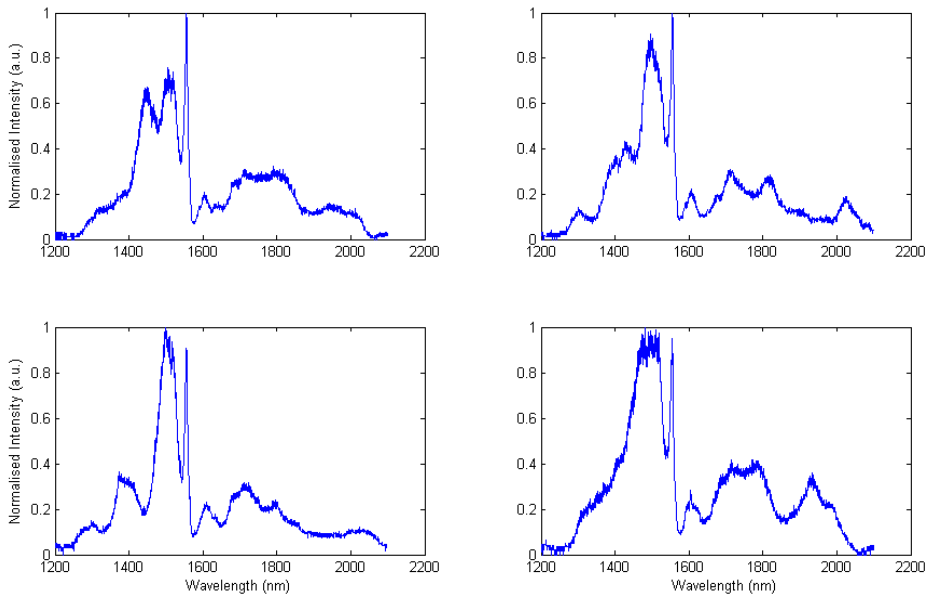

Figure 16 – Supercontinuum Generation – PM-DS-HNLF. The resulting spectral distributions (as illustrated) could be manipulated through the use of a fibre-based polarisation controller

Although the observed SC presented in Fig. 16 was almost octave-spanning and its spectral distribution controlled through polarisation controllers, the total fibre length of 100m suggested that the generated continuum may have encountered significant attenuation as it propagated along the fibre. Prolonged attenuation can suppress the SC generation process and therefore result in an observed spectrum that is an altered version of that initially produced over a shorter fibre length. As a result, a SC fibre cut-back measurement was taken to ensure optimum performance from the PM-DS-HNLF. This involved removing a 2m length of fibre from the reel and acquiring several SC measurements as the input pump power from the EDFA was increased from minimum to optimum power (in steps of 30mW, 75mW, 125mW and 200mW) with the effects of polarisation optimised at each interval. There were a total of three stages to this process. At each stage the fibre was halved and the measurements repeated. When the fibre length was 25cm it was no longer possible to easily splice the two fibres together; therefore, the process did not continue. The results are presented in Fig. 17 (a) – (d).

It is clear to see from Fig. 17 that this fibre cut-back measurement produced interesting results; however the generated supercontinuua never exceeded the spectral bandwidth of that obtained initially, nor did they yield a preferable (i.e. Gaussian) spectral distribution. Therefore, the remaining 98m of PM-DS-HNLF was spliced back into the system and the original SC used as the optical source.

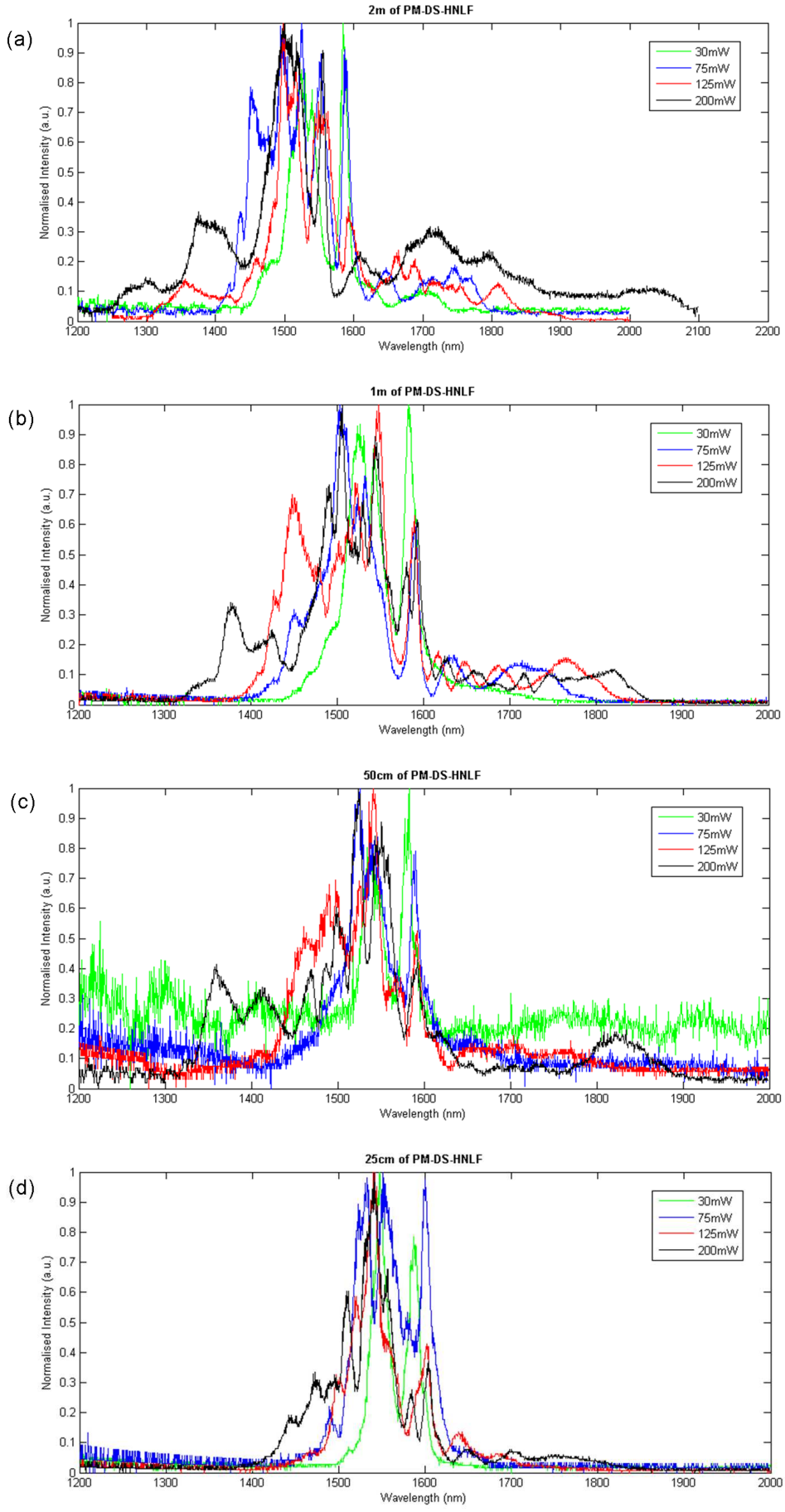

Figure 17 – Supercontinuum Generation cut-back analysis with resulting supercontinuum traces acquired at (a) 2m, (b) 1m, (c) 50cm and (d) 25cm of fibre at EDFA output powers of 30mW, 75mW, 125mW and 200mW

5.5.5 Balanced-Detection

One of the principal components in an OCT imaging system is the optical detector. Optical detectors can be categorised according to a number of different performance parameters. These include noise equivalent power (NEP) (this is the optical input power required to achieve a S/N ratio of 1), a spectral sensitivity ($\Delta\lambda$) that isolates the required wavelengths for a given application and the ease of implementation. These are all important performance-enhancing characteristics; however the overall performance of a single detector can be limited by unwanted internal noise - examples of which include photon noise (i.e. the random arrival of photons), photoelectron noise (i.e. photocarrier-generation efficiency) and receiver circuit noise (i.e. noise associated with passive electronic components within the detector). These parameters can be suppressed through detector research and development; however it is simply not possible for a single detector to eliminate noise that emanates from an external source.

Intensity noise fluctuations from the optical source can substantially degrade detector and hence system performance. Therefore, an ideal solution to overcome this issue is to employ the use of a balanced-detection scheme [39]. This configuration (Fig. 18) utilises two identical detectors and offers two main advantages over the single-detector alternative. The first is an increase in the system performance since intensity fluctuations from the source are cancelled out. The second is the ability to obtain an improved level of performance with reduced source power since both beamsplitter outputs are collected by the two detectors, minimising discarded source power.

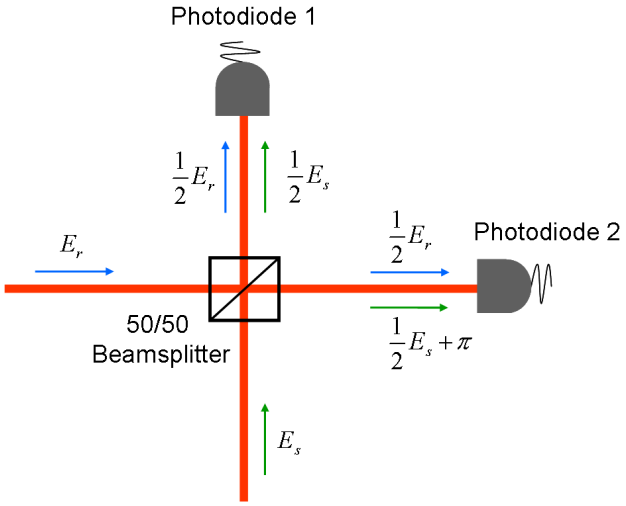

Figure 18 – Conceptual sketch outlining the principal of balanced-detection. The signal emanating from the reference arm sees no phase change on both transmission and reflection, whereas the sample arm signal sees a 180° phase change on reflection, but not in transmission. This enables the cancelation of source noise through photodiode signal subtraction

A major requirement for effective balanced-detection is ensuring that the source noise in each detector arrives in-phase (this is always the case), whereas the beat signal from the interfered reference and sample arms arrive 180° out-of-phase [46]. This is generally realised by considering the reflection-induced phase changes at the final beamsplitter before the detectors. The reference arm signal sees no phase change on either transmission or reflection at the beamsplitter, whereas the sample arm signal sees a 180° phase change on reflection, but not in transmission. Since the source noise after the beamsplitter outputs is in phase, the signal and noise can be separated (see Fig. 18). Therefore, when the 180° phase change is observed, by subtracting the two detector input signals, the source noise can be suppressed. The result is a balanced-detection S/N ratio that out performs that which is possible under conventional single-detector configurations; however, note that if the phase change is not observed and both noise and sample signals arrive in phase then the resulting signal subtraction reduces the output signal to zero. This performance was modelled in MATLAB and the results illustrated in Fig. 19 (a) for the in-phase arrangement and in (b) for the 180° out-of-phase arrangement.

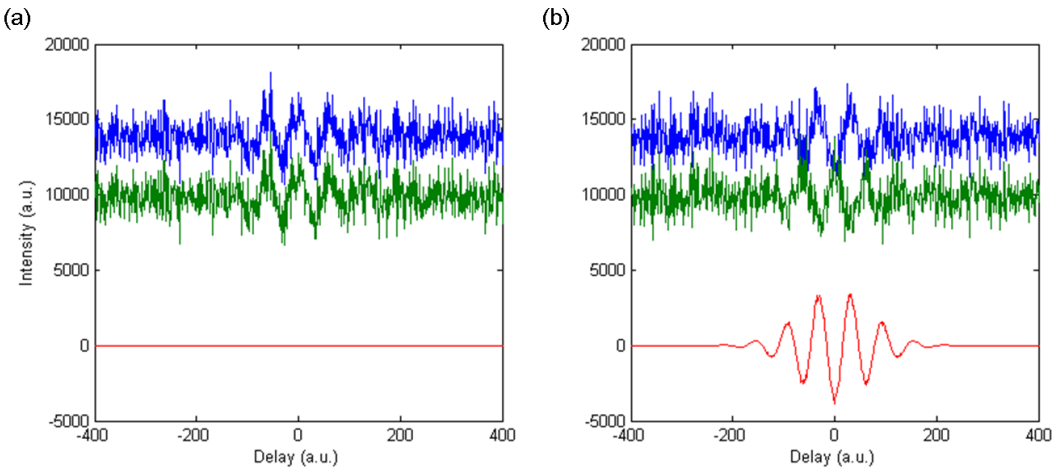

Figure 19 – Balanced-detection model results (a) The resulting balanced-detection output signal (red line) when the two detector signals (blue and green lines) are in phase and (b) when they are 180° out-of-phase

The detectors utilised in this work were extended indium gallium arsenide (Ext InGaAs) PIN photodiodes (model number IGA1.9-010, from Electro-Optical Systems). The photodiodes operated using a reversed bias voltage which was supplied by a 9V battery. The output voltage, which was proportional to the photocurrent and hence the intensity of the incident light, was measured across a 10k resistor. The photodiodes had a spectral responsivity ranging from 1.2µm to 2.1µm which coincided with the expected

bandwidth of the generated SC source. The NEP at 2.2µm ($4x10^{-13}$ $W/Hz^{1/2}$) was relatively high compared to detectors in the visible regime. This is due to the reduced bandgap which increases the level of thermal noise. The responsivity at 2.2µm (1.2 A/W) is equal to a quantum efficiency of about 68%.

The signals coming from both photodiodes were subtracted using an instrumentation amplifier (AD620). The circuit is depicted in Fig.20. This circuit contained a suitable variable resistor (100kΩ) in order to control the gain of the output signal when input signal levels were low or to reduce the signal level to within the ±1V acceptance level of the A2D card (this requirement is discussed later).

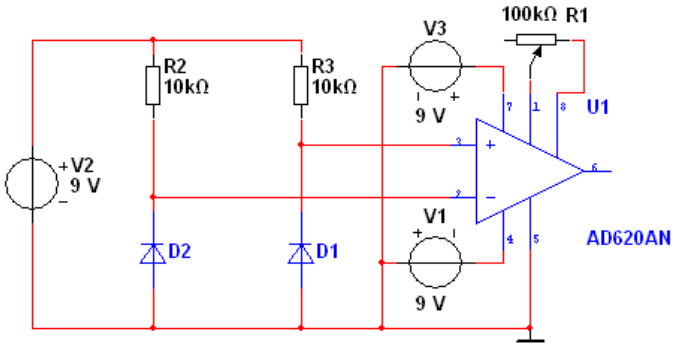

Figure 20 – Electronic circuit used for balanced-detection. The operational amplifier used is an instrumentation amplifier (AD620)

5.6 Experimental Implementation and Calibration

The experimental configuration that was implemented was a modified version of the earlier system described earlier. This was adapted again later to incorporate the balanced-detection scheme.

The linearly-polarised output from a modelocked stretched-pulse Er:fibre laser, operating at 1.55µm, was relay coupled into an EDFA to generate intense ultrafast optical pulses. The Er:fibre laser emitted ~160fs pulses at a repetition rate of 32 MHz with an average output power of 60mW. The resulting pulses from the EDFA were compressed using a suitable length of negative-dispersion SMF28 telecommunications optical fibre and measured to have durations of approximately 160fs with an average power of 200mW. The SMF28 fibre was fusion spliced onto a 100m length of PM-DS-HNLF to produce an optical bandwidth spanning 1.25 - 2.1µm. The SC was collimated using a suitable aspheric lens positioned on a fibre micro-block and coupled into a

standard Michelson interferometer that was optimised for minimum dispersion mismatch between the reference and sample arms. The reference arm initially used a double-passed scanning retro-reflector mirror to increase the optical observation window within the sample and the detector was an Ext InGaAs photodiode with an optical sensitivity covering 0.8 - 2.1µm. The resulting interferogram traces were displayed on a 9-bit vertical resolution Tektronix TDS3032 oscilloscope for real-time analysis. The OCT interferometer incorporated a 2-µm-thick pellicle beamsplitter with a 45% - 55% reflectivity range from 1 - 2µm. The focusing lens was changed from the 11mm focal length TAC4 aspheric lens to an uncoated 125mm focal length BK7 singlet (Δx =197µm, b=39.6mm) in order to concentrate on the axial resolution performance.

To calibrate our system we employed a HeNe-based Michelson interferometer to measure the displacement of the double-passed scanning retro-reflector used in the OCT interferometer. This allowed us to accurately determine the effective optical path length (OPL) of the reference arm, taking into account the acceleration / deceleration of the scanning retro-reflector, yielding a displacement scale for the OCT images. The resolution of our system was measured to be 2.5 µm (displacement) in air by extracting the envelope of the interferogram by taking its Hilbert-transform, then low-pass-filtering the result to obtain a smooth trace. The interferogram and envelope are shown in Fig. 21, where the scale is the effective displacement of the end-mirror in the reference arm, corresponding to the depth in an OCT image.

The bandwidth and profile of the OCT spectrum was measured by Fourier-transforming the interferogram shown in Fig. 21, and the resulting spectrum is shown in Fig. 22. The spectral bandwidth and shape are very similar to that recorded earlier using a monochromator, confirming that the OCT interferometer did not reduce the spectral bandwidth available in the SC. As a preliminary image we recorded an OCT section of a 145µm thick cover-slide. This image is shown in Fig. 23, with a depth scale that is corrected for refractive index (n~1.5), and the separation between the top and bottom surfaces of the slide is clearly visible and matches the expected physical thickness exactly. This axial profiling performance is clearly superior to that obtained previously using the initial system (see Fig. 7).

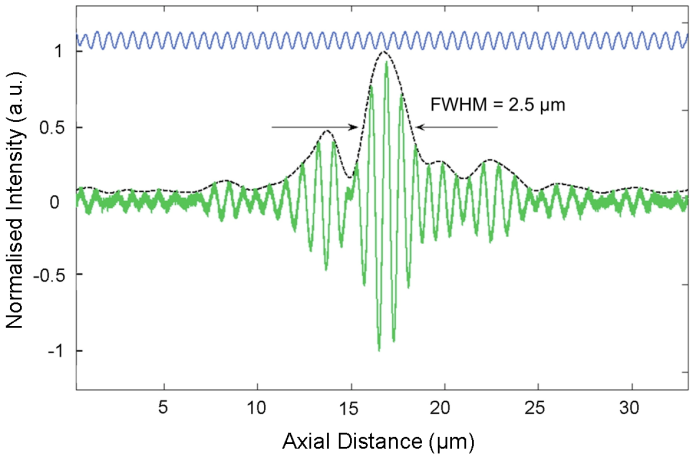

Figure 21 - Measured interferogram (green line) in air revealing 2.5 µm displacement resolution, and the resulting Hilbert-transform envelope (black dashed line) with accompanying HeNe fringes (blue) for calibration. The total optical path difference between the interferometer arms is twice the displacement of the reference arm and the OCT reference and sample arms both contained gold end-mirrors.

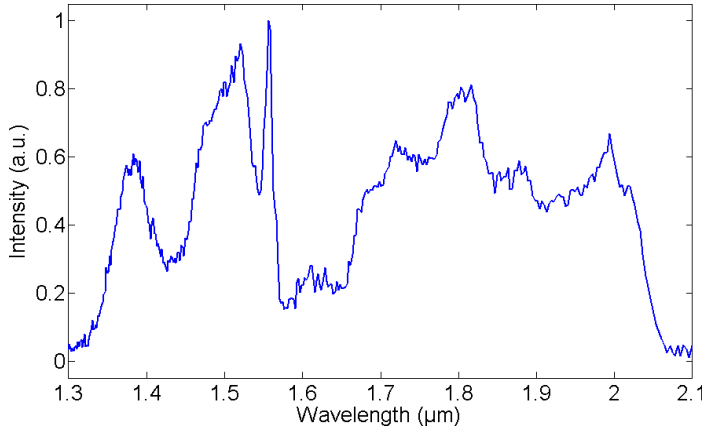

Figure 22 - Spectral content obtained through a Fourier-Transformation of the measured interferogram

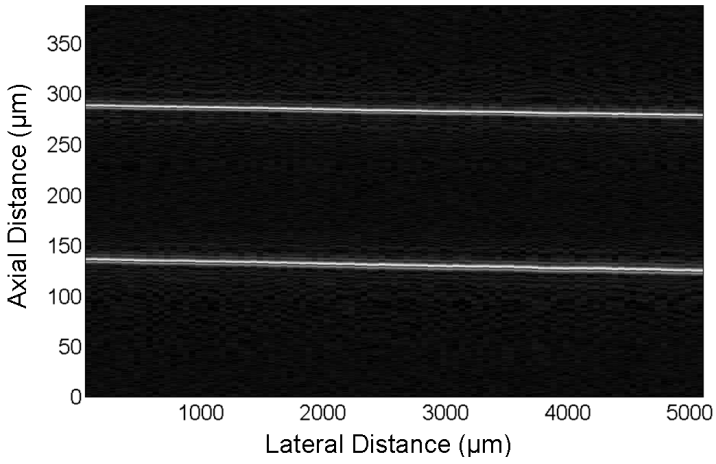

Figure 23 - OCT image of a cover-slide, with a physical depth scale corrected for the refractive index of the slide (n~1.5).

To include the balanced-detection scheme required a further modification of the experimental configuration. It was not possible to utilise only one beamsplitter in this arrangement, therefore a second beamsplitter was implemented but at the expense of returning to only a single-pass of the retro-reflecting reference arm mirror. This reduced the total optical scan range (i.e. axial profiling depth within the sample); however this had to be traded-off in return for improved system performance. The final experimental configuration is illustrated in Fig. 24.

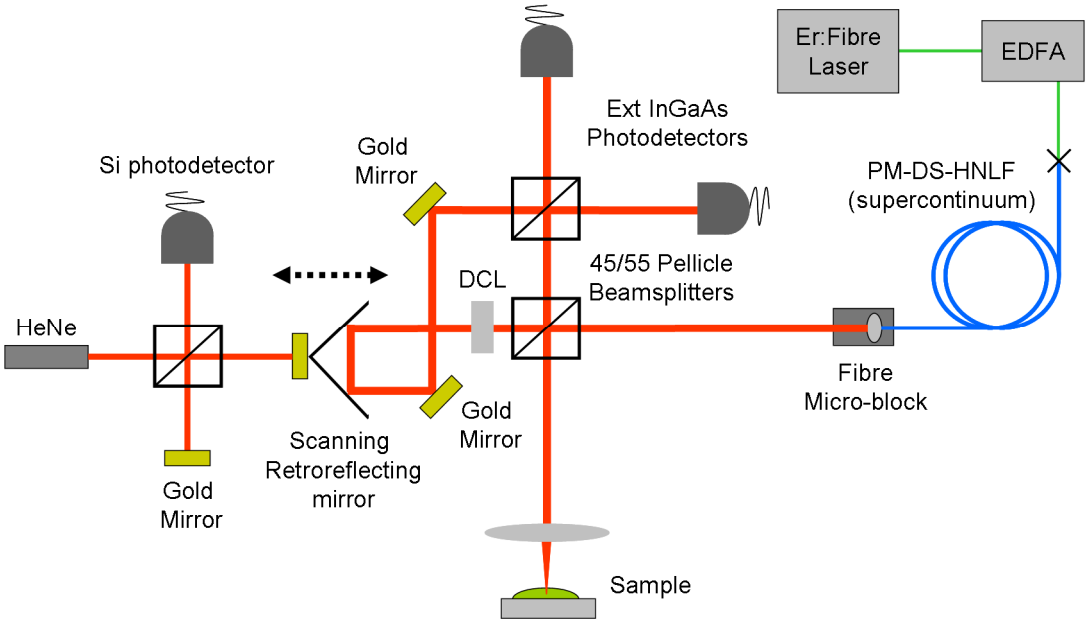

Figure 24 – Final experimental configuration utilising a supercontinuum source, balanced detection and a HeNe calibrated reference arm

Naturally, a vital aspect of the balanced-detection scheme is that the two detectors receive the same (i.e. balanced) optical power after transmission/reflection from the beamsplitter. This can be controlled by the transmission coefficient of the beamsplitter. The ideal case is when the beamsplitter acts as a perfect 50/50 coupler; however, if the beamsplitter does not correspond to this requirement then the system performance will be degraded. If one detector collects significantly more optical power than the other then the system will effectively operate in the single-detector regime since one detector becomes dominant. It is possible to influence an unbalanced scheme by introducing controllable attenuation. This may be implemented as a neutral-density filter wheel or, more crudely, by offsetting the optimum detector position slightly.

A rather obvious requirement in a balanced-detection scheme is that the two detectors have matching performance. It would be foolish to implement an optically balanced configuration with unbalanced detectors. A simple solution here, to remove any possible error, would be to employ identical detectors.

The experimental influence of balanced-detection is presented in Fig. 25. The signals from two photodiodes have been collected, normalised and displayed individually. These two signals have a significant noise level (the S/N ratio was measured to be 18.4) which would limit an OCT system; however, the resulting balanced-detection signal generates an improved OCT interferogram with an enhanced S/N ratio (the improved S/N ratio was measured to be 93).

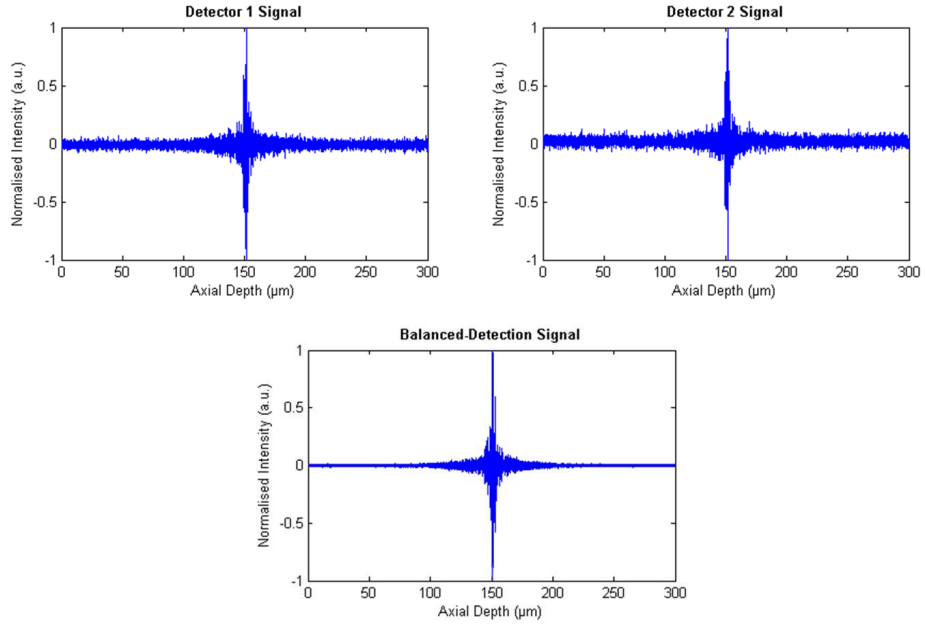

Figure 25 – Experimental balanced-detection verification to highlight the improved S/N ratio

In addition, to improve the lateral resolution of our system the original 11mm focal length TAC4 aspheric lens was re-introduced. The dispersion mismatch between the sample and reference arms was investigated by inserting a stack of BK7 microscope slides in the reference arm. Although the initial configuration required only a single microscope slide for adequate compensation, this had to be reassessed since an almost octave-spanning SC source was now implemented. The conclusion was that a stack of 8 microscope slides produced the optimum performance (i.e. the narrowest interferogram with a symmetric distribution).

Furthermore, to improve the data analysis stage of the system an Adlink PCI-9812 analogue-to-digital (A2D) card with a 12-bit vertical and ~20MHz sampling resolution was configured into a PC and used to acquire the resulting HeNe and OCT interferograms. This addition permitted the acquisition and manipulation of a greater data set at higher speeds; however, the A2D card could only accept a peak-to-peak OCT interferogram signal of less than 2V. Therefore, the variable gain on the balanced-detection circuit had to be adjusted for output signal control.

5.7 Silicon Integrated-Circuit Results

The target application of our OCT system was to develop a truly novel inspection technology for silicon IC failure analysis (FA). It was stated previously that there have been limited studies into OCT-based IC evaluation [27], hence it is highly desirable to develop an additional characterisation tool to aid the progression of semiconductor device FA.

The device under test was the Azuma Optical Probe Test Chip (OPTC) developed by Schlumberger. This IC was fabricated to serve as an optical, electrical and focused ion beam (FIB) test bed to assess the functionality of both the chip itself and the analytical evaluation tools mentioned. The Azuma OPTC chip contains a collection of individually fabricated circuits and structures located on a die size of 4766.6μm^2. This area describes the silicon die only and does not consider the protective plastic seal ring which is located around the die perimeter. Unfortunately, the device support information only contained a floor-plan schematic of this area to indicate where exactly these features could be found. Therefore, an infrared laser scanning microscope (IR-LSM) was utilised to obtain a reflectivity floor-plan of the chip. This was acquired by overlaying a number of LSM images together since a suitable objective lens was not available to map out the entire die area in one single image; however, this created dark to light boundary features located across the image due to overlapping the individual images of varying contrast.

This reflectivity image is presented in Fig. 26 (a) and highlights the individual test features as well as the scan directions chosen for OCT analysis. The schematic floor-plan is illustrated in Fig. 26 (b). Note that the schematic diagram has been flipped to coincide with the scan directions and device features given in Fig. 26 (a). The scan direction was limited in the vertical direction (towards the bottom of the chip) due to the restricted range of the sample mounted translation stage. It is clear that both the LSM

reflection image and the device schematic are in agreement with each other. This allows for exact OCT image calibration since the measured feature positions on the chip can be mapped back to the precise coordinates given by the device schematic.

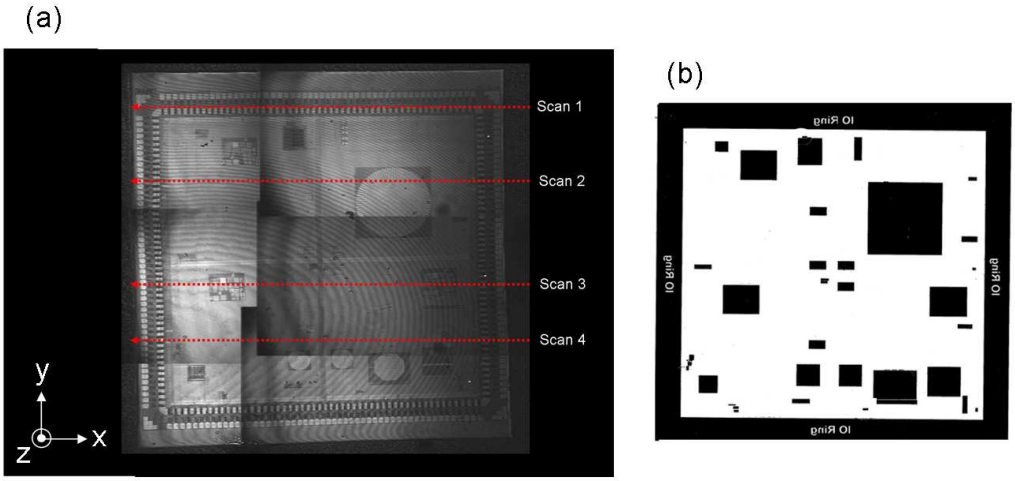

Figure 26 – Azuma Chip – (a) LSM fabrication floor plan highlighting specific device features and OCT scan directions (dotted red lines) and (b) a schematic diagram of the chip floor-plan highlighting specific device features and the protective plastic seal ring around the die perimeter

The first OCT silicon IC images, acquired along scan direction 1, are presented in Fig. 27 (a) and (b). The scan started from a position on the protective seal ring and finished at the opposite position located across the chip. This is verified on the OCT images by the acquisition of no sub-surface information at the extremes of each scan. The difference between these two images is the representation of OPL and how it affects OCT image interpretation. The refractive index, *n*, of silicon is approximately 3.5; hence any change in sample depth will be amplified by a factor of 3.5 since the OPL is *nL*, where *L* represents the physical length (or depth) of the inspected sample. Therefore, Fig. 27 (a) reveals that the silicon substrate is not perfectly uniform. Since the device layer of the chip was almost certainly fabricated on a linear platform, the deviation from uniformity of this layer on the initial OCT image suggests that the substrate thickness must be increasing, indicating a non-uniformity introduced by the chemical substrate-thinning process known to have been used on this device. This has been taken into consideration and, in order to present a more intuitive physical representation of the OCT images, all subsequent raw OCT images have been manipulated to remove any uniformity offset. This is illustrated in Fig. 27 (b).

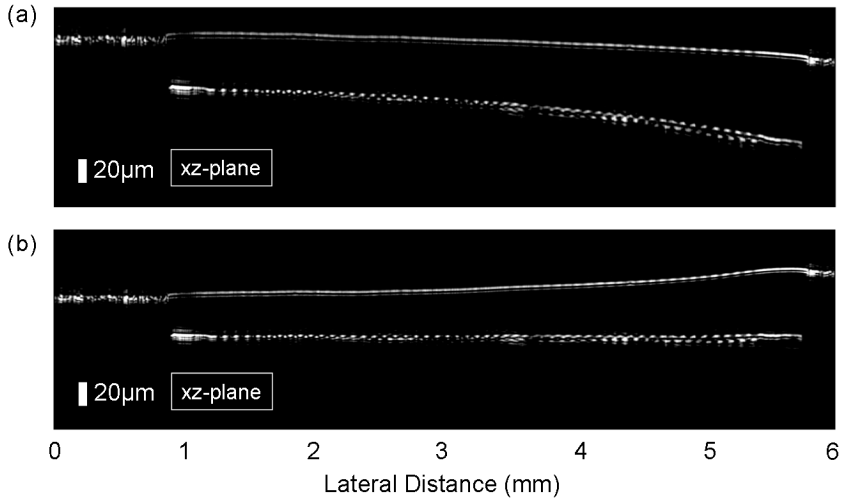

Figure 27 – Initial OCT Images of Azuma Chip – (a) The initial non-uniform OCT image and (b) the amended linear image.

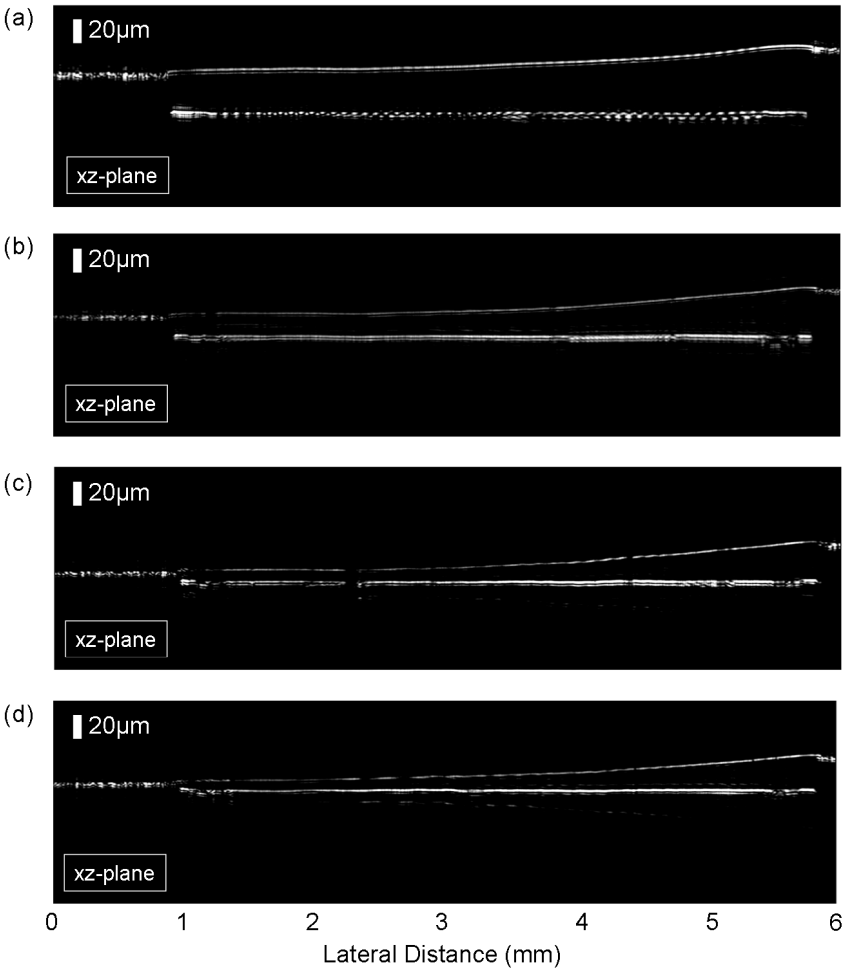

Figure 28 – OCT Images of Azuma Chip – The scan directions presented in (a)-(d) are highlighted by the red dotted lines in Fig. 19 (above)

The remaining OCT images, acquired at scan directions 1 through 4, are presented in Fig. 28 (a)-(d), respectively. These images have been amended to compensate for substrate non-uniformity. It is clear from these images that not only is the substrate non-uniform in the horizontal direction across the chip, it is also non-uniform across the vertical direction. This is confirmed by observing a continuous decrease in substrate thickness as the vertical scan direction is changed. This information has provided, for the first time, an OCT-based silicon IC characterisation tool for the assessment of device substrate uniformity. The ability to optically monitor substrate thickness offers a novel technology for assessing substrate polishing/thinning performance for device FA and quality control.

With regard to the inspection of sub-surface features on the chip, it is possible to infer additional information from the OCT scans. Scan direction 1 (Fig. 28 (a)) traversed a sequence of metallisation interconnections located at the perimeter of the device. These metal features were easy to investigate and observe due to their repetitive sequencing. This was observed on the OCT image as a periodic array of high and low reflectivity regions. In addition, towards the end of the scan it is clear that the single periodic track splits off into two depth-resolved features. This can be explained due to the slightly offset scan direction (the probe beam passes from one feature across to the adjacent feature) and the axial displacement of adjacent features due to the photolithography fabrication process. This image therefore reveals that not only is it possible to interrogate substrate thickness using this technology, it is also possible to assess the quality of device packaging and interconnection inspection. This would provide an alternative FA inspection tool for the evaluation of electronic device read-out.

The device information provided by Fig. 28 (b) highlights a number of interesting attributes about the sub-surface features under inspection. The first is the non-uniformity of the substrate thickness which has been discussed already. The second is that both the metal interconnected tracks located around the device perimeter and the largest chip test circuit are clearly identifiable and can be compared and calibrated against the LSM reflectivity image as presented in Fig. 26 (a) and (b). Fig. 29 (a) illustrates the calibrated OCT image acquired across the red dotted scan direction line and Fig. 29 (b) illustrates the LSM image. These two images reveal that there is a direct overlay between both the metal tracks and the large circuit feature. This is supported by the fact that the majority

of the device content at this particular location is redundant space; therefore the only interruptions along the OCT scan line direction will correspond to individual features.

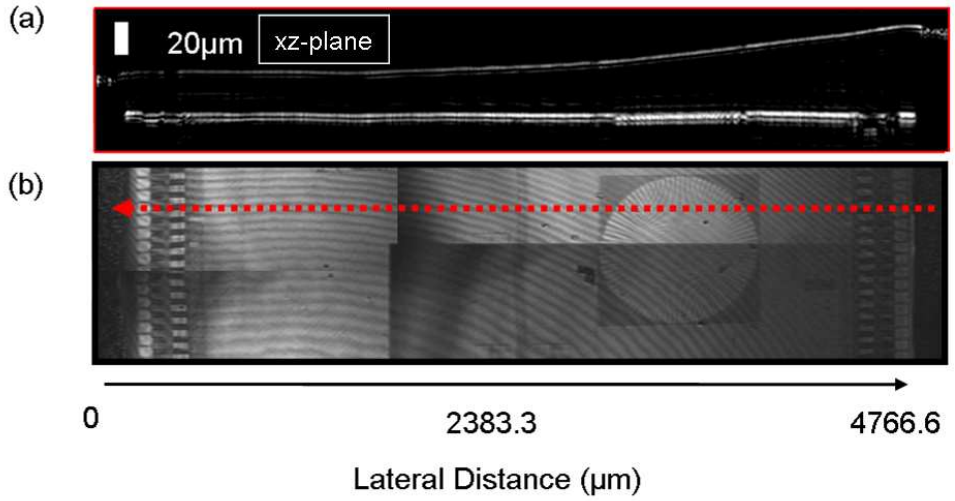

Figure 29 – Calibrated overlay between (a) the OCT image and (b) the LSM reflectance image. The OCT image was acquired along the scan direction indicated by the dotted red line

The third point about this image is the most important with regard to feature recognition. After closer inspection of both the acquired OCT image at scan direction 2 and the LSM floor-plan, it was noted that the circuit feature section on the OCT image and the circuit feature itself share a common connection. The OCT image appears to reveal a periodic structure that distinguishes itself from the majority of the scan. This structure has an angled distribution which is normal to the incident beam at the centre but fans out towards the edges. This can be explained after closer examination of the circuit feature using the LSM image. Fig. 30 (a) and (b) compare and contrast the two recorded images and confirm that this structural distribution across the OCT image corresponds to a radial fabrication distribution of the circuit feature. It is fortunate that the beam path traverses a location near the edge of this circuit since these positions will uncover the radial distribution better than if the beam were to pass across the centre of the circuit. In addition, since the lateral resolution of this system is approximately 20µm, it blurs out the finer central features but resolved the larger wedge-shaped features towards the edges of the radial distribution. This is a significant discovery since it provides the first sub-surface OCT interrogation of a device feature on a silicon IC and also suggests the evaluation limitations of our system.

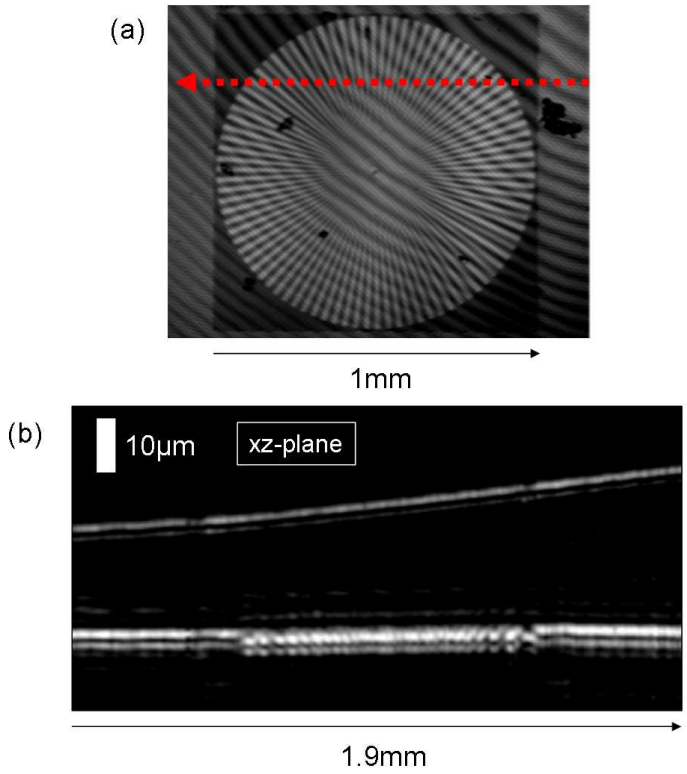

Figure 30 – (a) LSM image of Azuma chip circuit feature exposing radial fabrication distribution and (b) a magnified OCT image of this feature confirming this distribution. The OCT image was acquired along the scan direction indicated by the dotted red line

Figs 28 (c) and (d) unfortunately reveal no other additional information about the device under test other than the general points regarding substrate thickness and the location of the metallisation interconnected tracks discussed already. It is clear that Fig. 28 (c) accurately highlights the location of two standard resolution targets on the die; however the interrupted OCT scan line at these locations did not offer any further evaluation. Fig. 28 (d) simply traverses a completely redundant line across the chip.

The results presented above confirm that our high-resolution high-dynamic-range OCT evaluation system represents a promising new optical inspection tool for monitoring silicon IC substrate uniformity and general device feature tracking. This offers a novel FA technique to improve product yield and quality control; however, it was not possible to inspect the sub-micron features fabricated at the device layer of modern flip-chips with sufficient accuracy. Although the lack of an appropriate dispersion compensation mechanism in the reference arm of the Michelson interferometer reduced the measured axial resolution of 2.5µm (in air) by a factor of 3.5 (the refractive index of silicon) to become 714nm, the limited lateral resolution value offered by the TAC4 aspheric lens

(as well as the negative effects of refraction at the air/silicon boundary) was not ideal for the interrogation of custom semiconductor ICs.

The availability of limited resources and a limited budget therefore prevented an extensive IC evaluation to be performed; hence the second phase of the project was initiated which concentrated on the potential of the system for sub-surface imaging in painted and printed media.

5.8 OCT of Painted and Printed Media

This section concerns the evaluation of painted and printed media using a non-destructive TD-OCT optical imaging system for counterfeit prevention and artwork conservation

5.8.1 IBM Business Card

An ideal test sample to interrogate before commencing with the artwork examination came in the form of a personal IBM business card. This sample met all the required imaging criteria (i.e. slightly embossed surface features with a fair reflectivity). The IBM business card was imaged using both the initial system and the enhanced system. All images were acquired with *depth* priority and were laterally scanned across the spine of the letter 'I' on the IBM motif (see Fig. 31). The results are presented in Fig. 32 (initial system) and Fig. 33 (a) and (b) (enhanced system) and confirm that the updated system detects significantly more surface and sub-surface reflections. This corresponds to a mapping of the sample's features to a higher degree of accuracy. In addition, it is important to note that since Fig. 32 maps the sub-surface structure of the paper located below the IBM emblem it represents the first sub-surface OCT image acquired.

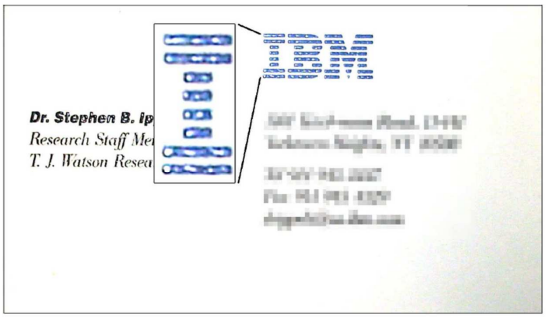

Figure 31 – Scanned image of the IBM business card illustrating the segmented direction of interest for Figs. 32 and 33

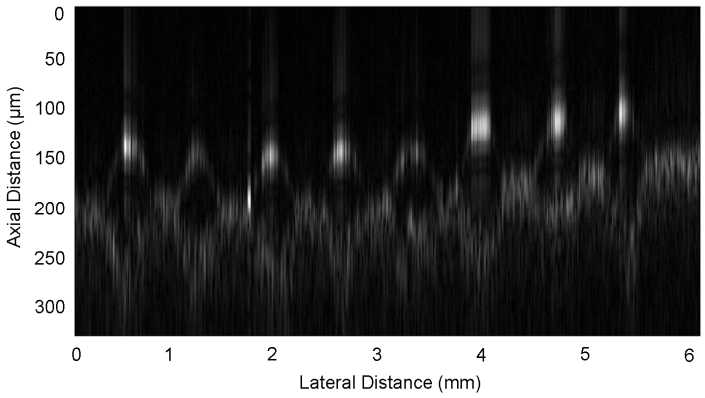

Figure 32 – OCT image of an IBM business card using the initial system (18µm axial resolution). The lateral distance traverses the vertically segmented spine of the 'I' in the IBM emblem – illustrated in Fig. 31

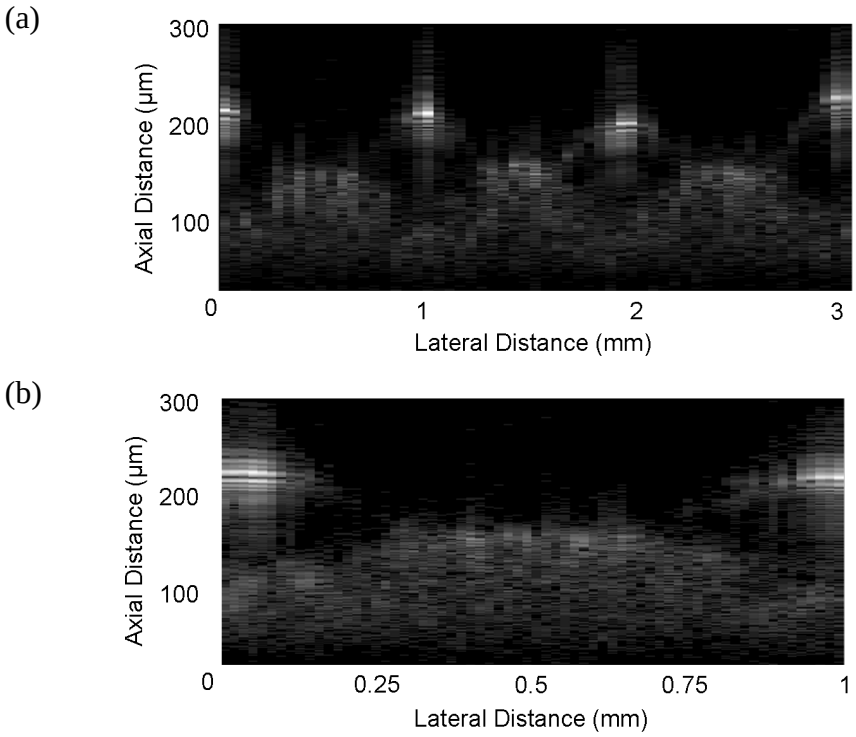

Figure 33 – Updated OCT images (2.5µm axial resolution) of the IBM business card highlighting (a) the first four embossed surface features and (b) a concentrated imaging area of the gap in between two embossed surface features

5.8.2 Banknote Counterfeit Protection Measures

The ability to resolve sub-surface features in certain materials opens up a plethora of attractive OCT applications. Conventionally, OCT has been applied to the evaluation of biological samples and this has developed into a mature technology which has uncovered a wide range of crucial discoveries; however, the attention and function of OCT systems need not be restricted to this particular subject area.

The security of international currency is constantly under review to prevent fraud. This technology is continuously expanding to incorporate the latest developments in anti-counterfeiting. There are a number of simple and complex security features fabricated into the generation of custom banknotes; including intricate printed geometries on the surface of the note, ultraviolet-sensitive ink and, in some cases, an interwoven metallic strip which extends from the top of the note to the bottom. This metallic strip presented an opportunity to test our OCT imaging, since its surface and sub-surface path through the note would be easily recognisable when viewed under the interrogation of an OCT system, returning a strong back-reflection. This idea was successfully investigated by acquiring OCT images of a suitable banknote as the probe beam traversed the metallic strip from orthogonal directions – i.e. normal to, and parallel with, the direction of the strip. The results are presented in Fig. 34 (a) and (b).

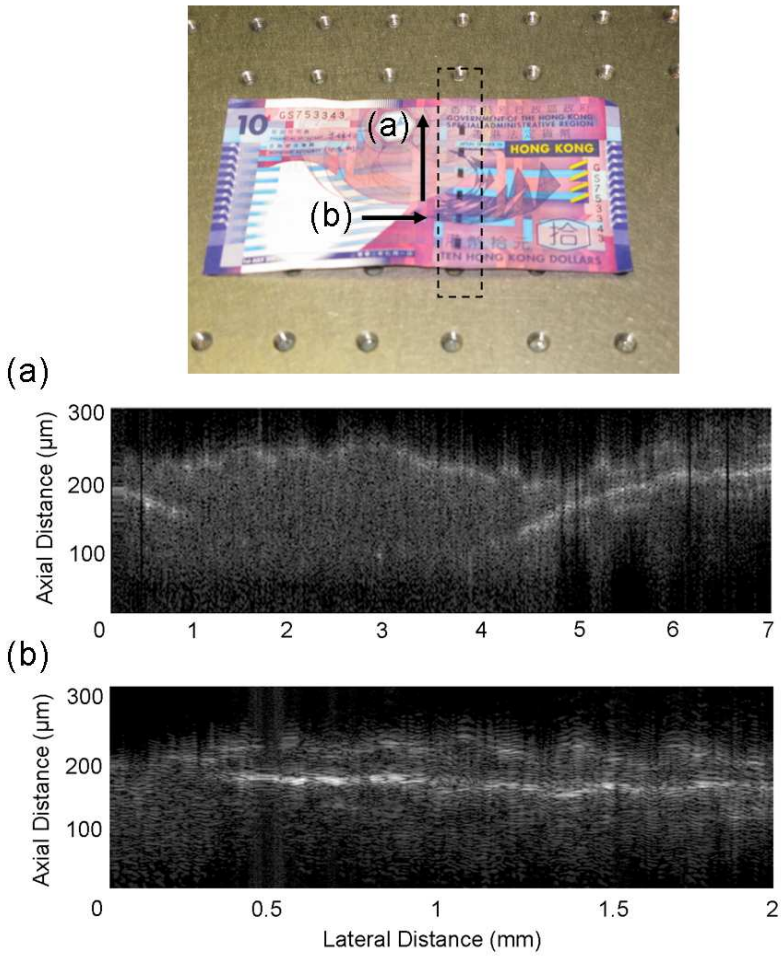

Figure 34 – Investigation into potential OCT banknote counterfeit technologies illustrating the presence of an interwoven metallic strip through the note acquired (a) parallel to and (b) normal to the strip path

Fig. 34 (a) and (b) reveal the expected presence of the strong back-reflection from the metallic strip as it traverses the banknote. Fig. 34 (a) highlights the oscillatory pathway of the metallic strip in the direction parallel to its pathway where the depth of its sub-surface extent is almost out of view. The thickness of the banknote was measured to be ~120µm which should be visible under the axial range of the OCT system; however, beam attenuation and strong metallic strip back-reflections limited the axial extension of the probe beam significantly. In addition, it is clear that the embossed surface features of the banknote are also resolved. This can be observed in both images.

These results confirm that an appropriate OCT system can be configured to assess the authenticity of potentially fraudulent banknotes. Not only it is possible to probe the interwoven metallic strip over a depth of ~300µm (the metallic strip's periodicity along scan direction (a) in Fig. 34 was 9mm), it is also possible to recognise certain design patterns on the top surface of the printed note. The embossed and/or periodically immersed physical features detected here are crucial aspects of counterfeit prevention that have been easily recognised and mapped using the enhanced OCT system.

5.8.3 Artwork Conservation

An additional benefit of this work was to apply OCT imaging to expose the hidden microstructures contained within various art samples. Since OCT provides a non-contact, non-invasive sub-surface imaging technique with the potential of achieving ultra-high-resolution it would be considered a specialist evaluation tool in the critical area of cultural heritage.

This approach was encouraged and supported by Dr. Christina Young from the Coultauld Institute of Art in London who generously supplied a variety of interesting art samples taken from actual paintings. The six samples were clearly labelled and accompanied by a general physical description for each. The aim was to investigate the possibility of distinguishing between different paint layers and, in an ideal case, offer statements with regard to the physical condition of each paint layer whilst measuring the effects of potential delamination.

All of the samples were imaged using both the initial and the enhanced systems with *depth* priority at an arbitrary position and were laterally scanned by approximately 500µm. Note that for the initial configuration images a double-pass of the retro-

reflecting gold mirror was available to double the axial profiling depth to ~600µm; however the improved final system only covers 300µm.

All recorded image data required additional post-processing before a suitable OCT image could be presented. This involved Fourier-filtering (initial system), or performing a Hilbert transformation (enhanced system) on, the measured interferograms in order to remove its internal carrier oscillations. The results for the initial system are displayed in Fig. 35 (a) and in Fig. 36 (a) and (b) for the final system. Each image is plotted against its corresponding optical microscope cross-section (Fig. 35 (b) and Fig. 36 (c) for initial and final images, respectively). An inverted logarithmic mapping was chosen for the initial images in order to present every detected feature and to remain consistant with conventional OCT image representation, whereas the final images are presented using a linear intensity scale. Furthermore, this was selected to compensate for the poor axial resolution of the initial system. Note that the nonlinear scanning motion of the reference arm mirror has not been linearised for the initial system's images. Hence, the initial images are not perfectly calibrated. This is evident in the artificially stretched top and bottom sections of each image.

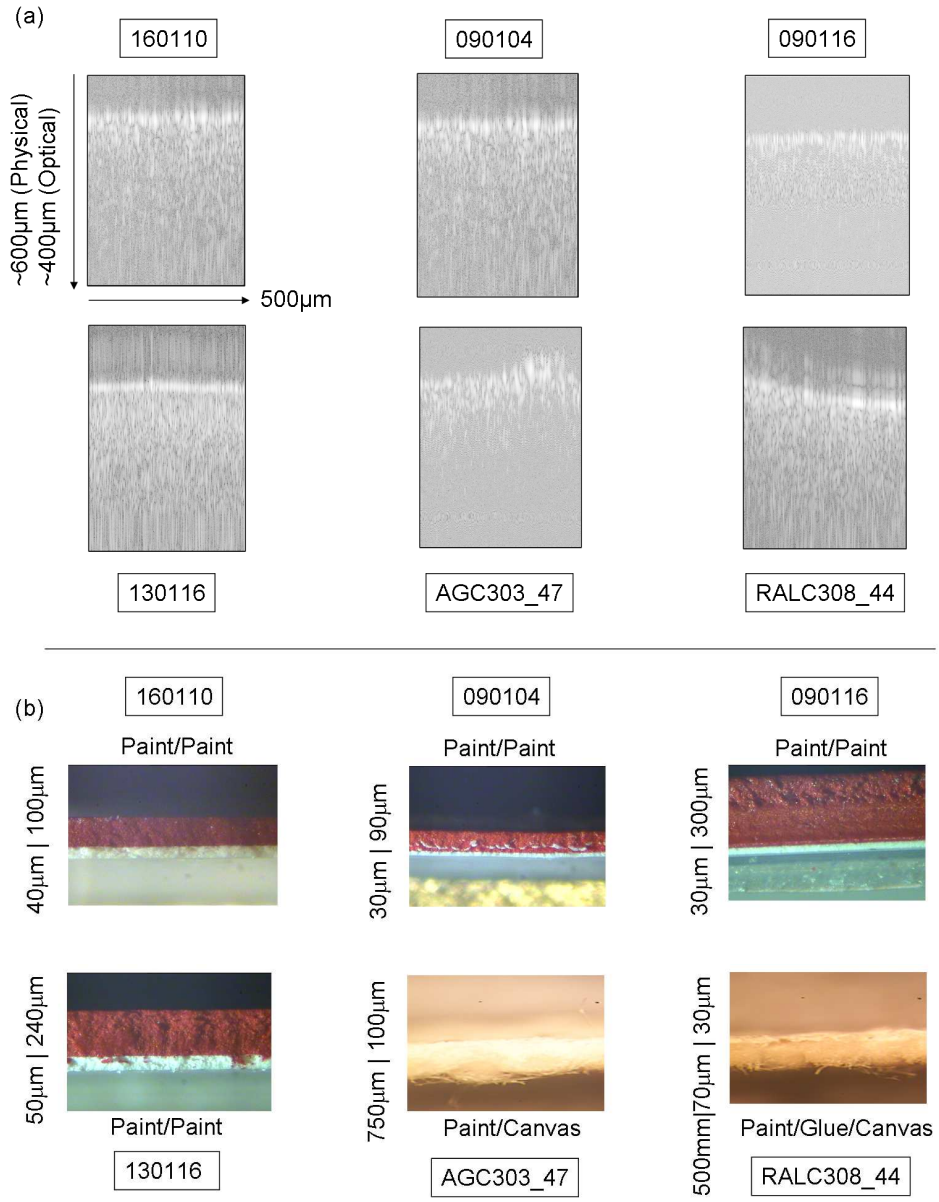

Figure 35 – (a) Initial OCT Art Images acquired with 18µm axial resolution and (b) accompanying optical microscope cross-sectional images

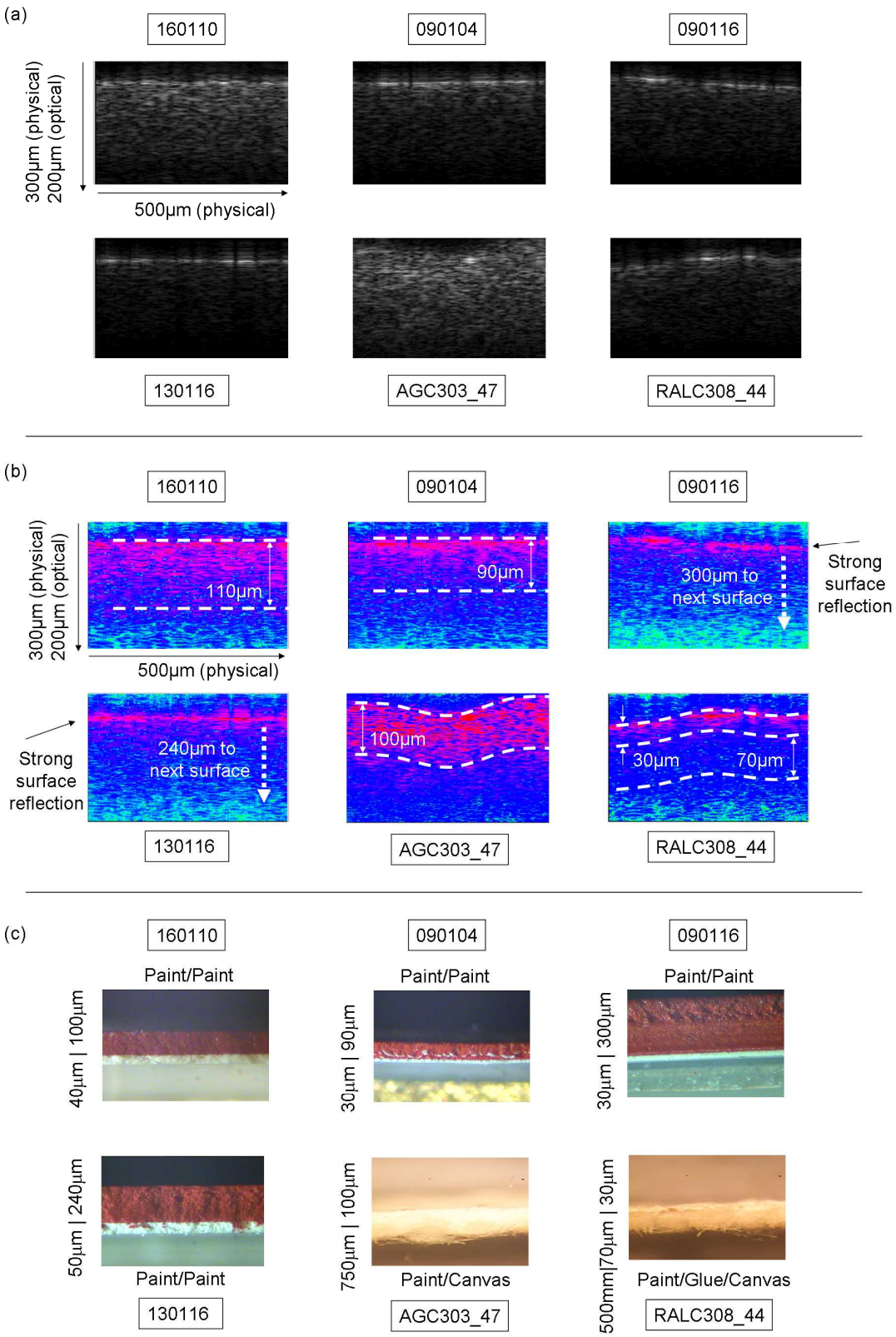

Figure 36 – (a) Final OCT Art Images acquired with 2.5µm axial resolution, (b) Matlab images with amended colormap and intensity scale and (c) accompanying optical microscope cross-sectional images

It is clear that both the initial and final grayscale images do not reveal any additional sub-surface features or distinctive layers when compared against each other. Therefore, an iterative manipulation procedure was initiated where each final image's visualised intensity was altered in an attempt to enhance any detected, but suppressed, feature(s) from within the image. This was performed in MATLAB were the image intensity could be amended and displayed using personal commands or unique MATLAB functions. The original final grayscale results and the corresponding new MATLAB and optical cross-sections are displayed in Fig. 36 (a), (b) and (c) respectively. The MATLAB images are plotted against a linear intensity scale using a custom colourmap.

The results in Fig. 36 (b) draw attention to some interesting features from within each image which were not initially obvious when displayed using a simple grayscale mapping. These enhanced images have allowed the first comparison to be made between the acquired OCT images and the optical cross-sections accompanying each art sample. Although there are no definite connections between the related OCT / microscope images, there are striking correlations between the optical features observed and the physical features present. These will be discussed below.

It is straightforward to compare samples 090116 and 130116. This is because the axial profiling window of the OCT system (which is set by the translation of the scanning reference arm mirror) was not large enough to interrogate the full depth profile of both samples. Therefore, it is clear that only a single top surface refection can be observed within the total scan range in each image.

The OCT images for samples 160110 and 090104 may reveal the presence of an intermediate sub-surface layer since the measured signal level beyond the strong surface reflection appears to extend to a depth of 110µm and 90µm, respectively, before it is attenuated and washed out. Note that this depth also corresponded to the actual physical depth measured by the optical microscope. It would be ideal to detect a secondary planar surface located beneath the top layer at the depth informed by the optical cross-section; however, this may not actually be possible due to a number of limiting factors associated with all of the images obtained. These will be discussed in detail later.

The highly structured environments of samples AGC303_47 and RALC308_44 are of particular interest since they provide advanced paint samples in that not only can their

detailed sub-surface structure be examined but their surface profile can also be investigated. Unfortunately, the OCT image for RALC308_44 offered little in terms of depth structure (although a 30µm thick first layer and an intermediate layer, located 70µm below the surface, may be recognisable). Nevertheless, it was still possible to map out a surface peak; however, the results for the AGC303_47 sample were more promising. The OCT image uncovered a 100µm thick paint layer which followed the surface profile quite clearly. This was investigated to confirm the true presence of the 100µm first paint layer by integrating the image signal across a selected window taken from the entire image. The result is presented in Fig. 37 (a) and (b).

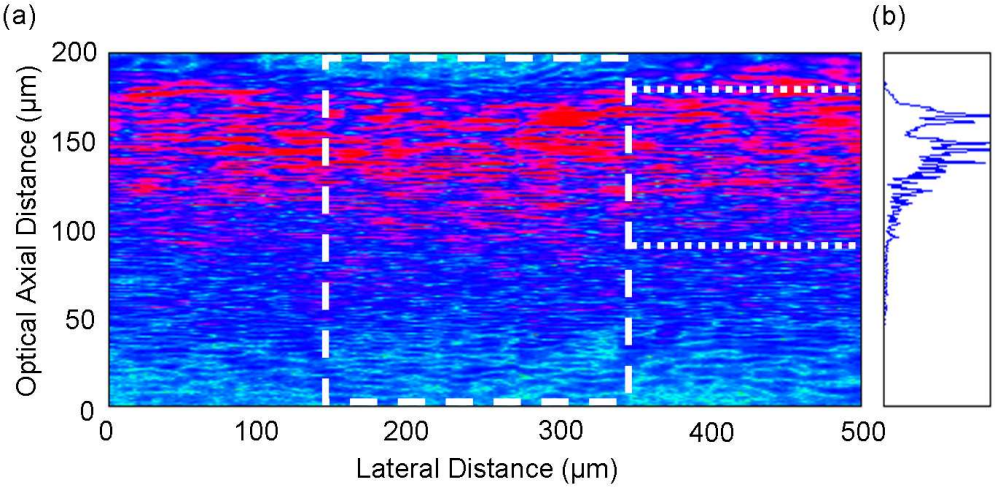

Figure 37 – Art samples (a) OCT image of sample AGC303_47. The white dashed box highlights the integration region – the result of which is presented in (b) as an accompanying single line plot. The white dotted lines highlight the reflected boundary layers

Having examined all of the art samples for hidden sub-surface features with limited success, it was noted afterwards that these test samples did not actually contain a top surface varnish layer. This was a significant discovery because large volumes of antique and contemporary artwork include this layer; not only for protection but also for enhanced appearance and prolonged existence. Therefore, an additional layer of varnish was applied to the 160110 sample and the result is presented in Fig. 38.

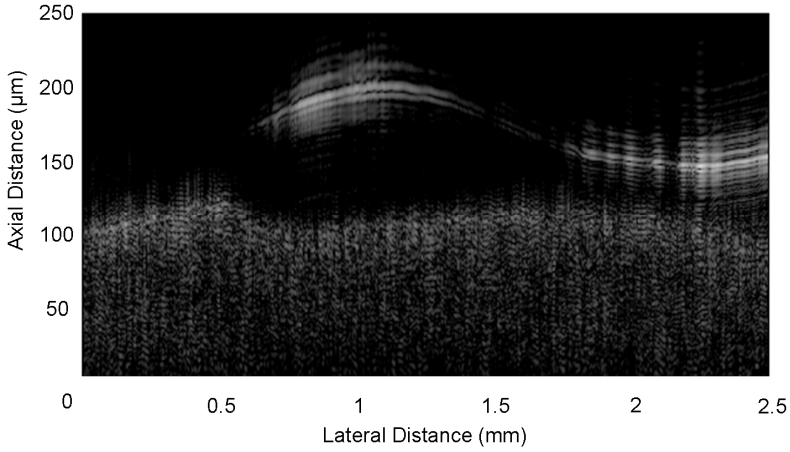

Figure 38 – Art samples – 060110 Varnish sample

Fig. 38 reveals a clear top surface varnish reflection with an accompanying, now intermediate, top surface paint layer. The sub-surface examination of the paint layer is similar to the non-varnish image of the 060110 sample acquired previously (as expected); however, with the varnish layer applied, the acquired image demonstrates an uneven paint profile. This can be attributed to the OPL difference induced by the varying thickness of the varnish layer which has a different refractive index to that of the paint layer. Furthermore, we note that this image has a marked resemblance to images obtained in other OCT artwork studies [47, 48].

As a continuation of the examination of protective transparent top surface layers, the applied varnish subject matter was replaced with the polyester substrate of sample 090116. The sheet was measured to have a thickness of ~100µm. This provided a suitable base layer for a 30µm thick intermediate paint layer before the application of the final 300µm top surface paint layer. It was noted previously that when this sample was imaged from the top surface it was not possible to obtain any sub-surface information since the axial extent of the OCT system's probing depth was only able to interrogate ~300µm (in air). Hence, the examination of this sample from the backside was interesting since the incident probe beam would not be heavily attenuated by the transparent polyester layer, which is ideal for sub-surface evaluation, yet would return clear back-reflections at each encountered layer. This was implemented and the results present in Fig. 39 (a) and (b).

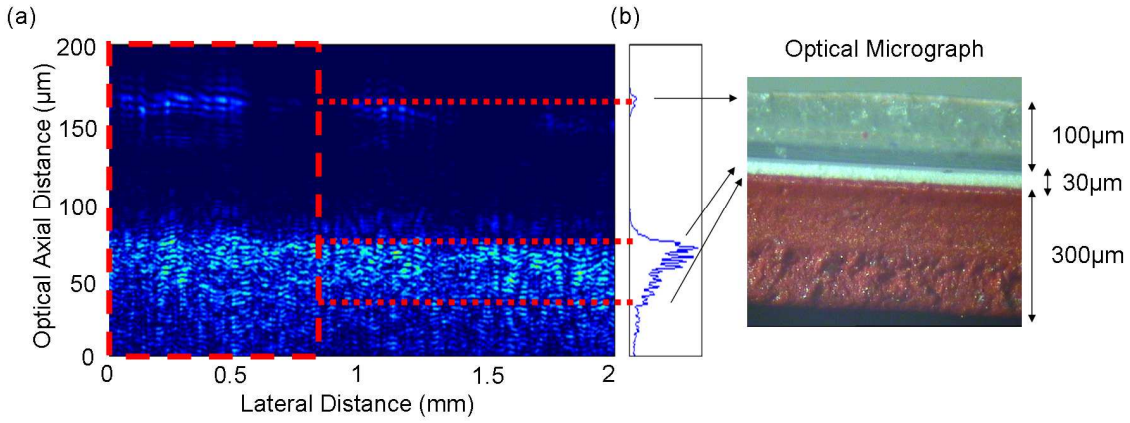

Figure 39 – (a) Polyester sheet analysis of sample 090116. The red dashed box highlights the integration region – the result of which is presented in (b) as an accompanying single line plot. The red dotted lines highlight the reflected boundary layers

It is clear that Fig. 39 (a) reveals three notable boundary layers. The first is highlighted by the top surface reflection of the transparent polyester sheet, the second layer is the reflection from the 30µm thick paint layer and the third is the reflection from the 30µm/300µm paint layer boundary. To confirm that these individual layers had actually been captured by the OCT image a similar evaluation to that performed earlier on sample AGC303_47 was reintroduced. The intensity (i.e. Hilbert transforms) within a windowed portion of the entire image was selected (highlighted by the red dashed box), integrated and plotted. The result is presented in Fig. 39 (b). This confirms the presence of three individual layers as expected.

5.9 Discussion

There are a number of important OCT performance-enhancing factors which have been discussed and implemented throughout this work. These primarily concern the configuration of a broad-bandwidth optical source for improved axial resolution, and the introduction of a balanced-detection scheme for local oscillator (source) noise suppression. Both of these topics have been utilised and explored in order to develop a time-domain OCT system for advanced non-destructive non-contact optical inspection of various materials. Since the axial resolution is inversely proportional to the optical bandwidth of the source, the generation of an almost octave spanning SC (1.2 - 2.1µm) has enhanced the ability to interrogate a sample by a factor of 8 – the original system demonstrated an axial resolution of 18µm whereas the improved system offered an axial resolution of ~2.5µm. In addition, the implementation of a balanced-detection scheme has been of significant value since the performance of a conventional single-detector

OCT system can be severely degraded by intensity fluctuations emanating from the optical source. By adhering to the required criteria for optimum dual-detection implementation, it was possible to improve the system's S/N ratio (improved from 18.4 to 93) by eliminating source noise as well as reducing the optical power required to obtain such performance; however, although the balanced-detector scheme and the generation of a SC were of considerable importance, their introduction came at a cost.

These limitations and other fundamental restrictions are discussed below. This will be separated into two sections; the first will consider the implications of imaging the silicon chip and then the painted and printed media.

The main limiting factors with regard to imaging the silicon chip were the requirement of sophisticated dispersion compensation in the reference arm of the Michelson interferometer as well as the limited axial (as a consequence of dispersion) and lateral resolution. The limited lateral resolution is a complicated parameter to optimise since a higher *NA* focusing lens will result in a smaller confocal parameter which will restrict the effective axial profiling depth. Also, a larger *NA* lens will suffer from increased refraction at the air/ silicon boundary which will negate this lateral resolution enhancing solution. It is be possible to enhance the axial resolution of the system by incorporating dispersion compensation in the reference arm; however this requires the use of a sophisticated automated solution that is beyond that which is possible with the available components of this project. The dispersion compensation mechanism would be required to make subtle compensation amendments in relation to the dispersion induced from each lateral scan location.

With regard to OCT imaging of painted and printed media, a number of limiting factors were present. First of all, it was not possible to implement a balanced-detection scheme into our existing system using only a single beamsplitter. A number of possible configurations were considered; however, the use of a single beamsplitter would result in a highly complex optical system which would consume a considerable period of time for construction and maintenance. Therefore, a second beamsplitter was used to ease construction and alignment issues; however this required the use of the retro-reflector in the reference arm in only a single-pass arrangement. The single-pass scheme resulted in a reduced optical delay along the reference arm and, therefore, a reduced axial profiling depth within the sample under investigation. As a result, this hindered the performance

of the OCT system since it confined the total examination window to a limited depth. It would be possible to overcome this limitation by combining multiple OCT images together according to the depths at which they had been acquired throughout a particular sample; however, this would increase the acquisition time and the system's complexity.

Secondly, a fundamental limitation associated with OCT is the attenuation and scattering of the incident optical beam. It is obvious that if a sample under investigation is highly scattering and/or high absorbing then the probability of detecting back-reflected light from below the surface will be low. This may be the case with the art samples since the majority of the images acquired contained low signal levels after a depth of only ~150µm. It is important that the probe beam maintains a high level of intensity as it traverses the sample otherwise it will not be possible to perform effective sub-surface evaluations.

In addition, the central role of any OCT system is to detect the presence of backscattered/reflected light. If this cannot be achieved then the system is ultimately flawed. Thus, one must consider the mechanisms behind the process of reflection within a given sample. Reflection essentially takes place as a consequence of the refractive index change at the interface of two different media. Therefore, it is required that there exists a significant refractive index change between neighbouring paint layers. Unfortunately, the details accompanying each sample did not disclose such information so it was not possible to predetermine the magnitude of potential sub-surface reflections. It was difficult to detect any distinct sub-surface interface at all within the art samples, no matter which sample was under investigation. Yet, it must be noted that the likelihood of measuring a planar sub-surface interface within an art sample may actually be of considerable difficulty due to the manner in which paints blend and fuse together. It would probably be more appropriate to anticipate a graded interface (as suggested by the descriptions of the paint layers above) instead of a simple linear boundary.

In general, the generation of a SC is of significant importance in any OCT system since it results in an improved axial resolution. Nonetheless, this necessary broad bandwidth can be difficult to maintain as it traverses the system since each element it encounters will influence it. Every transmission or reflection of the beam can alter its spectral attributes or manifest chromatic aberrations unless the appropriate materials and coating are adopted for each element the beam experiences. In addition, the effects of dispersion

will also be of significant importance since the dispersion induced by both the focusing lens and the sample must be compensated for in the reference arm to achieve optimum performance. All of these fundamental optical principles and parameters must be considered to avoid the reduction of power and bandwidth of the source. Moreover, even without the potentially negative effects induced by the optical system, the raw spectral profile of the SC alone can depreciate system performance since it is the inverse Fourier transform of the optical source which determines the shape of the resulting OCT interferogram. If the optical spectrum is highly structured then the interferogram will retain such structure. This can lead to the observation of unwanted ghost features in images which can create confusion when attempting to interpret results. It was possible to influence the spectral shape of the generated SC by adjusting the polarisation state which entered the PM-DS-HNLF; however this only resulted in a smoother interferogram distribution with a broader FWHM.

Finally, another issue with the implemented system was the dependence on the mechanically-scanning reference arm mirror. This time-domain OCT configuration requires the implementation of sensitive calibration procedures in order to accurately interpret its results. Due to the sinusoidal nature of the reference arm's mirror translation, the resulting interferogram traces will be stretched at the turning points of the scan range – as illustrated in the initial art results. This is because the mirror has effectively slowed down and stopped before retracing its translation path at its turning points. The scanning reference mirror's displacement can be easily calibrated by constructing a second Michelson interferometer which also uses the scanning mirror of the original OCT arrangement but measures the interferometric trace of a HeNe laser instead. This generates a precise optical ruler which can be used to linearise the OCT interferograms by mapping one trace against the other since each HeNe fringe period is 633nm; however, care must be taken at this stage since an unintentional error will translate across into all acquired images and provide defective results. This can manifest unintentional ghost features at the extremes of an image which may be regarded as true features.

5.10 Conclusions

This chapter has discussed the development of a time-domain ultra-high-resolution high-dynamic-range OCT imaging system for the sub-surface evaluation of silicon ICs and painted and printed media. Two individual experimental approaches have been

considered and constructed. The first was a standard free-space Michelson interferometer-based OCT system which was ultimately limited by its axial resolution performance (~18µm). The second system incorporated the implementation of both an almost octave-spanning SC source (~1-2µm), for improved axial resolution capabilities (~2.5µm in air), and a balanced-detection scheme for an enhanced S/N ratio. This system required a number of calibration issues to be addressed before suitable images could be acquired.

The results for this enhanced system demonstrated that it was possible to interrogate and profile the substrate thickness of a silicon IC as well as to accurately resolve sub-surface metal interconnected tracks and large circuit features. It was found that the imaged Azuma chip had a non-uniform substrate in both the horizontal and vertical directions which demonstrates that our improved system offers a novel polishing / thinning evaluation tool for device FA. Also, our system was able to resolve a radially distributed device feature which permits accurate device feature recognition.

With regard to the artwork samples, the improved system was able to detect the multiple sub-surface layers of samples AGC303_47 and 090116 (from the backside). The acquired images exposed the single 100µm first paint layer of sample AGC303_47 and both the 100µm and 30µm thick polyester and intermediate paint layer of sample 090116 respectively. Furthermore, the investigation of a protective top surface varnish layer was applied to sample 160110. This idea proved to be successful in that multiple sub-surface reflections were detected in the obtained image. This was similar to the backside evaluation of sample 090116 and that of other published work.

Moreover, the application of OCT to the investigation of printed banknotes suggested that it could have potential as a novel counterfeit detection tool. The enhanced system was able to map the woven pathway of a metallic strip, which was fabricated into the banknote, from imaging directions both normal to and parallel with the strip.

References

[1] D. Huang, E.A. Swanson, C.P. Lin, J.S. Schuman, W.G. Stinson, W. Chang, M.R. Hee, T. Flotte, K. Gregory, C.A. Puliafito, and J.G. Fujimoto, "Optical Coherence Tomography", *Science* **254**, 1178-1181 (1991)

[2] R.C. Youngquist, S. Carr, and D.E.N. Davies, "Optical Coherence-Domain Reflectometry - a New Optical Evaluation Technique", *Optics Letters* **12**, 158-160 (1987)

[3] J.A. Izatt, E.A. Swanson, M.R. Hee, D. Huang, J. Schuman, C.P. Lin, C.A. Puliafito, and J.G. Fujimoto, "Quantitative Assessment of Cataract Development with Optical Coherence Domain Reflectometry and Optical Coherence Tomography", *Investigative Ophthalmology & Visual Science* **33**, 1300 (1992)

[4] S. Chen, D.N. Wang, K.T.V. Grattan, A.W. Palmer, and G.L. Dick, "A Compact Optical-Device for Eye-Length Measurement", *IEEE Photonics Technology Letters* **5**, 729-731 (1993)

[5] J.A. Izatt, E.A. Swanson, M.R. Hee, D. Huang, C.P. Lin, J.S. Schuman, C.A. Puliafito, and J.G. Fujimoto, "Invivo Imaging of the Human Retina with Optical Coherence Tomography", *Investigative Ophthalmology & Visual Science* **34**, 761-761 (1993)

[6] E.A. Swanson, J.A. Izatt, M.R. Hee, D. Huang, C.P. Lin, J.S. Schuman, C.A. Puliafito, and J.G. Fujimoto, "In-Vivo Retinal Imaging by Optical Coherence Tomography", *Optics Letters* **18**, 1864-1866 (1993)

[7] J. Welzel, E. Lankenau, R. Birngruber, and R. Engelhardt, "Optical coherence tomography of the human skin", *Journal of the American Academy of Dermatology* **37**, 958-963 (1997)

[8] A. Baumgartner, S. Dichtl, C.K. Hitzenberger, H. Sattmann, B. Robl, A. Moritz, Z.F. Fercher, and W. Sperr, "Polarization-sensitive optical coherence tomography of dental structures", *Caries Research* **34**, 59-69 (2000)

[9] B. Hofer, B. Povazay, B. Hermann, A. Unterhuber, G. Matz, and W. Drexler, "Dispersion encoded full range frequency domain optical coherence tomography", *Optics Express* **17**, 7-24 (2009)

[10] M.C. Stumpf, S.C. Zeller, A. Schlatter, T. Okuno, T. Sudmeyer, and U. Keller, "Compact Er : Yb : glass-laser-based supercontinuum source for high-resolution optical coherence tomography", *Optics Express* **16**, 10572-10579 (2008)

[11] S.Y. Ryu, H.Y. Choi, J. Na, W.J. Choi, and B.H. Lee, "Lensed fiber probes designed as an alternative to bulk probes in optical coherence tomography", *Applied Optics* **47**, 1510-1516 (2008)

[12] X. Ping and G.F. James, "Ultrahigh resolution optical coherence tomography with femtosecond Ti : sapphire laser and photonic crystal fiber", *Chinese Science Bulletin* **53**, 1963-1966 (2008)

[13] C.A. Patil, N. Bosschaart, M.D. Keller, T.G. van Leeuwen, and A. Mahadevan-Jansen, "Combined Raman spectroscopy and optical coherence tomography device for tissue characterization", *Optics Letters* **33**, 1135-1137 (2008)

[14] J.C. Jasapara, S. Wielandy, and A.D. Yablon, "Fourier domain optical coherence tomography - A new platform for measurement of standard and microstructured fibre dimensions", *IEEE Proceedings-Optoelectronics* **153**, 229-234 (2006)

[15] W. Xu, D.L. Mathine, and J.K. Barton, "Analog CMOS design for optical coherence tomography signal detection and processing", *IEEE Transactions on Biomedical Engineering* **55**, 485-489 (2008)

[16] R. Kariya, D.L. Mathine, and J.K. Barton, "Analog CMOS circuit design and characterization for optical coherence tomography signal processing", *IEEE Transactions on Biomedical Engineering* **51**, 2160-2163 (2004)

[17] B.E. Bouma, *Optical Coherence Tomography (OCT)*. New York: Marcel Dekker, Inc (2002)

[18] A.M. Kowalevicz, T. Ko, I. Hartl, J.G. Fujimoto, M. Pollnau, and R.P. Salathe, "Ultrahigh resolution optical coherence tomography using a superluminescent light source", *Optics Express* **10**, 349-353 (2002)

[19] B.E. Bouma, G.J. Tearney, I.P. Bilinsky, B. Golubovic, and J.G. Fujimoto, "Self-phase-modulated Kerr-lens mode-locked Cr:forsterite laser source for optical coherence tomography", *Optics Letters* **21**, 1839-1841 (1996)

[20] G. Hausler and M.W. Linduer, "Coherence radar and spectral radar - New tools for detmatological diagnosis", *J. Biomed. Opt.* **3**, 21-31 (1998)

[21] R. Leitgeb, C.K. Hitzenberger, and A.F. Fercher, "Performance of fourier domain vs. time domain optical coherence tomography", *Optics Express* **11**, 889-894 (2003)

[22] E. Beaurepaire, A.C. Boccara, M. Lebec, L. Blanchot, and H. Saint-Jalmes, "Full-field optical coherence microscopy", *Optics Letters* **23**, 244-246 (1998)

[23] E. Zagaynova, N. Gladkova, N. Shakhova, G. Gelikonov, and V. Gelikonov, "Endoscopic OCT with forward-looking probe: clinical studies in urology and gastroenterology", *Journal of Biophotonics* **1**, 114-128 (2008)

[24] F.I. Feldchtein, G.V. Gelikonov, V.M. Gelikonov, R.V. Kuranov, A.M. Sergeev, N.D. Gladkova, A.V. Shakhov, N.M. Shakhova, L.B. Snopova, A.B. Terent'eva, E.V. Zagainova, Y.P. Chumakov, and I.A. Kuznetzova, "Endoscopic applications of optical coherence tomography", *Optics Express* **3**, 257-270 (1998)

[25] J.T. Oh and S.W. Kim, "Polarization-sensitive optical coherence tomography for photoelasticity testing of glass/epoxy composites", *Optics Express* **11**, 1669-1676 (2003)

[26] D. Stifter, A.D.S. Dufau, E. Breuer, K. Wiesauer, P. Burgholzer, O. Hoglinger, E. Gotzinger, M. Pircher, and C.K. Hitzenberger, "Polarisation-sensitive optical coherence tomography for material characterisation and testing", *Insight* **47**, 209-212 (2005)

[27] T. Anna, C. Shakher, and D.S. Mehta, "Simultaneous tomography and topography of silicon integrated-circuits using full-field swept-source optical coherence tomography", *Journal of Optics A - Pure and Applied Optics* **11** (2009)

[28] P. Targowski, B. Rouba, M. Wojtkowski, and A. Kowalczyk, "The application of optical coherence tomography to non-destructive examination of museum objects", *Studies in Conservation* **49**, 107-114 (2004)

[29] H. Liang, R. Cucu, G.M. Dobre, D.A. Jackson, J. Pedro, C. Pannell, D. Saunders, and A.G. Podoleanu, "Application of OCT to examination of easel paintings", *Second European Workshop on Optical Fibre Sensors: Proceedings* **5502**, 378-381 (2004)

[30] J. Marczak, A. Koss, P. Targowski, M. Gora, M. Strzelec, A. Sarzynski, W. Skrzeczanowski, R. Ostrowski, and A. Rycyk, "Characterization of Laser Cleaning of Artworks", *Sensors* **8**, 6507-6548 (2008)

[31] P. Targowski, B. Rouba, M. Gora, L. Tyminska-Widmer, J. Marczak, and A. Kowalczyk, "Optical coherence tomography in art diagnostics and restoration", *Applied Physics A - Materials Science & Processing* **92**, 1-9 (2008)

[32] E. Hecht, *Optics*: Addison-Wesley (1987)

[33] J.M. Schmitt, "Optical coherence tomography (OCT): A review", *IEEE Journal of Selected Topics in Quantum Electronics* **5**, 1205-1215 (1999)

[34] J.A. Izatt, M.R. Hee, G.M. Owen, E.A. Swanson, and J.G. Fujimoto, "Optical Coherence Microscopy in Scattering Media", *Optics Letters* **19**, 590-592 (1994)

[35] I.G. Cormack, F. Baumann, and D.T. Reid, "Measurement of group velocity dispersion using white light interferometry: A teaching laboratory experiment", *American Journal of Physics* **68**, 1146-1150 (2000)

[36] D. Choi, H. Hiko-Oka, T. Amano, H. Furukawa, F. Kano, M. Nakanishi, K. Shimizu, and K. Ohbayashi, "Numerical compensation of dispersion mismatch in discretely swept optical-frequency-domain-reflectometry optical coherence tomography", *Japanese Journal of Applied Physics Part 1-Regular Papers Brief Communications & Review Papers* **45**, 6022-6027 (2006)

[37] S.L. Hahn, *Hilbert transforms in signal processing*. Boston: Artech House Publishers (1996)

[38] J.M. Schmitt, "OCT elastography: imaging microscopic deformation and strain of tissue", *Optics Express* **3**, 199-211 (1998)

[39] G.L. Abbas, V.W.S. Chan, and T.K. Yee, "A Dual-Detector Optical Heterodyne Receiver for Local Oscillator Noise Suppression", *Journal of Lightwave Technology* **3**, 1110-1122 (1985)

[40] G.P. Agrawal, *Nonlinear Fiber Optics*. 4th Ed. New York: Academic Press (2006)

[41] J. Toulouse, "Optical nonlinearities in fibers: Review, recent examples, and systems applications", *Journal of Lightwave Technology* **23**, 3625-3641 (2005)

[42] G. Genty, S. Coen, and J.M. Dudley, "Fiber supercontinuum sources (Invited)", *Journal of the Optical Society of America B - Optical Physics* **24**, 1771-1785 (2007)

[43] J.M. Dudley, G. Genty, and S. Coen, "Supercontinuum generation in photonic crystal fiber", *Reviews of Modern Physics* **78**, 1135-1184 (2006)

[44] M.E. Fermann and I. Hartl, "Ultrafast Fiber Laser Technology", *IEEE Journal of Selected Topics in Quantum Electronics* **15**, 191-206 (2009)

[45] N. Nishizawa and T. Goto, "Widely wavelength-tunable ultrashort pulse generation using polarization maintaining optical fibers", *IEEE Journal of Selected Topics in Quantum Electronics* **7**, 518-524 (2001)

[46] T. Waite, "A balanced mixer for optical heterodyning: The Magic-T optical mixer", *Proc. IEEE* **54**, 334-335 (1966)

[47] H. Liang, M.G. Cid, R.G. Cucu, G.M. Dobre, A.G. Podoleanu, J. Pedro, and D. Saunders, "En-face optical coherence tomography - a novel application of non-invasive imaging to art conservation", *Optics Express* **13**, 6133-6144 (2005)

[48] B.J. Rouba, P. Karaszkiewicz, L. Tyminska-Widmer, M. Iwanicka, M. Gora, E. Kwiatkowska, and P. Targowski. *Optical coherence tomography for non-destructive investigations of structure of objects of art*. in *9th International Conference on NDT of Art*. 2008. Jerusalem, Isreal.

Chapter 6

Conclusions and Future Work

6.1 Introduction

This thesis has investigated ultra-high-resolution optical imaging in silicon integrated-circuits (IC) for the purpose of semiconductor device failure analysis (FA) and inspection. The two main goals of this work have been to develop and demonstrate novel sub-surface optical imaging methodologies by applying solid immersion lens (SIL) techniques to resolution-enhancing strategies, and also through the exploitation of interferometric metrology systems. The work performed here can be separated into two unique imaging modalities: laser signal injection microscopy and optical coherence tomography (OCT). A technical summary documenting the research and achievements of the work described in this thesis is presented below and a discussion on potential future work is also offered.

6.2 Technical Summary and Conclusions

In Chapter 3, the concept of SIL-enhanced two-photon optical beam induced current (TOBIC) imaging was introduced and its benefits in semiconductor IC inspection and analysis discussed [1]. The resolution enhancement available using this technique

derives from the unique magnification properties of SILs, and the nonlinear signal generation associated with TOBIC imaging. Magnification in SILs provides an optical lever effect which can localise the TOBIC carrier generation in a chip to a volume which is unattainable using conventional non-SIL illumination. This was investigated using the ray-tracing software ASAP and it was found that the lever effect is analogous to a magnification of n and n^2 for a lateral and axial physical translation of a hemispherical SIL (h-SIL), respectively, and a magnification of n^2 and $n^{3.5}$ for a super SIL (s-SIL), where n represents the refractive index of the material. This analysis was used to calibrate the acquired SIL-enhanced images. The dependence of the TOBIC signal provides a further opportunity for resolution enhancement. Since the signal is proportional to the squared intensity of the incident laser beam there is an effective reduction in the point-spread function (PSF) diameter when compared to a linear system, corresponding to an additional nonlinear resolution enhancement of a factor of $\sqrt{2}$.

The work in Chapter 3 also described the design and configuration of a suitable s-SIL and infrared microscope for image acquisition. This resulted in the demonstration of an ultra-high-resolution two-dimensional (2D) image of a 3×3 matrix of tungsten vias on a finger of n-doped silicon with a measured lateral resolution of 166nm [2, 3]. The resolution value was inferred from a line-cut through the image data which was fitted to a Gaussian error function to determine the width of the PSF. This result outperformed previous performance using a similar technique by a factor of 2 [4]. In addition, this imaging modality was extended to report the demonstration of a three-dimensional (3D) image of the same unique feature. By applying a peak-detection algorithm to a 3D stack of 2D images, which were acquired as the chip was translated through the focus of the laser beam, it was possible to resolve the axial extent of the imaged features with an accuracy of ~100nm [2, 3]. Therefore, the work performed in this chapter reported diffraction-limited sub-surface optical imaging of a silicon IC where the lateral resolution measured was only 11% of the free-space wavelength of the optical source. Subsequently, this work was published in Applied Physics Letter and was later noted to be one of the top-20 articles downloaded that month.

In Chapter 4, the performance of novel resolution-enhancing techniques was investigated. The techniques under consideration were pupil-function engineering and polarisation-dependent imaging. Initially, a theoretical and experimental proof-of-

concept approach was adopted to confirm that a pupil-plane filter could manipulate the PSF of a focused beam. This was achieved theoretically by modelling the focal-plane PSFs of various filter designs by manipulating their amplitude transmission functions in order to reveal an optimum aperture design. The model suggested that an annular-aperture, although generating considerable sidelobes, would generate the smallest PSF. These sidelobes were not of major concern, since the intensity-dependence of the TOBIC technique reduced their influence significantly. A set of custom apertures were fabricated and an experimental validation implemented by positioning the apertures immediately after the focusing lens in a simple imaging system and monitoring the resulting PSFs using a focal-plane CMOS camera. The experimental results demonstrated a reduction of the PSF of 60% when compared to its corresponding open-pupil value [5]. This confirmed that it was possible to exploit the use of pupil-plane annular transmission filters to obtain super-resolution performance.

In order to predict the effect of annular-apertures in a high numerical aperture (*NA*) imaging system we modelled the 3D electromagnetic energy density distribution of a linearly-polarised optical beam in the focal volume of an imaging system where *NA*=1. This model allowed us to investigate polarisation effects in image formation, which manifest themselves in the shape of the focal spot, which becomes increasingly elliptical as the *NA* approaches unity. These effects were modelled and analysed by calculating the vectorial Debye diffraction integral with a fast Fourier transform, as described by Leutenegger et al [6], allowing us to examine the effects of different aperture designs as the *NA* of the system was increased from 0 to 1. The results confirmed that the focal-plane energy density distribution becomes elliptical as the *NA* approaches unity and also that the use of an annular obscuration filter isolates the longitudinal component of the incident electric-field which results in an even narrower PSF. Following our preliminary theoretical study, these separate effects were then exploited experimentally and the results are described below.

Polarisation-dependent imaging was demonstrated in a silicon IC utilising an experimental configuration similar to that adopted in Chapter 3. The linearly-polarised output from a stretched-pulse Er:fibre laser was controlled by inserting a half-wave plate immediately before the imaging objective lens and the high-*NA* conditions were achieved by using a SIL. The area under investigation was the 3×3 matrix of tungsten vias on n-doped silicon fingers that were imaged previously. The polarisation-dependent

PSF was quantitatively examined by monitoring the TOBIC signal transition as the focus was scanned across a silicon-metal edge. A set of scans, recorded as the linear polarisation state was incrementally rotated through 360°, demonstrated a periodic variation in the resolution that indicated a maximum resolution of 251nm and a minimum resolution of 122nm. To qualitatively assess this polarisation dependence, two separate ultra-high-resolution 2D images were acquired using orthogonal polarisation and manifested the polarisation dependence as an apparent narrowing (widening) of the gaps between neighbouring silicon fingers when the polarisation state was parallel (orthogonal) to the finger edges. This work demonstrated, for the first time, the presence of vectorial effects in a real imaging system and led to a paper in Nature Photonics [7].

The next stage was to investigate the resolution-enhancing effects of a hybrid polarisation-dependent annular-aperture imaging system. The experimental configuration was similar that that used previously except for the introduction of obscuration apertures immediately before the objective lens. A comparison was made between the performance observed using a clear aperture and that obtained after the introduction of obscuration apertures where the centre 36% and 55% of the pupil was blocked. The results revealed a lateral resolution enhancement from 200×109nm to 112×70nm, an approximately 64% improvement in terms of the area of the focal spot, consistent with theory. We also observed that as the apertures were introduced the contrast of the recorded images became poorer, which resulted from the fact that annular pupil-plane apertures create extended depths of field. Therefore, improved lateral resolution was effectively obtained at the expense of poorer depth resolution since the obscuration apertures led to an increased TOBIC sensitivity depth through the sample. This effect, along with the optical and physical geometries of the imaging conditions, were modelled in MATLAB to obtain a semi-quantitative understanding of the TOBIC contrast mechanism by using vectorial theory to predict the size and structure of the optical intensity distribution in the focal region. The result revealed a contrast reduction when using an annular pupil-plane aperture, which was consistent with the experimental images obtained. Significantly, this work demonstrated that, for a nonlinear microscope already operating close to the limits of optical resolution, pupil-function engineering could further enhance the lateral resolution, but at the expense of poorer axial resolution. The work led to a publication in Applied Physics Letters [8].

Chapter 5 discussed the development of a time-domain ultra-high-resolution high-dynamic-range optical coherence tomography (OCT) imaging system for the sub-surface evaluation of silicon ICs and, in addition, painted and printed media. The experimental development was separated into two sections; the first concerned the construction of a Michelson interferometer-based time-domain OCT system, and the second concentrated on the development and implementation of advanced performance-enhancing techniques. The initial configuration utilised the spectral bandwidth of a 1550nm, modelocked erbium-doped fibre laser (~80nm) to generate an interferogram which had a full width at half maximum (FWHM) axial resolution of ~18µm. This was suitable for the examination of simple samples such as gold mirrors or microscope cover-slides; however the axial resolution was insufficient for the purposes of detecting intermediate sub-surface features within multi-layered semiconductor device and artwork samples. Therefore, the OCT system was enhanced by incorporating a supercontinuum (SC) source, for improved axial resolution capabilities, and a balanced-detection scheme to improve the signal-to-noise (S/N) ratio. The SC was generated by coupling the amplified optical pulses (160fs, 200mW average power) from a home-built erbium-doped fibre amplifier (EDFA) into a germanium-doped polarisation-maintaining dispersion–shifted highly nonlinear fibre (PM-DS-HNLF). The SC spanned an optical bandwidth from ~1 – 2µm which translated into an axial probing resolution of ~2.5µm. The balanced-detection scheme was constructed using a standard instrumentation amplifier. This method reduced the effects of source noise and offered improved sensitivity at reduced power levels, increasing the S/N ratio from 18.4 to 93. The resulting OCT system was calibrated using a second HeNe Michelson interferometer to linearise the acquired images.

The inspection of silicon ICs using the enhanced OCT imaging system provided a novel tool for device substrate thickness evaluation as well as an alternative substrate polishing / thinning quality control measure. It was found that the Azuma chip under inspection had a non-uniform substrate thickness across both lateral directions. In addition, the OCT system was able to accurately identify the metal interconnected tracks located around the device perimeter as well as a number of isolated test circuits which were fabricated across the chip. Moreover, the interrogation of the largest circuit feature revealed a fan-out distribution which was in agreement with the radial spatial distribution of the structure itself. This provided for the first time an accurate sub-surface profiling image of a silicon IC using an OCT imaging system. It therefore

offered a unique feature navigation protocol for the purposes of semiconductor device FA. These results are currently being prepared for submission into a relevant journal for publication consideration.

With regards to the evaluation of artwork samples, it was only possible to examine the sub-surface features within certain samples due to a number of fundamental and system-induced limitations. It was possible to detect the multiple sub-surface layers of certain samples, including a top paint and polyester layer, and a subsurface 100µm paint layer. In addition, the investigation of transparent protective layers was extended with the application of a top surface varnish layer to one sample, resulting in the generation of a multi-layered image which was similar to the results of other published work [9, 10].

Furthermore, the application of OCT to the investigation of printed banknotes suggested that it would be an interesting and alternative counterfeit detection methodology. It was possible to map the woven pathway of a metallic strip, which was fabricated into the banknote, using imaging directions both normal to and parallel to the strip.

6.3 Future Work

There are several considerations for potential future work with regards to the research documented in this thesis. The discussion of these experimental extensions will be separated into individual sections for clarity. The first two sections concern those ideas associated with nonlinear microscopy of silicon ICs, the next two sections concern additional imaging-enhancing techniques for OCT, and the last two sections discuss proposals which attempt to combine both the initial and latter research efforts addressed in this thesis.

6.3.1 Silicon ICs - Hybrid Phase / Amplitude Apertures

The performance of pupil-plane amplitude filters in nonlinear microscopy has been successfully demonstrated within this thesis [8]. The reduction from ~100nm to 70nm using an obscuration aperture suggest it would be interesting to evaluate the performance of annular-apertures that also manipulate the phase of the incident wavefront. This can be achieved by amending only the aperture's phase, and ignoring amplitude control, or by implementing a hybrid amplitude / phase filter design. Once a theoretical model had calculated the optimum filter design a suitable optical element could be fabricated and implemented into an imaging system to evaluate its

performance. These ideas have already been investigated and experimentally demonstrated in several samples [11, 12] but have not yet been suggested for the interrogation of silicon ICs, or in any nonlinear microscope.

Moreover, with regard to phase-only filters, these elements need not simply be positioned in the pupil-plane of an imaging system. Another approach would be to design and fabricate the required filter design onto a custom solid immersion lens (SIL) [13, 14].

6.3.2 Silicon ICs - Laser Signal Injection Failure Analysis

Although the TOBIC imaging technique was utilised for microscopy purposes in Chapter 3 and 4, it would be interesting to also pursue the laser signal injection technologies discussed in Chapter 1 to evaluate IC performance and reliability instead of visual quality. To determine that an IC will function to a high standard simply on the basis of a flawless optical inspection would be an ignorant assumption. Therefore, it would be wise to construct an integrated evaluation platform that is capable of both visual and electronic assessments with regards to device performance. Techniques such as laser assisted device alteration (LADA) and optical beam induced resistance change (OBIRCH) are promising optoelectronic technologies for determining device timing resolutions, fault localisation and signal probing. It would be relatively straightforward to implement such configurations using the existing nonlinear microscope system since it would only require the activation and control of the device under test, since the devices we used were not powered during the imaging experiments reported in this thesis.

6.3.3 OCT – Annular-Aperture Investigation

The lateral and axial resolutions associated with an OCT system are independent of each other – the lateral resolution is determined by the *NA* of the imaging lens and the axial resolution is inversely proportional to the optical bandwidth of the source; however, these two parameters can still influence each other in that the higher the *NA* of the imaging lens, the shorter the resulting confocal parameter which, in turn, reduces the system's depth-of-field (DOF). A small DOF limits the axial extent over which efficient optical probing can take place since a high-*NA* system creates a non-uniform optical intensity distribution throughout the sample. It is desirable to exploit a large DOF in an OCT system since this can enhance its ability to detect subtle axial features over a larger

range, particularly those features which are located before, or after, the focal-plane. This can be effectively achieved by implementing an annular amplitude pupil-plane filter. It is well known, and has been experimentally verified in Chapter 4, that these filters generate an extended DOF as well as an improved lateral resolution. Therefore, by employing a suitable filter in an OCT system it would be possible to enhance both the lateral and axial performance without introducing any negative consequences.

6.3.4 OCT – Polarisation-Dependent Imaging

The polarisation-dependent imaging demonstrated in Chapter 4 highlighted that it was possible to manipulate both the spatial geometry and orientation of the focal-plane energy density distribution in order to enhance resolution performance. This technique is suitable for visual inspection purposes but fails to reveal any material information about the sample under investigation. Polarisation-dependent OCT on the other hand does provide such information in that the reflectivity of certain materials is dependent on the polarisation state of the incident beam. Not only that, but it has been demonstrated in the biomedical and material sciences that parameters such as stress, strain, birefringence and elasticity are also influenced by the polarisation state [15-18]. This would be of significant interest to the semiconductor FA community since the evaluation of packaging-induced stress or even wafer-level stress / strain on the performance of silicon ICs would provide a novel characterisation which is not yet available.

6.3.5 Multiple Image Acquisition for IC Failure Analysis

The semiconductor device FA community relies on a number of different characterisation protocols to be initiated in an iterative manner during device test. It would therefore be highly desirable to save time and effort during this stage by accommodating multiple inspection and test based procedures during one acquisition. Therefore, if a device under test could be suitably mounted and probed both optically and electronically, it would offer the possibility of obtaining a reflectance, a TOBIC and an OCT image of a specific area at the same time. This could enhance the efficiency of semiconductor device testing considerably and could also be simple to implement.

6.3.6 SIL-Enhanced OCT

Finally, an exciting and truly novel consideration for semiconductor device inspection would be to introduce a suitable SIL into an OCT imaging system. This proposal would

provide a natural link between the initial work concerning SIL-enhanced resolution-enhancing techniques and the latter developments of an ultra-high-resolution OCT imaging system. The performance-enhancing properties of improved lateral and axial resolution, as well as increased collection efficiency, would harness both the transmission and reflection benefits of a SIL in a unique manner. Applied to a custom OCT system this would significantly improve both the lateral profiling performance as well as the axial confinement (similar to optical coherence microscopy) required for detailed semiconductor IC analysis.

References

[1] K.A. Serrels, E. Ramsay, P.A. Dalgarno, B.D. Gerardot, J.A. O'Connor, R.H. Hadfield, R.J. Warburton, and D.T. Reid, "Solid immersion lens applications for nanophotonic devices", *Journal of Nanophotonics* **2**, 021854 (2008)

[2] E. Ramsay, K.A. Serrels, M.J. Thomson, A.J. Waddie, M.R. Taghizadeh, R.J. Warburton, and D.T. Reid, "Three-dimensional nanoscale subsurface optical imaging of silicon circuits", *Applied Physics Letters* **90**, 131101 (2007)

[3] E. Ramsay, K.A. Serrels, M.J. Thomson, A.J. Waddle, R.J. Warburton, M.R. Taghizadeh, and D.T. Reid, "Three-dimensional nanometric sub-surface imaging of a silicon flip-chip using the two-photon optical beam induced current method", *Microelectronics Reliability* **47**, 1534-1538 (2007)

[4] E. Ramsay, N. Pleynet, D. Xiao, R.J. Warburton, and D.T. Reid, "Two-photon optical-beam-induced current solid-immersion imaging of a silicon flip chip with a resolution of 325 nm", *Optics Letters* **30**, 26-28 (2005)

[5] E. Ramsay, K.A. Serrels, A.J. Waddie, M.R. Taghizadeh, and D.T. Reid, "Optical super-resolution with aperture-function engineering", *American Journal of Physics* **76**, 1002-1006 (2008)

[6] M. Leutenegger, R. Rao, R.A. Leitgeb, and T. Lasser, "Fast focus field calculations", *Optics Express* **14**, 11277-11291 (2006)

[7] K.A. Serrels, E. Ramsay, R.J. Warburton, and D.T. Reid, "Nanoscale optical microscopy in the vectorial focusing regime", *Nature Photonics* **2**, 311-314 (2008)

[8] K.A. Serrels, E. Ramsay, D.T. Reid, "70 nm resolution in subsurface optical imaging of silicon integrated-circuits using pupil-function engineering", *Applied Physics Letters* **94**, 073113 (2009)

[9] H. Liang, M.G. Cid, R.G. Cucu, G.M. Dobre, A.G. Podoleanu, J. Pedro, and D. Saunders, "En-face optical coherence tomography - a novel application of non-invasive imaging to art conservation", *Optics Express* **13**, 6133-6144 (2005)

[10] B.J. Rouba, P. Karaszkiewicz, L. Tyminska-Widmer, M. Iwanicka, M. Gora, E. Kwiatkowska, and P. Targowski. *Optical coherence tomography for non-destructive investigations of structure of objects of art*. in *9th International Conference on NDT of Art*. 2008. Jerusalem, Isreal.

[11] S.F. Pereira and A.S. van de Nes, "Superresolution by means of polarisation, phase and amplitude pupil masks", *Optics Communications* **234**, 119-124 (2004)

[12] H.X. Luo and C.H. Zhou, "Comparison of superresolution effects with annular phase and amplitude filters", *Applied Optics* **43**, 6242-6247 (2004)

[13] E. Coyne and F. Zachariasse, "A working method for prototyping solid immersion blazed-phase diffractive optics for near-infrared laser microscopy", *Journal of Micromechanics and Microengineering* **18** (2008)

[14] Y.J. Zhang, C.W. Zheng, and H.C. Xiao, "Improving the resolution of a solid immersion lens optical system using a multiphase Fresnel zone plate", *Optics and Laser Technology* **37**, 444-448 (2005)

[15] J.M. Schmitt, "OCT elastography: imaging microscopic deformation and strain of tissue", *Optics Express* **3**, 199-211 (1998)

[16] R.G. Cucu, A.G. Podoleanu, R.B. Rosen, A.B. Boxer, and D.A. Jackson, "En face polarization sensitive optical coherence tomography", *Optical Coherence Tomography and Coherence Techniques* **5140**, 113-119 (2003)

[17] K. Wiesauer, A.D.S. Dufau, E. Gotzinger, M. Pircher, C.K. Hitzenberger, and D. Stifter, "Non-destructive quantification of internal stress in polymer materials by polarisation sensitive optical coherence tomography", *Acta Materialia* **53**, 2785-2791 (2005)

[18] K. Wiesauer, M. Pircher, E. Gotzinger, C.K. Hitzenberger, R. Oster, and D. Stifter, "Investigation of glass-fibre reinforced polymers by polarisation- sensitive, ultra-high resolution optical coherence tomography: Internal structures, defects and stress", *Composites Science and Technology* **67**, 3051-3058 (2007)